

AN ABSTRACT OF THE THESIS OF

Harrison T. Ko for the degree of Master of Science in Civil Engineering presented on April 2, 2013.

Title: Hydraulic Experiments on Impact Forces from Tsunami-Driven Debris

Abstract approved: _____

Daniel T. Cox

Impact by an idealized shipping container on a column were observed for tsunami flow in a large-scale wave flume modeled at the O.H. Hinsdale Wave Research Laboratory at Oregon State University. Two specimen types, aluminum and acrylic, were tested; and each specimen was tested in two orientations, longitudinal and transverse. The debris specimens were constructed to be 1:5 scaled versions of standard shipping containers with container capacities of one twenty-foot equivalent unit (TEU). Hydraulic experiments were compared with corresponding in-air impact experiments using the same experimental configuration to assess the hydrodynamic effects in increasing the impact force. Experiments were conducted by varying flow conditions, velocity, nonstructural mass, impact angle, and debris specimen material. Hydraulic Longitudinal Aluminum Test results showed a 10% increase in measured impact force when compared to the corresponding In-Air Test. Transverse Aluminum and Longitudinal Acrylic Tests showed upwards of a 40% increase in measured impact force when compared to their corresponding In-Air Tests. The impact durations measured from the in-air test provided a lower bound for the impact duration measured for the in water tests. Hydraulic effects were shown to increase the impact duration by an average of 20%. Nonstructural mass was shown to have no significant impact on the measured peak impact force, however an increase of non-structural mass appeared to increase the measured impulse as expected.

©Copyright by Harrison T. Ko
April 2, 2013
All Rights Reserved

Hydraulic Experiments on Impact Forces from Tsunami-Driven
Debris

by

Harrison T. Ko

A THESIS

submitted to

Oregon State University

in partial fulfillment of
the requirements for the
degree of

Master of Science

Presented April 2, 2013
Commencement June 2013

Master of Science thesis of Harrison T. Ko presented on April 2, 2013.

APPROVED:

Major Professor, representing Civil Engineering

Head of the School of Civil and Construction Engineering

Dean of the Graduate School

I understand that my thesis will become part of the permanent collection of Oregon State University libraries. My signature below authorizes release of my thesis to any reader upon request.

Harrison T. Ko, Author

ACKNOWLEDGEMENTS

Funding for this research was provided by the National Science Foundation through the NSF George E. Brown, Jr. Network for Earthquake Engineering Simulation (CMMI-1041666). This funding is gratefully acknowledged. I would like to acknowledge the NSF project team of H. Ronald Riggs, Clay Naito, and Marcelo Kobayashi. I would also like to thank the Network for Earthquake Engineering Simulation (NEES) and O.H. Hinsdale Wave Research Lab Staff of Timothy Maddux, Jason Killian, Melora Park, Alicia Lyman-Holt, and Adam Ryan. REU students were also very helpful in conducting experiments, and as such I would like to acknowledge Amy Kordosky and Patrick Bassal. I would also like to thank Manfred Dittrich from the Oregon State University machine shop.

Additionally, I would like to thank my family and friends for all their support.

TABLE OF CONTENTS

	<u>Page</u>
1 Introduction	1
2 Literature Review	3
3 Materials and Methods	9
3.1 Methodology	9
3.1.1 Large Wave Flume and Wavemaker	9
3.1.2 Instrumentation	10
3.1.2.1 Wave Gages	11
3.1.2.1.1 Resistance	11
3.1.2.1.2 Ultrasonic	12
3.1.2.2 Acoustic Doppler Velocimeters (ADV)	13
3.1.2.3 Cameras	13
3.1.2.3.1 Panasonic HD Integrated Cameras	13
3.1.2.3.2 Panasonic High Definition Video Camera	13
3.1.2.3.3 GoPro HERO2	13
3.1.2.4 Load Cells	14
3.1.2.4.1 CLC-300K	14
3.1.2.4.2 HSW-50K	14
3.1.2.4.3 Waterproofing	15
3.1.2.5 Strain Gages	16
3.1.2.6 Column Assembly	17
3.1.2.6.1 Column	17
3.1.2.6.2 Supports	19
3.1.2.6.3 Sleeve	19
3.1.3 Specimen	20
3.1.3.1 Aluminum	22
3.1.3.2 Acrylic	23
3.1.3.3 Nonstructural Mass	24
3.1.4 Guide Wires	26
3.1.4.1 Longitudinal	26
3.1.4.2 Transverse	27
3.1.5 Optical Tracking Methods	28
3.1.5.1 Hydrodynamics (PIV)	28
3.1.5.2 In-Air Test	33
3.1.5.3 In-Water Test	36

TABLE OF CONTENTS (Continued)

	<u>Page</u>
3.1.5.3.1 Velocity Tracking	36
3.1.5.3.2 Angle Measurement	40
3.1.6 Wave Conditions	42
3.1.6.1 Wave Paddle Displacement	42
3.1.6.2 Hydrodynamics Test	44
3.1.6.3 In-Water Test	45
3.2 Test Plan	46
3.2.1 Hydrodynamics Test	46
3.2.1.1 Setup	46
3.2.1.2 Examples of Data	47
3.2.1.3 Repeatability	49
3.2.2 In-Air Test	50
3.2.2.1 Longitudinal Aluminum	51
3.2.2.1.1 Setup	51
3.2.2.1.2 Examples of Data	54
3.2.2.1.3 Repeatability	57
3.2.2.1.4 Load Cell Comparison	57
3.2.2.1.4.1 CLC-300K with and without waterproofing	57
3.2.2.1.4.2 CLC-300K vs. HSW-50K	59
3.2.2.1.5 Effect of Nonstructural Mass	59
3.2.2.1.6 Contact Position Sensitivity	60
3.2.2.1.7 Pitch Angle Test	62
3.2.3 Longitudinal Acrylic	64
3.2.3.1 Setup	64
3.2.3.2 Examples of Data	66
3.2.4 Transverse Aluminum	69
3.2.4.1 Setup	69
3.2.4.2 Examples of Data	72
3.2.5 In-Water Test	75
3.2.5.1 Longitudinal Aluminum	75
3.2.5.1.1 Setup	75
3.2.5.1.2 Water depths and wave conditions	77
3.2.5.1.2.1 $h_2 = 13.3$ cm	77
3.2.5.1.2.2 $h_2 = 20.9$ cm	82
3.2.5.1.2.3 $h_2 = 30.1$ cm	83
3.2.5.1.3 Nonstructural Mass	84

TABLE OF CONTENTS (Continued)

	<u>Page</u>
3.2.5.1.3.1 $M_{NS} = 0$ kg	84
3.2.5.1.3.2 $M_{NS} = 50.2$ kg	85
3.2.5.1.3.3 $M_{NS} = 99.4$ kg	86
3.2.5.2 Longitudinal Acrylic	87
3.2.5.2.1 Setup	87
3.2.5.2.2 Water depths and wave conditions	88
3.2.5.2.2.1 $h_2 = 13.3$ cm	88
3.2.5.2.2.2 $h_2 = 20.9$ cm	90
3.2.5.2.2.3 $h_2 = 30.1$ cm	91
3.2.5.3 Transverse Aluminum	92
3.2.5.3.1 Setup	92
3.2.5.3.2 Water depths and wave conditions	93
3.2.5.3.3 Nonstructural Mass	93
3.2.5.3.3.1 $M_{NS} = 0$ kg	93
3.2.5.3.3.2 $M_{NS} = 50.2$ kg	95
3.2.5.4 Unconstrained Aluminum	96
3.2.5.4.1 Setup	96
3.2.5.4.2 Examples of Data	97
3.2.5.5 Destructive	99
3.2.5.5.1 Setup	100
3.2.5.5.2 Examples of Data	100
 4 Results	 103
4.1 Hydrodynamics Test	103
4.1.1 Comparison of ADV to PIV measurements	103
4.1.2 Flow Speed vs. Error Function Period	103
4.2 In-Air Test	104
4.2.1 Longitudinal Aluminum	104
4.2.2 Longitudinal Acrylic	105
4.2.3 Transverse Aluminum	106
4.2.4 Comparisons	107
4.2.5 Impulse	108
4.2.5.1 Comparison of Different Tests	109
4.2.5.2 Effect of Nonstructural Mass	111
4.3 In-Water Test	112

TABLE OF CONTENTS (Continued)

	<u>Page</u>
4.3.1 Longitudinal Aluminum	112
4.3.1.1 Flow Speed vs. Impact Velocity	112
4.3.1.2 Impact Force Time History comparison	115
4.3.1.2.1 Comparison to In-Air Impact Force	115
4.3.1.2.2 Comparison of Nonstructural Masses	119
4.3.1.3 Peak Force vs. Impact Velocity	126
4.3.1.3.1 Scatter Plot	126
4.3.1.3.2 Averaged by Wave Condition	127
4.3.1.3.3 Normalized by Corresponding In-Air Impact Force	128
4.3.1.3.4 Incremental Difference	129
4.3.1.4 Impact Duration	130
4.3.1.5 Normalized Impact Force vs. Froude Number	131
4.3.1.6 Impulse	132
4.3.1.6.1 J_p	133
4.3.1.6.2 J_{30}	134
4.3.1.6.3 J_p vs. J_{30}	135
4.3.2 Longitudinal Acrylic	136
4.3.2.1 Flow Speed vs. Impact Velocity	136
4.3.2.2 Impact Force Time History comparison	138
4.3.2.3 Peak Force vs. Impact Velocity	140
4.3.2.3.1 Scatter Plot	140
4.3.2.3.2 Averaged by Wave Condition	141
4.3.2.3.3 Normalized by Corresponding In-Air Impact Force	142
4.3.2.3.4 Incremental Difference	143
4.3.2.4 Impact Duration	144
4.3.2.5 Normalized Impact Force vs. Froude Number	145
4.3.2.6 Impulse	146
4.3.2.6.1 J_p	146
4.3.2.6.2 J_{30}	147
4.3.2.6.3 J_p vs. J_{30}	148
4.3.3 Transverse Aluminum	149
4.3.3.1 Flow Speed vs. Impact Velocity	149
4.3.3.2 Impact Force Time History comparison	151
4.3.3.2.1 Comparison to In-Air Impact Force	151
4.3.3.2.2 Comparison of Nonstructural Masses	153
4.3.3.3 Peak Force vs. Impact Velocity	155

TABLE OF CONTENTS (Continued)

	<u>Page</u>
4.3.3.3.1 Scatter Plot	155
4.3.3.3.2 Normalized by Corresponding In-Air Impact Force	156
4.3.3.3.3 Incremental Difference	157
4.3.3.4 Impact Duration	158
4.3.3.5 Normalized Impact Force vs. Froude Number	159
4.3.3.6 Impulse	160
4.3.3.6.1 J_p	160
4.3.3.6.2 J_{30}	161
4.3.3.6.3 J_p vs. J_{30}	162
4.3.4 Unconstrained Aluminum	163
4.3.4.1 Impact Angle Histogram	163
4.3.4.2 Impact Angle Histogram Separated by Initial Orientation .	164
5 Discussion	166
5.1 Hydrodynamics Test	166
5.1.1 Idealized Inundation Flow	166
5.1.2 Surface PIV	167
5.2 In-Air Test	167
5.2.1 Peak Impact Force vs. Impact Velocity	167
5.2.2 Load Cells	167
5.2.3 Contact Area Considerations	168
5.2.4 Slope Comparison	168
5.2.5 Impulse vs. Impact Velocity	169
5.2.6 Impact Duration	169
5.3 In-Water Test	173
5.3.1 Peak Impact Force vs. Impact Velocity	173
5.3.2 Load Cell Viability	173
5.3.3 Impact Force Variability	174
5.3.4 Nonstructural Mass Effect	174
5.3.5 Slope Comparison	175
5.3.6 Impact Duration	177
5.3.7 The “Added Mass” Effect	180
6 Conclusion	182

TABLE OF CONTENTS (Continued)

	<u>Page</u>
Appendices	188
A Notation	189
A.1 List of Variables	190
B List of Experiments	192
B.1 NEES Notebook Naming Convention	193

LIST OF FIGURES

Figure	Page
3.1 Large Wave Flume setup at O.H. Hinsdale Wave Research Laboratory. “wg” refers to resistance wave gage locations, “uswg” refers to ultrasonic wave gage locations, and “adv” refers to velocimeter locations. Test section was located between bays 17 and 18. Figure created by Timothy Maddux. . . .	10
3.2 Ultrasonic wave gage installed in wave flume. Location uswg3 is shown. . .	12
3.3 CLC-300K load cell, (A) front view, (B) side view	14
3.4 HSW-50K load cell, (A) front view with rounded button, (B) side view with standard button	15
3.5 Waterproofing material applied to CLC-300K load cell	16
3.6 Strain gage adhered to side opposite of load cell on column assembly	17
3.7 Strain gage adhered to load cell side of column assembly	17
3.8 View of column assembly facing opposite the wave paddle. Dimensions are included.	18
3.9 View of column assembly facing the wave paddle.	18
3.10 Photograph of one of the supports of the column assembly on the wave flume wall. Identical support is located on the opposite wall. Dimensions are included.	19
3.11 Photograph of stainless steel sleeve used to attach the load cell to the column assembly. Manufactured to allow sleeve to move up and down the column. .	20
3.12 Schematic for debris specimen. The dimensions shown in this drawing were used to manufacture both of the specimen. These dimensions correspond to a 1:5 scale model of the standard 20 ft (6.10 m) intermodal container. . . .	21
3.13 Orientation convention for debris specimen in large wave flume. Longitudinal orientation was defined as when the major axis of the debris specimen was parallel to the x-axis. Longitudinal orientation corresponded to an impact angle of 0°. Transverse orientation was defined as when the minor axis of the debris specimen was parallel to the x-axis. Transverse orientation corresponded to an impact angle of 90°.	22
3.14 Photographs shown for aluminum debris specimen, (A) side view with lid removed (B) front view with lid removed (C) top view with lid.	23

LIST OF FIGURES (Continued)

<u>Figure</u>	<u>Page</u>
3.15 Photographs of acrylic debris specimen.	24
3.16 Photograph of nonstructural mass placed in aluminum debris specimen. Four hot rolled steel plates with wooden block supports are shown.	25
3.17 Another view of nonstructural mass inside aluminum specimen. Photograph is shown after in-air trial is performed. Steel plates are shown to have shifted to the front of the specimen.	25
3.18 Photograph of guide wire setup for longitudinal in-water test.	27
3.19 Photograph of guide wire setup for transverse in-water test. The tethers shown in the photograph were used to position the specimen for each trial as well as maintain orientation during each trial.	28
3.20 Video sequence of hydrodynamics test trial number 3 for water depth of $h_2 = 0$ for times, (A) 60 s, (B) 61 s, (C) 62 s.	29
3.21 Video sequence, converted to binary (black and white) of hydrodynamics test trial number 3 for water depth of $h_2 = 0$ for times, (A) 60 s, (B) 61 s, (C) 62 s.	29
3.22 PIV analysis performed on video section associated with Fig. 3.21B using PIVlab in Matlab. Green arrows represent unfiltered velocity vectors, yellow arrows represent filtered vectors.	31
3.23 Styrofoam packing peanuts were added to the wave flume as seeding material to track the water surface.	32
3.24 The seeded water surface shown in Fig. 3.23 converted to a binary image. .	32
3.25 PIV analysis performed on seeded water flowing at $h_2 = 13.3$ cm with $T_{erf} =$ 30 s.	33
3.26 Video frame of In-Air Longitudinal Test using Panasonic HD camera. The view point of this frame was used to track the velocity of the debris as it swung and collided with the load cell. The orange circle painted in the bottom right hand corner of the specimen was used to track debris movement.	34

LIST OF FIGURES (Continued)

<u>Figure</u>	<u>Page</u>
3.27 Tracking algorithm applied to in-air longitudinal aluminum test. The trajectory of the orange circle is shown by the lines connecting the red dots. A bounding box is plotted around the object of interest in each frame to ensure that the correct object is being tracked. Note that the orange circle is being tracked, not the bounding box.	35
3.28 Video frame of in-water longitudinal test captured using overhead Panasonic HD integrated camera before perspective correction.	37
3.29 Video frame of in-water longitudinal test captured using overhead Panasonic HD integrated camera after perspective correction.	38
3.30 Video sequence of tracking algorithm applied to trial 12 from in-water longitudinal aluminum test at $h_2 = 13.3$ cm at times (A) 1 s (B) 3 s (C) 5 s (D) 6 s.	38
3.31 Velocity tracking output from in-water longitudinal aluminum test shown in Fig. 3.30. Debris velocity shown in the top plot, debris orientation shown in bottom plot.	39
3.32 Velocity tracking output from stationary debris specimen in large wave flume.	40
3.33 Detected edges plotted on top of original binary image for debris specimen in large wave flume.	41
3.34 Wave paddle displacement for error function periods used in this study. Full 4 m stroke was used for all periods.	42
3.35 Offshore wave heights measured at wg1 for certain T_{erf} . Wave gage measurement were taken at a water depth of $h_1 = 266.4$ cm, $h_2 = 30.1$ cm . . .	43
3.36 Inundation depths measured at uswg4 for certain T_{erf} . Wave gage measurement were taken at a water depth of $h_1 = 266.4$ cm, $h_2 = 30.1$ cm	44
3.37 Example of Hydrodynamic Test data from trial 8: $h_1 = 2.47$ m, $h_2 = 0.103$ m, $T_{erf} = 30$ s. Sampling locations for each instrument correspond with Fig. 3.1. Time axes were synchronized with the start signal of the wavemaker.	48
3.38 Time variation of wave paddle displacement and free surface variation from Hydrodynamics Test trials 17-21. Test conditions of: $h_1 = 2.57$ m, $h_2 = 0.203$ m, $T_{erf} = 20$ s. All 5 tests are superimposed onto one another. . . .	49

LIST OF FIGURES (Continued)

<u>Figure</u>	<u>Page</u>
3.39 Standard deviations of time variation of wave paddle displacement and free surface variation from Hydrodynamics Test trials 17-21. Test conditions of: $h_1 = 2.57$ m, $h_2 = 0.203$ m, $T_{erf} = 20$ s. Note that the y -axis on panel 4 has twice the order of magnitude of the other 3 panels.	50
3.40 Schematic for In-Air longitudinal test.	51
3.41 Resting point for debris specimen relative to load cell during In-Air longitudinal aluminum test.	52
3.42 Measuring tape used to measure pullback distance, X	53
3.43 Pullback process of debris specimen for longitudinal aluminum test.	53
3.44 Plot of debris impact velocity, v_I vs. pullback distance, X for In-Air longitudinal test.	54
3.45 Impact force time history measured by waterproofed CLC-300K load cell for In-Air longitudinal aluminum test trial 8 at $v_I = 1.41$ m/s	55
3.46 Detail of impact force time history over 5 s, measured by waterproofed CLC-300K load cell for In-Air longitudinal aluminum test trial 8 at $v_I = 1.41$ m/s	56
3.47 Detail of impact force time history over 100 ms, measured by waterproofed CLC-300K load cell for In-Air longitudinal aluminum test trial 8 at $v_I = 1.41$ m/s	56
3.48 Detail of impact force time history over 2 ms, measured by waterproofed CLC-300K load cell for In-Air longitudinal aluminum test trial 8 at $v_I = 1.41$ m/s	57
3.49 Comparison of peak force, F_p vs. impact velocity, v_I for the waterproofed and CLC-300K load cell before waterproofing. Forces measured from waterproofed load cell (\blacklozenge), forces measured from load cell before waterproofing (\blacklozenge). Data measured from In-Air longitudinal aluminum test.	58
3.50 Comparison of peak force, F_p vs. impact velocity, v_I for the HSW-50K and waterproofed CLC-300K load cell. CLC-300K load cell (\bullet), HSW-50K load cell (\blacktriangleright). Data measured from In-Air longitudinal aluminum test.	59

LIST OF FIGURES (Continued)

<u>Figure</u>	<u>Page</u>
3.51 Comparison of peak force, F_p vs. impact velocity, v_I for nonstructural mass values of $M_{NS} = 0$ and $M_{NS} = 50.2$ kg. $M_{NS} = 0$ kg (\circ), $M_{NS} = 50.2$ kg (\bullet). Data measured from In-Air longitudinal aluminum test.	60
3.52 Photographs of the “centered” and “off-center” contact positions for the In-Air longitudinal aluminum test.	61
3.53 Comparison of peak force, F_p vs. impact velocity, v_I for “centered” and “off-center” contact positions between aluminum debris specimen and load cell for In-Air longitudinal aluminum test. “Centered” contacts (\bullet), “off-center” contacts (\blacktriangle).	62
3.54 Pitch angle (ϕ) test setup with (a) $\phi = 0^\circ$ (b) $\phi = 5.7^\circ$	63
3.55 Effect of pitch angle (ϕ) on measured peak impact force. $\phi = 0^\circ$ (\circ), $\phi = 3.0^\circ$ (\blacktriangle), $\phi = 5.7^\circ$ (\square).	64
3.56 Photograph of the setup for the In-Air longitudinal acrylic test.	65
3.57 Plot of debris impact velocity, v_I vs. pullback distance, X for In-Air acrylic test.	66
3.58 Impact force time history measured by waterproofed CLC-300K load cell for In-Air longitudinal acrylic test trial 4 at $v_I = 0.72$ m/s detailed over 10 s.	67
3.59 Detail of impact force time history over 1 s, measured by waterproofed CLC-300K load cell for In-Air longitudinal acrylic test trial 4 at $v_I = 0.72$ m/s.	67
3.60 Detail of impact force time history over 100 ms, measured by waterproofed CLC-300K load cell for In-Air longitudinal acrylic test trial 4 at $v_I = 0.72$ m/s.	68
3.61 Detail of impact force time history over 10 ms, measured by waterproofed CLC-300K load cell for In-Air longitudinal acrylic test trial 4 at $v_I = 0.72$ m/s.	68
3.62 Detail of impact force time history over 4 ms, measured by waterproofed CLC-300K load cell for In-Air longitudinal acrylic test trial 4 at $v_I = 0.72$ m/s	69
3.63 Schematic for In-Air transverse aluminum test.	70
3.64 Photograph of the In-Air transverse aluminum test.	71

LIST OF FIGURES (Continued)

<u>Figure</u>	<u>Page</u>
3.65 Plot of debris impact velocity, v_I vs. pullback distance, X for In-Air transverse test.	72
3.66 Impact force time history measured by waterproofed CLC-300K load cell for In-Air transverse aluminum test trial 9 at $v_I = 0.59$ m/s	73
3.67 Detail of impact force time history over 1 s, measured by waterproofed CLC-300K load cell for In-Air transverse aluminum test trial 9 at $v_I = 0.59$ m/s	73
3.68 Detail of impact force time history over 100 s, measured by waterproofed CLC-300K load cell for In-Air transverse aluminum test trial 9 at $v_I = 0.59$ m/s	74
3.69 Detail of impact force time history over 10 ms, measured by waterproofed CLC-300K load cell for In-Air transverse aluminum test trial 9 at $v_I = 0.59$ m/s	74
3.70 Detail of impact force time history over 4.5 ms, measured by waterproofed CLC-300K load cell for In-Air transverse aluminum test trial 9 at $v_I = 0.59$ m/s	75
3.71 Examples of (A) “Bad” contact and (B) “Good” contact between debris specimen and load cell as observed underwater with GoPro HERO2.	76
3.72 Time variation of free surface elevation and force response from In-Water longitudinal aluminum test: $h_1 = 2.50$ m, $h_2 = 0.13$ m, $T_{erf} = 30$ s, trial 12.	78
3.73 Detail of impact force time history over 5 s, for In-Water longitudinal aluminum test: $h_1 = 2.50$ m, $h_2 = 0.13$ m, $T_{erf} = 30$ s, trial 12.	79
3.74 Detail of impact force time history over 0.2 s, for In-Water longitudinal aluminum test: $h_1 = 2.50$ m, $h_2 = 0.13$ m, $T_{erf} = 30$ s, trial 12.	79
3.75 Detail of impact force time history over 0.003 s, for In-Water longitudinal aluminum test: $h_1 = 2.50$ m, $h_2 = 0.13$ m, $T_{erf} = 30$ s, trial 12.	80
3.76 Detail of impact force time history over 0.003 s, for In-Water longitudinal aluminum test: $h_1 = 2.50$ m, $h_2 = 0.13$ m, $T_{erf} = 30$ s, trial 12.	80
3.77 Impact force time histories of five trials, detailed over 0.003 s, for In-Water longitudinal aluminum test: $h_1 = 2.50$ m, $h_2 = 0.13$ m, $T_{erf} = 30$ s, trial 11-15.	81

LIST OF FIGURES (Continued)

<u>Figure</u>	<u>Page</u>
3.78 Impact force time histories of trials 7, 11, 18, 26. Each trial represents one of the T_{erf} used for In-Water longitudinal aluminum test: $h_1 = 2.50$ m, $h_2 = 0.13$ m	82
3.79 Impact force time histories of trials 3, 10, 14, 20. Each trial represents one of the T_{erf} used for In-Water longitudinal aluminum test: $h_1 = 2.57$ m, $h_2 = 0.209$ m	83
3.80 Impact force time histories of trials 1, 7, 15, 22, 27. Each trial represents one of the T_{erf} used for In-Water longitudinal aluminum test: $h_1 = 2.57$ m, $h_2 = 0.30$ m	84
3.81 Impact force time histories In-Water longitudinal aluminum test with $M_{NS} = 0$ kg and $T_{erf} = 30$ s. One representative time history for each of the water depths shown. t' refers to an adjusted time scale where $t' = 0$ is the start of impact.	85
3.82 Impact force time histories In-Water longitudinal aluminum test with $M_{NS} = 50.2$ kg and $T_{erf} = 30$ s. One representative time history for each of the water depths shown.	86
3.83 Impact force time histories In-Water longitudinal aluminum test with $M_{NS} = 99.4$ kg and $T_{erf} = 30$ s. One representative time history for each of the water depths shown.	87
3.84 Photograph of setup for In-Water longitudinal acrylic test.	88
3.85 Impact force time histories of trials 24-29 of In-Water longitudinal acrylic test at $h_1 = 2.50$ m, $h_2 = 0.13$ m, $T_{erf} = 30$ s. Each trial had identical conditions.	89
3.86 Impact force time histories of trials 5, 11, 20, 26 of In-Water longitudinal acrylic test at $h_1 = 2.50$ m, $h_2 = 0.13$ m. Each trial represents the maximum force measured for each T_{erf} used.	90
3.87 Impact force time histories of trials 3, 9, 15, 18 of In-Water longitudinal acrylic test at $h_1 = 2.57$ m, $h_2 = 0.21$ m. Each trial represents the maximum force measured for each T_{erf} used.	91
3.88 Impact force time histories of trials 1, 2, 4, 6 and 7 of In-Water longitudinal acrylic test at $h_1 = 2.66$ m, $h_2 = 0.301$ m, $T_{erf} = 20$ s. Each trial had identical conditions.	92

LIST OF FIGURES (Continued)

<u>Figure</u>	<u>Page</u>
3.89 Impact force time histories of trials 16, 18, 19, 20, 21, and 22 of In-Water transverse aluminum test at $h_1 = 2.66$ m, $h_2 = 0.301$ m, $T_{erf} = 30$ s with $M_{NS} = 0$. Each trial had identical conditions.	94
3.90 Impact force time histories of trials 2, 11, 16 and 28 of In-Water transverse aluminum test at $h_1 = 2.66$ m, $h_2 = 0.301$ m with $M_{NS} = 0$ kg. Each trial represented the maximum impact force measured for each T_{erf}	95
3.91 Impact force time histories of trials 2, 11, 16 and 28 of In-Water transverse aluminum test at $h_1 = 2.66$ m, $h_2 = 0.301$ m with $M_{NS} = 50.2$ kg. Each trial represented the maximum impact force measured for each T_{erf}	96
3.92 Video sequence of unconstrained In-Water aluminum test trial 27.	97
3.93 Velocity and orientation output from unconstrained In-Water aluminum test trial 27.	98
3.94 Impact force time histories from various measured impact angles, θ_f . Time histories aligned at peak forces for clarity.	99
3.95 Photograph of destructive test right before impact.	100
3.96 Impact force time histories for Destructive Test trials 1-6. Each test was run at $T_{erf} = 40$ s.	101
3.97 Impact force time histories for Destructive Test trials 2 and 7. Trial 2 represents the highest impact force measured for $T_{erf} = 40$ s, trial 7 represents the highest impact force measured for $T_{erf} = 25$ s.	102
4.1 Maximum flow speed measured by surface PIV compared against T_{erf} for different water depths. $h_2 = 13.3$ cm (\circ), $h_2 = 20.9$ cm (\triangle), $h_2 = 30.1$ cm (\square).	104
4.2 F_p plotted against v_I for the In-Air longitudinal aluminum test. Trials conducted before the In-Water test (\circ), trials conducted after the In-Water test (\bullet). The black line fitted to the data had a slope of 48.5 kN s/m.	105
4.3 F_p plotted against v_I for the In-Air longitudinal acrylic test. The black line fitted to the data had a slope of 26.12 kN s/m.	106
4.4 F_p plotted against v_I for the In-Air transverse aluminum test. The black line fitted to the data had a slope of 35.22 kN s/m.	107

LIST OF FIGURES (Continued)

Figure	Page
4.5 F_p plotted against v_I for the all of the In-Air tests. The fitted black lines from Fig. 4.2 - 4.4 are shown. Longitudinal aluminum (\bullet), longitudinal acrylic (\diamond), transverse aluminum (\square).	108
4.6 Definition of integration regions for impulse variables J_p and J_{30} on an impact force time series from In-Water Longitudinal Aluminum Test with 99.4 kg of nonstructural mass.	109
4.7 Comparison of J_p vs. v_I calculated from the In-Air longitudinal aluminum (\circ), longitudinal acrylic (\diamond), and transverse aluminum tests (\square).	110
4.8 Comparison of J_{30} vs. v_I calculated from the In-Air longitudinal aluminum (\circ), longitudinal acrylic (\diamond), and transverse aluminum tests (\square).	110
4.9 Comparison of J_p vs. v_I calculated from the In-Air longitudinal aluminum test with $M_{NS} = 0$ kg (\circ) and $M_{NS} = 50.2$ kg (\bullet).	111
4.10 Comparison of J_{30} vs. v_I calculated from the In-Air longitudinal aluminum test with $M_{NS} = 0$ kg (\circ) and $M_{NS} = 50.2$ kg (\bullet).	112
4.11 Maximum flow speeds compared with debris impact velocities for In-Water longitudinal aluminum tests. For flow speeds, $h_2 = 13.3$ cm (\circ), $h_2 = 20.9$ cm (Δ), $h_2 = 30.1$ cm (\square). For debris impact velocities, $M_{NS} = 0$ kg (\cdot), $M_{NS} = 50.2$ kg (\times), $M_{NS} = 99.4$ kg ($+$). Red represents $h_2 = 13.3$ cm, blue represents $h_2 = 20.9$ cm, and magenta represents $h_2 = 30.1$ cm.	113
4.12 Normalized aluminum debris impact velocities, v^* with respect to the average measured surface flow speeds from PIV. The impact velocities from Fig. 4.11 were divided by the flow velocity lines shown. $M_{NS} = 0$ kg (\cdot), $M_{NS} = 50.2$ kg (\times), $M_{NS} = 99.4$ kg ($+$). Red represents $h_2 = 13.3$ cm, blue represents $h_2 = 20.9$ cm, and magenta represents $h_2 = 30.1$ cm.	114
4.13 Average impact force time history for In-Water longitudinal aluminum test with $v_I = 0.66$ m/s. Determined from 5 time histories, 90% confidence interval for peak force shown. Thick black line represents averaged impact force time history.	115

LIST OF FIGURES (Continued)

<u>Figure</u>	<u>Page</u>
4.14 Average impact force time history for In-Water longitudinal aluminum test with $v_I = 0.66$ m/s compared with In-Air longitudinal aluminum test at approximately the same impact velocity. 90% confidence interval for peak force for In-Water test shown. Dashed line represents In-Air impact force time history.	116
4.15 Average impact force time history for In-Water longitudinal aluminum test with $v_I = 0.85$ m/s. Determined from 5 time histories, 90% confidence interval for peak force shown. Thick black line represents averaged impact force time history.	117
4.16 Average impact force time history for In-Water longitudinal aluminum test with $v_I = 0.85$ m/s compared with In-Air longitudinal aluminum test at approximately the same impact velocity. In-Air impact force impact history (- - -).	117
4.17 Average impact force time history for In-Water longitudinal aluminum test with $v_I = 1.2$ m/s. Determined from 5 time histories, 90% confidence interval for peak force shown. Thick black line represents averaged impact force time history.	118
4.18 Average impact force time history for In-Water longitudinal aluminum test with $v_I = 1.2$ m/s compared with In-Air longitudinal aluminum test at approximately the same impact velocity. In-Air impact force impact history (- - -).	119
4.19 Impact force time history for In-Water longitudinal aluminum test trial 12 at $h_2 = 30.1$ cm with $M_{NS} = 0$ kg, $T_{erf} = 30$ s, $v_I = 0.75$ m/s.	120
4.20 Impact force time history for In-Water longitudinal aluminum test trial 12 at $h_2 = 30.1$ cm with $M_{NS} = 50.2$ kg, $T_{erf} = 30$ s, $v_I = 0.75$ m/s.	121
4.21 Impact force time history for In-Water longitudinal aluminum test trial 19 at $h_2 = 30.1$ cm with $M_{NS} = 99.4$ kg, $T_{erf} = 30$ s, $v_I = 0.71$ m/s	121
4.22 Average impact force time history for In-Water longitudinal aluminum test at $h_2 = 30.1$ cm with $v_I = 0.90$ m/s and $M_{NS} = 0$ kg. Determined from 5 time histories. Thick black line represents averaged impact force time history.122	

LIST OF FIGURES (Continued)

<u>Figure</u>	<u>Page</u>
4.23 Average impact force time history for In-Water longitudinal aluminum test at $h_2 = 30.1$ cm with $v_I = 0.90$ m/s and $M_{NS} = 50.2$ kg. Determined from 5 time histories. Thick black line represents averaged impact force time history.	123
4.24 Average impact force time history for In-Water longitudinal aluminum test at $h_2 = 30.1$ cm with $v_I = 0.86$ m/s and $M_{NS} = 99.4$ kg. Determined from 5 time histories. Thick black line represents averaged impact force time history.	123
4.25 Comparison between impact force time histories of different M_{NS} for In-Water longitudinal aluminum test. $M_{NS} = 0$ kg (blue -), $M_{NS} = 50.2$ kg (red - - -), $M_{NS} = 99.4$ kg (black \cdots). $v_I = 0.90$ m/s for $M_{NS} = 0$ kg and $M_{NS} = 50.2$ kg. $v_I = 0.86$ m/s for $M_{NS} = 99.4$ kg.	124
4.26 Impact force time histories for In-Water longitudinal aluminum test, five trials superimposed on one another at $h_2 = 30.1$ cm with $M_{NS} = 0, 50.2,$ and 99.4 kg, $T_{erf} = 30$ s, $v_I \sim 0.9$ m/s.	125
4.27 Average impact force time histories for In-Water longitudinal aluminum test superimposed on one another at $h_2 = 30.1$ cm with $M_{NS} = 0, 50.2,$ and 99.4 kg, $T_{erf} = 30$ s, $v_I \sim 0.9$ m/s. $M_{NS} = 0$ kg (blue -), $M_{NS} = 50.2$ kg (red - - -), $M_{NS} = 99.4$ kg (black \cdots)	126
4.28 Plot of F_p vs. v_I for the In-Water longitudinal aluminum tests. $h_2 = 13.3$ cm, $M_{NS} = 0$ kg (red \circ). $h_2 = 20.9$ cm, $M_{NS} = 0$ kg (blue \triangleright). $h_2 = 20.9$ cm, $M_{NS} = 99.4$ kg (blue \square). $h_2 = 30.1$ cm, $M_{NS} = 0$ kg (black \square). $h_2 = 30.1$ cm, $M_{NS} = 50.2$ kg (black \blacksquare). $h_2 = 30.1$ cm, $M_{NS} = 99.4$ kg (black \blacklozenge). In-Air longitudinal aluminum test (-) (Fig. 4.2).	127
4.29 Plot of F_p vs. v_I for all In-Water longitudinal aluminum tests, averaged by T_{erf} . $h_2 = 13.3$ cm, $M_{NS} = 0$ kg (red \circ). $h_2 = 20.9$ cm, $M_{NS} = 0$ kg (blue \triangleright). $h_2 = 20.9$ cm, $M_{NS} = 99.4$ kg (blue \square). $h_2 = 30.1$ cm, $M_{NS} = 0$ kg (black \square). $h_2 = 30.1$ cm, $M_{NS} = 50.2$ kg (black \blacksquare). $h_2 = 30.1$ cm, $M_{NS} = 99.4$ kg (black \blacklozenge). In-Air longitudinal aluminum test (-) (Fig. 4.2). 90% confidence intervals for velocity and peak force shown.	128
4.30 Plot of In-Water peak force normalized by empirically determined In-Air impact force, F_N , vs. v_I for the In-Water longitudinal aluminum tests. $h_2 = 13.3$ cm, $M_{NS} = 0$ kg (red \circ). $h_2 = 20.9$ cm, $M_{NS} = 0$ kg (blue \triangleright). $h_2 = 20.9$ cm, $M_{NS} = 99.4$ kg (blue \square). $h_2 = 30.1$ cm, $M_{NS} = 0$ kg (black \square). $h_2 = 30.1$ cm, $M_{NS} = 50.2$ kg (black \blacksquare). $h_2 = 30.1$ cm, $M_{NS} = 99.4$ kg (black \blacklozenge)	129

LIST OF FIGURES (Continued)

<u>Figure</u>		<u>Page</u>
4.31	Plot of the numerical difference between In-Water peak force and the empirically determined In-Air impact force, F_d , vs. v_I for the In-Water longitudinal aluminum tests. $h_2 = 13.3$ cm, $M_{NS} = 0$ kg (red \circ). $h_2 = 20.9$ cm, $M_{NS} = 0$ kg (blue \triangleright). $h_2 = 20.9$ cm, $M_{NS} = 99.4$ kg (blue \square). $h_2 = 30.1$ cm, $M_{NS} = 0$ kg (black \square). $h_2 = 30.1$ cm, $M_{NS} = 50.2$ kg (black \blacksquare). $h_2 = 30.1$ cm, $M_{NS} = 99.4$ kg (black \blacklozenge)	130
4.32	Plot of impact duration, t_i , vs. v_I for the In-Water longitudinal aluminum tests. $h_2 = 13.3$ cm, $M_{NS} = 0$ kg (red \circ). $h_2 = 20.9$ cm, $M_{NS} = 0$ kg (blue \triangleright). $h_2 = 20.9$ cm, $M_{NS} = 99.4$ kg (blue \square). $h_2 = 30.1$ cm, $M_{NS} = 0$ kg (black \square). $h_2 = 30.1$ cm, $M_{NS} = 50.2$ kg (black \blacksquare). $h_2 = 30.1$ cm, $M_{NS} = 99.4$ kg (black \blacklozenge), Measured t_i from In-Air test ($-\bullet$).	131
4.33	Plot of F_N vs. Fr for the In-Water longitudinal aluminum tests. $h_2 = 13.3$ cm, $M_{NS} = 0$ kg (red \circ). $h_2 = 20.9$ cm, $M_{NS} = 0$ kg (blue \triangleright). $h_2 = 20.9$ cm, $M_{NS} = 99.4$ kg (blue \square). $h_2 = 30.1$ cm, $M_{NS} = 0$ kg (black \square). $h_2 = 30.1$ cm, $M_{NS} = 50.2$ kg (black \blacksquare). $h_2 = 30.1$ cm, $M_{NS} = 99.4$ kg (black \blacklozenge). . .	132
4.34	Integration regions defined for impulse values J_p and J_{30} shown on average impact force time histories for In-Water longitudinal aluminum test superimposed on one another at $h_2 = 30.1$ cm with $M_{NS} = 0, 50.2$, and 99.4 kg, $T_{erf} = 30$ s, $v_I \sim 0.9$ m/s. $M_{NS} = 0$ kg (blue $-$), $M_{NS} = 50.2$ kg (red $---$), $M_{NS} = 99.4$ kg (black \cdots)	133
4.35	Plot of J_p vs. v_I for In-Water longitudinal aluminum tests. $h_2 = 13.3$ cm, $M_{NS} = 0$ kg (red \circ). $h_2 = 20.9$ cm, $M_{NS} = 0$ kg (blue \triangleright). $h_2 = 20.9$ cm, $M_{NS} = 99.4$ kg (blue \square). $h_2 = 30.1$ cm, $M_{NS} = 0$ kg (black \square). $h_2 = 30.1$ cm, $M_{NS} = 50.2$ kg (black \blacksquare). $h_2 = 30.1$ cm, $M_{NS} = 99.4$ kg (black \blacklozenge). In-Air longitudinal test (magenta $*$).	134
4.36	Plot of J_{30} vs. v_I for In-Water longitudinal aluminum tests. $h_2 = 13.3$ cm, $M_{NS} = 0$ kg (red \circ). $h_2 = 20.9$ cm, $M_{NS} = 0$ kg (blue \triangleright). $h_2 = 20.9$ cm, $M_{NS} = 99.4$ kg (blue \square). $h_2 = 30.1$ cm, $M_{NS} = 0$ kg (black \square). $h_2 = 30.1$ cm, $M_{NS} = 50.2$ kg (black \blacksquare). $h_2 = 30.1$ cm, $M_{NS} = 99.4$ kg (black \blacklozenge). In-Air longitudinal test (magenta $*$).	135
4.37	Plot of J_p vs. J_{30} for In-Water longitudinal aluminum tests. $h_2 = 13.3$ cm, $M_{NS} = 0$ kg (red \circ). $h_2 = 20.9$ cm, $M_{NS} = 0$ kg (blue \triangleright). $h_2 = 20.9$ cm, $M_{NS} = 99.4$ kg (blue \square). $h_2 = 30.1$ cm, $M_{NS} = 0$ kg (black \square). $h_2 = 30.1$ cm, $M_{NS} = 50.2$ kg (black \blacksquare). $h_2 = 30.1$ cm, $M_{NS} = 99.4$ kg (black \blacklozenge). . .	136

LIST OF FIGURES (Continued)

<u>Figure</u>	<u>Page</u>
4.38 Maximum flow speeds compared with debris impact velocities for In-Water longitudinal acrylic tests. For flow speeds, $h_2 = 13.3$ cm (\circ), $h_2 = 20.9$ cm (\triangle), $h_2 = 30.1$ cm (\square). Dots represent debris impact velocities. Red represents $h_2 = 13.3$ cm, blue represents $h_2 = 20.9$ cm, and magenta represents $h_2 = 30.1$ cm.	137
4.39 Normalized acrylic debris impact velocities, v^* with respect to the average measured surface flow speeds from PIV. The impact velocities from Fig. 4.38 were divided by the flow velocity lines shown. Red represents $h_2 = 13.3$ cm, blue represents $h_2 = 20.9$ cm, and magenta represents $h_2 = 30.1$ cm.	138
4.40 Average impact force time history for In-Water longitudinal acrylic test with $v_I = 0.72$ m/s. Determined from 5 time histories, 90% confidence interval for peak force shown. Thick black line represents averaged impact force time history.	139
4.41 Average impact force time history for In-Water longitudinal acrylic test with $v_I = 0.72$ m/s compared with In-Air longitudinal acrylic test at approximately the same impact velocity. Dashed line represents In-Air impact force impact history. 90% confidence interval for peak In-Water force shown.	140
4.42 Plot of F_p vs. v_I for the In-Water longitudinal acrylic tests. $h_2 = 13.3$ cm (red \circ), $h_2 = 20.9$ cm (blue \triangleright), $h_2 = 30.1$ cm (black \square). The solid black line is taken from the In-Air longitudinal acrylic test (Fig. 4.3).	141
4.43 Plot of F_p vs. v_I for all In-Water longitudinal acrylic tests, averaged by T_{erf} . $h_2 = 13.3$ cm (red \circ), $h_2 = 20.9$ cm (blue \triangleright), $h_2 = 30.1$ cm (black \square). The solid black line is taken from the In-Air longitudinal acrylic test (Fig. 4.3). 90% confidence intervals for velocity and peak force shown.	142
4.44 Plot of In-Water peak force normalized by empirically determined In-Air impact force, F_N , vs. v_I for the In-Water longitudinal acrylic tests. $h_2 = 13.3$ cm (red \circ), $h_2 = 20.9$ cm (blue \triangleright), $h_2 = 30.1$ cm (black \square)	143
4.45 Plot of the numerical difference between In-Water peak force and the empirically determined In-Air impact force, F_d , vs. v_I for the In-Water longitudinal acrylic tests. $h_2 = 13.3$ cm (red \circ), $h_2 = 20.9$ cm (blue \triangleright), $h_2 = 30.1$ cm (black \square)	144

LIST OF FIGURES (Continued)

<u>Figure</u>	<u>Page</u>
4.46 Plot t_i , vs. v_I for the In-Water longitudinal acrylic tests. $h_2 = 13.3$ cm (red \circ), $h_2 = 20.9$ cm (blue \triangleright), $h_2 = 30.1$ cm (black \square). Measured t_i from In-Air test ($-$).	145
4.47 Plot of F_N vs. Fr for the In-Water longitudinal acrylic tests. $h_2 = 13.3$ cm (red \circ), $h_2 = 20.9$ cm (blue \triangleright), $h_2 = 30.1$ cm (black \square).	146
4.48 Plot of J_p vs. v_I for the In-Water longitudinal acrylic tests. $h_2 = 13.3$ cm (red \circ), $h_2 = 20.9$ cm (blue \triangleright), $h_2 = 30.1$ cm (black \square). In-Air longitudinal acrylic test (magenta $*$).	147
4.49 Plot of J_{30} vs. v_I for the In-Water longitudinal acrylic tests. $h_2 = 13.3$ cm (red \circ), $h_2 = 20.9$ cm (blue \triangleright), $h_2 = 30.1$ cm (black \square). In-Air longitudinal acrylic test (magenta $*$).	148
4.50 Plot of J_{30} vs. J_p for the In-Water longitudinal acrylic tests. $h_2 = 13.3$ cm (red \circ), $h_2 = 20.9$ cm (blue \triangleright), $h_2 = 30.1$ cm (black \square). Slope m_0 determined by line of best fit.	149
4.51 Maximum flow speeds compared with debris impact velocities for In-Water transverse aluminum tests. Flow speeds (\square). Debris impact velocities: $M_{NS} = 0$ kg (\bullet), $M_{NS} = 50.2$ kg (x).	150
4.52 Normalized transverse aluminum debris impact velocities, v^* with respect to the average measured surface flow speeds from PIV. The impact velocities from Fig. 4.38 were divided by the flow velocity lines shown. Debris impact velocities: $M_{NS} = 0$ kg (\bullet), $M_{NS} = 50.2$ kg (x).	151
4.53 Average impact force time history for In-Water transverse aluminum test with $v_I = 0.59$ m/s. Determined from 5 time histories, 90% confidence interval for peak force shown. Thick black line represents averaged impact force time history.	152
4.54 Average impact force time history for In-Water transverse aluminum test with $v_I = 0.59$ m/s compared with In-Air transverse aluminum test at approximately the same impact velocity. Dashed line represents In-Air impact force impact history. 90% confidence interval for peak In-Water force shown.	153
4.55 Impact force time history for In-Water transverse aluminum test trial 16 at $h_2 = 30.1$ cm with $M_{NS} = 0$ kg, $T_{erf} = 30$ s, $v_I = 0.79$ m/s.	154

LIST OF FIGURES (Continued)

Figure	Page
4.56 Impact force time history for In-Water transverse aluminum test trial 18 at $h_2 = 30.1$ cm with $M_{NS} = 50.2$ kg, $T_{erf} = 30$ s, $v_I = 0.75$ m/s.	155
4.57 Plot of F_p vs. v_I for the In-Water transverse tests. $h_2 = 30.1$ cm, $M_{NS} = 0$ kg (\diamond), $h_2 = 30.1$ cm, $M_{NS} = 50.2$ kg (\blacklozenge). The solid black line is taken from the In-Air transverse aluminum test (Fig. 4.4).	156
4.58 Plot of In-Water peak force normalized by empirically determined In-Air impact force, F_N , vs. v_I for the In-Water transverse aluminum tests. $h_2 = 30.1$ cm, $M_{NS} = 0$ kg (\diamond), $h_2 = 30.1$ cm, $M_{NS} = 50.2$ kg (\blacklozenge).	157
4.59 Plot of the numerical difference between In-Water peak force and the empirically determined In-Air impact force, F_d , vs. v_I for the In-Water transverse aluminum tests. $h_2 = 30.1$ cm, $M_{NS} = 0$ kg (\diamond), $h_2 = 30.1$ cm, $M_{NS} = 50.2$ kg (\blacklozenge).	158
4.60 Plot t_i , vs. v_I for the In-Water transverse aluminum tests. $h_2 = 30.1$ cm, $M_{NS} = 0$ kg (\diamond). $h_2 = 30.1$ cm, $M_{NS} = 50.2$ kg (\blacklozenge). Measured t_i from In-Air test ($-$).	159
4.61 Plot of F_N vs. Fr for the In-Water transverse aluminum tests. $h_2 = 30.1$ cm, $M_{NS} = 0$ kg (\diamond). $h_2 = 30.1$ cm, $M_{NS} = 50.2$ kg (\blacklozenge).	160
4.62 Plot of J_p vs. v_I for the In-Water transverse aluminum tests. $h_2 = 30.1$ cm, $M_{NS} = 0$ kg (\diamond). $h_2 = 30.1$ cm, $M_{NS} = 50.2$ kg (\blacklozenge). In-Air transverse aluminum test (magenta *).	161
4.63 Plot of J_{30} vs. v_I for the In-Water transverse aluminum tests. $h_2 = 30.1$ cm, $M_{NS} = 0$ kg (\diamond). $h_2 = 30.1$ cm, $M_{NS} = 50.2$ kg (\blacklozenge). In-Air transverse aluminum test (magenta *).	162
4.64 Plot of J_{30} vs. J_p for the In-Water transverse aluminum tests. $h_2 = 30.1$ cm, $M_{NS} = 0$ kg (\diamond). $h_2 = 30.1$ cm, $M_{NS} = 50.2$ kg (\blacklozenge).	163
4.65 PDF histogram for change in debris orientation, θ_d , for all 31 Unconstrained aluminum trials.	164
4.66 PDF histogram for change in debris orientation, θ_d , separated by initial orientation, θ_i . $\theta_i = 0^\circ$ (blue $-$), $\theta_i = 90^\circ$ (green $- -$), $45^\circ \leq \theta_i \leq 71^\circ$ (red \dots).	165

LIST OF FIGURES (Continued)

<u>Figure</u>	<u>Page</u>
5.1 Plot of the measured impact duration normalized by the predicted value estimated by Eq. 5.2, t_N , for In-Air longitudinal aluminum test.	170
5.2 Plot of the measured impact duration normalized by the predicted value estimated by Eq. 5.2, t_N , for In-Air longitudinal acrylic test.	171
5.3 Plot of the measured impact duration normalized by the predicted value estimated by Eq. 5.2, t_N , for In-Air transverse aluminum test.	172
5.4 Scatter Plot of F_p vs. v_I for the In-Water longitudinal aluminum tests with line fitted to upper envelope of impact force measurements. Line fitting performed by eye, slope of the line is 54 kN s/m. $h_2 = 13.3$ cm, $M_{NS} = 0$ kg (red \circ). $h_2 = 20.9$ cm, $M_{NS} = 0$ kg (blue \triangleright). $h_2 = 20.9$ cm, $M_{NS} = 99.4$ kg (blue \triangleleft). $h_2 = 30.1$ cm, $M_{NS} = 0$ kg (black \square). $h_2 = 30.1$ cm, $M_{NS} = 50.2$ kg (black \blacksquare). $h_2 = 30.1$ cm, $M_{NS} = 99.4$ kg (black \blacklozenge).	175
5.5 Scatter Plot of F_p vs. v_I for the In-Water transverse aluminum tests with line fitted to upper envelope of impact force measurements. Line fitting performed by eye, slope of the line is 45 kN s/m. $h_2 = 30.1$ cm, $M_{NS} = 0$ kg (\diamond), $h_2 = 30.1$ cm, $M_{NS} = 50.2$ kg (\blacklozenge).	176
5.6 Combined scatter plot of F_p vs. v_I for the In-Water and In-Air aluminum tests without nonstructural mass. In-Water longitudinal: $h_2 = 13.3$ cm (red \circ), $h_2 = 20.9$ cm (blue \triangleright), $h_2 = 30.1$ cm (black \square). In-Water Transverse: $h_2 = 30.1$ cm (\diamond). In-Air longitudinal (green \bullet black $-$), In-Air transverse (cyan \blacklozenge and red $- -$).	177
5.7 Plot of the measured impact duration normalized by the predicted value estimated by Eq. 5.2, t_N , for In-Water longitudinal aluminum test. $h_2 = 13.3$ cm, $M_{NS} = 0$ kg (red \circ). $h_2 = 20.9$ cm, $M_{NS} = 0$ kg (blue \triangleright). $h_2 = 20.9$ cm, $M_{NS} = 99.4$ kg (blue \triangleleft). $h_2 = 30.1$ cm, $M_{NS} = 0$ kg (black \square). $h_2 = 30.1$ cm, $M_{NS} = 50.2$ kg (black \blacksquare). $h_2 = 30.1$ cm, $M_{NS} = 99.4$ kg (black \blacklozenge).	178
5.8 Plot of the measured impact duration normalized by the predicted value estimated by Eq. 5.2, t_N , for In-Water longitudinal acrylic test. $h_2 = 13.3$ cm (red \circ), $h_2 = 20.9$ cm (blue \triangleright), $h_2 = 30.1$ cm (black \square).	179
5.9 Plot of the measured impact duration normalized by the predicted value estimated by Eq. 5.2, t_N , for In-Water transverse aluminum test. $M_{NS} = 0$ kg (\diamond) $M_{NS} = 50.2$ kg (\blacklozenge).	180

LIST OF TABLES

<u>Table</u>		<u>Page</u>
3.1	Installment locations of instrumentation in the large wave flume. Locations are given based on the coordinate axes defined in Fig. 3.1. All units are listed in meters.	11
3.2	Flow conditions used for Hydrodynamic Experiments	45
3.3	Flow conditions used for In-Water Experiments	46
3.4	Peak force measurements from repeatability test of In-Air longitudinal aluminum test at $X = 91.44$ cm	58
4.1	Comparison of ADV to PIV measurements from wave front tracking.	103

LIST OF APPENDIX TABLES

<u>Table</u>		<u>Page</u>
B.1	List of Experiments with NEES notebook names included.	193

Chapter 1: Introduction

Tsunami-driven debris are known to pose a significant threat to structures within the inundation zone (NRC, 2004). A proper characterization of the forces involved with the debris is vital to the life-safety related to vertical tsunami evacuation shelters (FEMA, 2008). To properly design structures to withstand the demands of tsunami driven debris, it is important to quantify the impact forces generated by these events. Shipping containers are found in all parts of the world, especially at port locations. The standard 6.10 m (20 ft) shipping container has an empty mass of 2,230 kg, and a full mass of 24,000 kg, and corresponding to the shipping capacity of one twenty-foot equivalent unit (TEU). When full, this corresponds to a nominal draft of 1.58 m. Consequently, floating shipping containers are a significant debris impact threat to structures within their flow path.

Damage due to impact of shipping containers have been reported during the Indian Ocean tsunami of December 26, 2004 in Sri Lanka and Thailand (Rossetto et al., 2007) as well as recent tsunamis in Samoa on September 29, 2009 and Chile on February 27, 2010 (Robertson et al., 2010a, b). While, it may be feasible to move or secure other large debris, such as boats and heavy vehicles, with sufficient early warning, it would not be possible to transfer all of the shipping containers in a port within a short-time interval (Madurapperuma and Wijeyewickrema, 2012). Thus, it is important to consider the impact of water-borne shipping containers when designing building in tsunami inundation zones.

In this study, 1:5 scale in-water and in-air debris impact experiments were conducted in the Long Wave Flume at O.H. Hinsdale Research Lab. These experiments were part of a collaborative study involving the University of Hawaii (UH), Lehigh University (LU), and Oregon State University (OSU) on debris impact forces on structures. Numerical modeling was conducted at Hawaii University while full scale in-air impact tests were conducted at Lehigh University (Riggs et al., 2013). Experiments examined model shipping container impact on a steel column. The purpose of these experiments was to determine the difference between the impact forces measured in the in-air and in-water tests. The in-air tests were based on full scale experiments conducted at Lehigh University (Piran Aghl et al., 2013). In-water tests were conducted using inundation flow generated by wave paddle displacement which generated a similar range of debris velocities. The results between these two types

of experiments were compared against one another to quantify the hydraulic effect on the debris impact force.

Chapter 2: Literature Review

Impact from high mass debris at relatively low velocities has received some attention in literature, particularly concerning flow-driven woody debris (Haehnel and Daly, 2002, Haehnel and Daly, 2004, Matsutomi, 2009). Shipping containers have also been considered by a few authors (Mitzutani et al., 2005, Mitutani et al., 2006, Kumagai et al., 2006, Yeom et al., 2009, Madurapperuma and Wijeyewickrema, 2012). Guidelines for debris impact forces, at least in the United States, are based on rigid-body impact dynamics, as well as experimental data. Nevertheless, there is no consensus on how to define these forces (Kobayashi et al., 2012).

ASCE 7's approach is a fairly common method for quantifying the expected impact force (ASCE, 2006). This method is based on impulse momentum and two rigid bodies. The impulse momentum based approach results in the form shown in Eq. 2.1.

$$F = \frac{\pi m_p v_f}{2\Delta t} \quad (2.1)$$

where F is the maximum impact force, m_p is the total mass of the debris, v_f is the impact velocity of the debris, and Δt is the impact duration (time to reduce the debris velocity to zero). There are different recommended values for Δt used throughout literature. ASCE 7 recommends that a value of 0.03 s. The Coastal Construction Manual (CCM), using a similar formulation for impact force, recommends values from 0.1 to 1.0 s (FEMA, 2006, FEMA, 2011). From Eq. 2.1, it is clear that this discrepancy in the value of Δt results in a difference in the order of magnitude of the impact force. Hence, it is unclear what value of Δt the structural designer should use (FEMA, 2008). Additionally, some guidelines include a provision to increase the estimated impact force due to the 'added mass' of the fluid. An example is presented in Eq. 2.2 (FEMA, 2008).

$$F_i = C_m u_{max} \sqrt{k m} \quad (2.2)$$

where C_m is the added mass coefficient, u_{max} is the maximum flow velocity carrying the debris at the site, and m and k are the mass and the effective stiffness of the debris, respectively. FEMA recommended that the added mass coefficient be taken as $C_m = 2.0$.

There was, however, no justification for the value utilized for the C_m .

In addition to the impulse momentum and contact stiffness formulations, another common approach was based on work-energy and follows Eq. 2.3 (Haehnel and Daly, 2004).

$$F_i = \frac{mu_o^2}{S} = \frac{wu_o^2}{gS} \quad (2.3)$$

where w is the weight of the debris, g the gravitational constant, u_o the impact velocity, and S the stopping distance of the debris distance debris travels from the point of contact with the target until the debris is fully stopped.

The recommended formulas given by ASCE 7 and FEMA to estimate impact force due to water-borne debris are based on simplified elastic analyses (Madurapperuma and Wijeyewickrema, 2012). Peak forces calculated from these formulae disagree by an order of magnitude and thus should not be used to assess the vulnerability of a structure in a tsunami risk region (Madurapperuma and Wijeyewickrema, 2010).

Haehnel and Daly (2004) developed a 1 degree of freedom impact force model for a log impacting a structure assuming a rigid structure. The descriptive equation for the model was given by

$$(m_1 + Cm_f)\ddot{x} + \hat{k}x = 0 \quad (2.4)$$

where where m_1 = mass of the log; C = added mass coefficient; m_f = mass of the displaced fluid; and \hat{k} = effective contact stiffness of the collision. The variable x is the summation of the compression of the target face and the log during impact and rebound and the dot notation indicates the time derivative of x . Given the linear relationship between the penetration depth and the normal force, $F = \hat{k}x$, the maximum impact force, $F_{i,max}$ was predicted using

$$F_{i,max} = u_1 \sqrt{\hat{k}(m_1 + Cm_f)} \quad (2.5)$$

Eq. 2.5 follows a form very similar to Eq. 2.2. The main difference here is that the added mass coefficient, C , is in the square root, while in Eq. 2.2 it is outside of the square root.

Flume experiments were conducted with woody debris under steady flow conditions. Results suggested that the maximum impact force is a function of the impact velocity the relative velocity between the debris and structure, the mass of the debris, and the effective stiffness of the collision between the object and structure. It was independent of the properties of the structure if the structure was considered to be rigid. The added mass of the water and the eccentricity and obliqueness of the collision also affected the maximum

impact load.

Nouri et al. (2010) used flume experiments to investigate the tsunami debris impact on free standing structures. The bore used in the experiment was generated from a dam break. Hollow columns made from plexi-glass, both rectangular and circular, were tested. 2 different sized logs were used as debris specimen. Strings were attached to the sides of the log to keep the debris from washing away after impact. 2 different impoundment depths were used at 0.75 m and 1.0 m.

Observations were also made regarding the impact duration, which has been shown (see Eq. 2.1) to be a crucial factor in estimating forces on structures as it directly influences the acceleration of the debris which impacts the structure (Nouri et al., 2010). The impact was determined in a somewhat subjective manner by examining the time series. The average impact duration was found to be 0.0075 seconds. The impact duration was found to be independent of debris mass and velocity, which was not in agreement with Haehnel and Daly (2004).

Madurapperuma and Wijeyewickrema (2012), examined the impact of a tsunami water-borne shipping container on a reinforced concrete (RC) building using high-fidelity finite element analysis. It was found that peak contact forces increase almost linearly with increasing container velocity up to 2 m/s. Impact duration was found to generally decrease with increasing container velocity which contradicts observations made by Nouri et al. (2010). For the range of velocities used in the finite element analysis, the average impact duration was found to be approximately 1.4×10^{-3} s which was an on a lower order of magnitude than the value recommended by ASCE 7 (ASCE, 2008).

Another approach was presented that estimated the maximum superposed force due to simultaneous or near-simultaneous collision of pieces of driftwood accompanying tsunami inundation flow and its probability of occurrence (Matsutomi, 2009). This method was presented by examining various aspects of the collision. The aspects examined were the collision force and collision velocity, acceleration distance within which the moving velocity of floating objects became almost the same as the inundation flow velocity, duration time Δt and rise time Δt_p from star to peak collision force, and the collision probability of floating objects.

Maximum collision force F_m of a single piece of driftwood using this approach is estimated with Eq. 2.6 :

$$\frac{F_m}{\gamma D_w^2 L_w} = 1.6 C_{MA} \left(\frac{v_{A0}}{\sqrt{g D_w}} \right)^{1.2} \left(\frac{\sigma_f}{\gamma L_w} \right)^{0.4} \quad (2.6)$$

where γ was the unit weight, v_{A0} was the collision velocity, and σ_f was the yield stress of driftwood and C_{MA} is an apparent mass coefficient that depends on the size, shape, and arrangement of structures driftwood collides with, the types of flow, driftwood location in the flow field, and ranges 1.1-1.7 for driftwood located at the tip of inundation flow, 0.5-1.7 for driftwood located at the tip of a strong bore, and 1.9 for driftwood accompanying a steady flow or quasi-steady flow behind the tip of the inundation flow or strong bore.

In 2009, Yeom et al. published a computational study investigating the drift model container collision using a rigid object (Yeom et al., 2009). The results of the model were compared with scaled down flume experiments that were presented in the paper. Comparison of the model with the experiments shows that the computational model could be used as a possible analysis tool.

Recently, a study was conducted by Kobayashi et al. (2012) that formulated a one-dimensional model for acoustic wave propagation to model the impact by flexible water-borne debris. The main purpose of this paper was to disagree with the previous notion that water-borne debris impact can be dealt with using rigid-body dynamics. This paper proposes that the debris is in fact flexible when compared to the structure. Rigid-body dynamics are considered to be valid when the impact duration is much larger than the natural period of each of the impacting bodies, which is not validated in any study. An analytical solution was obtained for this model and was shown to provide a good estimate for the initial impact force and duration. Small-scale in air tests were performed to validate the model.

The solution from the 1D acoustic model agreed with the small-scale in air tests and suggested that the impact force is not a function of total mass, as assumed by previous literature. The model was also shown to be capable of dealing with the separation and re-impact of debris. The analytical 1D results were compared with the results from a 2D finite element analysis. The 1D model was suggested to not be as effective after the acoustic wave from the water reaches the wall. Based on the 2D model, the increase of the impact force by the water can be much less than the 1D model predicts.

The influence of the gravity waves on the impact force happened at a much longer timescale than the initial acoustic impact response. The effect of the gravitational phase was to retard the subsequent impact, but it did not increase the impact force. In general, the fluid did not increase the impact force for solid projectiles. For skeletal structures, such as the container, the fluid may increase the maximum impact force, because of the large fluid to-structure area ratio, but additional work was needed to quantify and clarify this.

Haehnel and Daly (2004) also considered different angles of impact in their laboratory flume experiments. In these experiments, the angle of impact was controlled, and the effect on the normalized force was observed. The experiments were conducted under steady flow conditions. Results from these experiments shows that the angle of impact had a significant effect on the force that was exerted. Haehnel and Daly define the impact angle of 0° as when the major axis of the debris is parallel to the direction of flow, and 90° as when the major axis of the debris is perpendicular to the direction of flow. It was observed that the maximum force was experienced at an impact angle of 0° and quickly dropped off as the impact angle began to increase. The normalized impact force continued to increase with impact angle until it reached 90° . Additionally, at 0° the added mass effects were negligible, and the mass of the log could be used directly to compute the impact force. Eccentric and oblique impacts diagrams showed that impact orientation systematically reduced the maximum impact force as each is increased.

It was noted during flume experiments, conducted by Braudrick and Grant, concerning the initial movement of logs in rivers, that rotation did occur as the log specimens were transported down the flume (Braudrick and Grant, 2000). These experiments began by placing their log specimens (wooden cylindrical dowels) in the flume. The experiments were conducted with steady flow and the flow was gradually increased until the log specimen began to initiate transport.

The logs were initially placed at 3 different orientations, 0° , 45° , and 90° . The 0° orientation corresponds to the log being parallel to the direction of flow, while 90° corresponds to the log being oriented normal to the direction of flow.

While the results were primarily concerned with depth ratios that corresponded to movement of the logs with various dimensions and presence of rootwads, the interesting aspect of the results were the observations concerning the stability of the logs. It was observed that logs initially oriented at 0 degrees were more stable than the logs oriented at 45° or 90° regardless of length. It was observed that pivoting appeared to be an important process for initiating motion for all pieces but particularly for those oriented at 45° and 90° .

From previous studies, a couple conclusions can be drawn. Tsunami-driven debris pose a significant threat to structures within the inundation zone, yet there was no consensus on how to define the impact forces from water-borne debris. Contradicting observations have been made about the impact duration associated with debris impact. Impact angle was observed to be a significant factor in impact force, yet little work has been conducted

in the way of determining the debris' propensity to rotate during propagation. This study investigated these issues by conducting 1:5 wave flume experiments.

The experiments in this study were conducted in conjunction with a set of full scale in-air experiments at Lehigh University (Piran Aghl et al., 2013). Piran Aghl et al. conducted swinging in-air tests using a fully sized 6.10 m (20 ft) shipping container. The results from these tests shows a linear relationship between impact velocity and impact force following an equation of the form:

$$F = v\sqrt{KM} \quad (2.7)$$

where F is the impact force, v is the impact velocity, M is the structural mass of the container, and K is the stiffness:

$$K = \frac{EA}{L} \quad (2.8)$$

where E is the modulus of elasticity, A is the structural area (or contact area) and L is the length of the shipping container.

The in-air test from the Lehigh Experiments were repeated on a 1:5 scale using the model shipping containers constructed for this study. The results from the in-air test provided the basis for comparison with the in-water experiments.

Chapter 3: Materials and Methods

3.1 Methodology

3.1.1 Large Wave Flume and Wavemaker

Experiments were conducted in the Large Wave Flume (LWF) at O.H. Hinsdale Wave Research Laboratory (HWRL) at Oregon State University. The wave flume was 110 m long, 3.7 m wide, 4.6 m deep, and was capable of holding up to 350,000 gallons of water. The wave flume was equipped with a piston type wave maker with a maximum stroke length of 4 m and a maximum speed of 4 m/s. Concrete slabs were installed to create the bathymetry in the wave flume. Seven slabs were used to form beach with a 1:12 slope and nine slabs were used to form a flat beach region after the beach. Rocks were placed at the end of the flume opposite the wave paddle to dissipate wave energy. Fig. 3.1 shows the coordinate axis system, installment locations of instrumentation, and the test section located between bays 17 and 18.

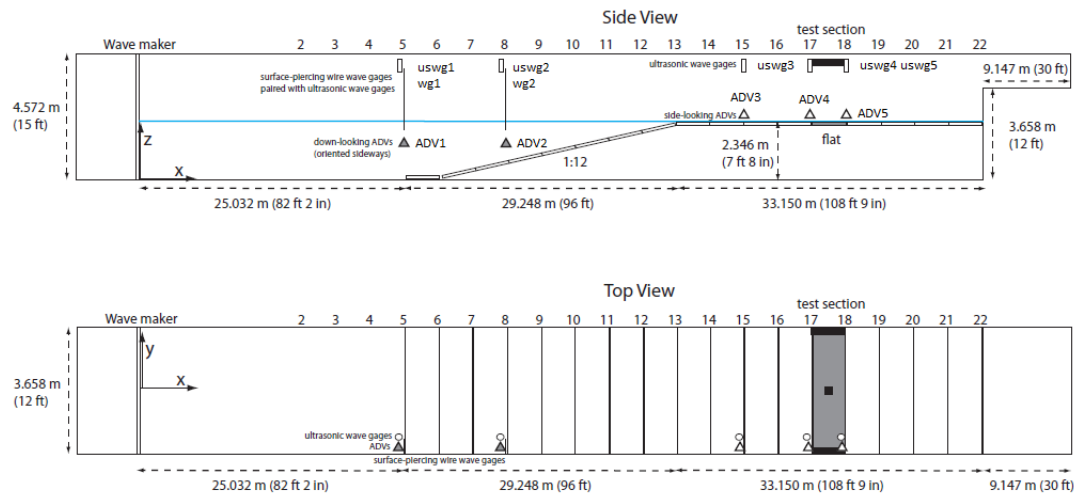


Figure 3.1: Large Wave Flume setup at O.H. Hinsdale Wave Research Laboratory. “wg” refers to resistance wave gage locations, “uswg” refers to ultrasonic wave gage locations, and “adv” refers to velocimeter locations. Test section was located between bays 17 and 18. Figure created by Timothy Maddux.

3.1.2 Instrumentation

Table 3.1 lists the installment locations for the instruments used in the experiment. All of the coordinate locations were based on the axes defined in Fig. 3.1. Units listed in meters.

All data was recorded and stored using a National Instruments 64-channel PXI-based real-time data acquisition system. The software used to control the data acquisition process was LabVIEW 8.

Table 3.1: Installment locations of instrumentation in the large wave flume. Locations are given based on the coordinate axes defined in Fig. 3.1. All units are listed in meters.

Data Column	Sensor Name	placement (x)	placement (y)	placement (z)
wmdisp	TMPO-LWM		0.000	
wmwg	TWG-LWM		0.000	
level	PRES-8482	13.960	-1.530	0.320
wg1	RWG-2260-01	24.930	-1.370	
wg2	RWG-2260-012	35.889	-1.376	
uswg1	DS-6555	24.870	-1.380	4.250
uswg2	DS-6663	35.833	-1.375	4.247
uswg3	DS-6666	61.431	-1.373	4.249
uswg4	DS-6554	68.771	-1.368	4.243
uswg5	DS-6664	72.429	-1.378	4.243
adv1	ADV-DL-7248	24.930	-1.420	1.240
adv2	ADV-DL-7208	35.890	-1.421	1.236
load1	neesdebris_load_1	70.740	0.010	2.470
strain1	neesdebris_strain_1	70.870	0.011	3.079
strain2	neesdebris_strain_2	71.076	0.007	3.083

The values “wmdisp” referred to the displacement of the wave paddle which is measured by a temposonic linear position sensor manufactured by MTS Systems Corporation. The value “wmwg” referred to the resistance wave gage attached to the wave paddle. The value “level” referred to the level sensor. The other values listed in Table 3.1 are described in the following sections.

3.1.2.1 Wave Gages

3.1.2.1.1 Resistance

Resistance wave gages were used to measure the free surface profile at locations wg1 and wg2 as shown in Fig. 3.1. Resistance wave gages were not used around the test section to avoid the risk of the damage from debris. These wave gages were designed and constructed at Oregon State university. This design avoided static drift and non-stationary calibration constants by using current sensing rather than voltage sensing (Dibble and Sollitt, 1989).

3.2 mm diameter stainless steel welding rods spaced at 26 mm were used as the sensing element. Calibration of wave gages was conducted by wave lab staff between each change in water depth. Sampling rate for resistance wave gages was 50 Hz.

3.1.2.1.2 Ultrasonic

Fig. 3.2 shows an ultrasonic wave gage installed in the wave flume. Five ultrasonic wave gages were used to measure the free surface profile at locations uswg1, uswg2, uswg3, uswg4, and uswg5 as shown in Fig. 3.1. Ultrasonic wave gages were purchased from Banner Engineering. Calibration of wave gages was conducted by wave lab staff between each change in water depth. Sampling rate for ultrasonic wave gages was 50 Hz.



Figure 3.2: Ultrasonic wave gage installed in wave flume. Location uswg3 is shown.

3.1.2.2 Acoustic Doppler Velocimeters (ADV_s)

Acoustic Doppler velocimeters (ADV_s) were used to measure flow velocities in the x-direction at locations ADV1, ADV2, ADV3, ADV4, and ADV5 as shown in Fig. 3.1. ADV_s were developed by Nortek AS. Calibration was provided by factory. Despiking of ADV data was performed using Matlab scripts provided by the wave lab. Despiking script followed method outlined by Goring and Nikora (Goring and Nikora, 2002).

3.1.2.3 Cameras

3.1.2.3.1 Panasonic HD Integrated Cameras

We used two overhead Panasonic HD Integrated Cameras (model: AW-HE50HN). Overhead cameras were mounted above bays 12 and 16 to view the test section. Mounting locations coincided with available ceiling supports for camera placement. These cameras were used to observe the experiment from above and provide the video footage necessary to utilize optical methods to track surface flow and debris velocities. These cameras were capable of sampling at rate of 60 frames per second.

3.1.2.3.2 Panasonic High Definition Video Camera

A Panasonic high definition (model: HDC-SD80) video camera was used. This camera was a hand held digital camcorder with manual exposure controls. This camera was capable of sampling at a rate of 60 frames per second.

3.1.2.3.3 GoPro HERO2

GoPro HERO2 cameras were used for their underwater capabilities. These cameras were capable of capturing video at 30 frames per second. Casing and mounting equipment allowed for the deployment of these cameras underwater.

3.1.2.4 Load Cells

3.1.2.4.1 CLC-300K

The CLC-300K load cell is shown from two different angles in Fig. 3.3. This load cell was developed by Transducer Techniques and was acquired from Lehigh University. The CLC-300K load cell was a high capacity compression load cell. The loading diameter of the load cell was engineered slightly convex for accurate load distribution. The CLC-300K was rated with a capacity of 1334 kN (300 kips) with a 32 kHz response. Factory calibration was used.

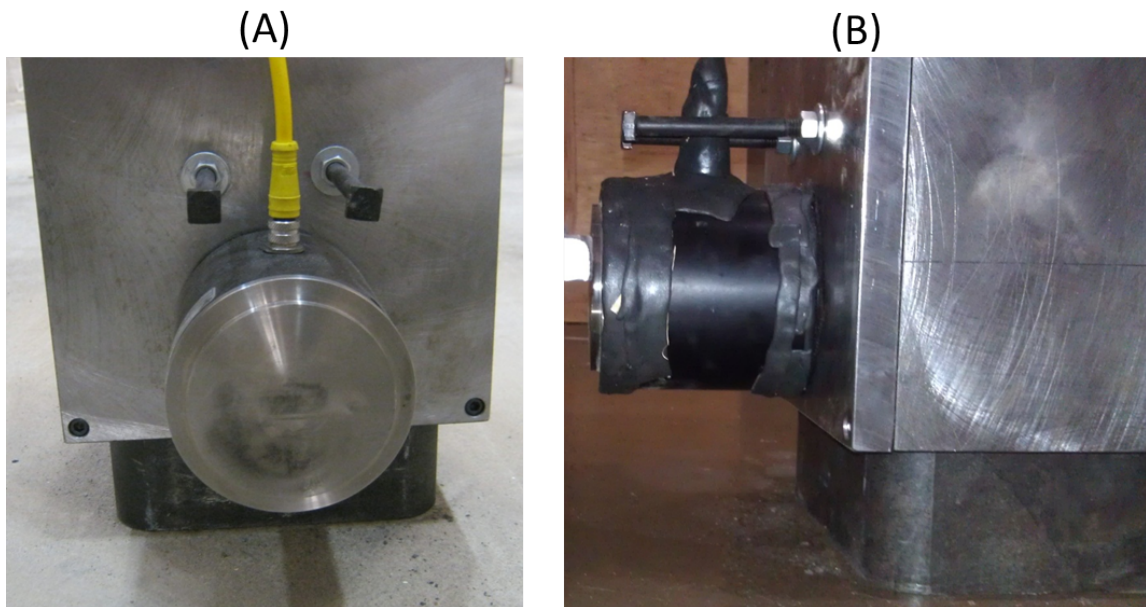


Figure 3.3: CLC-300K load cell, (A) front view, (B) side view

3.1.2.4.2 HSW-50K

The HSW-50K load cell is shown from two different angles in Fig. 3.4. The HSW-50K was a hermetically sealed load cell capable of compression and tension developed by Transducer Techniques. The hermetically sealed nature of the load cell allowed for its usage underwater. The HSW-50K was rated for 222 kN (50 kips) with a 9.6 kHz response. Factory calibration was used.

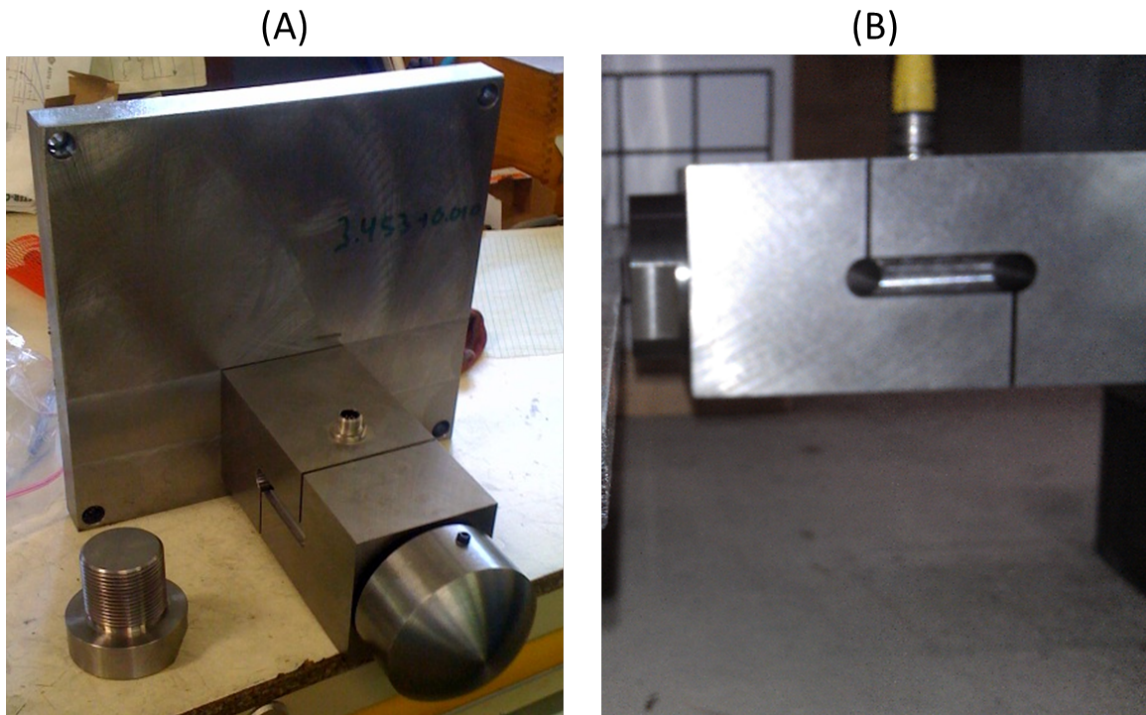


Figure 3.4: HSW-50K load cell, (A) front view with rounded button, (B) side view with standard button

3.1.2.4.3 Waterproofing

Waterproofing material was applied to the CLC-300K cell in the form of a M-coat FB-2 Butyl Rubber Sealant manufactured by Micro-Measurements. Micro-Measurements was part of Vishay Precision Group, Inc.



Figure 3.5: Waterproofing material applied to CLC-300K load cell

3.1.2.5 Strain Gages

Fig. 3.6 and Fig. 3.7 show the strain gages mounted onto the two faces of the column along the x-axis of the wave flume. These strain gages were manufactured by Micro-Measurements.



Figure 3.6: Strain gage adhered to side opposite of load cell on column assembly



Figure 3.7: Strain gage adhered to load cell side of column assembly

3.1.2.6 Column Assembly

3.1.2.6.1 Column

Fig. 3.8 and Fig. 3.9 show the column assembly. The debris was chosen to impact a column to reduce the obstruction of the inundation flow. The column prevented complications associated with reflection.

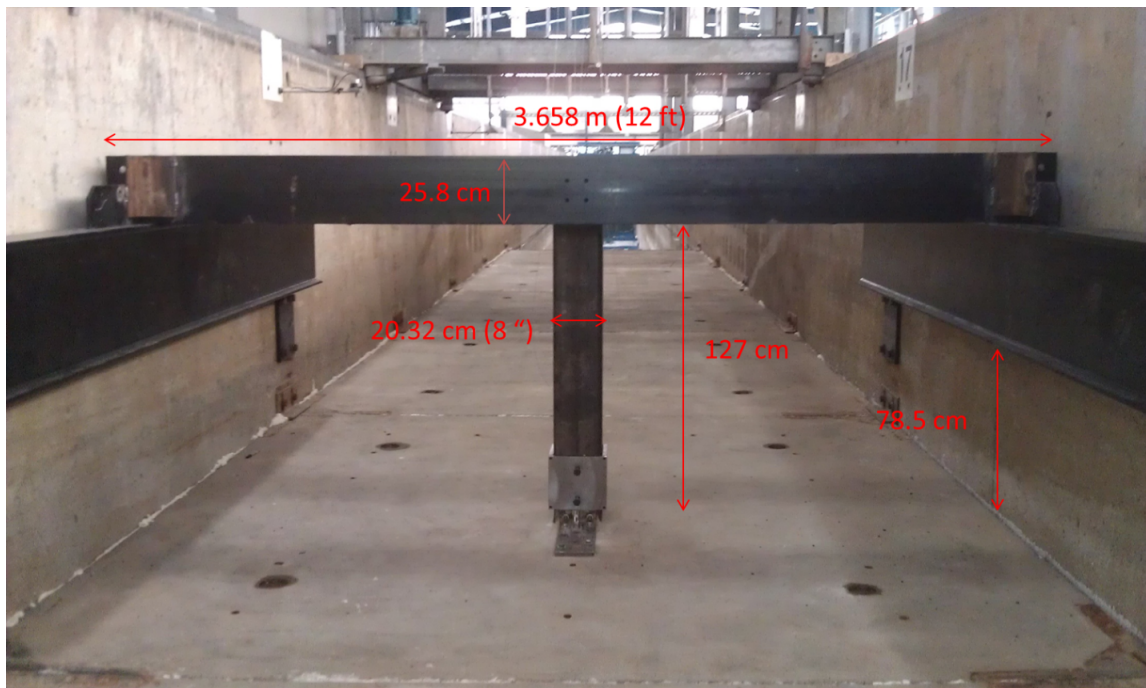


Figure 3.8: View of column assembly facing opposite the wave paddle. Dimensions are included.



Figure 3.9: View of column assembly facing the wave paddle.

3.1.2.6.2 Supports

Fig. 3.10 shows the side support for the column assembly. The supports for the column assembly were implemented to ensure that the rigidity of the structure relative to the debris.



Figure 3.10: Photograph of one of the supports of the column assembly on the wave flume wall. Identical support is located on the opposite wall. Dimensions are included.

3.1.2.6.3 Sleeve

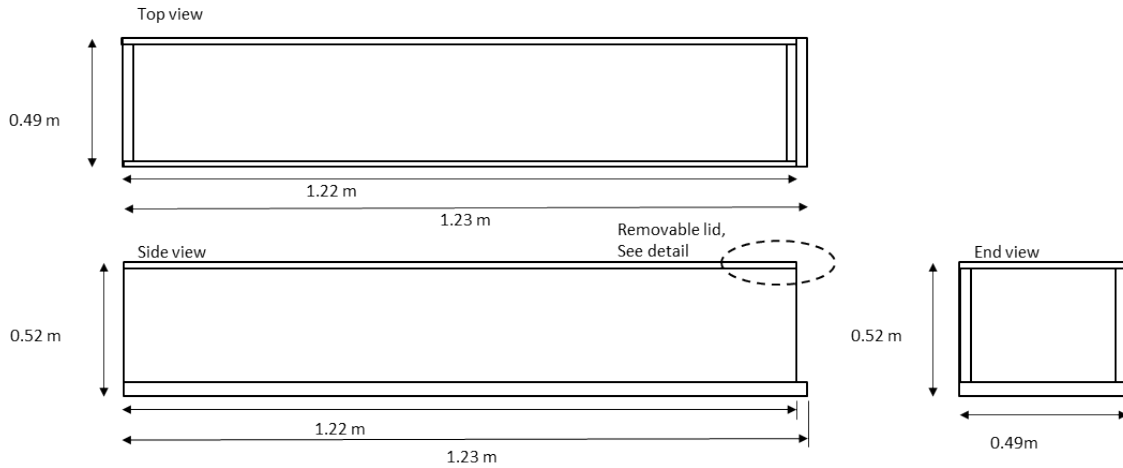
Fig. 3.11 shows a close up view of the load cell sleeve. This sleeve was manufactured in the machine shop at Oregon State University. The sleeve is made of stainless steel and can be moved up and down the column.



Figure 3.11: Photograph of stainless steel sleeve used to attach the load cell to the column assembly. Manufactured to allow sleeve to move up and down the column.

3.1.3 Specimen

Fig. 3.12 shows the schematic for the debris specimen used for the experiments. The dimensions shown corresponded to a 1:5 scale model of the standard intermodal container. The standard intermodal container is 20 feet (6.1 m) long, 8 feet (2.44 m) wide, and 9 feet 6 inches (2.90 m) tall. The 1:5 scale corresponded to dimensions of 1.22 m x 0.49 m x 0.58 m. As shown in Eq. 2.7 and Eq. 2.8, the contact area played a significant role in the impact force. The bottom plates of the debris specimen were extended to create a more consistent area for impact. The lids of the specimen were also removable to allow for addition of non-structural mass.



Notes:

Bottom is 1 in (24 mm) thick
 Sides and top are 0.5 in (12 mm) thick
 Top can be removed and sealed with stainless steel machine screws

Figure 3.12: Schematic for debris specimen. The dimensions shown in this drawing were used to manufacture both of the specimen. These dimensions correspond to a 1:5 scale model of the standard 20 ft (6.10 m) intermodal container.

It was important to define a convention for the orientation of the debris for the experiments. Fig. 3.13 shows a diagram that defined debris orientation with respect to the large wave flume. Longitudinal orientation was defined as when the major axis of the debris specimen was parallel to the x-axis. Longitudinal orientation corresponded to an impact angle of 0° . Transverse orientation was defined as when the minor axis of the debris specimen was parallel to the x-axis. Transverse orientation corresponded to an impact angle of 90° .

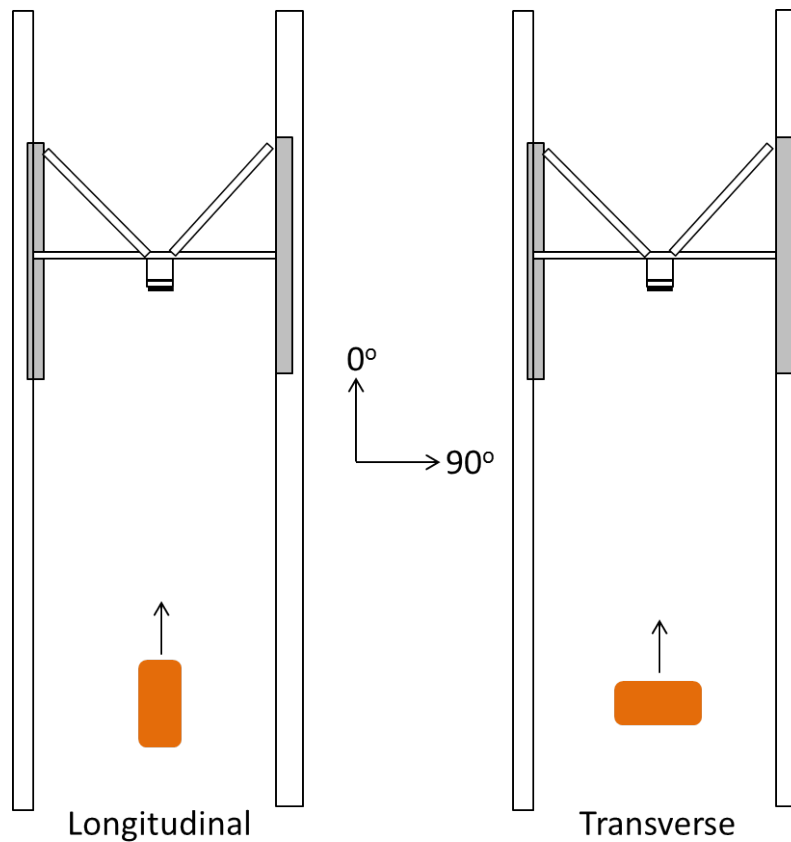


Figure 3.13: Orientation convention for debris specimen in large wave flume. Longitudinal orientation was defined as when the major axis of the debris specimen was parallel to the x-axis. Longitudinal orientation corresponded to an impact angle of 0° . Transverse orientation was defined as when the minor axis of the debris specimen was parallel to the x-axis. Transverse orientation corresponded to an impact angle of 90° .

3.1.3.1 Aluminum

Fig. 3.14 shows 3 different views of the aluminum debris specimen used in the experiments. The aluminum specimen was manufactured at Mechanical Design Inc. located in Albany, Oregon. The specimen followed the specifications given by Fig. 3.12. As shown in Fig. 3.14A and Fig. 3.14B, support beams were included to strengthen the structure of the specimen. Fig. 3.14C shows tethers attached to the specimen in the wave flume. These

tethers were used to reorient the specimen for each experimental trial. The orange lid is shown in Fig. 3.14C and was colored in this manner for the optical tracking methods. The weight of the aluminum debris specimen was measured to be 53.98 kg (119.0 lbs). The draft of the aluminum debris specimen was measured to be 9.1 cm.

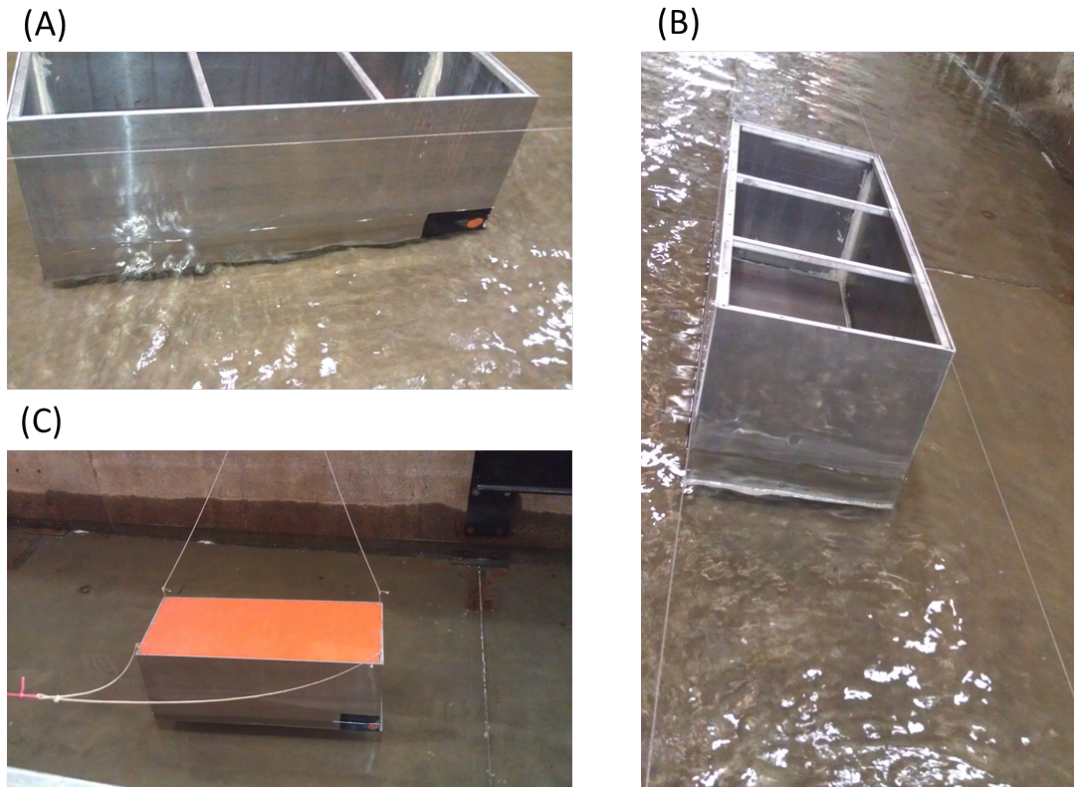


Figure 3.14: Photographs shown for aluminum debris specimen, (A) side view with lid removed (B) front view with lid removed (C) top view with lid.

3.1.3.2 Acrylic

Fig. 3.15 shows a photograph of the acrylic debris specimen in the machine shop at Oregon State University. The dimensions for the acrylic specimen are the same as the aluminum and the specifications are given by Fig. 3.12. The acrylic specimen was manufactured at Envision Acrylics, Inc. located in Beaverton, Oregon. The lid for the acrylic specimen was also painted orange for the optical tracking methods. The weight of the acrylic debris

specimen was measured to be 50.43 kg (111.19 lbs) which was almost the same as the aluminum specimen. The draft of the acrylic debris specimen was measured to be 8.7 cm.



Figure 3.15: Photographs of acrylic debris specimen.

3.1.3.3 Nonstructural Mass

Fig. 3.16 and Fig. 3.17 show photographs of the nonstructural mass used for the experiments. The nonstructural mass took the form of four hot rolled steel plates. The dimensions of the four plates were 43.18 cm x 57.15 cm x 1.27 cm (17 in x 22.5 in x 0.5 in). Dimensions were chosen such that two plates would almost encompass the surface area of the bottom of the specimen. Weights of each the four plates were 24.6 kg (54.2 lbs). Steel plates were added in pairs in increments of 49.2 kg. Wood blocks were also added to facilitate the removal of the nonstructural mass and to protect the specimen. The weight of the wooden blocks amounted to 1.0 kg. Thus, nonstructural mass amounts used for the experiments were 0 kg, 50.2 kg, and 99.4 kg and the corresponding drafts for the aluminum specimen were 9.1 cm, 17.5 cm, and 26 cm respectively.



Figure 3.16: Photograph of nonstructural mass placed in aluminum debris specimen. Four hot rolled steel plates with wooden block supports are shown.



Figure 3.17: Another view of nonstructural mass inside aluminum specimen. Photograph is shown after in-air trial is performed. Steel plates are shown to have shifted to the front of the specimen.

3.1.4 Guide Wires

Guide wires were installed in the large wave flume between bays 15 and 18. The purpose of the guide wires was to control the movement of the debris specimen as it propagated down the flume. The guide wires allowed for the debris specimen to maintain a consistent impact angle for each series of in-water tests. The setup of the guide wires allowed for the specimen to move freely along the x-axis and z-axis, but not the y-axis. Two different guide wire setups were used during the in-water tests.

3.1.4.1 Longitudinal

Fig. 3.18 shows the guide wire setup for the longitudinal in-water tests. The guide wires spanned across bay 15 and bay 18 and maintained the debris specimen's orientation at 0° . The distance between the guide wires was the width of minor axis of the specimen with 5 cm of extra space on each side.

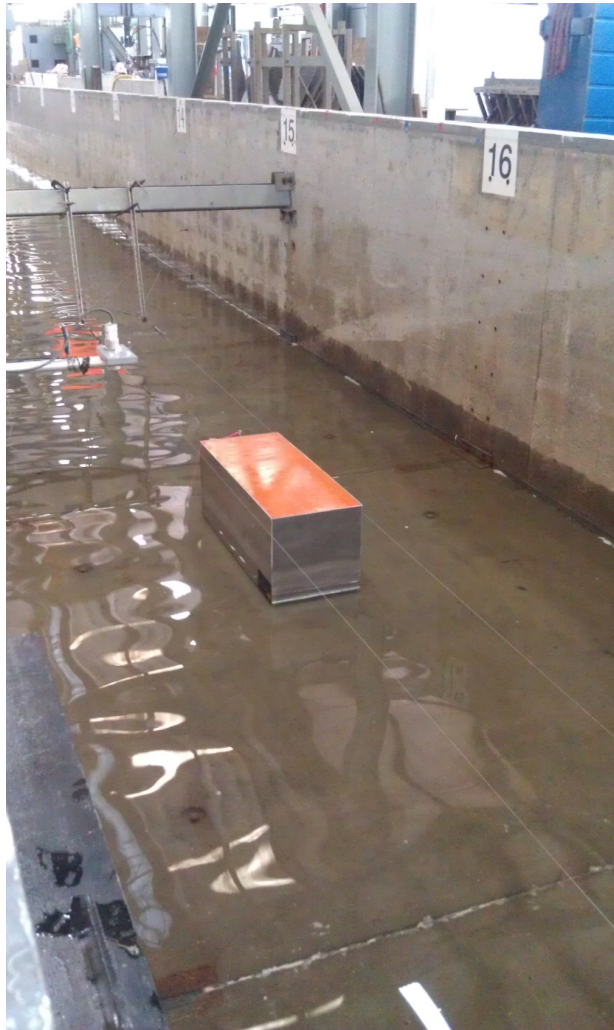


Figure 3.18: Photograph of guide wire setup for longitudinal in-water test.

3.1.4.2 Transverse

Fig. 3.19 shows the guide wire setup for the transverse in-water tests. These guide wires spanned across bay 15 and bay 18 and maintained the debris specimen's orientation at 90° . The distance between the guide wires was the width of major axis of the specimen with 5 cm of extra space on each side. Since the specimen was still capable of rotating within the boundaries of the transverse guide wire setup, tethers were also used to maintain the

orientation of the specimen is it propagated with the flow. Individuals from the wave lab staff were positioned on both sides of the large wave flume for each trial to ensure that contact between the specimen and the load cell was made at a 90° angle.



Figure 3.19: Photograph of guide wire setup for transverse in-water test. The tethers shown in the photograph were used to position the specimen for each trial as well as maintain orientation during each trial.

3.1.5 Optical Tracking Methods

Optical tracking methods were a key component to this study. This section is organized into three subsections. Each subsection describes the optical tracking methods used for a particular type of experiment in this study.

3.1.5.1 Hydrodynamics (PIV)

Fig. 3.20 shows a video sequence from hydrodynamics test trial 3 at $h_2 = 0$. In this trial, a turbulent bore propagated through the test section. The foam shown was isolated from

the rest of the video by using a brightness threshold to convert the video frames to binary images (black and white). If the pixel exceeded a certain brightness, the new picture matrix would return a 1 for that coordinate, otherwise a 0 would be returned. The video was also rectified to correct for perspective distortion by transforming pixel coordinates to surveyed coordinates. This process is shown in Fig. 3.21.

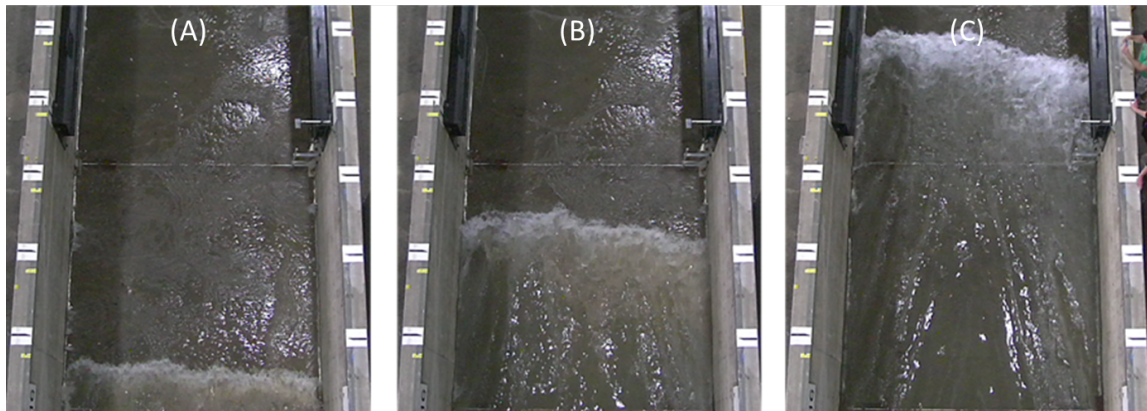


Figure 3.20: Video sequence of hydrodynamics test trial number 3 for water depth of $h_2 = 0$ for times, (A) 60 s, (B) 61 s, (C) 62 s.

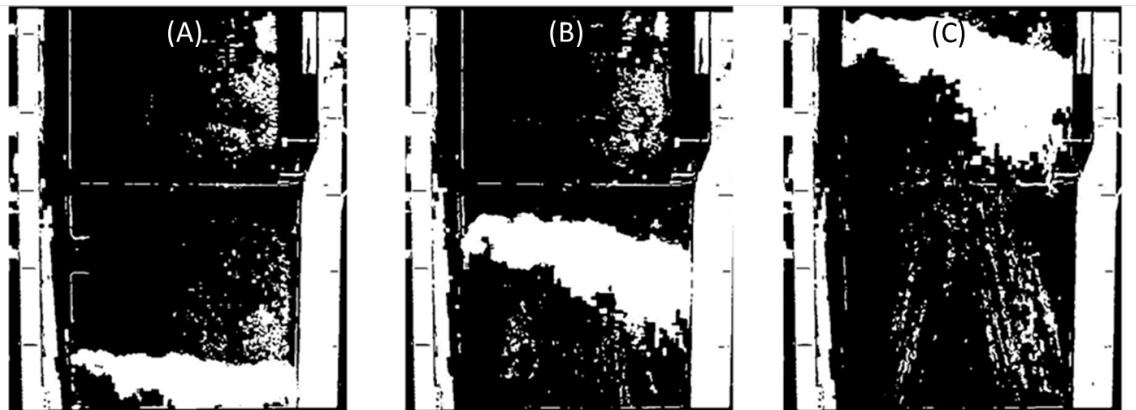


Figure 3.21: Video sequence, converted to binary (black and white) of hydrodynamics test trial number 3 for water depth of $h_2 = 0$ for times, (A) 60 s, (B) 61 s, (C) 62 s.

After the video files were converted, the front of the wave was tracked by using PIVlab in Matlab. PIVlab was a time-resolved particle image velocimetry software that calculates

the velocity distribution between particle image pairs written by W. Thielicke. Each frame in the binary video was loaded into PIVlab in the form of image pairs, and the PIV analysis was performed after properly calibrating each image to surveyed coordinates.

Fig. 3.22 shows PIV analysis performed on the binary video shown in Fig. 3.21. The region of interest is drawn around the moving foam, and the arrows represent the velocity vectors. Green arrows represent unfiltered velocity vectors, yellow arrows represent filtered vectors. The results from the wave front tracking shows that this method was adequate for tracking foam. However, since idealized inundation flow did not have a turbulent bore front, seeding material was required to measure flow velocities for the other wave conditions.

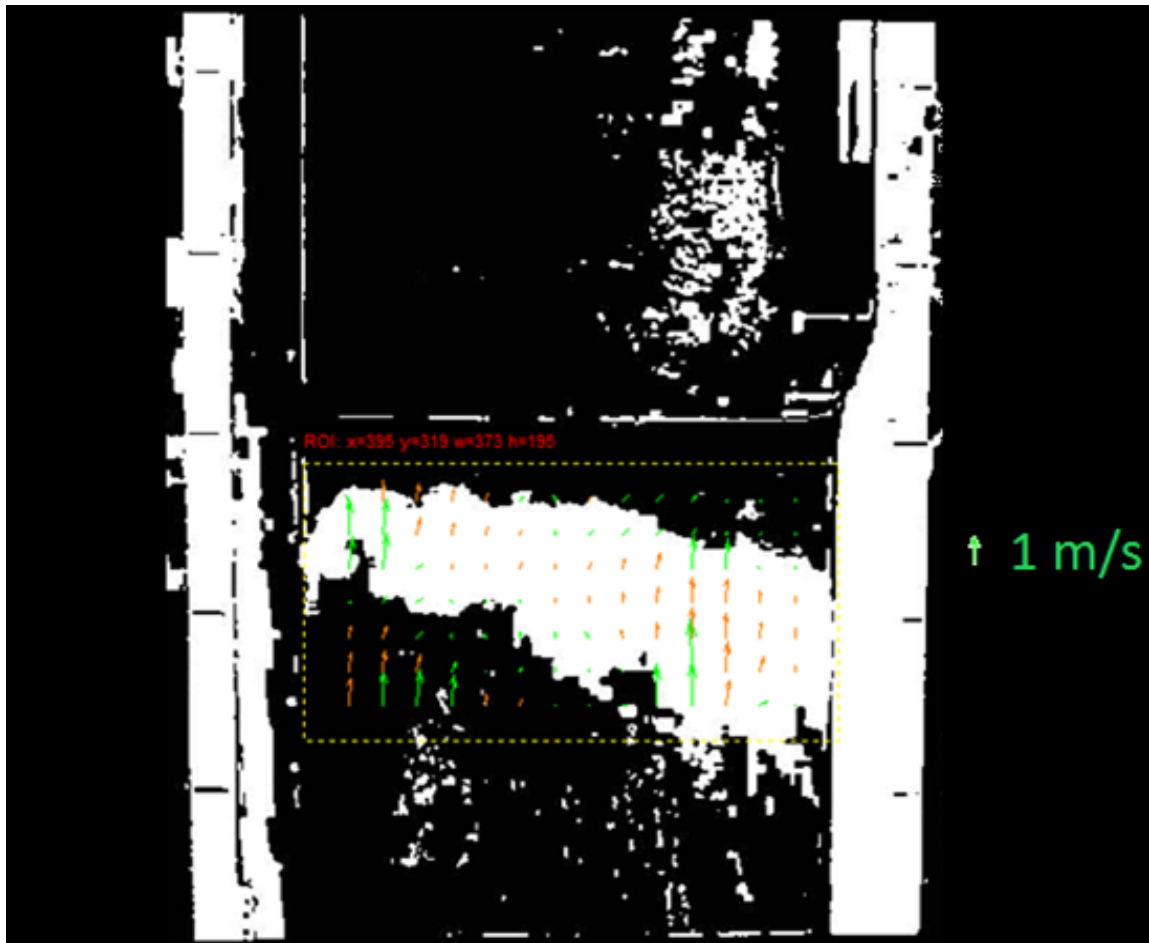


Figure 3.22: PIV analysis performed on video section associated with Fig. 3.21B using PIVlab in Matlab. Green arrows represent unfiltered velocity vectors, yellow arrows represent filtered vectors.

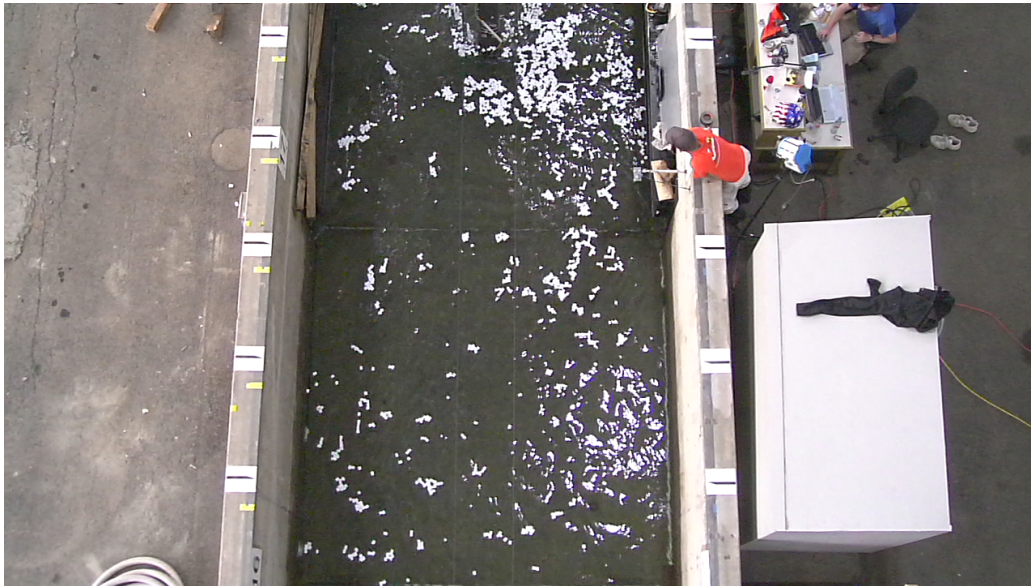


Figure 3.23: Styrofoam packing peanuts were added to the wave flume as seeding material to track the water surface.

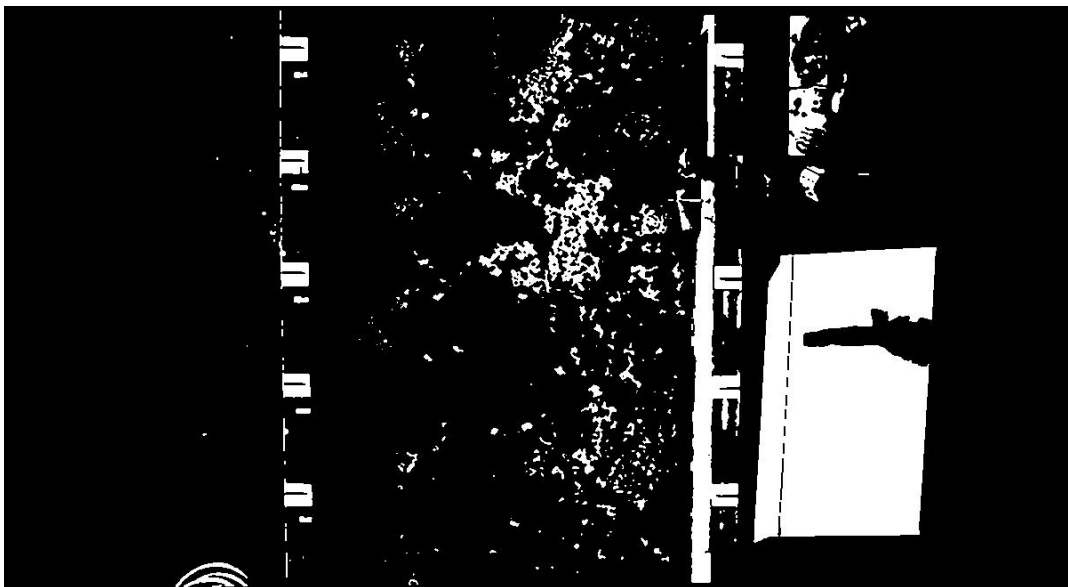


Figure 3.24: The seeded water surface shown in Fig. 3.23 converted to a binary image.

Fig. 3.23 shows a photograph of the seeding material added to the large wave flume to track the surface of the water. Styrofoam packing peanuts were chosen due to their accessibility, cost, and color. The white color of the packing peanuts was able to pass through a threshold similar to the one used to track the foam. Fig. 3.23 shows the binary image produced from passing the seeded water through the brightness threshold.

By seeding the water, the flow velocity could be measured for the entire test section of the wave flume. Fig. 3.25 shows the PIV analysis of the seeded water in the test section.

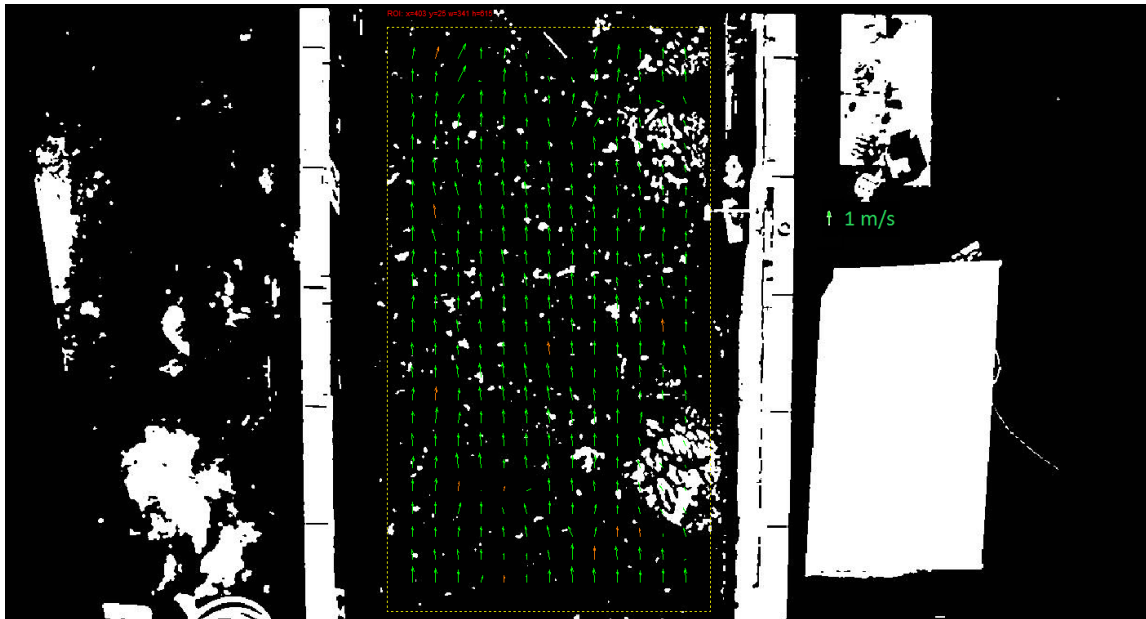


Figure 3.25: PIV analysis performed on seeded water flowing at $h_2 = 13.3$ cm with $T_{erf} = 30$ s.

Fig. 3.25 shows that velocity vectors were obtained throughout the entire test section. Additionally, less filtering was required as evidenced by the greater proportion of green arrows.

3.1.5.2 In-Air Test

Fig. 3.26 shows the camera view of the Panasonic HD camera used for the in-air tests. This view was used to track the velocity of the swinging in-air test. An orange circle, 5 cm in diameter, was painted in the bottom right hand corner of the debris specimen. A

color based tracking algorithm (Fieguth and Terzopoulos, 1997) was used to extract the orange color from each frame of video. The color-based object tracking method operated by extracting a particular color from a video frame. This technique subtracted one color from an image, effectively creating a hole identified as the object of interest in the image.



Figure 3.26: Video frame of In-Air Longitudinal Test using Panasonic HD camera. The view point of this frame was used to track the velocity of the debris as it swung and collided with the load cell. The orange circle painted in the bottom right hand corner of the specimen was used to track debris movement.

Since color data were stored in rgb (red-green-blue) matrices, the most convenient choices for color were red green and blue. In the case of this study, the color red was chosen because of its contrast with water and the other surroundings in the HWRL. The color orange had sufficiently high red color matrix values to be used in this process. The first step of the color extraction was converting the original image into a gray scale image and then subtracting either the red, green, or blue matrix.

The subtracted image was converted into a binary using the function “im2bw” in which all values that exceed a certain threshold of brightness are assigned a 1 while all others are assigned 0. Since a certain color matrix was subtracted from the gray scale image, this left

all regions of that color in the gray scale image with lower values of gray which resulted in the pixels of the region to be brighter, allowing for the extraction of the object. These pixels were then connected together by using the function “bwarealabel” allowing for the application of the “regionprops” function which allows for the centroid of the object to be obtained. In this manner, the centroid for the object of a particular color was tracked from frame to frame in video. By using the change in centroid positioning and camera frame rate, the velocity of the object could be tracked.

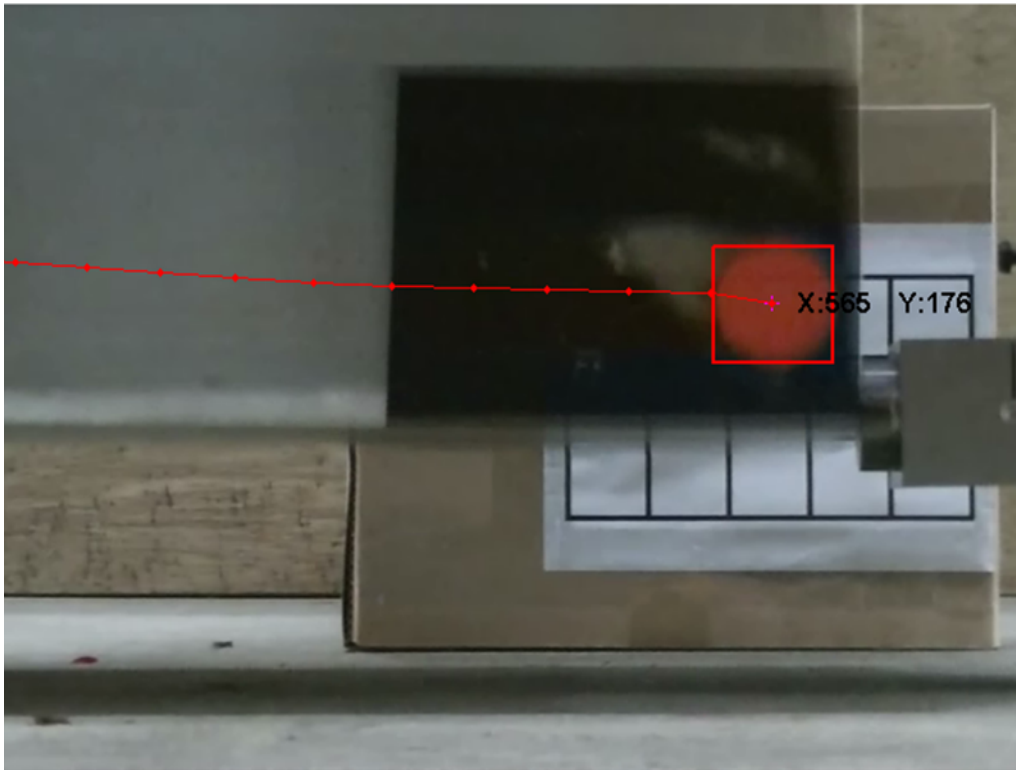


Figure 3.27: Tracking algorithm applied to in-air longitudinal aluminum test. The trajectory of the orange circle is shown by the lines connecting the red dots. A bounding box is plotted around the object of interest in each frame to ensure that the correct object is being tracked. Note that the orange circle is being tracked, not the bounding box.

Fig. 3.27 shows the application of the tracking algorithm to video footage from the in-air longitudinal aluminum test. The trajectory of the orange circle was plotted by connecting the centroids of the orange circle from each video frame. A red bounding box

was plotted on top of the object of interest to ensure that the correct object was being tracked. The velocity of the orange dot was calculated by relating the change in centroid from frame to frame with the video frame rate. Pixel velocity was converted to matrix units by calibrating pixel distance with the known diameter of the tracked circle.

3.1.5.3 In-Water Test

3.1.5.3.1 Velocity Tracking

The velocity tracking procedure for the in-water test followed the same color based object tracking algorithm that was applied to the in-air test. The same paint used for the orange circle in the in-air test was applied to the lids of the debris specimen. The main difference was that since the overhead Panasonic HD integrated cameras were used, a perspective correction was required. Since it could not be ensured that the ceiling cameras would always be perpendicular to the desired field of view, it was necessary to correct for any possible distortions that would arise due to the camera perspective.

A 2D projective transformation was performed by matching pixel points on the individual video frames to real world measured values. The real world measured values were acquired using surveying equipment. The pixel to real world transformation was mapped onto a homography matrix which was used to transform every frame in the video. Fig. 3.28 and Fig. 3.29 show the effect of the perspective correction.

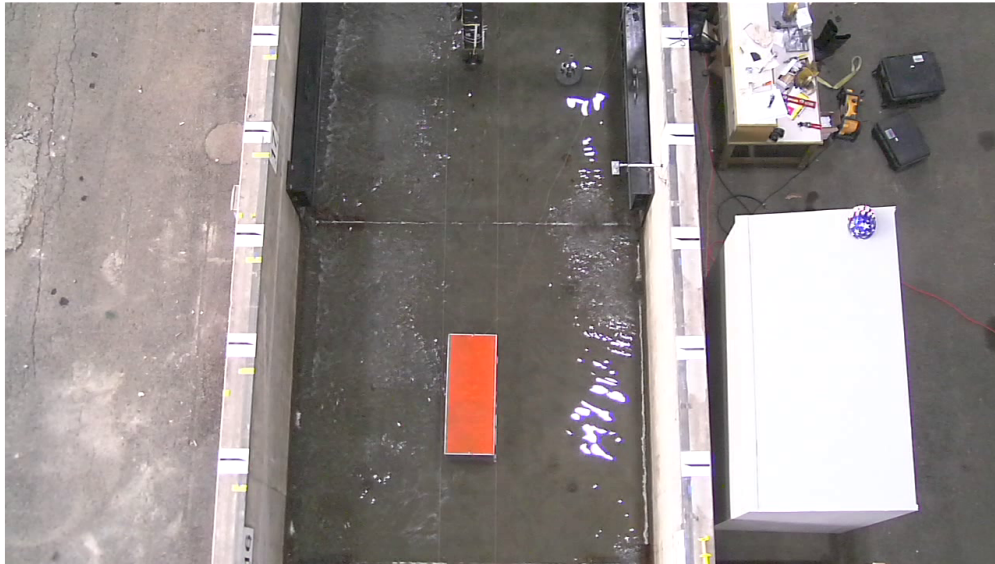


Figure 3.28: Video frame of in-water longitudinal test captured using overhead Panasonic HD integrated camera before perspective correction.



Figure 3.29: Video frame of in-water longitudinal test captured using overhead Panasonic HD integrated camera after perspective correction.

Fig. 3.29 shows how the image of the LWF was rectified. Notice how the walls of the LWF became parallel as the image underwent the transformation. In addition, the markings on the top of the walls of the LWF became equidistant from one another. The perspective transform shown was applied for all overhead video footage analyzed in this study.

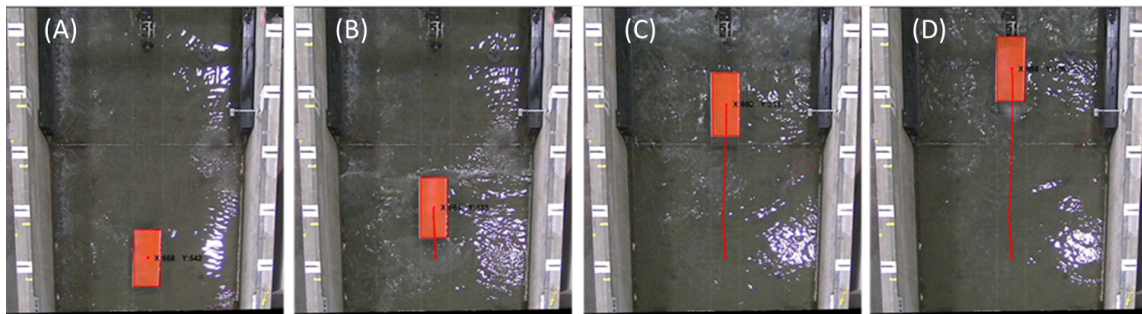


Figure 3.30: Video sequence of tracking algorithm applied to trial 12 from in-water longitudinal aluminum test at $h_2 = 13.3$ cm at times (A) 1 s (B) 3 s (C) 5 s (D) 6 s.

Fig. 3.30 shows a video sequence of the object tracking method applied to trial 12 from

in-water longitudinal aluminum test at $h_2 = 13.3$ cm. The velocity time history from this trial is shown in Fig. 3.31.

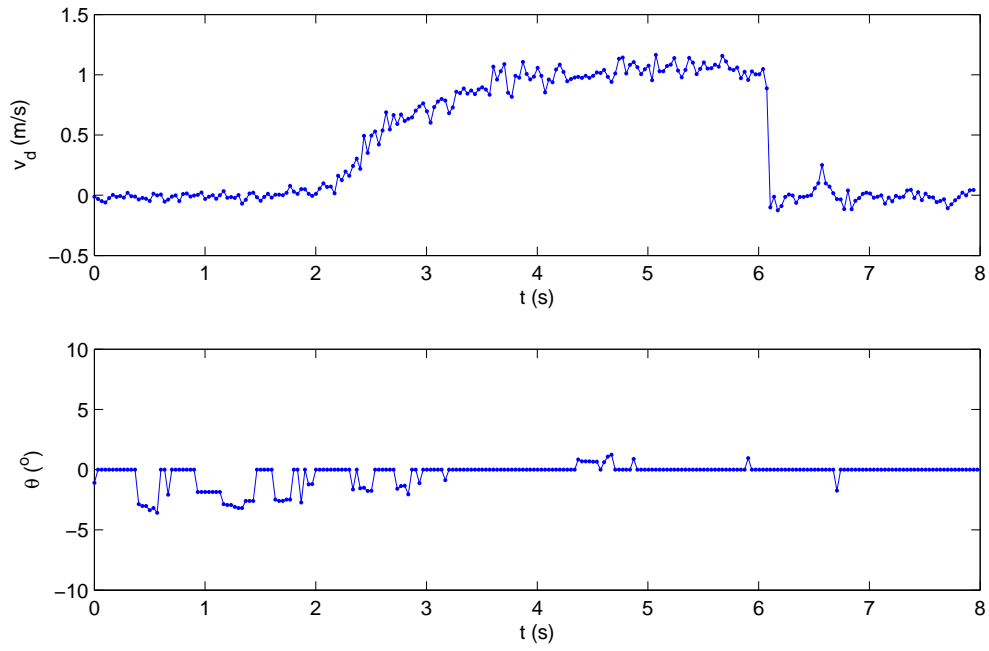


Figure 3.31: Velocity tracking output from in-water longitudinal aluminum test shown in Fig. 3.30. Debris velocity shown in the top plot, debris orientation shown in bottom plot.

Fig. 3.31 shows that the velocity of the debris specimen was at a constant velocity before making impact with the load cell. The orientation, θ of the debris was shown to be around 0° throughout the propagation, with variations less than 5° . Additionally, the error of the optical tracking method was determined by tracking a stationary object. The aluminum debris specimen was placed in the wave flume and held by ropes on both ends. The variation in the velocity of the stationary object is shown in Fig. 3.32.

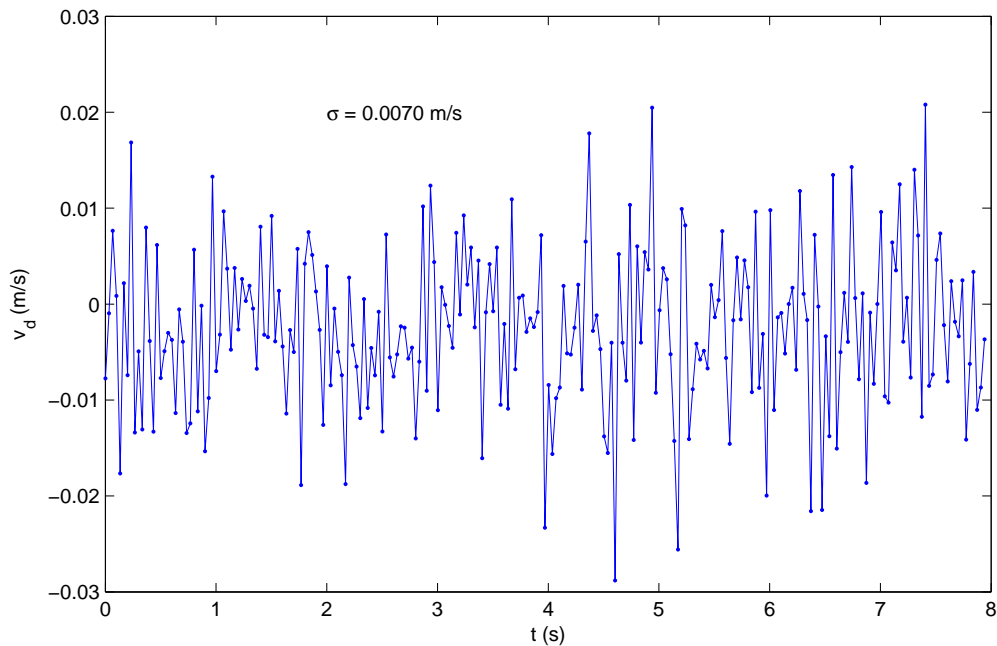


Figure 3.32: Velocity tracking output from stationary debris specimen in large wave flume.

Fig. 3.32 shows that the velocity of the stationary debris had a standard deviation of 0.0070 m/s. Since the velocities measured from the in-water test were on the order of 1 m/s, this amount of error accounted for less than 1% of the measured velocity. This was considered to be acceptable. It should also be mentioned that the debris specimen was not necessarily completely stationary during this test. Therefore it would appropriate to state that the pixel error associated with the velocity measurement is no worse than 0.0070 m/s.

3.1.5.3.2 Angle Measurement

Impact angles were measured by using the binary images created from the color extraction algorithm. After the video frames were converted to binary an edge detection algorithm was used in Matlab.

The algorithm developed for the determination of debris orientation from an image focused on the edge detection of an object based on gradients in the pixel data. This edge detection method assumed that the greatest change in color data would be detected at

the edges of objects in the image. In Matlab, this edge detection algorithm was applied using by first converting the colored image into a gray scale image, and then using the edge function with the prewitt method and a defined threshold. The defined threshold allowed the user to set the standard for what was defined as an edge of an object.

After the edge was identified, the angle of orientation was determined by using a Hough Transformation. This procedure was conducted in Matlab and was able to determine the coordinates of the endpoints of the lines derived from the edge detection. From these lines, the angle of orientation could also be calculated. Fig. 3.33 shows the detected edges plotted on top of the original binary image.

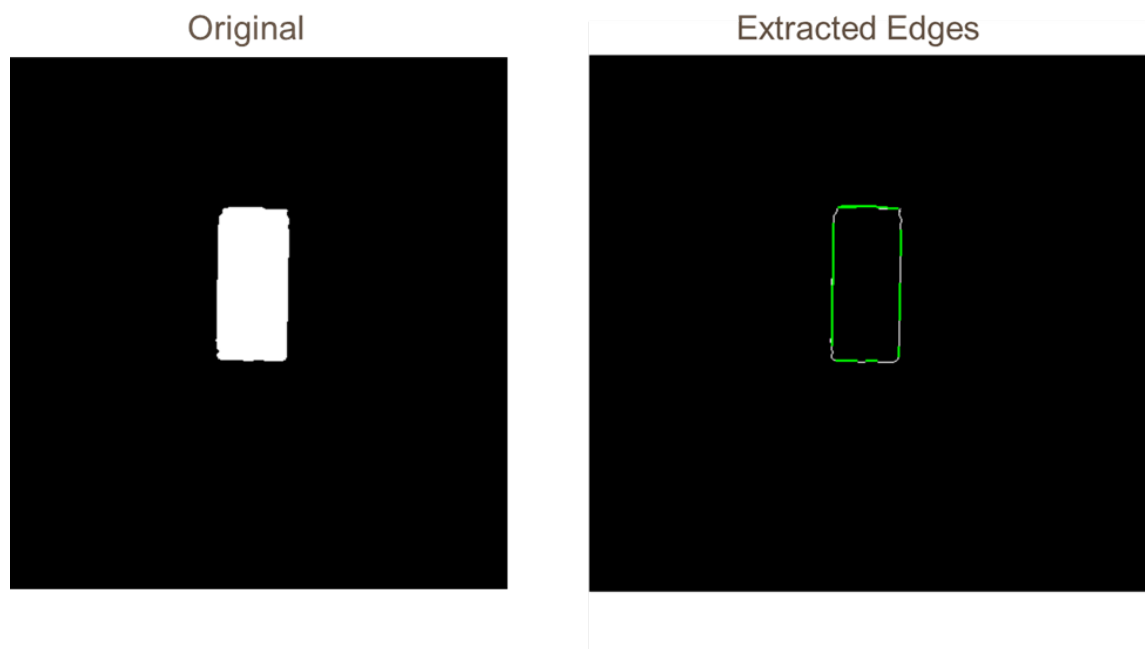


Figure 3.33: Detected edges plotted on top of original binary image for debris specimen in large wave flume.

Sample orientation output from this angle measuring method was shown in Fig. 3.31.

3.1.6 Wave Conditions

3.1.6.1 Wave Paddle Displacement

Since this was an idealized study of debris driven by tsunami inundation, error functions were used to generate wave paddle displacement. With this method, the full 4 m stroke of the wavemaker was utilized, even for relatively small wave heights. This maximized the volume and duration of the tsunami inundation process. For this study, error function periods (time for the wave paddle to travel the full 4 m stroke), denoted as T_p , between 20 seconds and 45 seconds were used. Given the bathymetry setup in the large wave flume, these error function periods generated the most realistic flow conditions for driving the debris. Fig. 3.34 shows a plot of the wave paddle displacements, S , associated with error function periods used in this study.

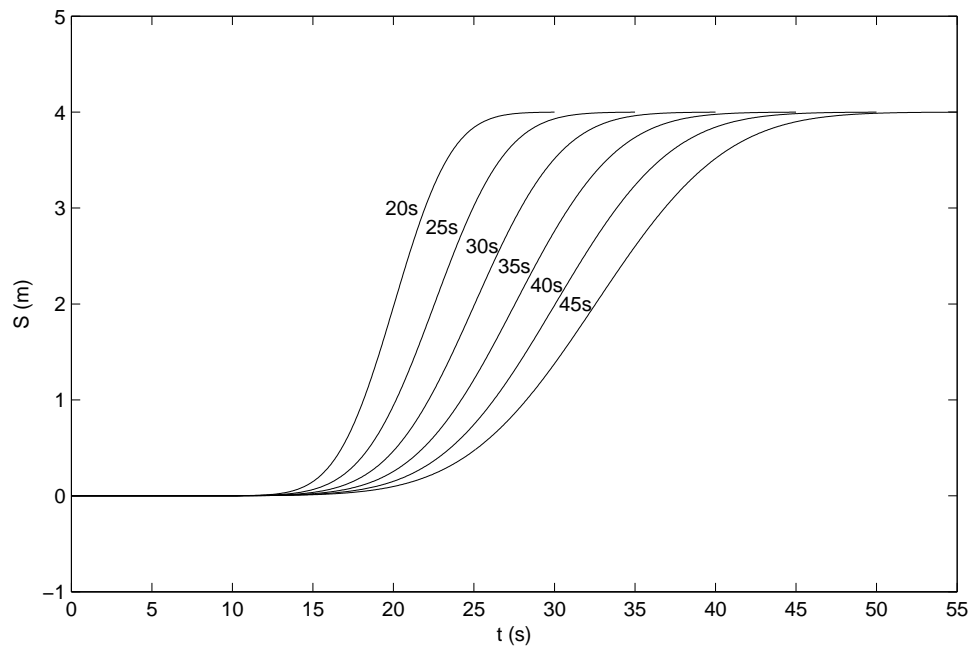


Figure 3.34: Wave paddle displacement for error function periods used in this study. Full 4 m stroke was used for all periods.

As shown in Fig. 3.34, shorter error function periods result in steeper wave paddle

displacements.

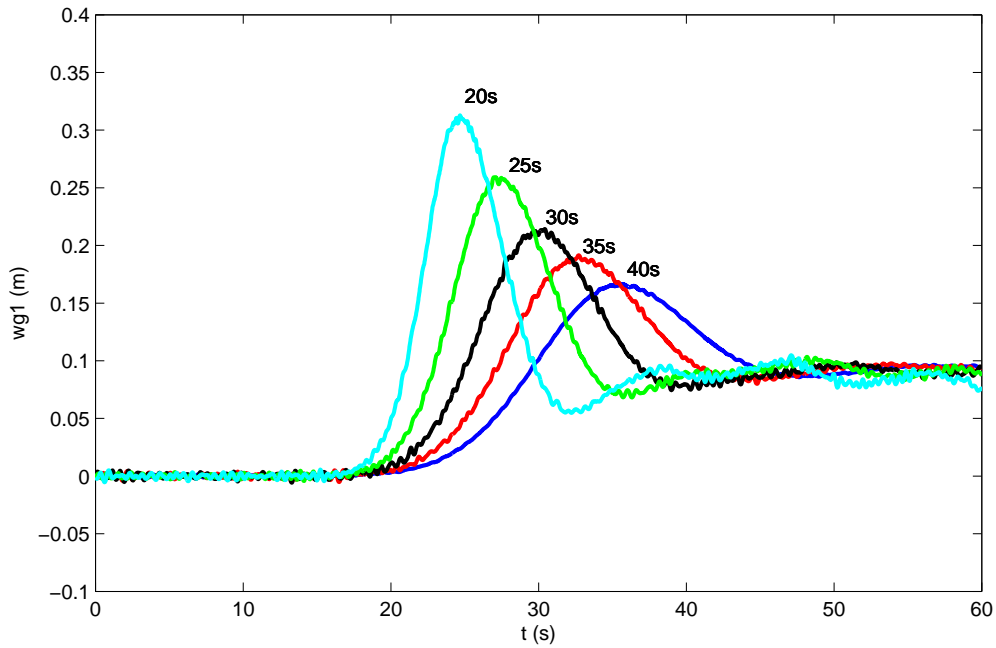


Figure 3.35: Offshore wave heights measured at wg1 for certain T_{erf} . Wave gage measurements were taken at a water depth of $h_1 = 266.4$ cm, $h_2 = 30.1$ cm

Fig. 3.35 shows offshore wave height measurements associated with certain T_{erf} at $h_1 = 266.4$ cm, $h_2 = 30.1$ cm. Fig. 3.35 shows that shorter T_{erf} corresponds to bigger and faster waves.

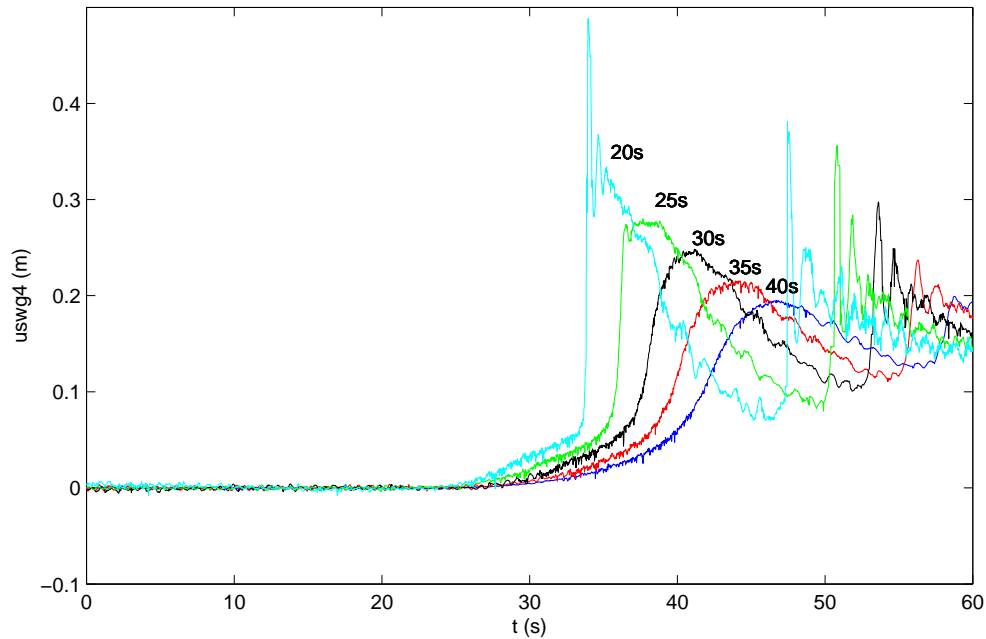


Figure 3.36: Inundation depths measured at uswg4 for certain T_{erf} . Wave gage measurements were taken at a water depth of $h_1 = 266.4$ cm, $h_2 = 30.1$ cm

Fig. 3.36 shows inundation depth measurements at the test section associated with certain T_{erf} at $h_1 = 266.4$ cm, $h_2 = 30.1$ cm. Shorter T_{erf} corresponded to greater inundation depth and faster inundation flow speeds. Additionally, the inundation depth measurement showed a spike for the $T_{erf} = 20$ s case. The spike corresponded to an unbroken wave propagating through the test section. This wave condition marked the limiting case for the inundation flow. Waves generated for $T_{erf} < 20$ s produced turbulent bores propagating through the test section, which did not fit the criteria for idealized inundation flow.

3.1.6.2 Hydrodynamics Test

Table 3.2 shows the wave conditions and water depths used for the Hydrodynamic experiments. In addition, the wave conditions for the In-Water experiments (Table 3.3) were also

duplicated. h_1 refers to the still water depth measured at the wave paddle, and h_2 refers to the still water depth measured in the test section. These input parameters provided the necessary flow conditions to perform wave front tracking and wave flume repeatability testing.

Table 3.2: Flow conditions used for Hydrodynamic Experiments

Flow Condition #	h_1 (cm)	h_2 (cm)	T_{erf} (s)
1	234.6	0	30
2	234.6	0	25
3	234.6	0	20
4	234.6	0	15
5	234.6	0	10
6	246.6	10.3	30
7	246.6	10.3	25
8	246.6	10.3	20
9	246.6	10.3	15
10	246.6	10.3	10
11	256.6	20.3	30
12	256.6	20.3	25
13	256.6	20.3	20
14	256.6	20.3	15
15	256.6	20.3	10

3.1.6.3 In-Water Test

Table 3.3 shows the wave conditions and water depths used for the In-Water experiments. 13 total wave conditions were used over three different water depths. These conditions gave the widest range of velocities that matched the criteria for idealized inundation flow.

Table 3.3: Flow conditions used for In-Water Experiments

Flow Condition #	h_1 (cm)	h_2 (cm)	T_{erf} (s)
1	249.6	13.3	45
2	249.6	13.3	40
3	249.6	13.3	35
4	249.6	13.3	30
5	257.2	20.9	40
6	257.2	20.9	35
7	257.2	20.9	30
8	257.2	20.9	25
9	266.4	30.1	40
10	266.4	30.1	35
11	266.4	30.1	30
12	266.4	30.1	25
13	266.4	30.1	20

3.2 Test Plan

Three different types of tests were conducted in this study, the Hydrodynamics Test, the In-Air Test, and the In-water Test. The details of each of these tests will be covered in the follow sections.

3.2.1 Hydrodynamics Test

The purpose of the series of hydrodynamics experiments was to determine what flow conditions would be appropriate for the debris impact experiments as well as ensure the applicability to use optical methods to obtain flow velocities.

3.2.1.1 Setup

The Hydrodynamic Test used the large wave flume and bathymetry setup shown in Fig. 3.1. Water depths and wave conditions were varied as shown in Table 3.2 and Table 3.3.

Wave gage, ADV, and camera data were sampled for each trial.

3.2.1.2 Examples of Data

Fig. 3.37 shows an example of the data from Hydrodynamic Test trial 8 with test conditions: $h_1 = 2.47$ m, $h_2 = 0.103$ m, $T_{erf} = 30$ s. The instrument used to sample data for each plot is shown on the y -axes. Instrument locations correspond with Fig. 3.1 and Table 3.1. Time axes were synchronized with the start signal of the wavemaker ($t = 0$ at wavemaker start signal).

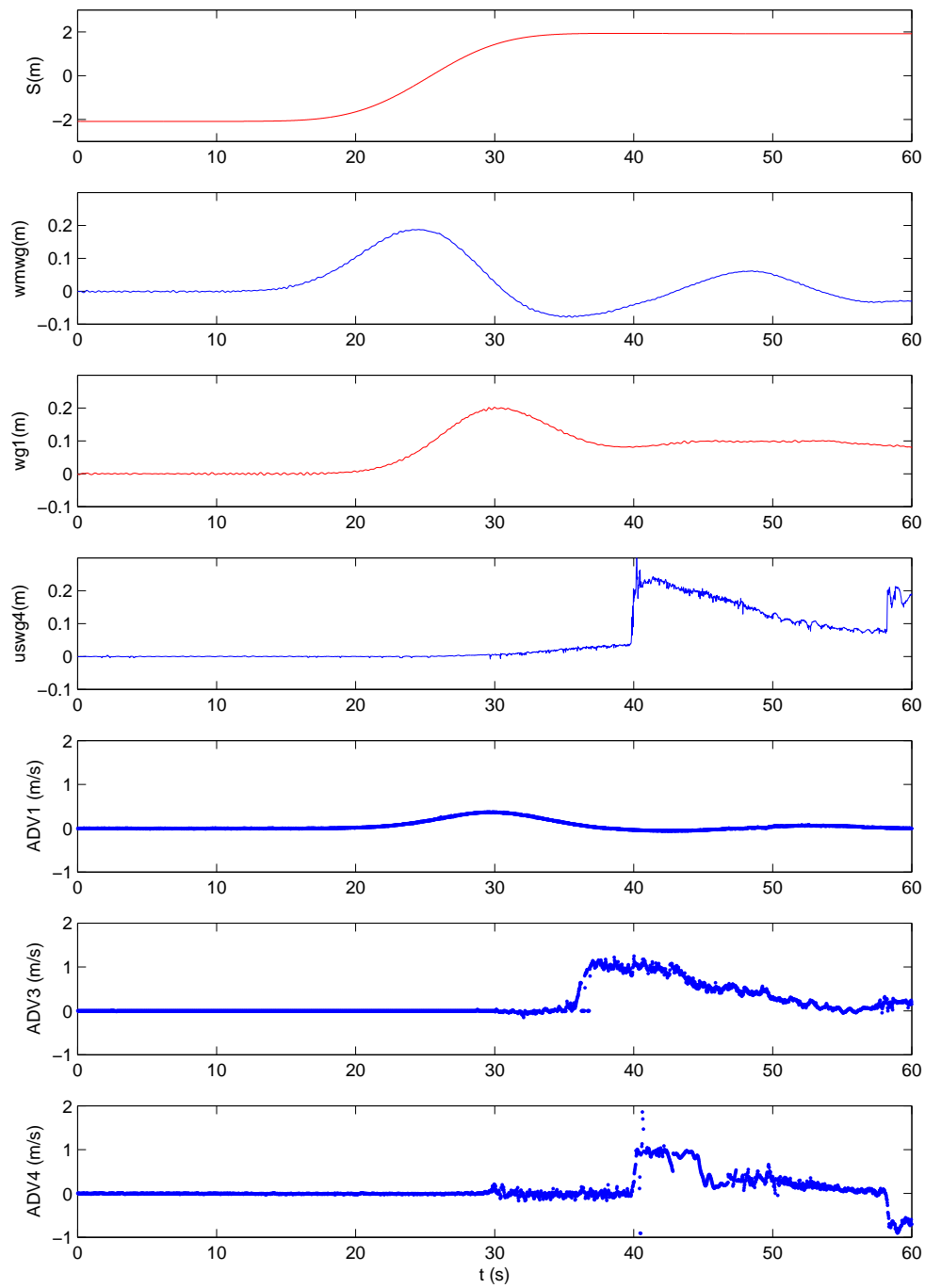


Figure 3.37: Example of Hydrodynamic Test data from trial 8: $h_1 = 2.47$ m, $h_2 = 0.103$ m, $T_{erf} = 30$ s. Sampling locations for each instrument correspond with Fig. 3.1. Time axes were synchronized with the start signal of the wavemaker.

3.2.1.3 Repeatability

Fig. 3.38 shows the time variation of wave paddle displacement and free surface variation from Hydrodynamics Test trials 17-21 superimposed on top of one another. The conditions for each of these trials were identical with $h_1 = 2.57$ m, $h_2 = 0.203$ m, $T_{erf} = 20$ s. Fig. 3.38 indicated that the large wave flume was capable of producing repeatable flow conditions.

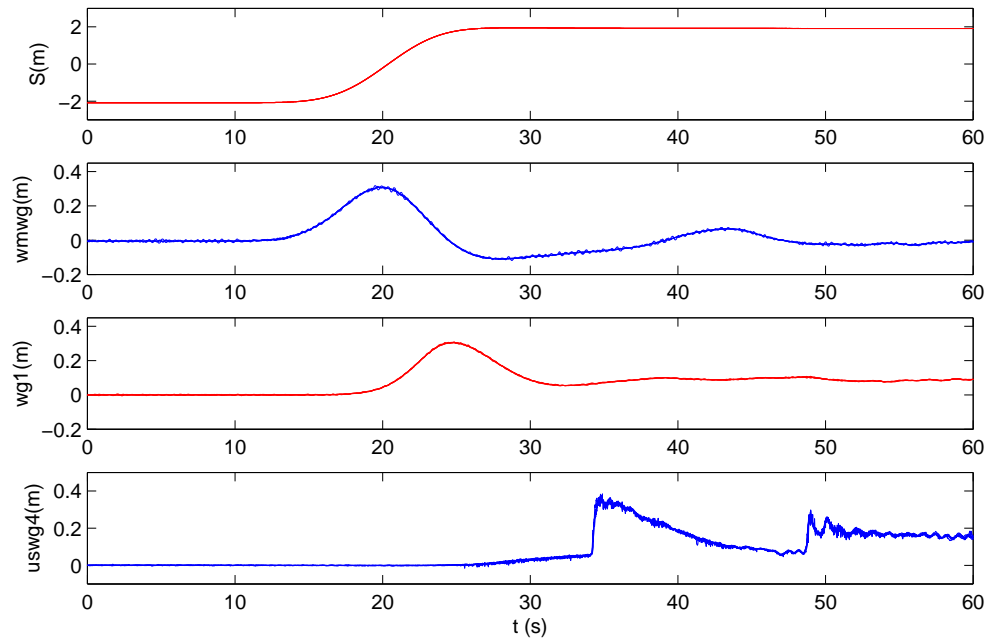


Figure 3.38: Time variation of wave paddle displacement and free surface variation from Hydrodynamics Test trials 17-21. Test conditions of: $h_1 = 2.57$ m, $h_2 = 0.203$ m, $T_{erf} = 20$ s. All 5 tests are superimposed onto one another.

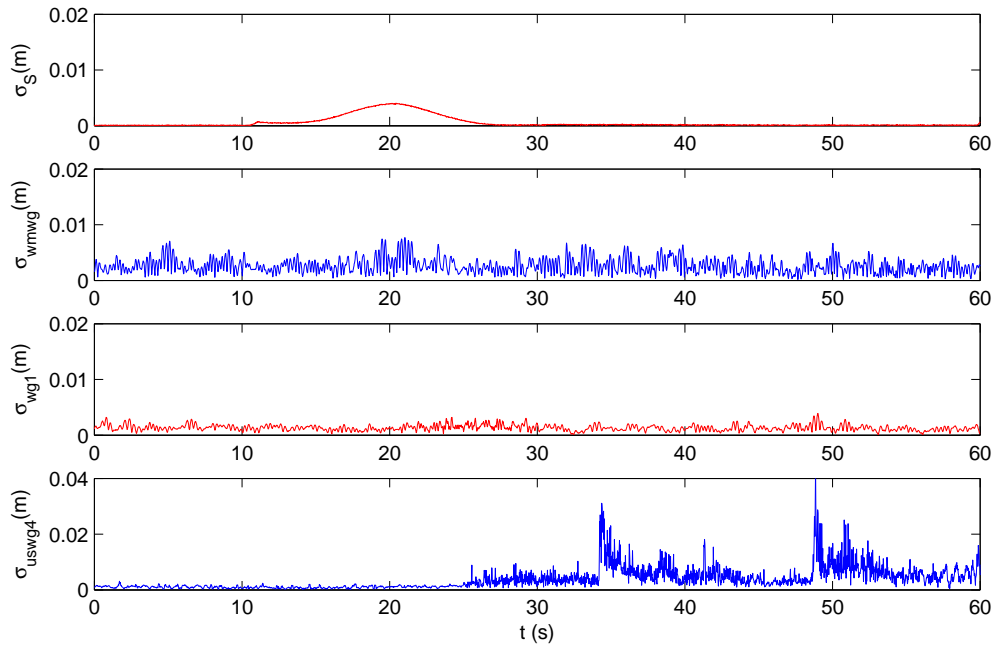


Figure 3.39: Standard deviations of time variation of wave paddle displacement and free surface variation from Hydrodynamics Test trials 17-21. Test conditions of: $h_1 = 2.57$ m, $h_2 = 0.203$ m, $T_{erf} = 20$ s. Note that the y -axis on panel 4 has twice the order of magnitude of the other 3 panels.

Fig. 3.39 shows the standard deviations for the measurements shown in Fig. 3.38. The standard deviation was very small for S , $wmwg$, and $wg1$. The standard deviation was higher for the measured inundation flow height on the test section, $uswg4$. This discrepancy in standard deviations suggested that flow variations over the test section were due to natural variation.

3.2.2 In-Air Test

In-Air tests were conducted in the wave flume in order to provide a basis for comparison for the In-Water debris impact tests. Three different types In-Air experiments were conducted in this study. The longitudinal orientation was used for the aluminum and acrylic specimen, while the transverse orientation was only used for the aluminum specimen.

3.2.2.1 Longitudinal Aluminum

3.2.2.1.1 Setup

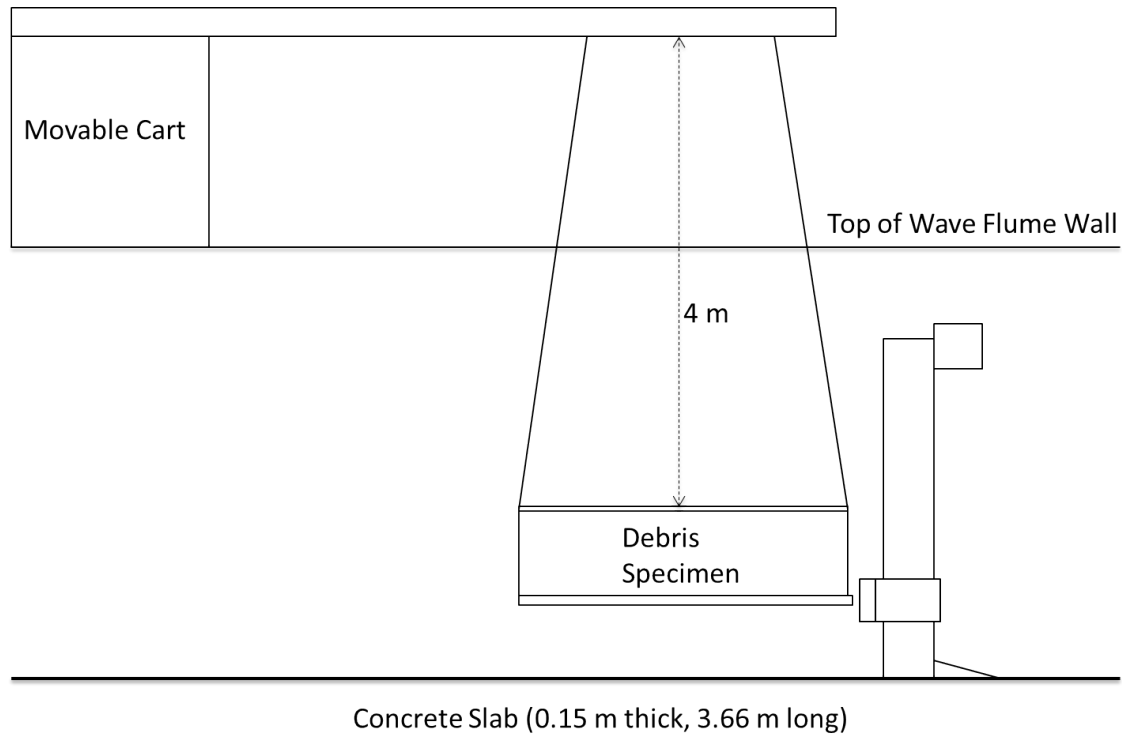


Figure 3.40: Schematic for In-Air longitudinal test.

Fig. 3.40 shows a schematic for the In-Air longitudinal aluminum test. The test was setup to allow for the suspended debris specimen to swing into the load cell. The specimen was suspended 4 m from a beam that was attached to a movable cart on top of the wave flume walls. Four cables were used and are attached to the four corners of the top of the debris specimen using eye bolts. The suspended debris specimen was lined up such that the extended bottom plate rested just in front of the load cell (Fig. 3.41).



Figure 3.41: Resting point for debris specimen relative to load cell during In-Air longitudinal aluminum test.

For each trial, a specific pullback distance, X , was used to cause the debris to swing like a pendulum into the load cell. Pullback distance was determined by placing measuring tape on the wave flume floor. The measuring tape was lined up with the shadow of the debris specimen (Fig. 3.42). The pullback process was conducted by an individual pulling back on the specimen. The distance was determined by the movement of the shadow on the measuring tape.



Figure 3.42: Measuring tape used to measure pullback distance, X .



Figure 3.43: Pullback process of debris specimen for longitudinal aluminum test.

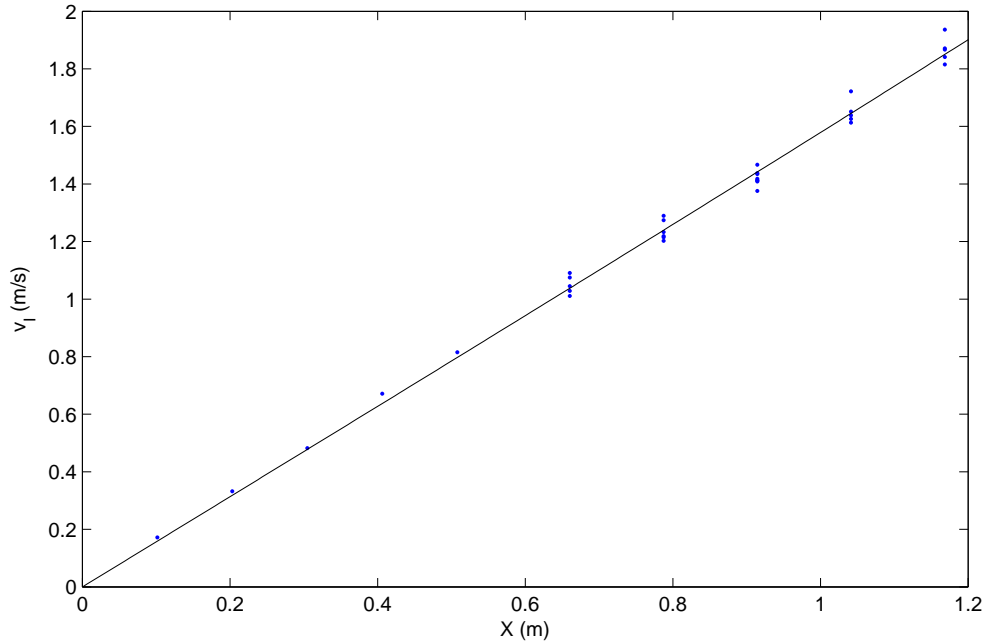


Figure 3.44: Plot of debris impact velocity, v_I vs. pullback distance, X for In-Air longitudinal test.

Fig. 3.44 shows the relationship between debris impact velocity, v_I , and pullback distance, X for the In-Air longitudinal aluminum test. A nearly linear relationship between the two variables was. This nearly linear relationship was observed due to the small amplitude of the pendulum setup (maximum amplitude of 0.3 rad).

3.2.2.1.2 Examples of Data

Fig. 3.45 - 3.48 show the load cell output from In-Air longitudinal aluminum test trial 8 at $v_I = 1.41$ m/s with different time scales. Fig. 3.45 shows that the impact duration was very small. Additionally, a secondary impact can also sometimes be observed by a secondary peak shortly after the primary impact. This was due to the specimen bouncing off the load cell and returning for a second impact. In all cases, the second impact has a smaller magnitude in the measured force. Fig. 3.48 shows the detailed impact force time history over 2 ms. It shows that the resolution of the time history of the impact force is quite good,

suggesting that the real peak impact force was captured during each trial. It was observed that the impact duration was around 1.6 ms. The maximum impact observed from the In-Air longitudinal aluminum tests was around 100 kN which corresponded to 7.5% of the capacity of the CLC-300K load cell.

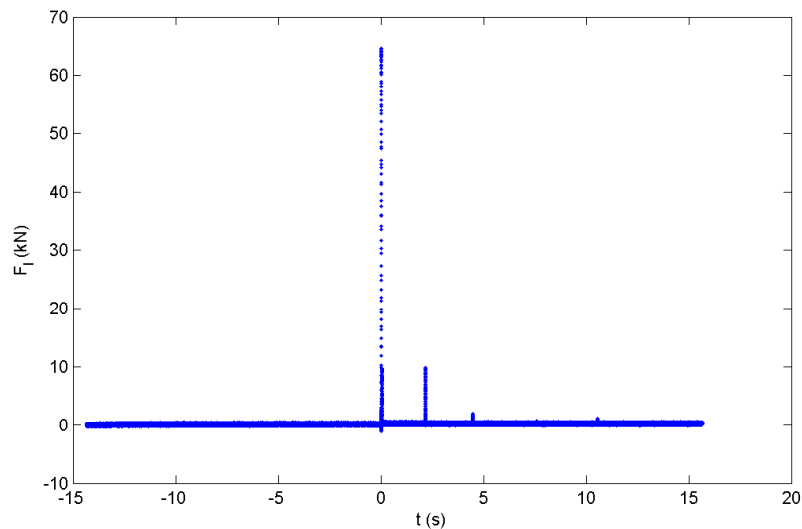


Figure 3.45: Impact force time history measured by waterproofed CLC-300K load cell for In-Air longitudinal aluminum test trial 8 at $v_I = 1.41$ m/s

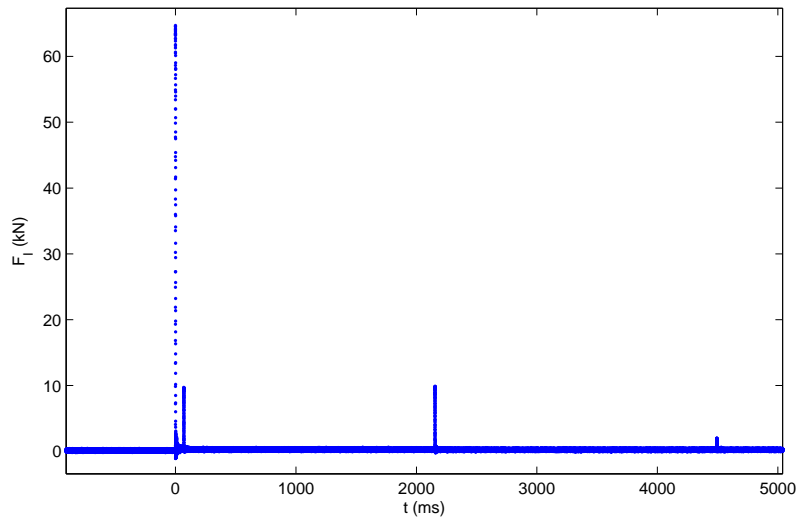


Figure 3.46: Detail of impact force time history over 5 s, measured by waterproofed CLC-300K load cell for In-Air longitudinal aluminum test trial 8 at $v_I = 1.41$ m/s

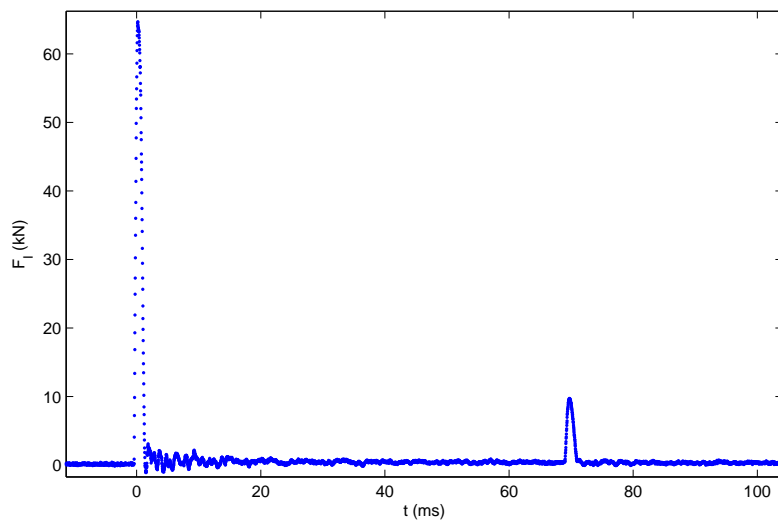


Figure 3.47: Detail of impact force time history over 100 ms, measured by waterproofed CLC-300K load cell for In-Air longitudinal aluminum test trial 8 at $v_I = 1.41$ m/s

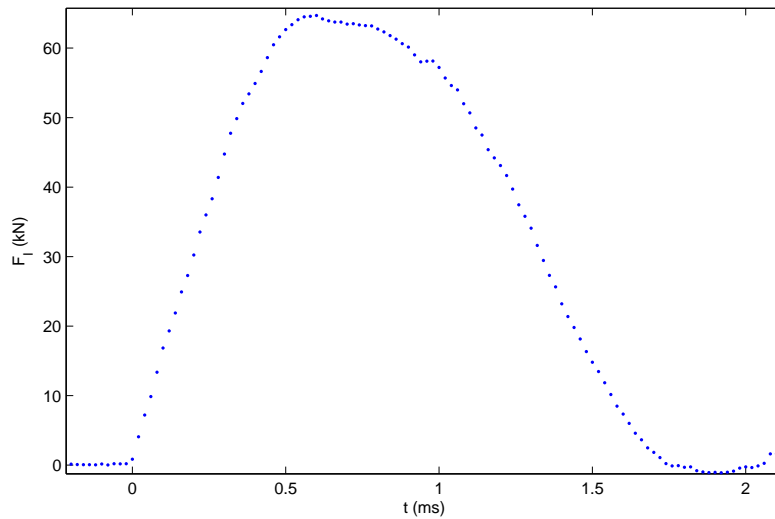


Figure 3.48: Detail of impact force time history over 2 ms, measured by waterproofed CLC-300K load cell for In-Air longitudinal aluminum test trial 8 at $v_I = 1.41$ m/s

3.2.2.1.3 Repeatability

The repeatability of the In-Air test was examined by repeating the test condition of $X = 91.44$ cm (36 in) six times. The peak force measurements from the repeatability analysis is shown in Table 3.4. The repeatability analysis shows the the variation of the peak forces in six trials was 2.3% of the average measured peak force. The consistency shown by the repeatability analysis suggested that In-Air test trials did not have to be repeated multiple times.

3.2.2.1.4 Load Cell Comparison

3.2.2.1.4.1 CLC-300K with and without waterproofing Fig. 3.49 shows the effect of waterproofing on the CLC-300K load cell based on the peak force, F_p vs. impact velocity, v_I relationship. Filled diamonds represent forces measured from waterproofed load cell. Data measured from In-Air longitudinal aluminum test. Fig. 3.49 shows that the waterproofing did not have a significant effect on the peak forces measured.

Table 3.4: Peak force measurements from repeatability test of In-Air longitudinal aluminum test at $X = 91.44$ cm

X (cm)	F_p (kN)
91.4	72.9
91.4	74.6
91.4	73.4
91.4	71.4
91.4	70.0
91.4	73.5
Mean	72.6
StDev	1.7
%StDev	2.28

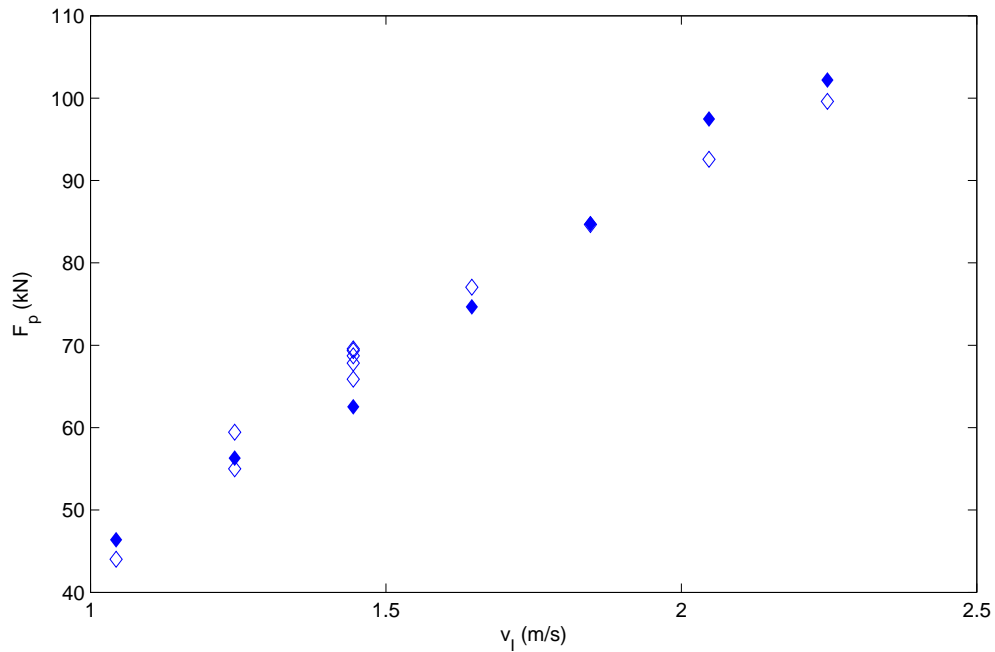


Figure 3.49: Comparison of peak force, F_p vs. impact velocity, v_I for the waterproofed and CLC-300K load cell before waterproofing. Forces measured from waterproofed load cell (◆), forces measured from load cell before waterproofing (◇). Data measured from In-Air longitudinal aluminum test.

3.2.2.1.4.2 CLC-300K vs. HSW-50K Fig. 3.50 shows the comparison of the peak force, F_p vs. impact velocity, v_I relationship for the HSW-50K and CLC-300K load cells. CLC-300K load cell (\circ), HSW-50K load cell (\triangleright). Fig. 3.50 shows that there may have been a slight offset as the HSW-50K force readings appeared to be a bit higher overall. The difference was not substantial and from this point we decided to use the CLC-300K load cell moving forward due to the higher frequency response.

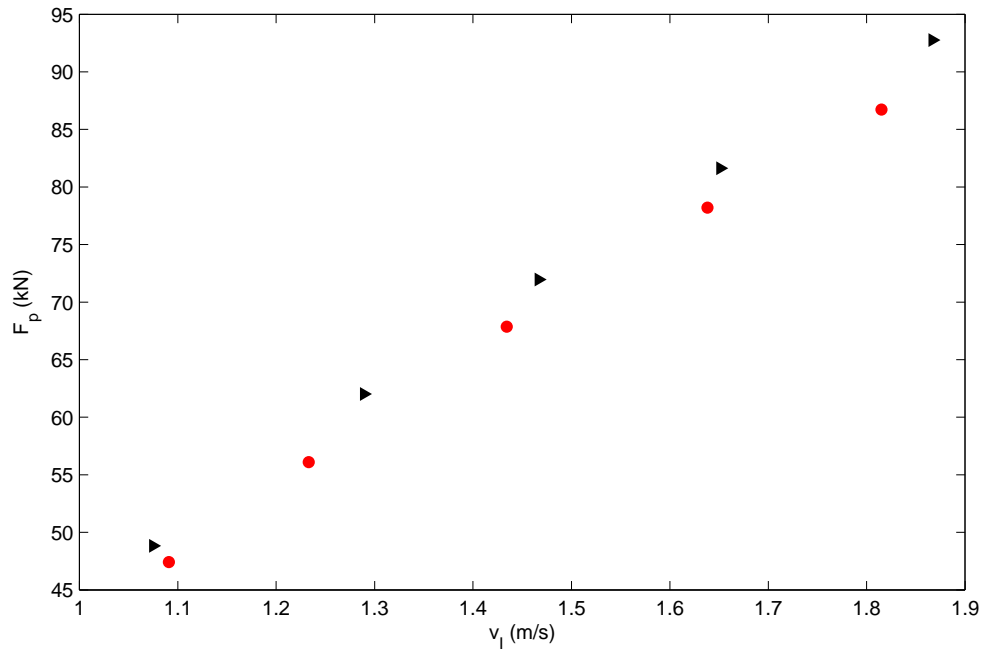


Figure 3.50: Comparison of peak force, F_p vs. impact velocity, v_I for the HSW-50K and waterproofed CLC-300K load cell. CLC-300K load cell (\bullet), HSW-50K load cell (\blacktriangleright). Data measured from In-Air longitudinal aluminum test.

3.2.2.1.5 Effect of Nonstructural Mass

Fig. 3.51 shows the comparison of the F_p vs. v_I relationship for nonstructural mass values of $M_{NS} = 0$ and $M_{NS} = 50.2$ kg. Aside from the case at $v_I = 2.1$ m/s, the nonstructural mass did not appear to have a significant effect on the measured peak impact force from the debris. The $v_I = 2.1$ m/s case was likely due to poor contact between the debris and

the load cell (see section 3.2.2.1.6).

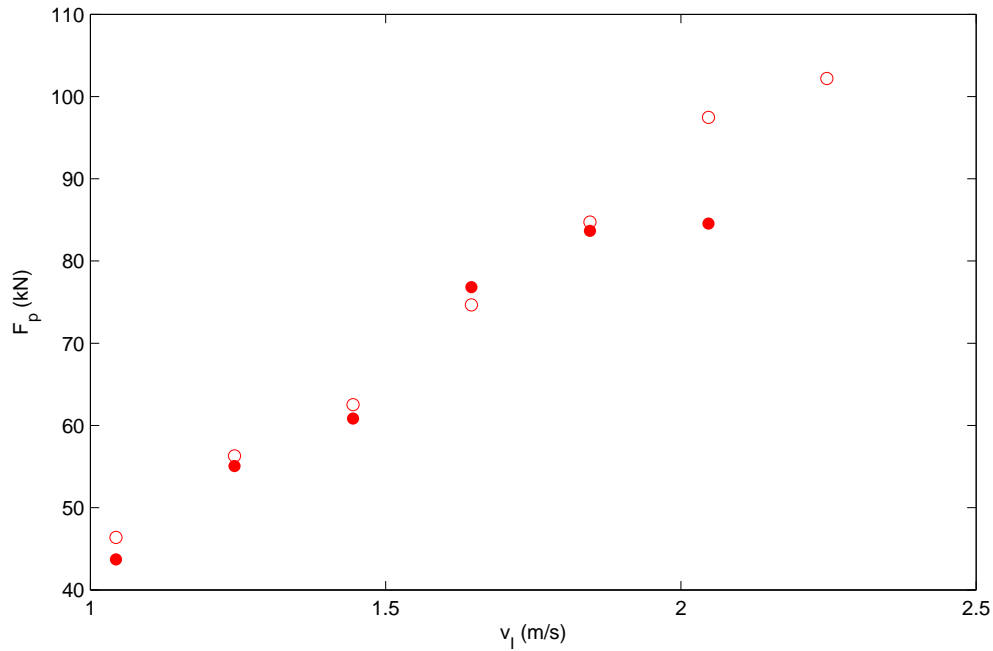


Figure 3.51: Comparison of peak force, F_p vs. impact velocity, v_I for nonstructural mass values of $M_{NS} = 0$ and $M_{NS} = 50.2$ kg. $M_{NS} = 0$ kg (\circ), $M_{NS} = 50.2$ kg (\bullet). Data measured from In-Air longitudinal aluminum test.

3.2.2.1.6 Contact Position Sensitivity

The sensitivity of contact positioning between the debris and the load cell was investigated by adjusting the resting point of the suspended debris specimen. Two different cases were considered, the standard “centered” and the “off-center” positions (Fig. 3.52). The “off-center” position was selected to be the extreme case where the debris was making contact with the edge of the load cell.

Fig. 3.53 shows the comparison of the F_p vs. v_I relationship for the “centered” and “off-center” contact positions between aluminum debris specimen and load cell for In-Air longitudinal aluminum test. Overall, Fig. 3.53 indicated that the measured impact forces were sensitive to the contact position between the specimen and the load cell. Off-center

impacts had lower peak impact force measurements across the range of velocities tested.

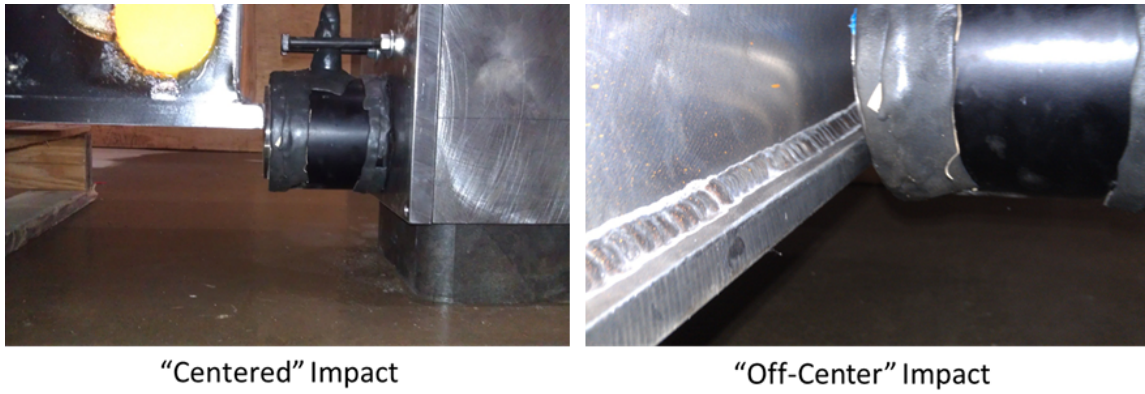


Figure 3.52: Photographs of the "centered" and "off-center" contact positions for the In-Air longitudinal aluminum test.

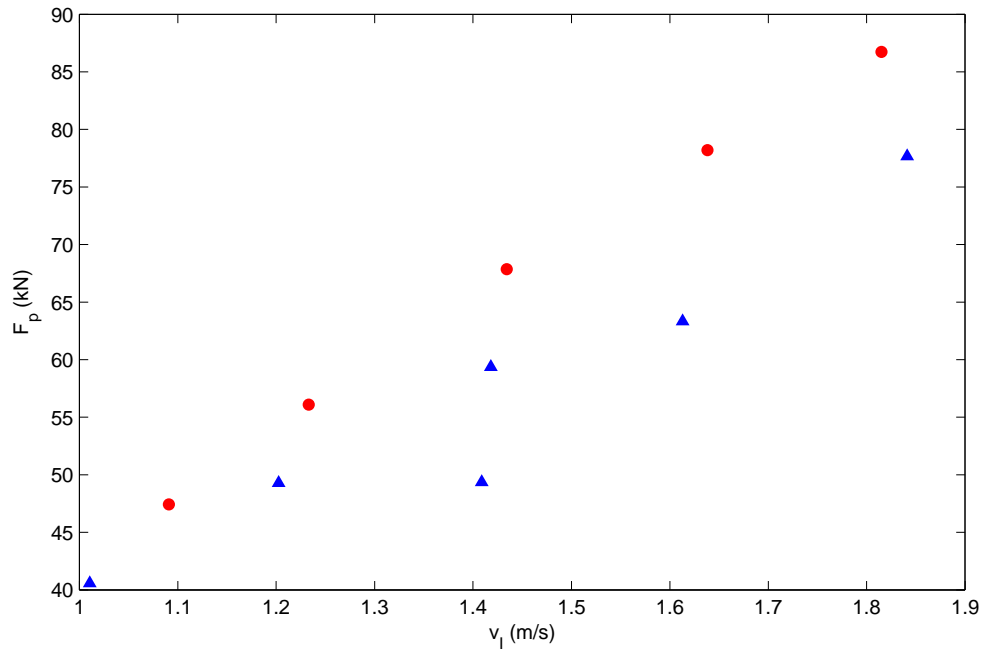


Figure 3.53: Comparison of peak force, F_p vs. impact velocity, v_I for “centered” and “off-center” contact positions between aluminum debris specimen and load cell for In-Air longitudinal aluminum test. “Centered” contacts (●), “off-center” contacts (▲).

3.2.2.1.7 Pitch Angle Test

Fig. 3.54 shows the setup for the In-Air pitch angle test. This test investigated the effect of pitch angle, ϕ , (the slope of the major axis of the debris) on the measured peak impact force. ϕ was adjusted by increasing or decreasing the lengths of the cables attached to the front and back of the debris specimen. Using this method, a maximum pitch angle of $\phi = 5.7^\circ$ was obtained. A pullback distance of $X = 66.04$ cm was repeated five times for $\phi = 3.0^\circ$ and five times for $\phi = 5.7^\circ$.

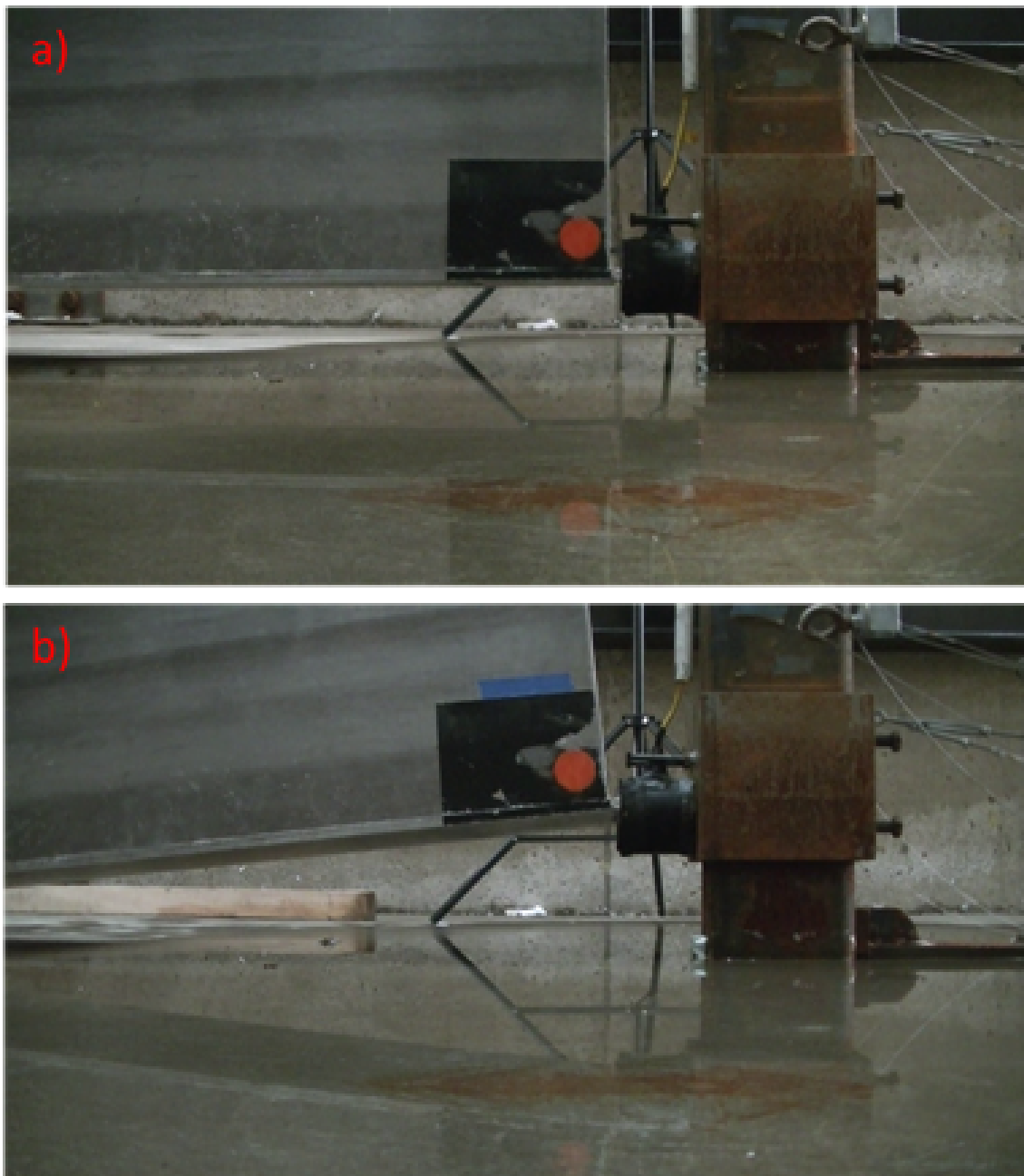


Figure 3.54: Pitch angle (ϕ) test setup with (a) $\phi = 0^\circ$ (b) $\phi = 5.7^\circ$.

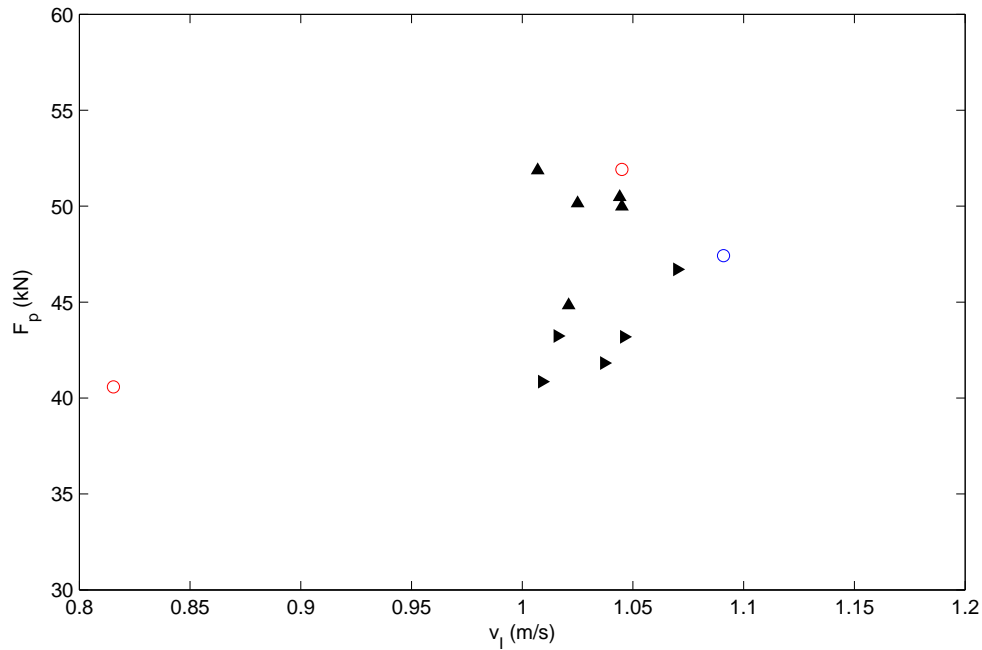


Figure 3.55: Effect of pitch angle (ϕ) on measured peak impact force. $\phi = 0^\circ$ (\circ), $\phi = 3.0^\circ$ (\blacktriangle), $\phi = 5.7^\circ$ (\blacktriangleright).

Fig. 3.55 shows the effect of pitch angle (ϕ) on measured peak impact force with circles representing $\phi = 0^\circ$, standard triangles representing $\phi = 3.0^\circ$, and sideways triangles representing $\phi = 5.7^\circ$. Fig. 3.55 shows that the pitch angle could have an effect on the accuracy and consistency of the peak force measurements. Unfortunately, only a very small range of pitch angles could be tested. However, this did indicate another aspect that could contribute to the measurement variability for the In-Water test.

3.2.3 Longitudinal Acrylic

3.2.3.1 Setup

Fig. 3.56 shows a photograph of In-Air longitudinal acrylic test. The test setup was identical to that used by the In-Air longitudinal aluminum test (Fig. 3.40). Fig. 3.57 shows the relationship between v_I and X for the In-Air longitudinal acrylic test. A nearly linear

relationship, consistent with the aluminum case, was observed.

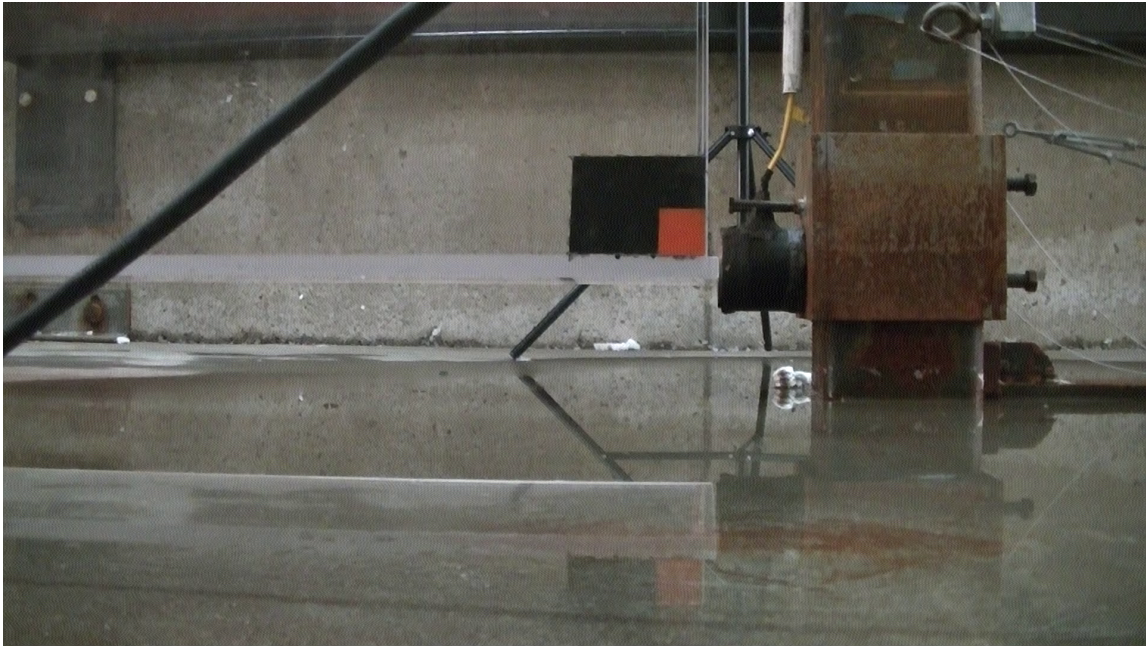


Figure 3.56: Photograph of the setup for the In-Air longitudinal acrylic test.

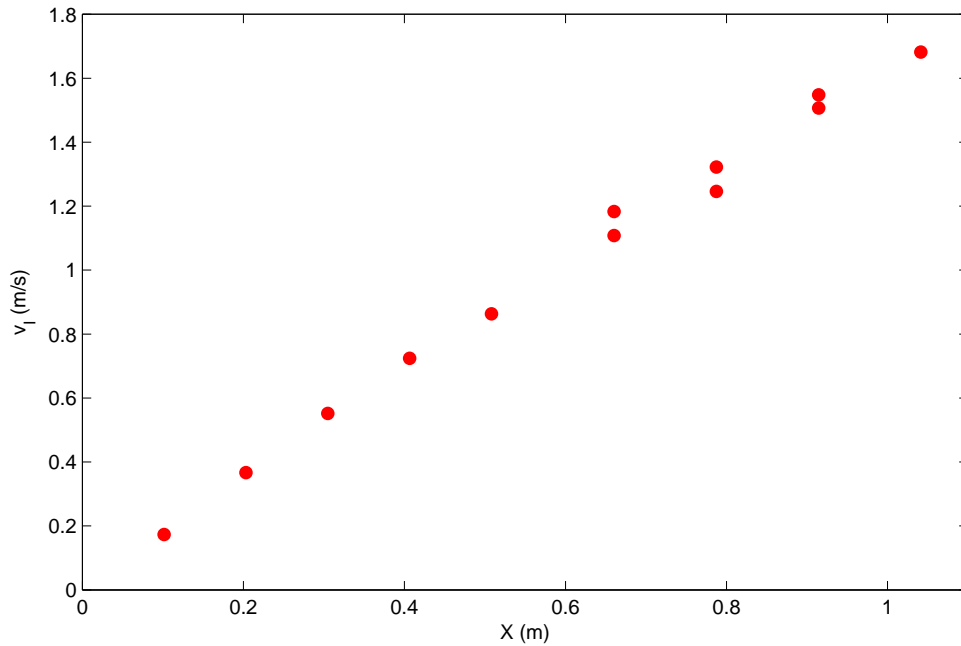


Figure 3.57: Plot of debris impact velocity, v_I vs. pullback distance, X for In-Air acrylic test.

3.2.3.2 Examples of Data

Fig. 3.58 - 3.62 shows the load cell output from In-Air longitudinal acrylic test trial 4 at $v_I = 0.72$ m/s with different time scales. Fig. 3.58 shows that there were many additional impacts that occur after the primary impact. This was due to the specimen bouncing off the load cell and returning for a second impact. The acrylic specimen bounce produced more additional impacts than the aluminum specimen. All of the additional impacts had smaller magnitudes in the measured force. Fig. 3.48 shows the detailed impact force time history over 4 ms. It was observed that the impact duration was around 4 ms. The maximum impact observed from the In-Air longitudinal acrylic tests was around 50 kN which corresponded to 3.8% of the capacity of the CLC-300K load cell.

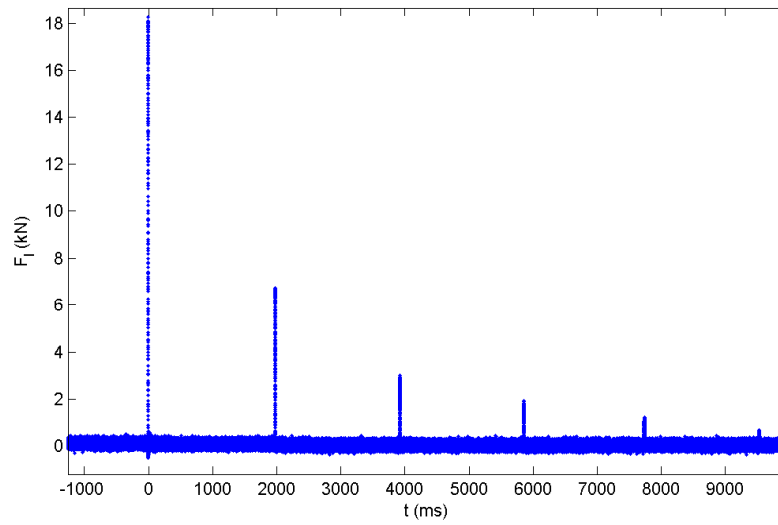


Figure 3.58: Impact force time history measured by waterproofed CLC-300K load cell for In-Air longitudinal acrylic test trial 4 at $v_I = 0.72$ m/s detailed over 10 s.

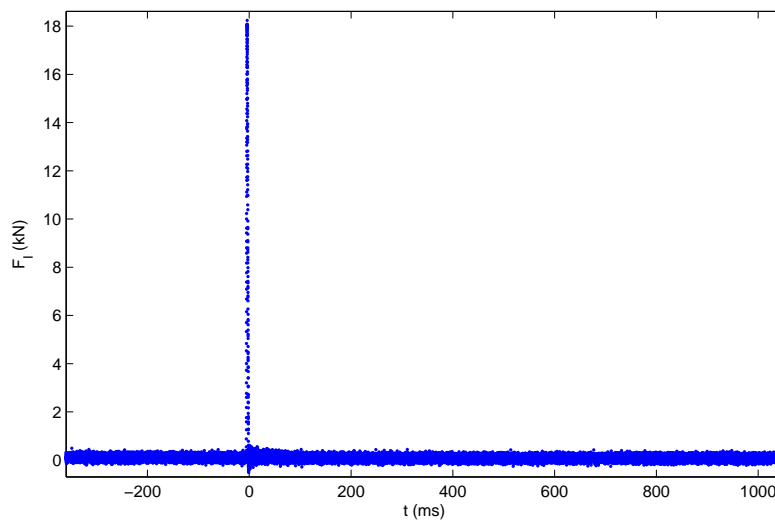


Figure 3.59: Detail of impact force time history over 1 s, measured by waterproofed CLC-300K load cell for In-Air longitudinal acrylic test trial 4 at $v_I = 0.72$ m/s.

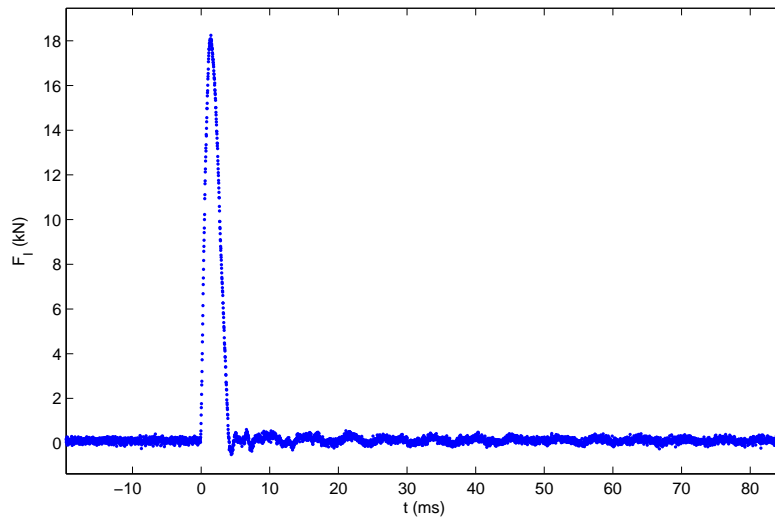


Figure 3.60: Detail of impact force time history over 100 ms, measured by waterproofed CLC-300K load cell for In-Air longitudinal acrylic test trial 4 at $v_I = 0.72$ m/s.

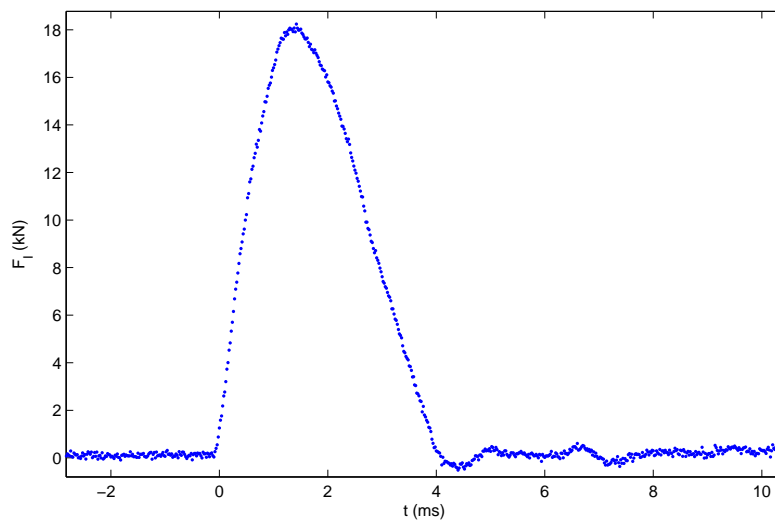


Figure 3.61: Detail of impact force time history over 10 ms, measured by waterproofed CLC-300K load cell for In-Air longitudinal acrylic test trial 4 at $v_I = 0.72$ m/s.

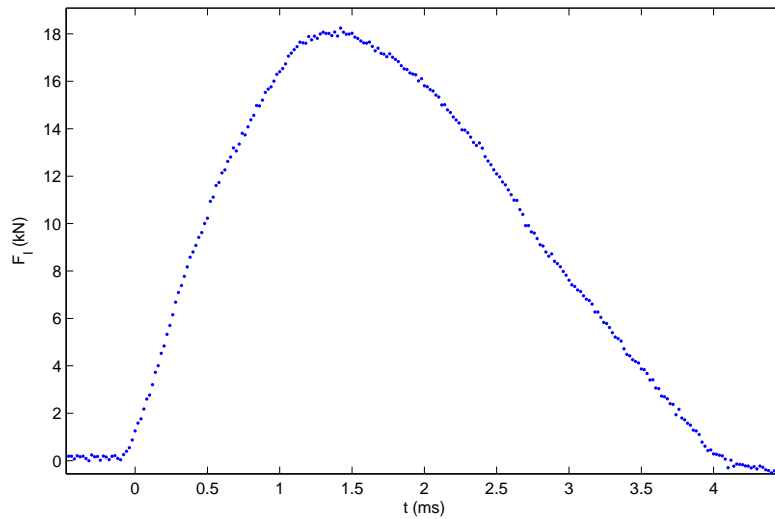


Figure 3.62: Detail of impact force time history over 4 ms, measured by waterproofed CLC-300K load cell for In-Air longitudinal acrylic test trial 4 at $v_I = 0.72$ m/s

3.2.4 Transverse Aluminum

3.2.4.1 Setup

Fig. 3.63 shows the schematic for the In-Air transverse aluminum test. This test setup followed the same idea as the In-Air longitudinal tests. In this case, the specimen was suspended underneath the movable cart for more stability. The specimen was suspended 1.6 m below the movable cart. Since the bottom plate did not extend along the minor axis of the specimen, a smaller range of velocities was used to prevent damage. The specimen was lined up such that the resting point for the bottom plate of the specimen made slight contact with the center of the load cell. The Panasonic HD digital camcorder was used to track the velocities of the swinging debris. An orange square was painted in the bottom right corner of one of the smaller faces of the debris for tracking purposes.

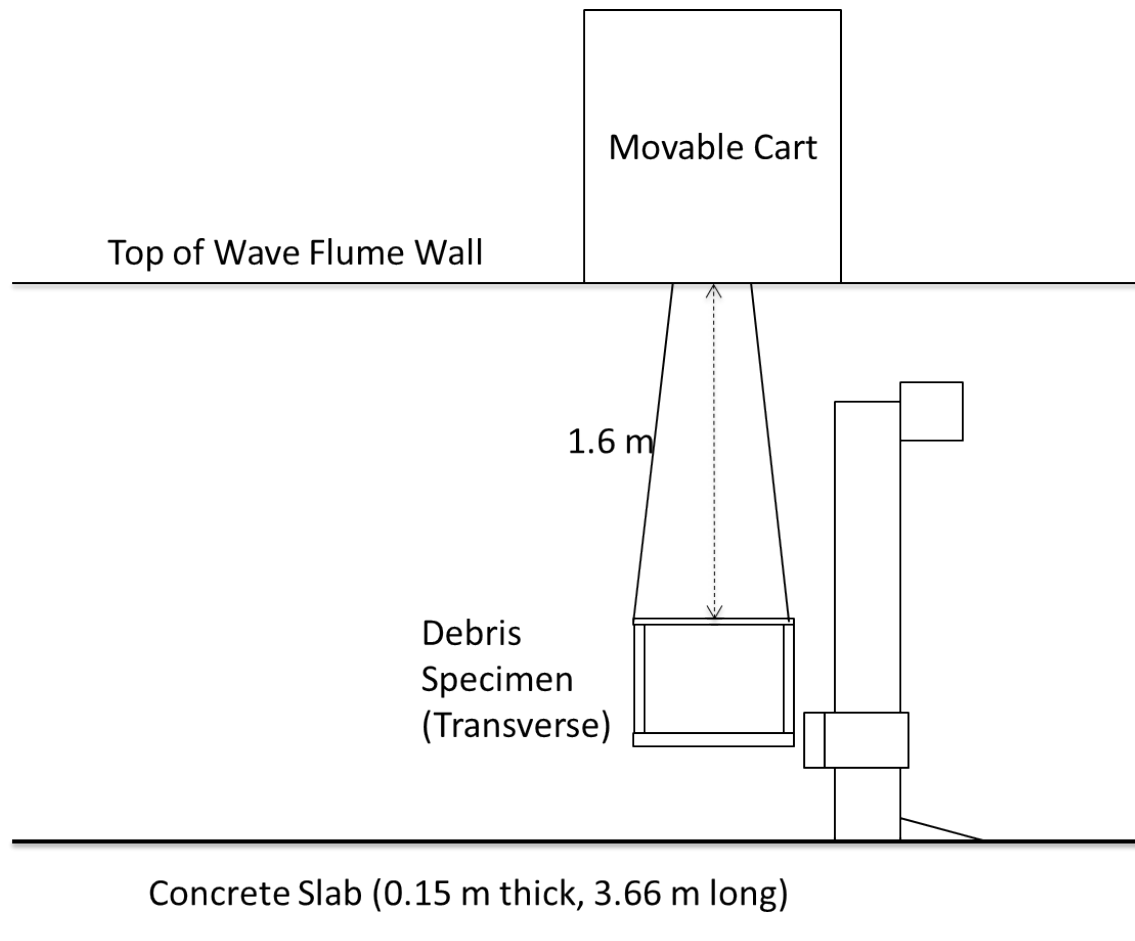


Figure 3.63: Schematic for In-Air transverse aluminum test.



Figure 3.64: Photograph of the In-Air transverse aluminum test.

Fig. 3.65 shows relationship between debris impact velocity v_I and X for the In-Air transverse aluminum test. The relationship was observed to be less linear than what was observed in the longitudinal cases. This difference in linearity was due to the shortening of the cable length and thus the amplitude of the pendulum.

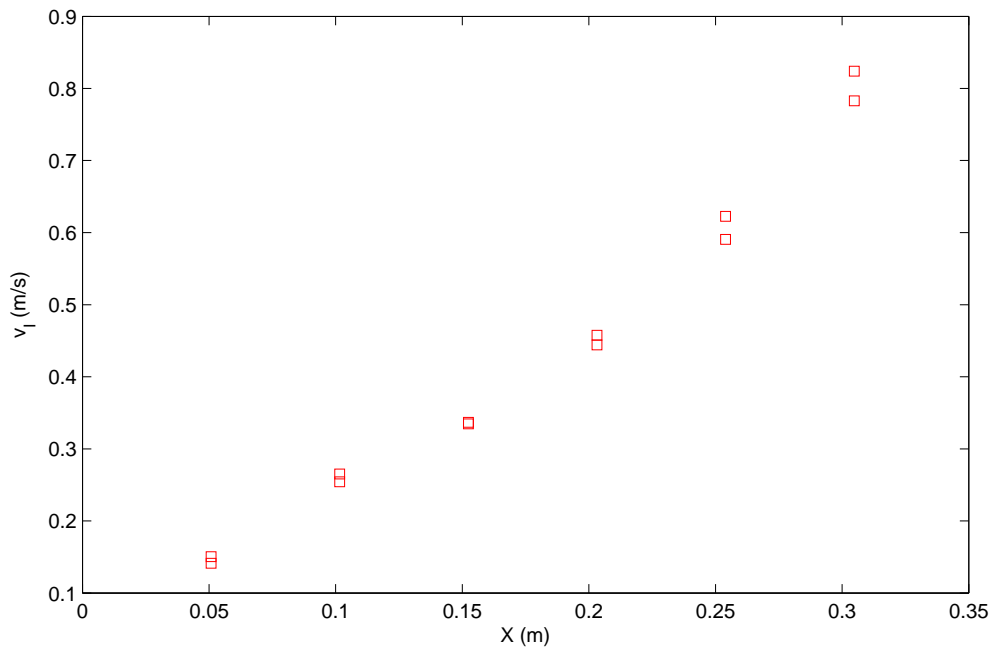


Figure 3.65: Plot of debris impact velocity, v_I vs. pullback distance, X for In-Air transverse test.

3.2.4.2 Examples of Data

Fig. 3.66 - 3.70 shows the impact force time history from In-Air transverse aluminum test trial 9 at $v_I = 0.59$ m/s with different time scales. Fig. 3.58 shows that there were additional impacts that occurred after the primary impact. This was, again, due to the specimen bouncing off the load cell and returning for a secondary impacts. All of the additional impacts had smaller magnitudes measured peak force. Fig. 3.48 shows the primary impact detailed over 4.5 ms. It was observed that the duration of the primary impact was around 2 ms, however residual effects appeared to continue for another 8 ms. The maximum impact observed from the In-Air transverse aluminum tests was around 25 kN which corresponded to 1.9% of the capacity of the CLC-300K load cell.

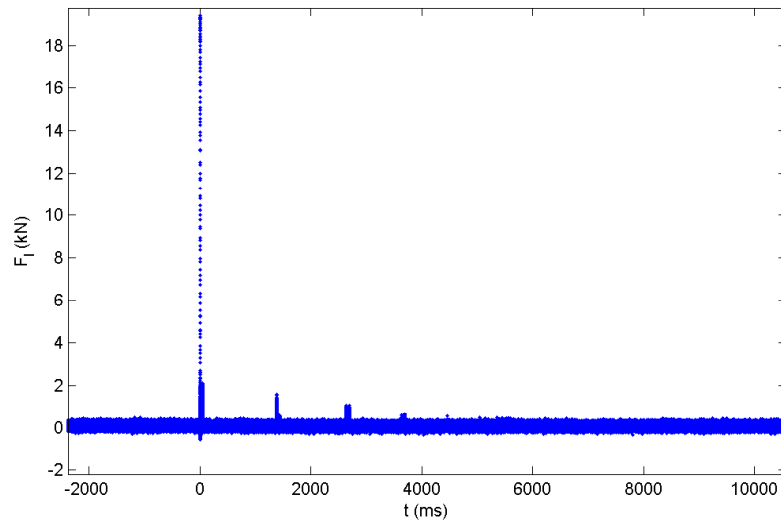


Figure 3.66: Impact force time history measured by waterproofed CLC-300K load cell for In-Air transverse aluminum test trial 9 at $v_I = 0.59$ m/s

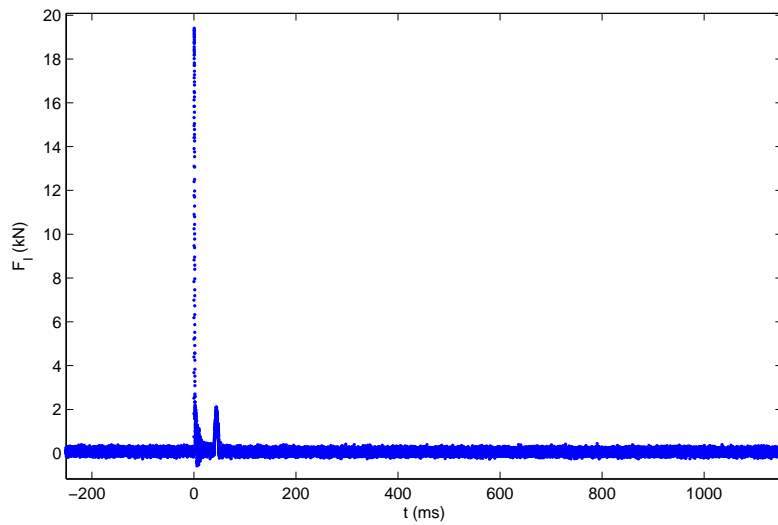


Figure 3.67: Detail of impact force time history over 1 s, measured by waterproofed CLC-300K load cell for In-Air transverse aluminum test trial 9 at $v_I = 0.59$ m/s

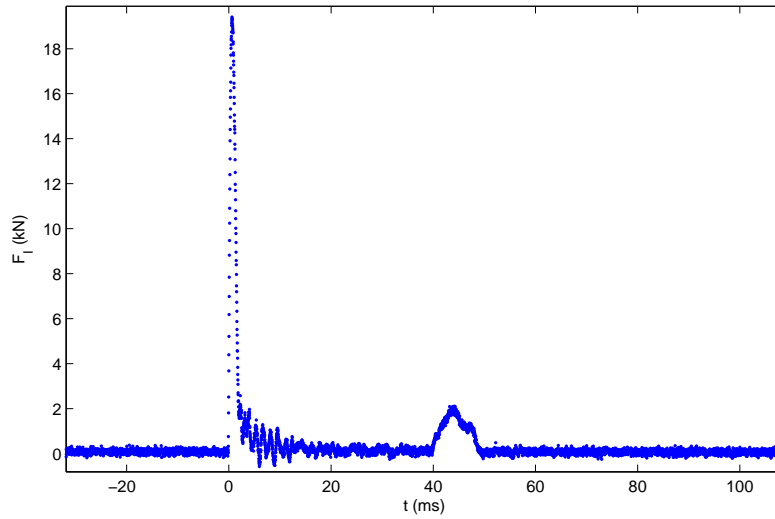


Figure 3.68: Detail of impact force time history over 100 s, measured by waterproofed CLC-300K load cell for In-Air transverse aluminum test trial 9 at $v_I = 0.59$ m/s

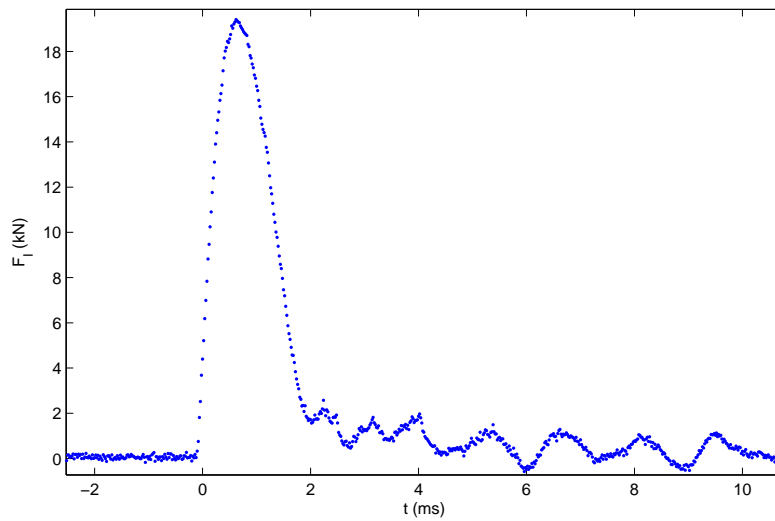


Figure 3.69: Detail of impact force time history over 10 ms, measured by waterproofed CLC-300K load cell for In-Air transverse aluminum test trial 9 at $v_I = 0.59$ m/s

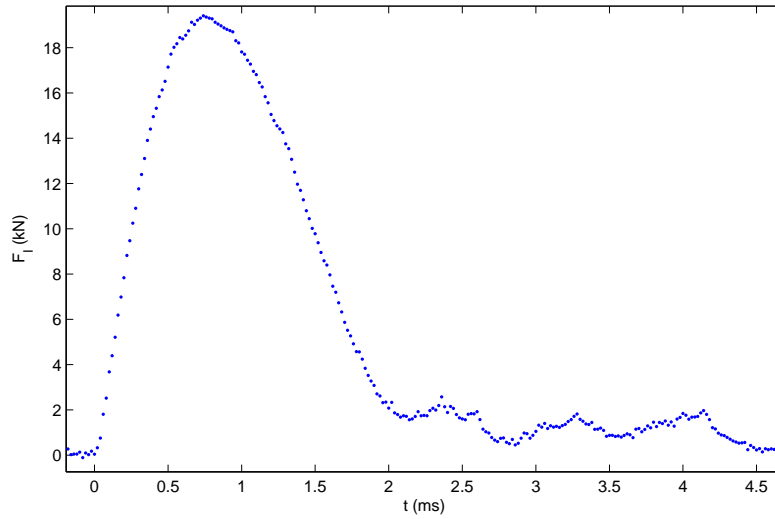


Figure 3.70: Detail of impact force time history over 4.5 ms, measured by waterproofed CLC-300K load cell for In-Air transverse aluminum test trial 9 at $v_I = 0.59$ m/s

3.2.5 In-Water Test

3.2.5.1 Longitudinal Aluminum

3.2.5.1.1 Setup

The setup for the In-Water longitudinal aluminum test used the wave flume and bathymetry setup shown in Fig. 3.1 and the guide wire setup shown in Fig. 3.18. The debris specimen was placed 3 - 4 m away from the column in $-x$ direction. The debris specimen was transported toward the column using long waves generated by error function wave paddle displacement. Velocities were measured by using the color based object tracking method mentioned in section 3.5.3 (Fig. 3.30). Water depths and wave conditions were shown in Table 3.3.

The GoPro HERO2 camera was placed in the $-y$ direction of the load cell. The GoPro HERO2 camera was used to determine the quality of the contact made between the specimen and the load cell for each trial. “Good” trials were defined as when the extended bottom plate of the load cell made solid contact near the center of the load

cell. “Bad” contacts were contacts that exhibited impact that was not centered on the load cell face. This was important considering the variability in impact forces due to poor contact observed in the In-Air tests. Fig. 3.71 shows examples of “good” and “bad” contact between debris specimen and load cell as observed underwater with GoPro HERO2.

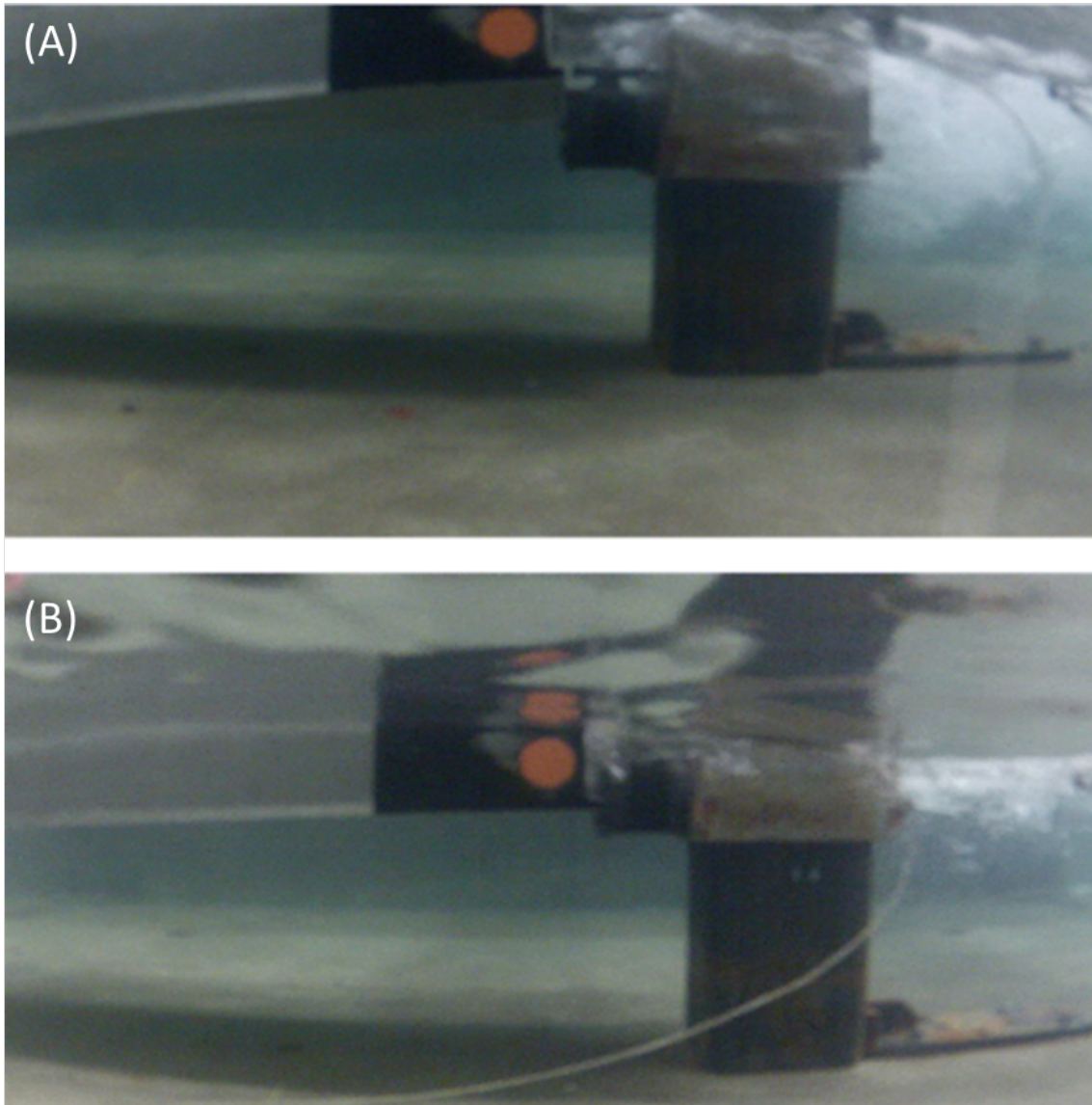


Figure 3.71: Examples of (A) “Bad” contact and (B) “Good” contact between debris specimen and load cell as observed underwater with GoPro HERO2.

The underwater cameras were used to ensure that 5 “Good” trials were obtained for each set of wave and nonstructural mass conditions. The position of the load cell sleeve was adjusted based on the video footage. In most cases, the load cell sleeve had to be adjusted between each wave condition.

3.2.5.1.2 Water depths and wave conditions

3.2.5.1.2.1 $h_2 = 13.3$ cm Fig. 3.72 shows the time variation of free surface elevation and force response from In-Water test: $h_1 = 2.50$ m, $h_2 = 0.13$ m, $T_{erf} = 30$ s, trial 12. In comparison to the relative time scales of the inundation flow, the impact duration was small relative to the time scale of the flow.

Fig. 3.73 - 3.76 shows the detailed impact force time history for In-Water longitudinal aluminum test: $h_1 = 2.50$ m, $h_2 = 0.13$ m, $T_{erf} = 30$ s, trial 12. Fig. 3.76 shows that additional impact force was experienced almost immediately after the primary impact. This additional impact force was very small relative to the primary impact.

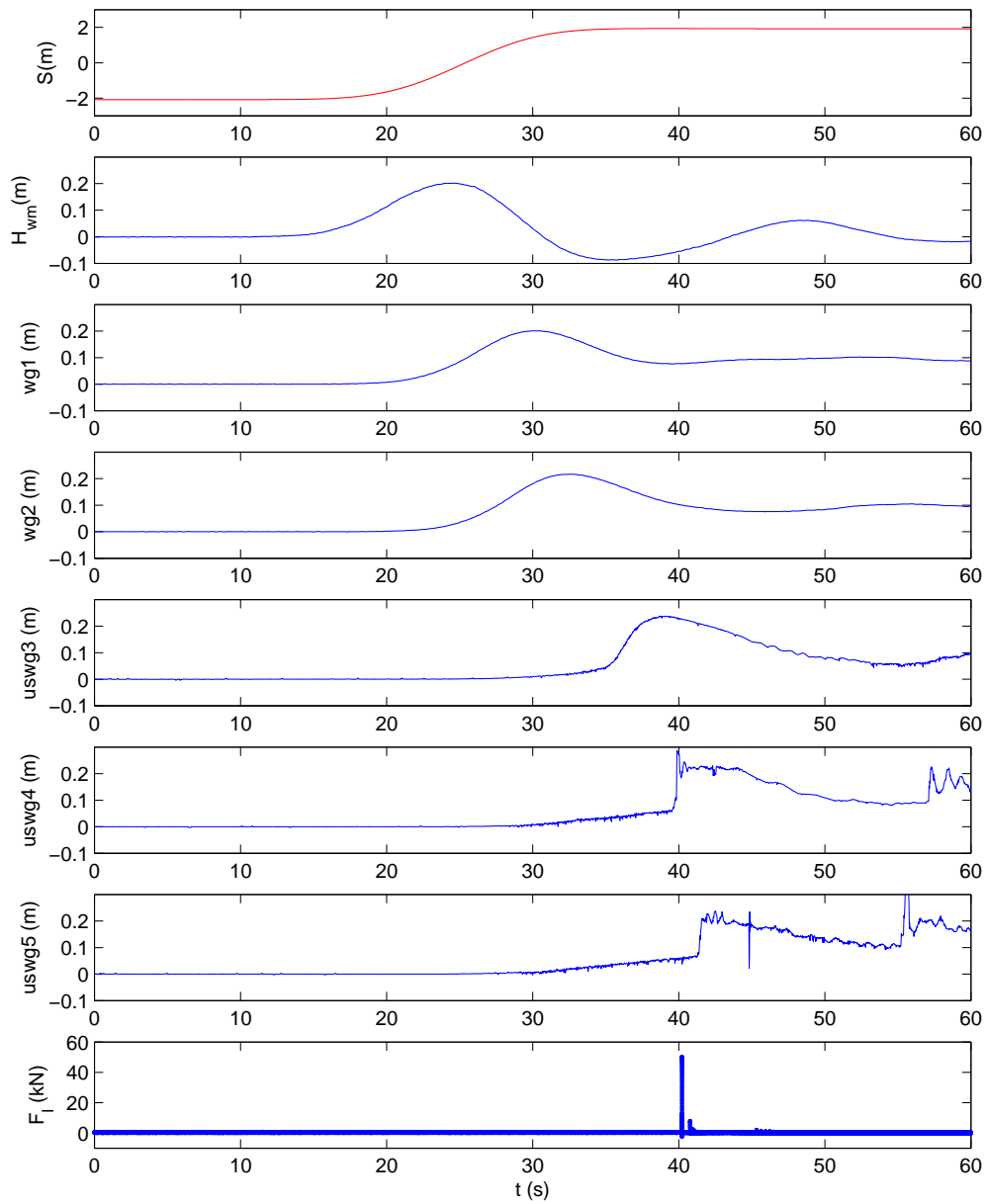


Figure 3.72: Time variation of free surface elevation and force response from In-Water longitudinal aluminum test: $h_1 = 2.50$ m, $h_2 = 0.13$ m, $T_{erf} = 30$ s, trial 12.

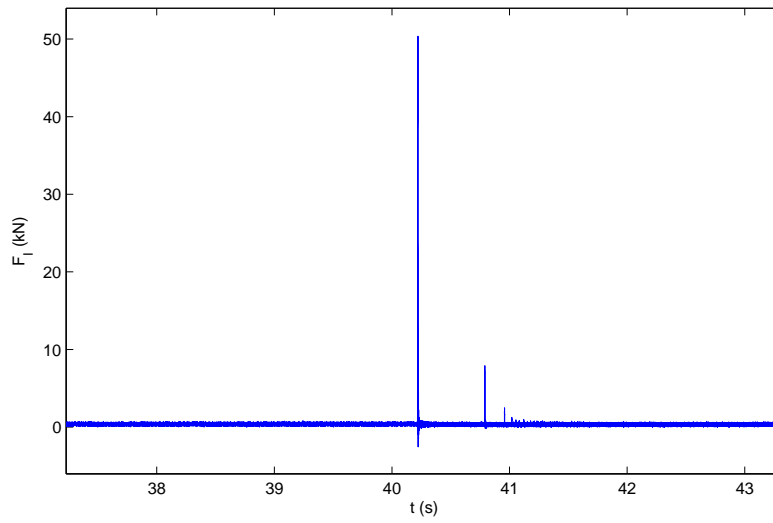


Figure 3.73: Detail of impact force time history over 5 s, for In-Water longitudinal aluminum test: $h_1 = 2.50$ m, $h_2 = 0.13$ m, $T_{erf} = 30$ s, trial 12.

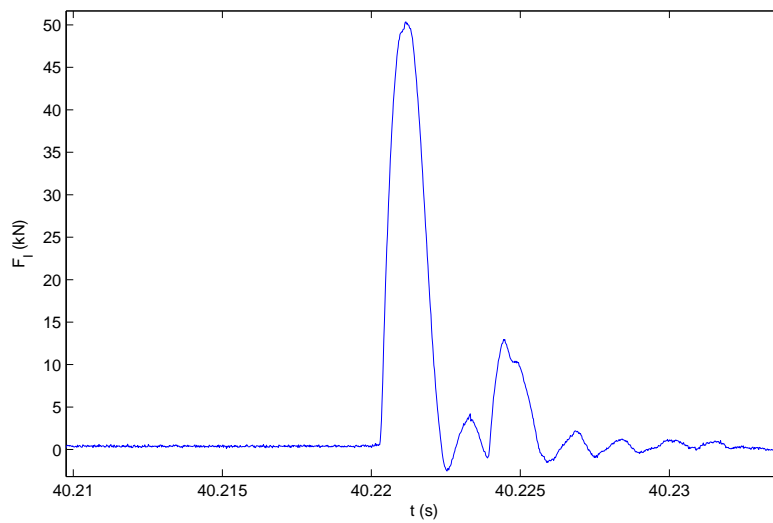


Figure 3.74: Detail of impact force time history over 0.2 s, for In-Water longitudinal aluminum test: $h_1 = 2.50$ m, $h_2 = 0.13$ m, $T_{erf} = 30$ s, trial 12.

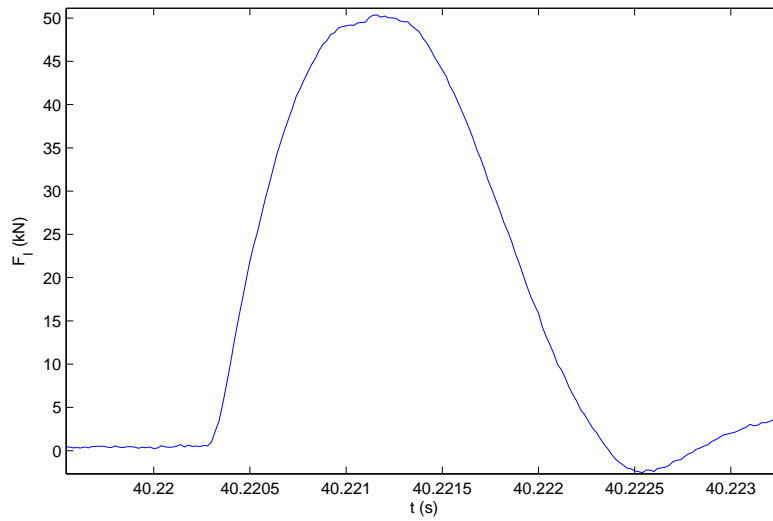


Figure 3.75: Detail of impact force time history over 0.003 s, for In-Water longitudinal aluminum test: $h_1 = 2.50$ m, $h_2 = 0.13$ m, $T_{erf} = 30$ s, trial 12.

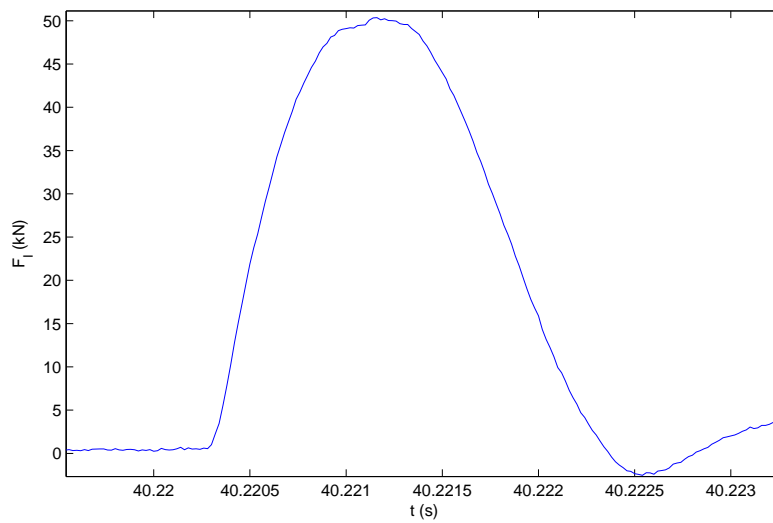


Figure 3.76: Detail of impact force time history over 0.003 s, for In-Water longitudinal aluminum test: $h_1 = 2.50$ m, $h_2 = 0.13$ m, $T_{erf} = 30$ s, trial 12.

Fig. 3.77 shows the impact force time histories of five repeated trials of In-Water longitudinal aluminum test at $h_1 = 2.50$ m, $h_2 = 0.13$ m, $T_{erf} = 30$ s, trial 11-15. Overall, the repeatability of these trials was quite good. The impact durations of two lowest peak force trials were slightly longer than the for the other three.

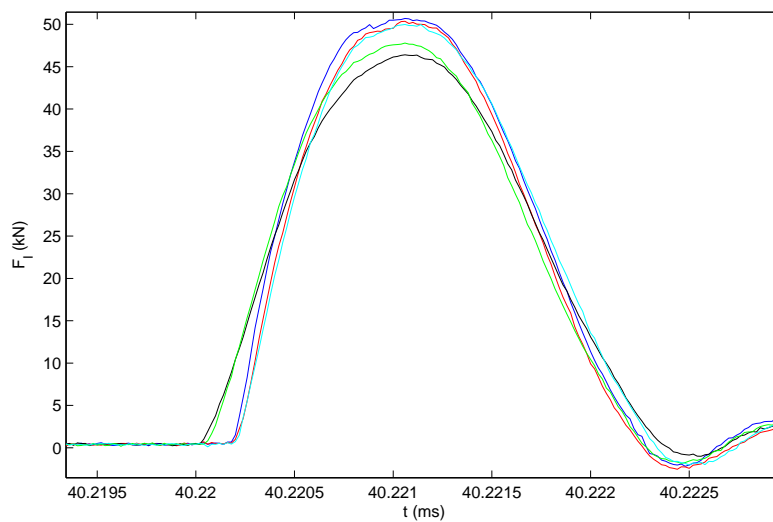


Figure 3.77: Impact force time histories of five trials, detailed over 0.003 s, for In-Water longitudinal aluminum test: $h_1 = 2.50$ m, $h_2 = 0.13$ m, $T_{erf} = 30$ s, trial 11-15.

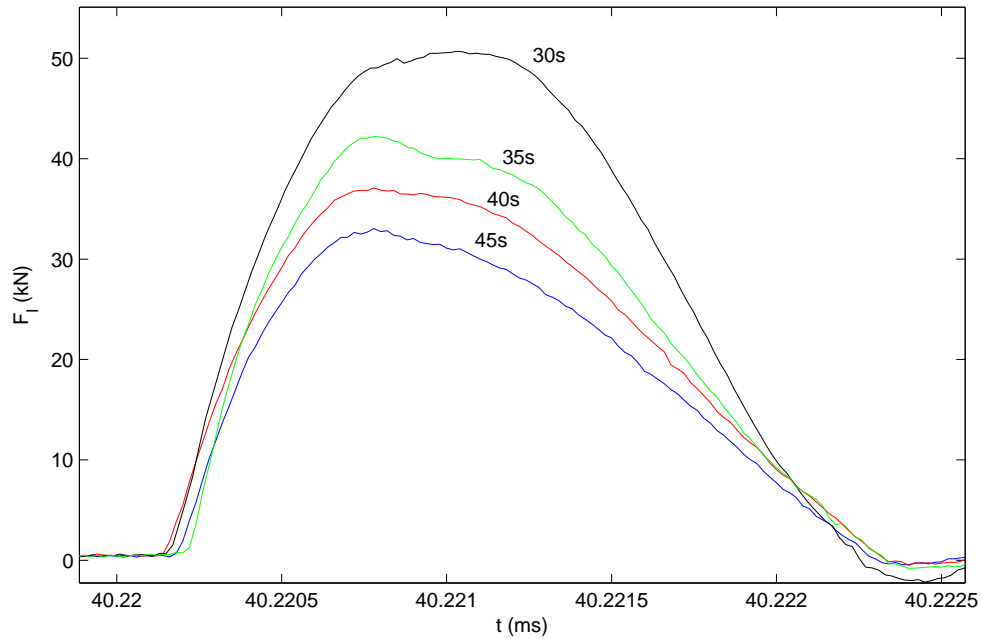


Figure 3.78: Impact force time histories of trials 7, 11, 18, 26. Each trial represents one of the T_{erf} used for In-Water longitudinal aluminum test: $h_1 = 2.50$ m, $h_2 = 0.13$ m

Fig. 3.78 shows the impact force time histories of trials 7, 11, 18, 26. Each trial represents a different T_{erf} that was used for In-Water longitudinal aluminum test at $h_1 = 2.50$ m, $h_2 = 0.13$ m. T_{erf} of 45s, 40s, 35s, and 30s were used. Measured impact force was shown to increase as T_{erf} decreased.

3.2.5.1.2.2 $h_2 = 20.9$ cm Fig. 3.79 shows the impact force time histories of trials 3, 10, 14, 20. Each trial represents a different T_{erf} that was used for In-Water longitudinal aluminum test at $h_1 = 2.57$ m, $h_2 = 0.21$ m. T_{erf} of 40s, 35s, 30s, and 25s were used. Measured impact force was shown to increase as T_{erf} decreased.

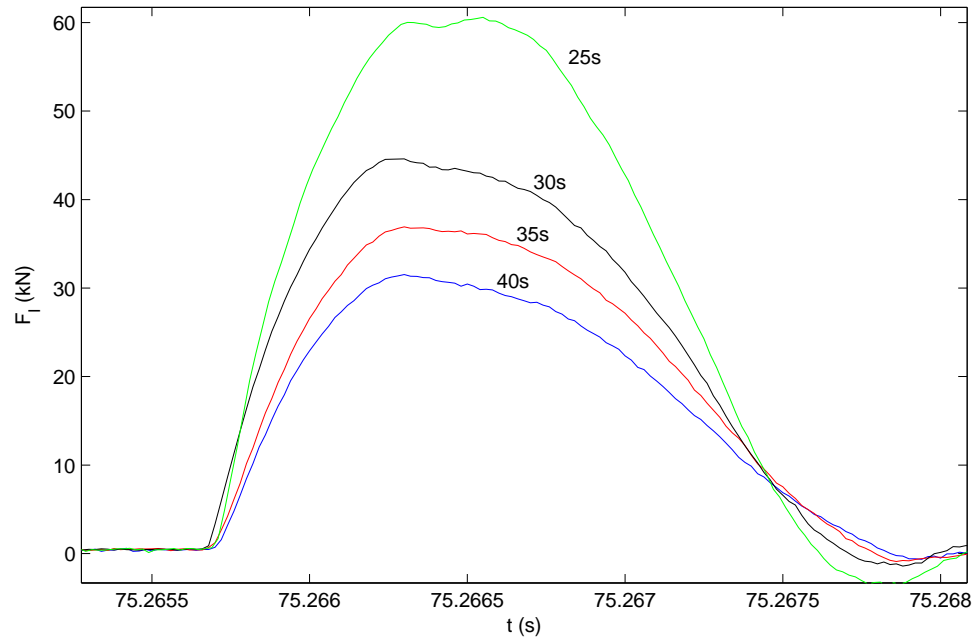


Figure 3.79: Impact force time histories of trials 3, 10, 14, 20. Each trial represents one of the T_{erf} used for In-Water longitudinal aluminum test: $h_1 = 2.57$ m, $h_2 = 0.209$ m

3.2.5.1.2.3 $h_2 = 30.1$ cm Fig. 3.80 shows the impact for time histories of trials 1, 7, 15, 22, 27. Each trial represents a different T_{erf} that was used for In-Water longitudinal aluminum test at $h_1 = 2.66$ m, $h_2 = 0.301$ m. T_{erf} of 40s, 35s, 30s, 25s, and 20s were used. Measured impact force was shown to increase as T_{erf} decreased.

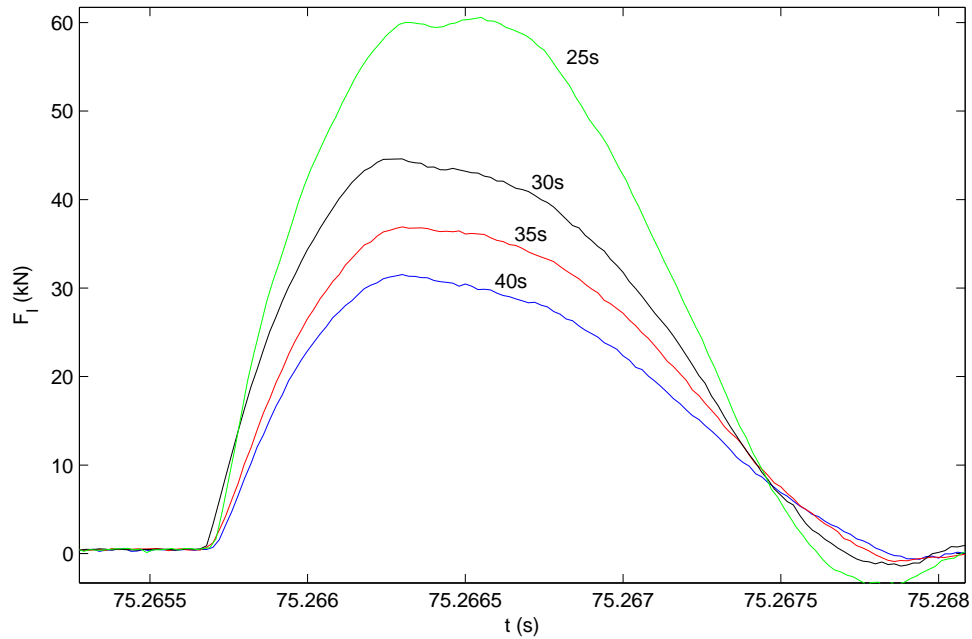


Figure 3.80: Impact force time histories of trials 1, 7, 15, 22, 27. Each trial represents one of the T_{erf} used for In-Water longitudinal aluminum test: $h_1 = 2.57$ m, $h_2 = 0.30$ m

3.2.5.1.3 Nonstructural Mass

Three different nonstructural mass amounts were used during the In-Water longitudinal aluminum test, $M_{NS} = 0$ kg, $M_{NS} = 50.2$ kg, and $M_{NS} = 99.4$ kg.

3.2.5.1.3.1 $M_{NS} = 0$ kg Fig. 3.81 shows the Impact force time histories of In-Water longitudinal aluminum test with $M_{NS} = 0$ kg and $T_{erf} = 30$ s. One representative time history for each of the water depths was shown. Impact force is shown to decrease with water depth because wave speed decreases with water depth for the same T_{erf} . t' refers to an adjusted time scale where $t' = 0$ is the start of impact.

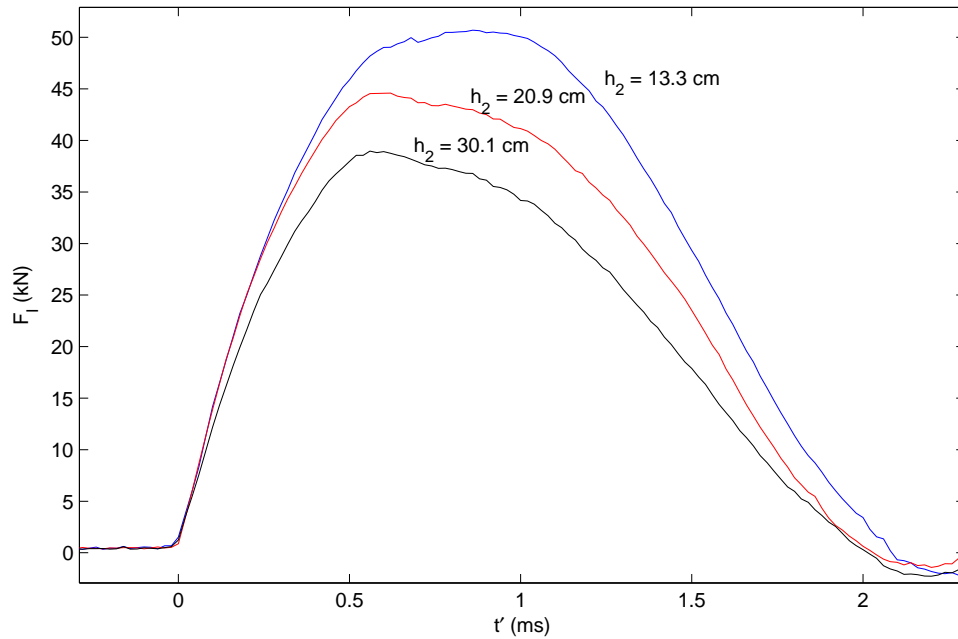


Figure 3.81: Impact force time histories In-Water longitudinal aluminum test with $M_{NS} = 0$ kg and $T_{erf} = 30$ s. One representative time history for each of the water depths shown. t' refers to an adjusted time scale where $t' = 0$ is the start of impact.

3.2.5.1.3.2 $M_{NS} = 50.2$ kg Fig. 3.82 shows the Impact force time histories of In-Water longitudinal aluminum test with $M_{NS} = 50.2$ kg and $T_{erf} = 30$ s. One representative time history for each of the water depths was shown. Impact force is shown to decrease with water depth because wave speed decreases with water depth for the same T_{erf} . Only two water depths are shown because the draft of the container was too large for the specimen to float at $h_2 = 13.3$ cm.

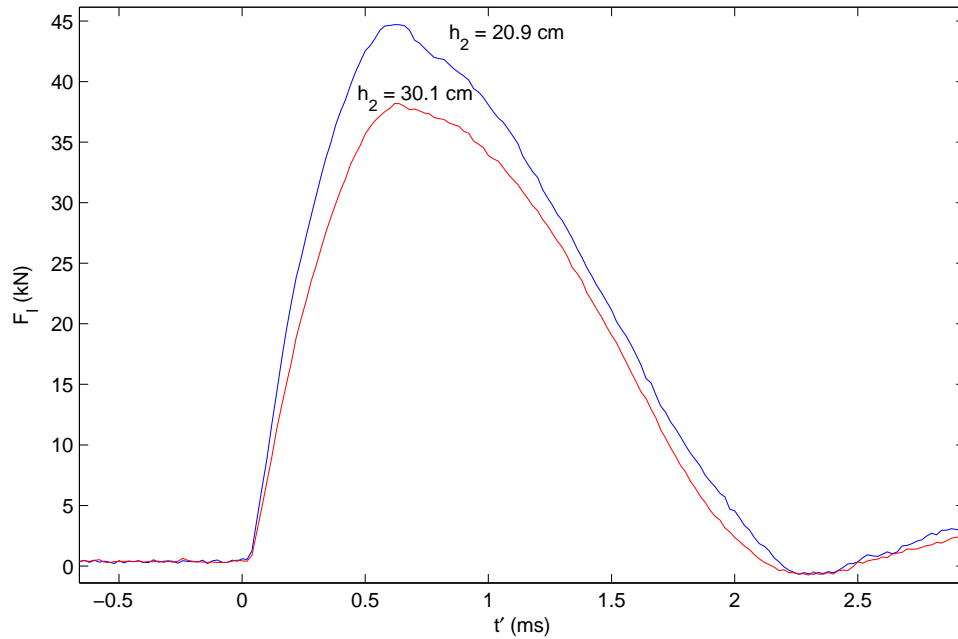


Figure 3.82: Impact force time histories In-Water longitudinal aluminum test with $M_{NS} = 50.2$ kg and $T_{erf} = 30$ s. One representative time history for each of the water depths shown.

3.2.5.1.3.3 $M_{NS} = 99.4$ kg Fig. 3.83 shows the Impact force time histories of In-Water longitudinal aluminum test with $M_{NS} = 99.4$ kg and $T_{erf} = 30$ s. One representative time history for each of the water depths was shown. Impact force is shown to decrease with water depth because wave speed decreases with water depth for the same T_{erf} . Only one water depth is shown because the draft of the container was too large for the specimen to float at $h_2 = 13.3$ cm and $h_2 = 20.9$ cm.

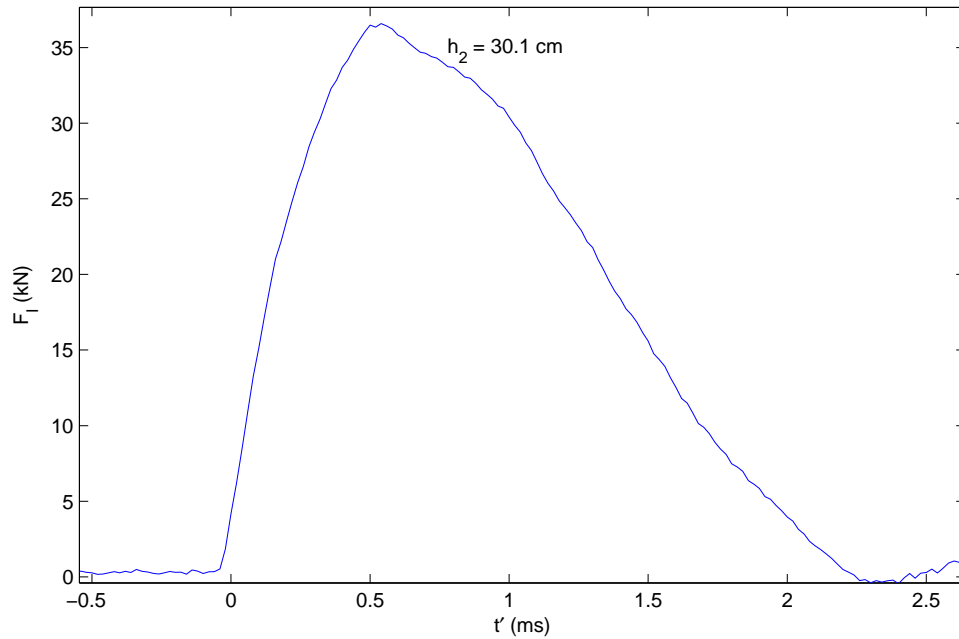


Figure 3.83: Impact force time histories In-Water longitudinal aluminum test with $M_{NS} = 99.4$ kg and $T_{erf} = 30$ s. One representative time history for each of the water depths shown.

3.2.5.2 Longitudinal Acrylic

3.2.5.2.1 Setup

Fig. 3.84 shows the setup for the In-Water longitudinal acrylic test. The In-Water longitudinal acrylic test used the same exact setup as the In-Water longitudinal aluminum test. No nonstructural mass was added to avoid damaging the acrylic specimen.



Figure 3.84: Photograph of setup for In-Water longitudinal acrylic test.

3.2.5.2.2 Water depths and wave conditions

3.2.5.2.2.1 $h_2 = 13.3$ cm Fig. 3.85 shows the impact force time histories of trials 24-29 of In-Water longitudinal acrylic test at $h_1 = 2.50$ m, $h_2 = 0.13$ m, $T_{erf} = 30$ s. Overall, the In-Water acrylic test was observed to exhibit more variability among the repeated trials. Most of the time histories shown had similar shapes. One trial had a noticeably longer impact duration than the others shown. The typical impact duration appeared to be around 5 ms.

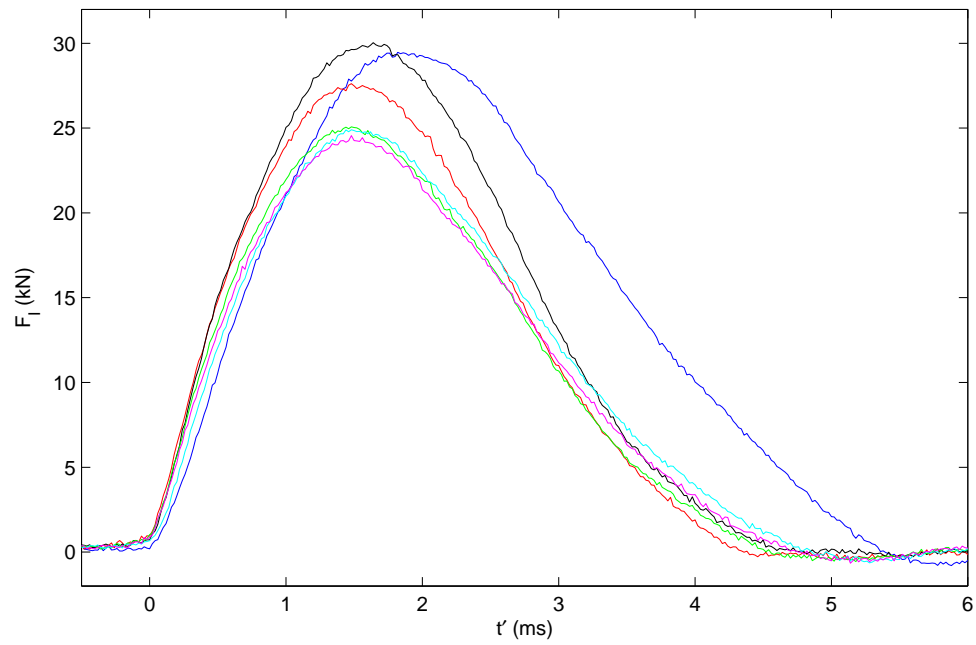


Figure 3.85: Impact force time histories of trials 24-29 of In-Water longitudinal acrylic test at $h_1 = 2.50$ m, $h_2 = 0.13$ m, $T_{erf} = 30$ s. Each trial had identical conditions.

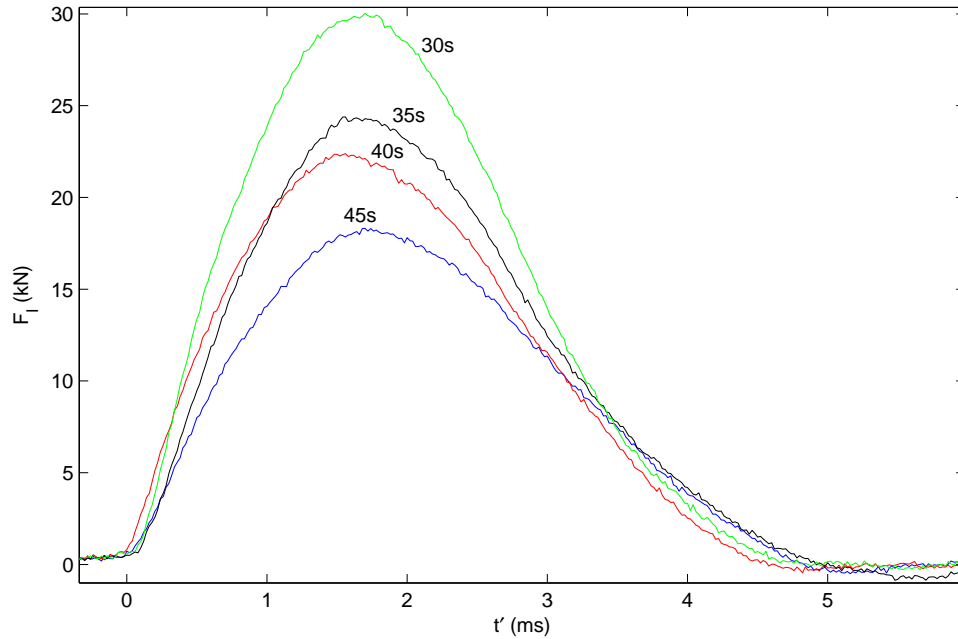


Figure 3.86: Impact force time histories of trials 5, 11, 20, 26 of In-Water longitudinal acrylic test at $h_1 = 2.50$ m, $h_2 = 0.13$ m. Each trial represents the maximum force measured for each T_{erf} used.

Fig. 3.86 shows the impact for time histories of trials 5, 11, 20, and 26. Each trial represents a different T_{erf} that was used for In-Water longitudinal acrylic test at $h_1 = 2.50$ m, $h_2 = 0.13$ m. T_{erf} of 45s, 40s, 35s, and 35s were used. Measured impact force was shown to increase as T_{erf} decreased.

3.2.5.2.2.2 $h_2 = 20.9$ cm Fig. 3.87 shows the impact for time histories of trials 3, 9, 15, and 18. Each trial represents a different T_{erf} that was used for In-Water longitudinal acrylic test at $h_1 = 2.57$ m, $h_2 = 0.21$ m. T_{erf} of 45s, 40s, 35s, and 35s were used. In this case, the $T_{erf} = 25$ s force time history was observed to have a lower peak force than the $T_{erf} = 30$ s.

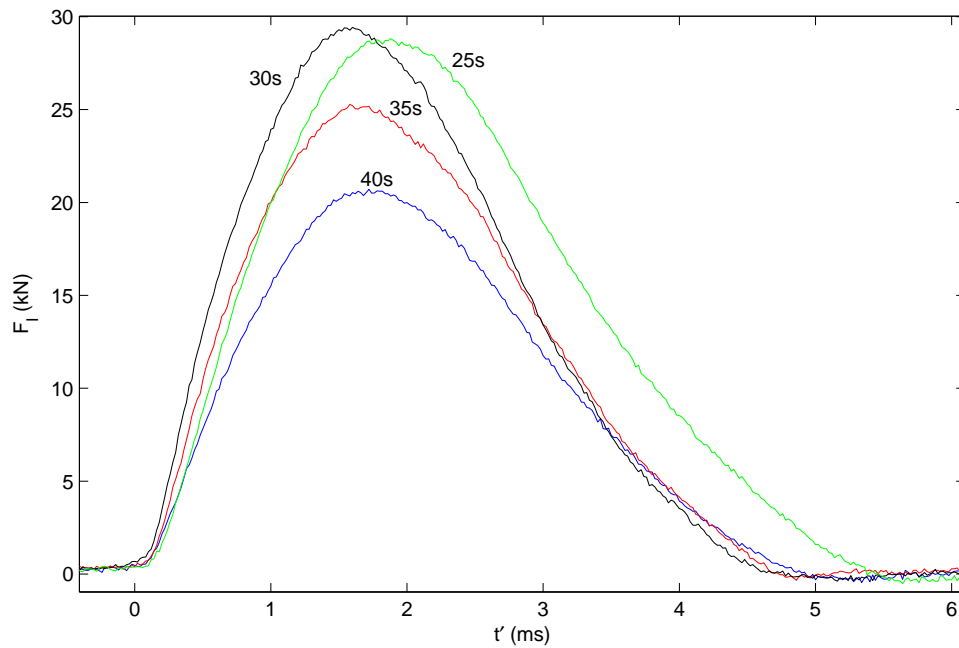


Figure 3.87: Impact force time histories of trials 3, 9, 15, 18 of In-Water longitudinal acrylic test at $h_1 = 2.57$ m, $h_2 = 0.21$ m. Each trial represents the maximum force measured for each T_{erf} used.

3.2.5.2.2.3 $h_2 = 30.1$ cm Fig. 3.88 shows the impact for time histories of trials 1, 2, 4, 6 and 7. Only one wave condition, $T_{erf} = 20$ s was used. In this case, the consistency of this was quite good. All the force time histories appeared to have a similar shape. Impact duration was observed to be around 6 ms.

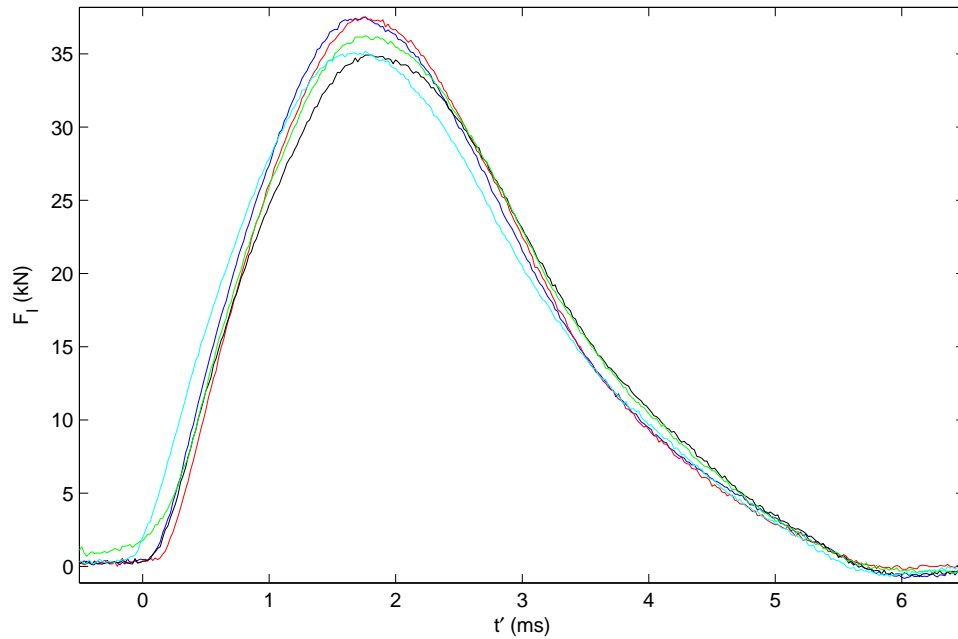


Figure 3.88: Impact force time histories of trials 1, 2, 4, 6 and 7 of In-Water longitudinal acrylic test at $h_1 = 2.66$ m, $h_2 = 0.301$ m, $T_{erf} = 20$ s. Each trial had identical conditions.

3.2.5.3 Transverse Aluminum

3.2.5.3.1 Setup

The setup for the In-Water transverse aluminum test used the wave flume and bathymetry setup shown in Fig. 3.1 and the guide wire setup shown in Fig. 3.19. The debris specimen was placed 3 - 4 m away from the column in $-x$ direction. The debris specimen was transported toward the column using long waves generated by error function wave paddle displacement. Tethers were attached to the ends of the major axis of the debris specimen. These tethers were held on both sides of the wave flume by members of the wave lab staff. The tethers were only used to guide the specimen to ensure that a 90° impact was made between the specimen and the column. Velocities were measured by using the color based object tracking method mentioned in section 3.5.3 (Fig. 3.30). Only one water depth, $h_2 = 0.30$ m was tested. Two different amounts of nonstructural mass, $M_{NS} = 0$ kg and

$M_{NS} = 50.2$ kg, were used.

3.2.5.3.2 Water depths and wave conditions

Wave conditions 9-12 from Table 3.3 were used.

3.2.5.3.3 Nonstructural Mass

3.2.5.3.3.1 $M_{NS} = 0$ kg Fig. 3.89 shows impact force time histories of trials 16, 18, 19, 20, 21, and 22 of In-Water transverse aluminum test at $h_1 = 2.66$ m, $h_2 = 0.301$ m, $T_{erf} = 30$ s with $M_{NS} = 0$. From the time histories, the transverse aluminum test appeared to be much less consistent than the longitudinal tests. The impact durations, in particular, were much more variable. This variability was likely due to the fact that there was no extended bottom along the minor axis of the debris. The lack of a consistent contact area likely contributed to the variability observed in the impact forces.

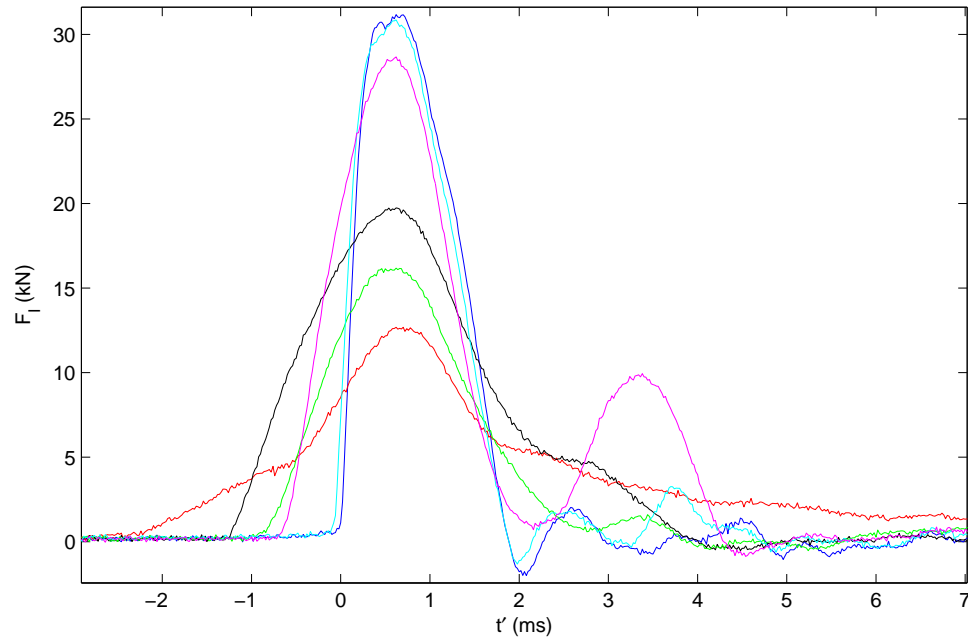


Figure 3.89: Impact force time histories of trials 16, 18, 19, 20, 21, and 22 of In-Water transverse aluminum test at $h_1 = 2.66$ m, $h_2 = 0.301$ m, $T_{erf} = 30$ s with $M_{NS} = 0$. Each trial had identical conditions.

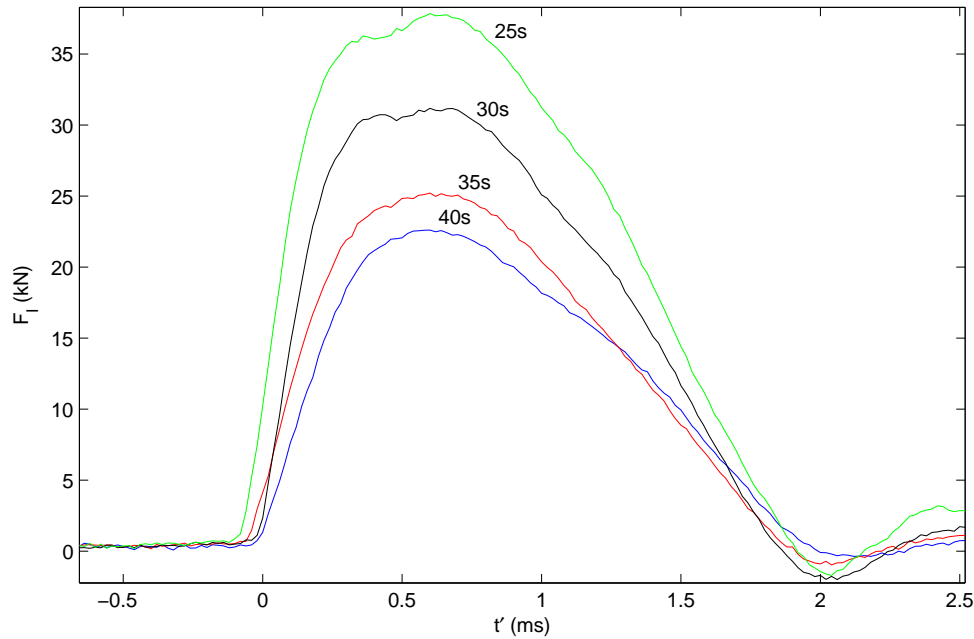


Figure 3.90: Impact force time histories of trials 2, 11, 16 and 28 of In-Water transverse aluminum test at $h_1 = 2.66$ m, $h_2 = 0.301$ m with $M_{NS} = 0$ kg. Each trial represented the maximum impact force measured for each T_{erf} .

Fig. 3.90 shows the impact force time histories of trials 2, 11, 16 and 28 of In-Water transverse aluminum test at $h_1 = 2.66$ m, $h_2 = 0.301$ m with $M_{NS} = 0$ kg. Each of the time histories represents the maximum impact force measured for each T_{erf} . The maximum impact force cases appeared to have similar shapes for each T_{erf} . The impact duration for these time histories appeared to be around 2 ms.

3.2.5.3.3.2 $M_{NS} = 50.2$ kg Fig. 3.91 shows the impact force time histories of trials 2, 8, and 18 of In-Water transverse aluminum test at $h_1 = 2.66$ m, $h_2 = 0.301$ m with $M_{NS} = 50.2$ kg. Each of the time histories represents the maximum impact force measured for each T_{erf} . The maximum impact force cases appeared to have similar shapes for each T_{erf} . Secondary and tertiary impacts were visible and occur at the same time for each of the time histories. The duration of the primary impact appeared to be around 2 ms for each case.

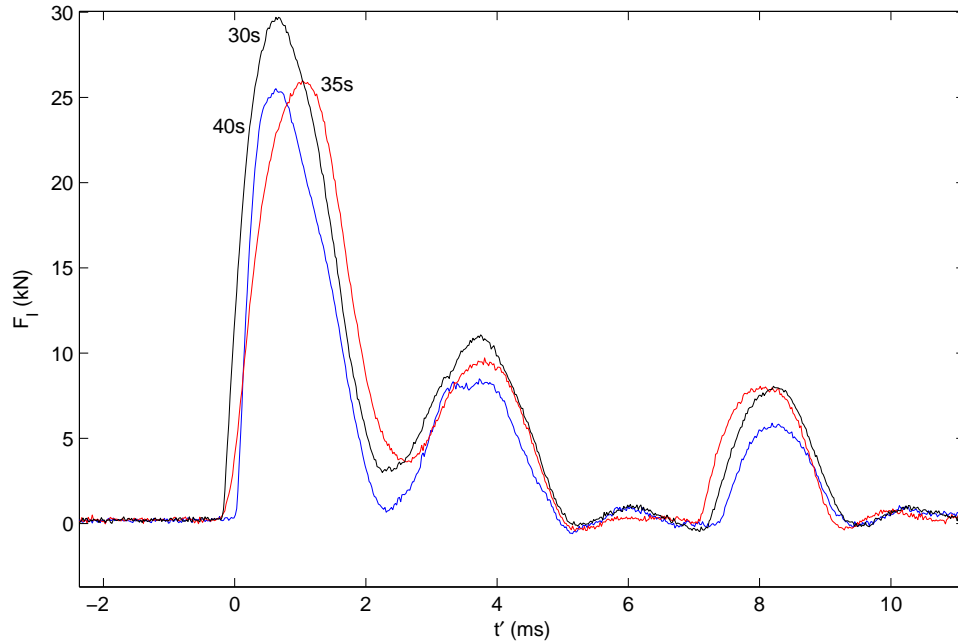


Figure 3.91: Impact force time histories of trials 2, 11, 16 and 28 of In-Water transverse aluminum test at $h_1 = 2.66$ m, $h_2 = 0.301$ m with $M_{NS} = 50.2$ kg. Each trial represented the maximum impact force measured for each T_{erf} .

3.2.5.4 Unconstrained Aluminum

The purpose of the unconstrained In-Water aluminum test was to determine the debris specimens propensity to rotate during propagation.

3.2.5.4.1 Setup

Fig. 3.92 shows the video sequence for unconstrained In-Water aluminum test trial 27. The setup for the unconstrained In-Water aluminum test used the the wave flume and bathymetry setup shown in Fig. 3.1. No guide wires were used. The specimen was placed into position 3-4 m upstream from the column by tethers that were attached to the ends of the major axis. The tethers were only used to position the specimen before each trial began. Various starting orientations ranging from 0° to 0° were used. The water depth

was set at $h_1 = 2.57$ m, $h_2 = 0.21$ m. $T_{erf} = 30$ s was repeated for each trial.

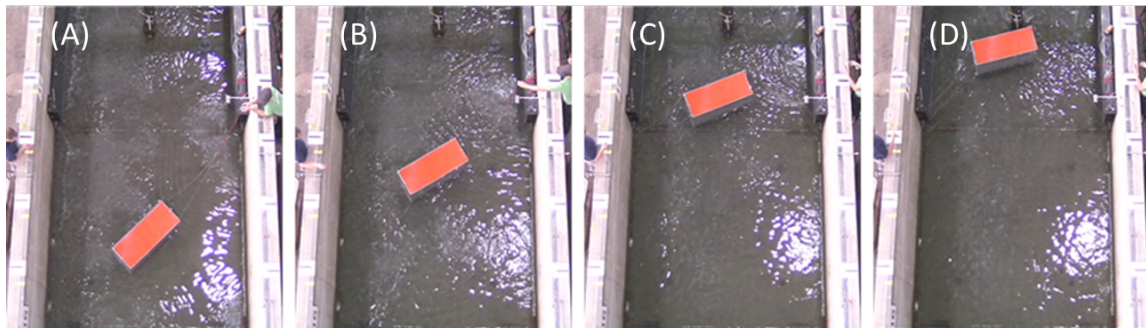


Figure 3.92: Video sequence of unconstrained In-Water aluminum test trial 27.

3.2.5.4.2 Examples of Data

Fig. 3.93 shows the velocity and orientation output for trial 27 of the unconstrained In-Water aluminum test. The velocity was shown to be much like what was witnessed from the other In-Water tests in that the debris attains a constant velocity before impact. The orientation plot shows that the specimen started at 45° and gradually rotated to 76° . This case exhibited the most rotation out of all the experiments conducted

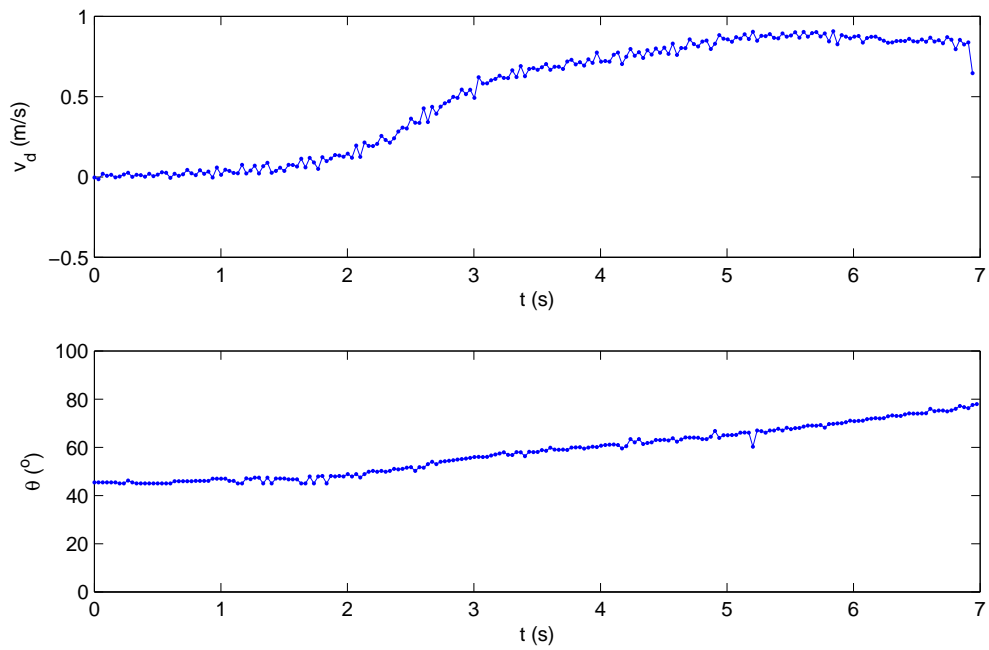


Figure 3.93: Velocity and orientation output from unconstrained In-Water aluminum test trial 27.

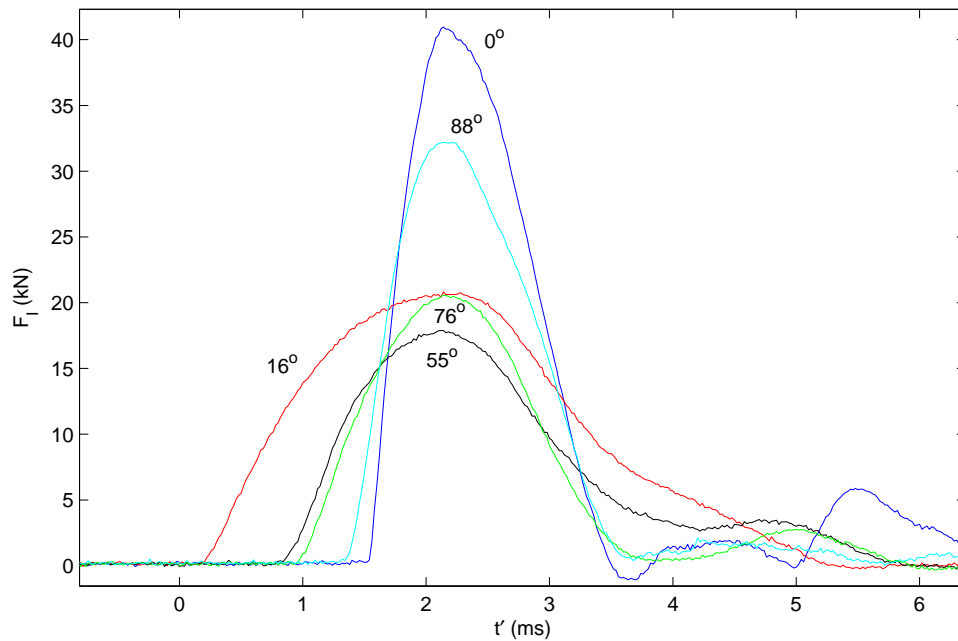


Figure 3.94: Impact force time histories from various measured impact angles, θ_f . Time histories aligned at peak forces for clarity.

Fig. 3.94 shows the impact force time histories from various measured impact angles. One of the issues with these force measurements was the uncertainty of the quality of contact. Considering the variability already witnessed in the constrained cases, it is difficult to determine what variables are contributing to the impact force readings shown.

3.2.5.5 Destructive

The purpose of the destructive test was to observe the impact force time histories for cases in which structural damage was incurred on the debris specimen. The idea of the test was to adjust the impact in a way that would cause damage to the specimen. Unfortunately, we were unable to damage the specimen using the wave conditions that simulated idealized inundation flow.

3.2.5.5.1 Setup

The setup for the Destructive Test was very similar to that of the In-Water transverse aluminum test. The main difference was the load cell positioning. Instead of attempting to make the impact between the bottom plate of the specimen and the load cell, the load cell was raised such that contact was made between the middle of the specimen face. Fig. 3.95 shows a video still taken right before impact of the destructive test. The water depth was $h_1 = 2.57$ m, $h_2 = 0.21$ m.

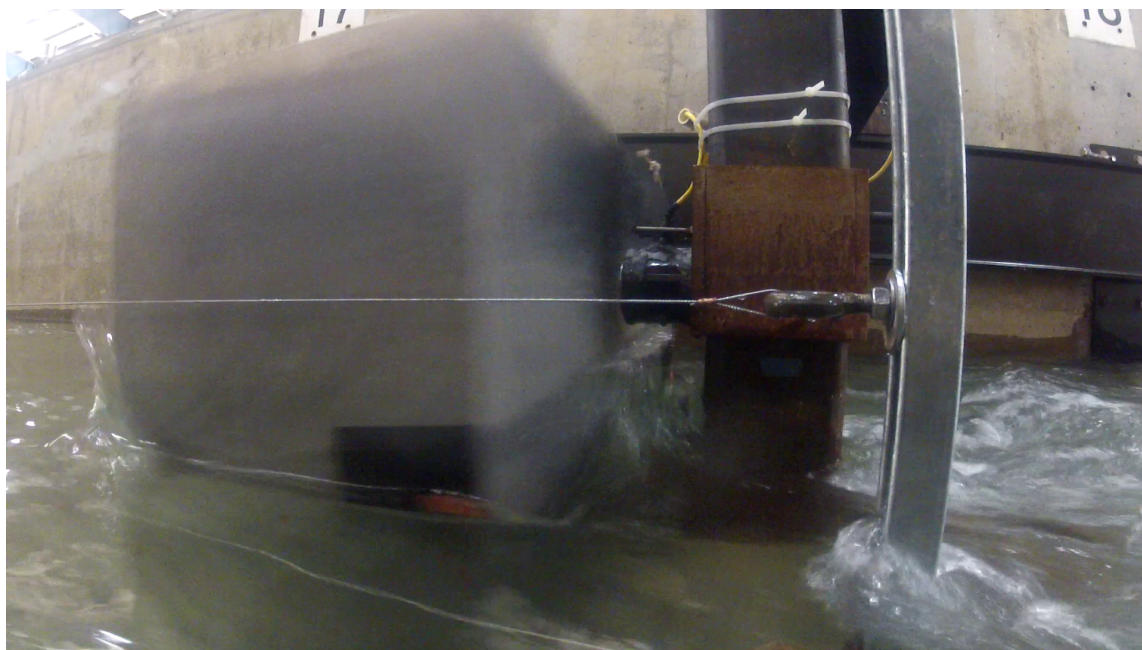


Figure 3.95: Photograph of destructive test right before impact.

3.2.5.5.2 Examples of Data

Fig. 3.96 shows the impact time histories of 6 repetitions of the Destructive Test at $T_{erf} = 40$ s. The peak impact forces for these test were observed to be in the range of 2 - 4 kN, which was much lower than the other In-Water tests. The 4 kN peak force corresponded to 0.3% of the capacity of the CLC-300K load cell. Additionally, the impact durations were in the range of 40 ms which was much longer than previously observed. The noise in the load cell signal appears amplified since the magnitude of the y -scale was small.

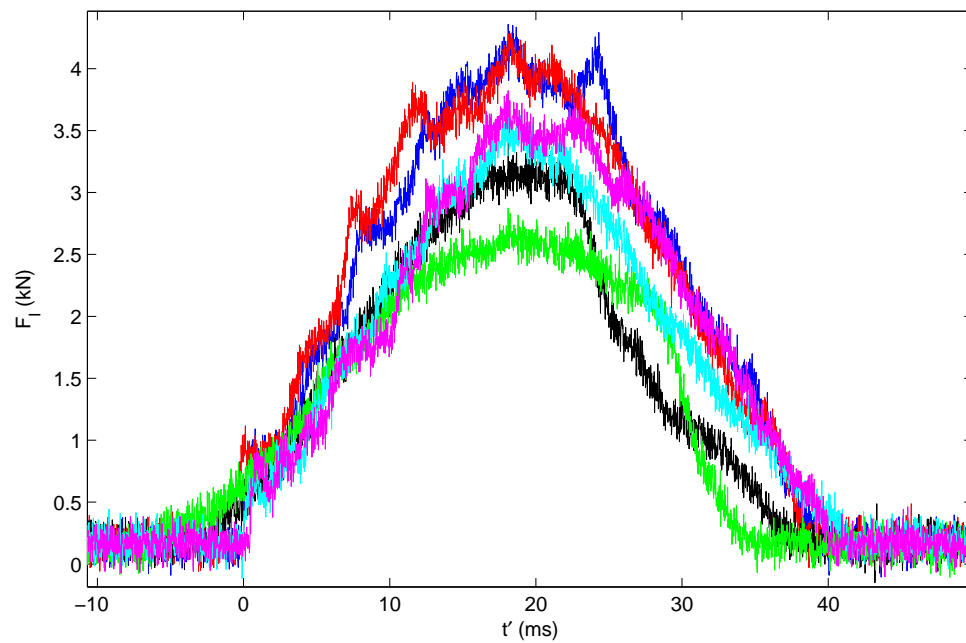


Figure 3.96: Impact force time histories for Destructive Test trials 1-6. Each test was run at $T_{erf} = 40$ s.

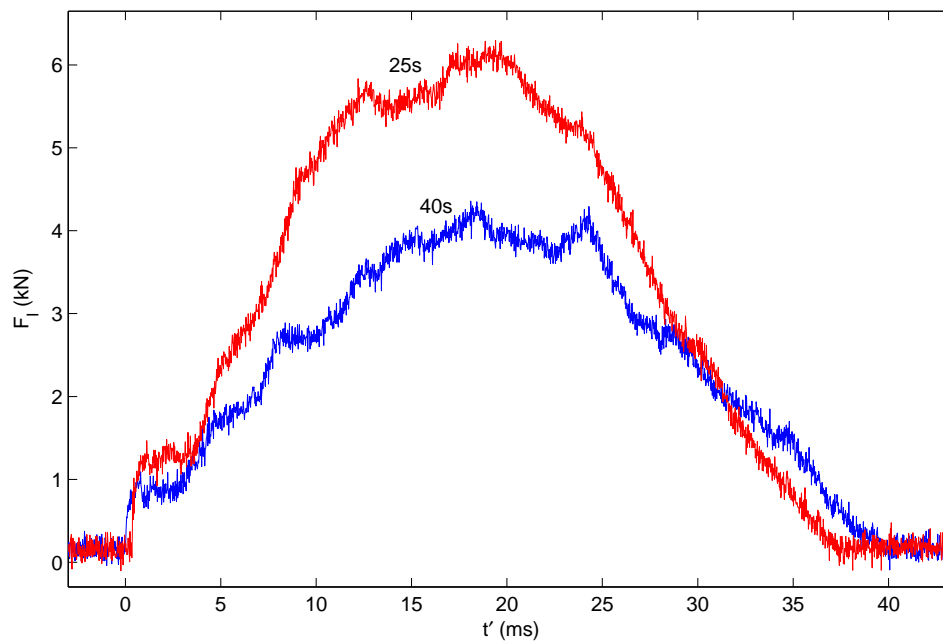


Figure 3.97: Impact force time histories for Destructive Test trials 2 and 7. Trial 2 represents the highest impact force measured for $T_{erf} = 40$ s, trial 7 represents the highest impact force measured for $T_{erf} = 25$ s.

Fig. 3.97 shows the Impact force time histories for Destructive Test trials 2 and 7. Trial 2 represents the highest impact force measured for $T_{erf} = 40$ s, trial 7 represents the highest impact force measured for $T_{erf} = 25$ s. $T_{erf} = 25$ s represented the limiting case for idealized inundation flow at the water depth being used. The specimen did not incur damage, thus the time histories between the two time series look very similar. Impact duration was observed to be around 40 ms for both trials.

Chapter 4: Results

4.1 Hydrodynamics Test

4.1.1 Comparison of ADV to PIV measurements

Table 4.1 shows the comparison of the ADV and PIV measurements for wave front speeds from the Hydrodynamics test. The measurements from the PIV compared quite well to those of the ADV. This supported the PIVlab method used to obtain these velocity measurements, and also the image rectification scheme utilized to correct for perspective error.

The error in most cases was quite low, with the maximum error measured 7.56%. The cases with higher error were the cases with the longest T_{erf} . The higher errors were associated with the smaller waves which corresponded to less foam that could be tracked. The results from the PIV vs. ADV comparison provided the impetus to use seeding material to obtain the surface flow velocities.

Table 4.1: Comparison of ADV to PIV measurements from wave front tracking.

h_1 (cm)	h_2 (cm)	T_{erf} (s)	u_{PIV} (m/s)	u_{ADV} (m/s)	$Error$ (%)
234.6	0	20	1.79	1.80	0.48
234.6	0	25	1.58	1.60	1.28
234.6	0	25	1.68	1.70	1.60
234.6	0	30	1.56	1.64	4.91
234.6	0	30	1.56	1.69	7.56

4.1.2 Flow Speed vs. Error Function Period

Fig. 4.1 shows the plot of maximum flow speed measured by surface PIV compared against T_{erf} for different water depths. Maximum flow speed was shown to increase as T_{erf} decreases. Flow speed was shown to decrease as water depth increases for a particular T_{erf} .

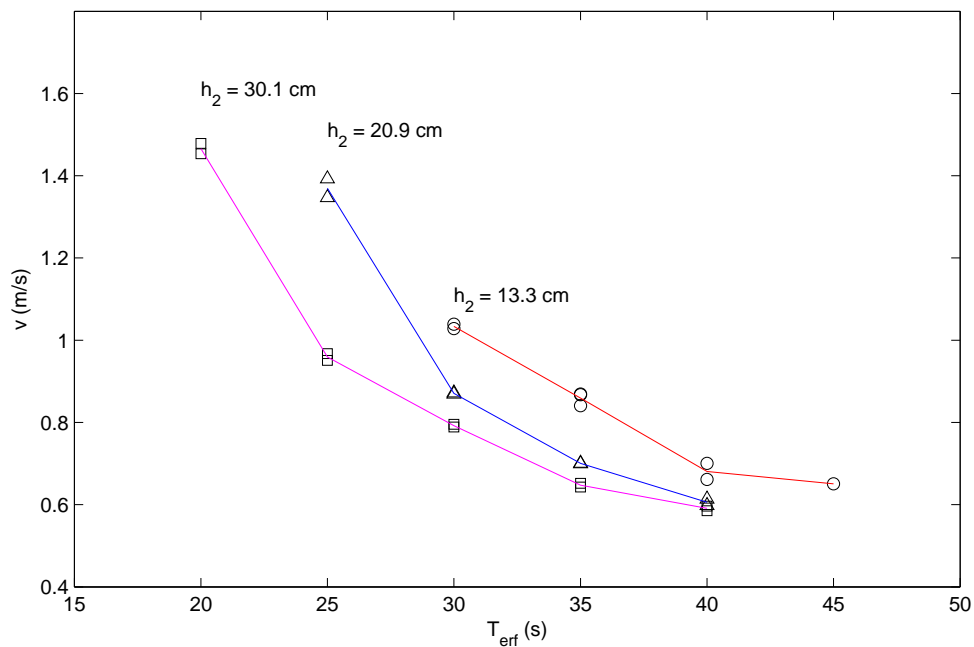


Figure 4.1: Maximum flow speed measured by surface PIV compared against T_{ert} for different water depths. $h_2 = 13.3$ cm (\circ), $h_2 = 20.9$ cm (\triangle), $h_2 = 30.1$ cm (\square).

4.2 In-Air Test

4.2.1 Longitudinal Aluminum

Fig. 4.2 shows the F_p vs. v_I relationship for the In-Air longitudinal aluminum test. The measurements indicated that there was a linear relationship between the two variables. A line was fitted through the data with a slope of 48.50 kN s/m. This slope corresponded to a stiffness of $K = 4.36 \times 10^7$ N/m.

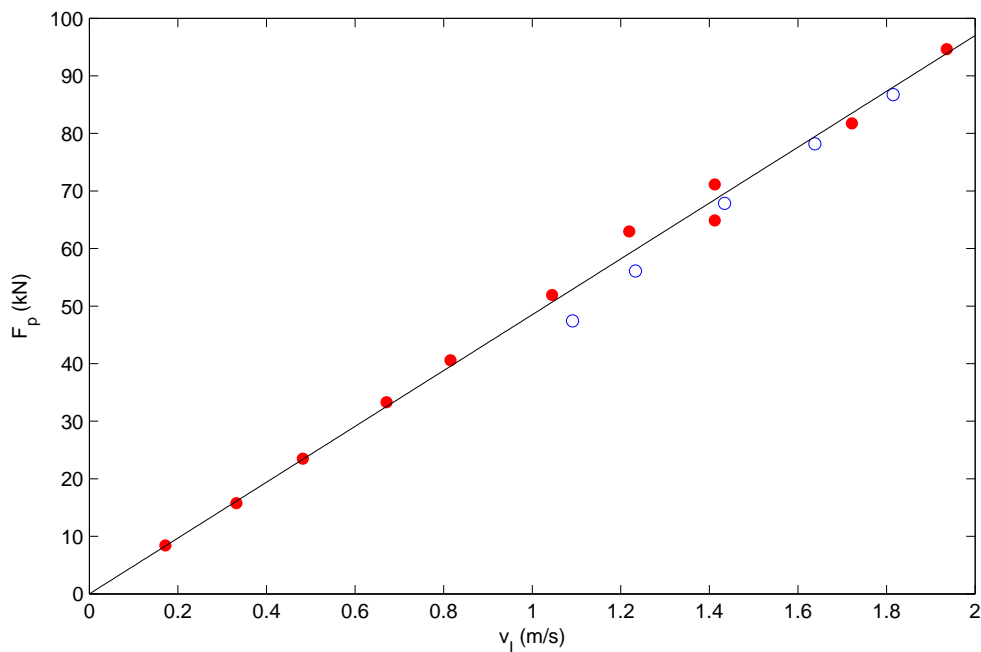


Figure 4.2: F_p plotted against v_I for the In-Air longitudinal aluminum test. Trials conducted before the In-Water test (\circ), trials conducted after the In-Water test (\bullet). The black line fitted to the data had a slope of 48.5 kN s/m.

4.2.2 Longitudinal Acrylic

Fig. 4.3 shows the F_p vs. v_I relationship for the In-Air longitudinal acrylic test. The data indicated that there was a strong linear relationship between the two variables from 0 - 1 m/s. At speeds greater than 1 m/s, the F_p measurements diverge. The trend observed in the 0 - 1 m/s range appears to fit through the middle of the divergent data. A line was fitted through the data with a slope of 26.12 kN s/m. This slope corresponded to a stiffness of $K = 1.35 \times 10^7$ N/m.

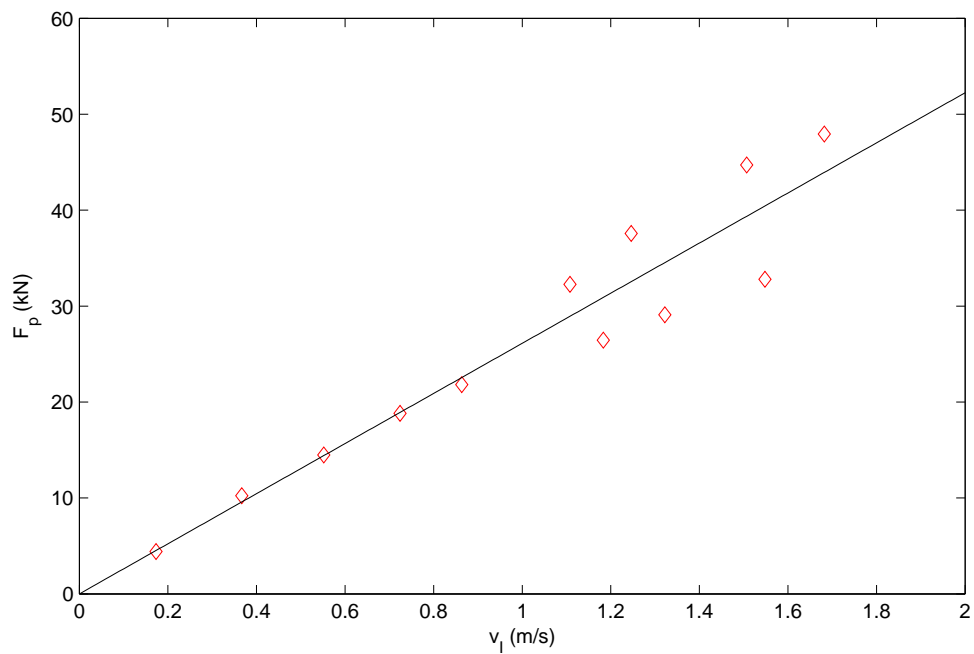


Figure 4.3: F_p plotted against v_I for the In-Air longitudinal acrylic test. The black line fitted to the data had a slope of 26.12 kN s/m.

4.2.3 Transverse Aluminum

Fig. 4.4 shows the F_p vs. v_I relationship for the In-Air transverse aluminum test. The data indicated that there was a linear relationship between the two variables. A line was fitted through the data with a slope of 35.22 kN s/m. This slope corresponded to a stiffness of $K = 2.30 \times 10^7$ N/m.

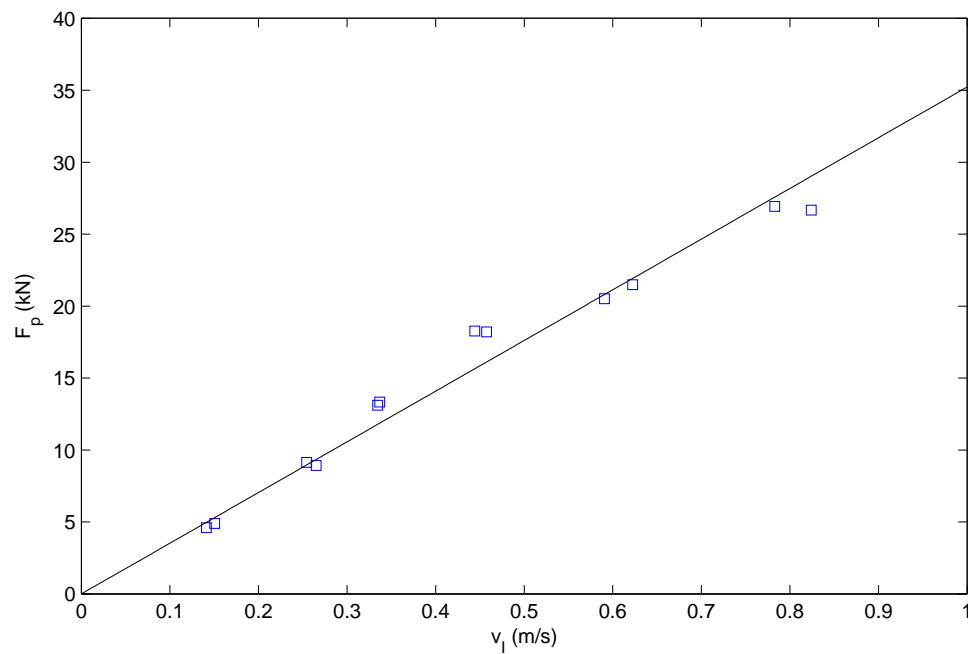


Figure 4.4: F_p plotted against v_I for the In-Air transverse aluminum test. The black line fitted to the data had a slope of 35.22 kN s/m.

4.2.4 Comparisons

Fig. 4.5 compared the peak force measurements from the different In-Air tests to one another. The longitudinal aluminum test had the largest slope out of the three, while longitudinal acrylic had the smallest slope.

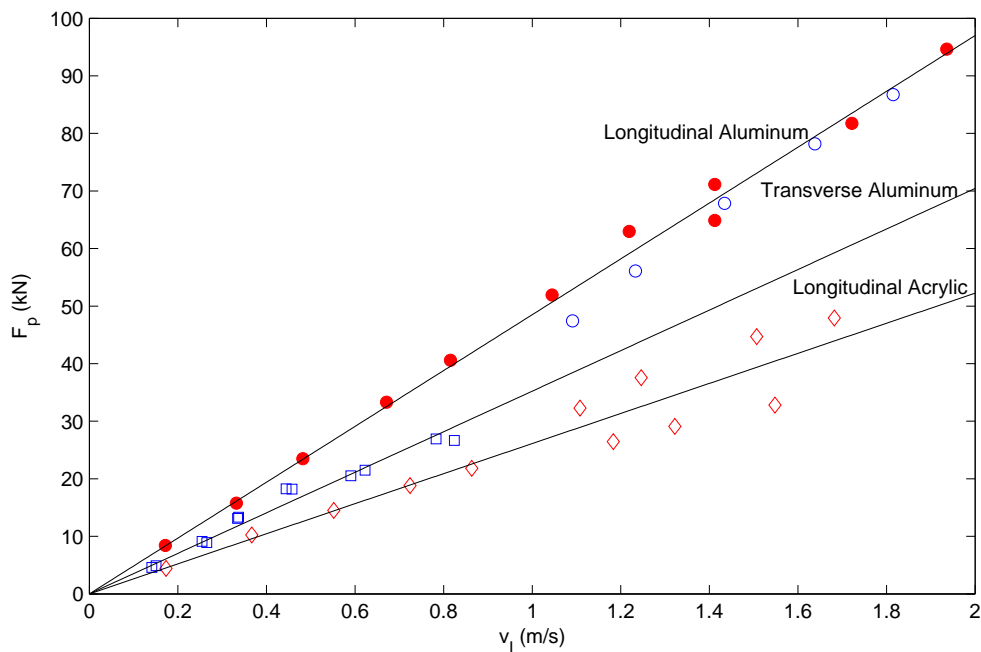


Figure 4.5: F_p plotted against v_I for the all of the In-Air tests. The fitted black lines from Fig. 4.2 - 4.4 are shown. Longitudinal aluminum (\bullet), longitudinal acrylic (\diamond), transverse aluminum (\square).

4.2.5 Impulse

Impulse values were determined by integrating the impact force time series. Two different variables were used to represent calculated impulses. J_p represents the impulse value determined from integrating over the primary impact peak of the impact force time series. J_{30} represents the impulse value determined from integrating for a 30 ms period after the beginning of the primary impact peak of the time series. The primary purpose of the J_{30} variable was to account for any additional momentum that may have resulted from contents (nonstructural mass) shifting during impact. Fig. 4.6 graphically defines these variables on an impact force time series from In-Water Longitudinal Aluminum Test with 99.4 kg of nonstructural mass.

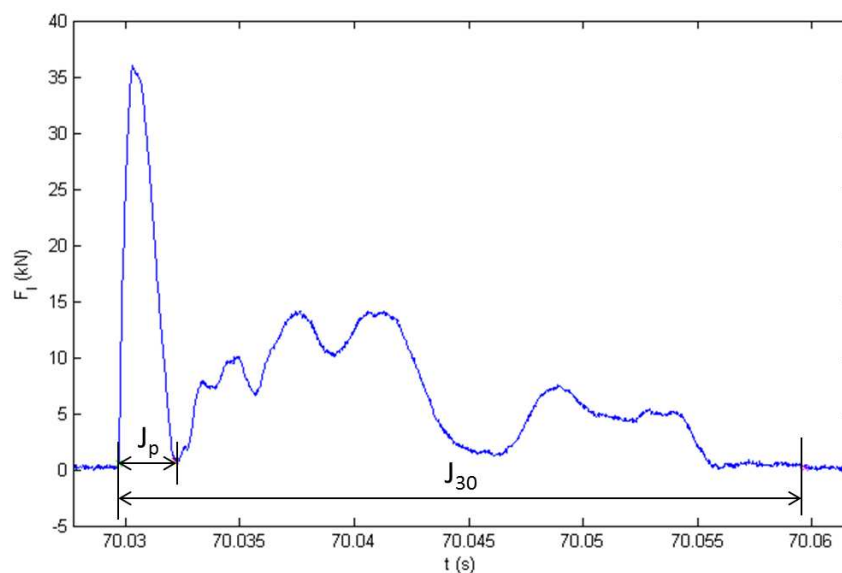


Figure 4.6: Definition of integration regions for impulse variables J_p and J_{30} on an impact force time series from In-Water Longitudinal Aluminum Test with 99.4 kg of nonstructural mass.

4.2.5.1 Comparison of Different Tests

Fig. 4.7 shows the comparison of J_p vs. v_I calculated from the In-Air longitudinal aluminum, longitudinal acrylic, and transverse aluminum tests. Fig. 4.8 shows the comparison of J_{30} calculated from the In-Air longitudinal aluminum, longitudinal acrylic, and transverse aluminum tests. The comparisons showed that the calculated impulses were very close to one another. The differences observed in peak force observed from the different In-Air tests were equalized by the overall impulse.

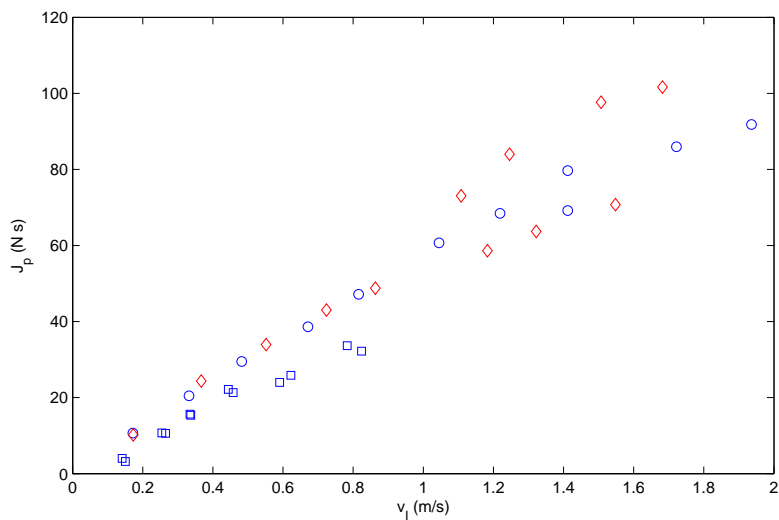


Figure 4.7: Comparison of J_p vs. v_I calculated from the In-Air longitudinal aluminum (○), longitudinal acrylic (◇), and transverse aluminum tests (□).

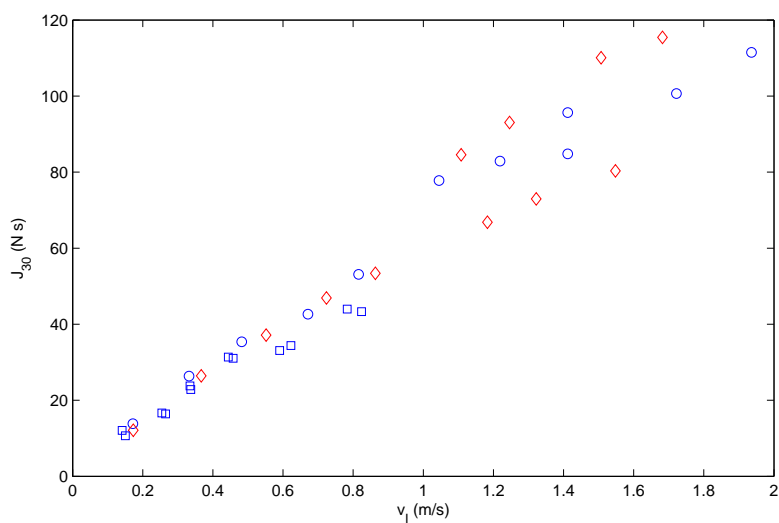


Figure 4.8: Comparison of J_{30} vs. v_I calculated from the In-Air longitudinal aluminum (○), longitudinal acrylic (◇), and transverse aluminum tests (□).

4.2.5.2 Effect of Nonstructural Mass

Fig. 4.9 shows the comparison of J_p vs. v_I for In-Air longitudinal aluminum test with different values of M_{NS} . The comparison from Fig. 4.9 corresponded with the F_p vs. v_I comparison shown in Fig. 3.51. The impulse values show a relationship very similar to what was observed in Fig. 3.51. Overall the impulse values integrated over the primary impact peak did not differ significantly based on the amount of nonstructural mass.

Fig. 4.10 shows the comparison of J_{30} vs. v_I for In-Air longitudinal aluminum test with different values of M_{NS} . The comparison from Fig. 4.9 also corresponded with the F_p vs. v_I comparison shown in Fig. 3.51. In this case, the impulse values calculated from integrating over 30 ms were much higher for the cases with $M_{NS} = 50.2$ kg than the cases with $M_{NS} = 0$ kg.

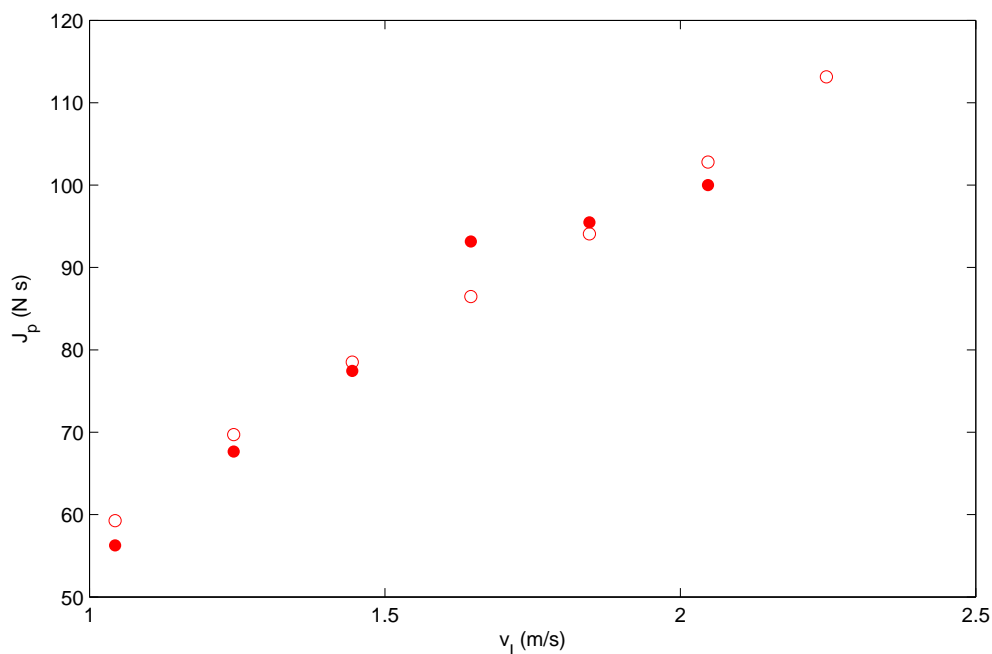


Figure 4.9: Comparison of J_p vs. v_I calculated from the In-Air longitudinal aluminum test with $M_{NS} = 0$ kg (\circ) and $M_{NS} = 50.2$ kg (\bullet).

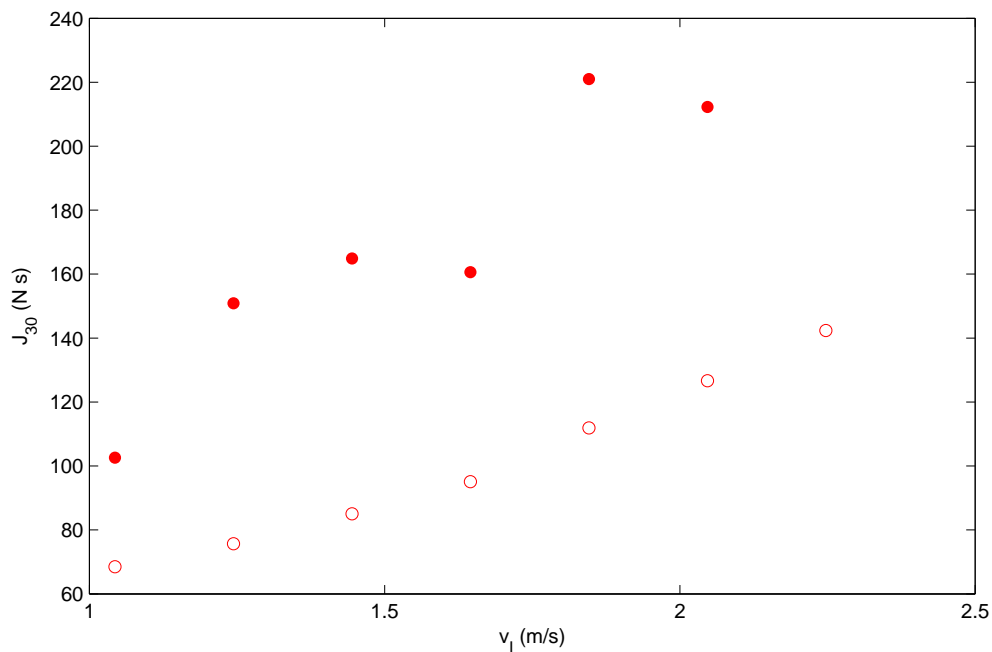


Figure 4.10: Comparison of J_{30} vs. v_I calculated from the In-Air longitudinal aluminum test with $M_{NS} = 0$ kg (○) and $M_{NS} = 50.2$ kg (●).

4.3 In-Water Test

4.3.1 Longitudinal Aluminum

4.3.1.1 Flow Speed vs. Impact Velocity

Fig. 4.11 shows the maximum flow speeds compared with debris impact velocities for In-Water longitudinal aluminum tests. Overall, the debris velocities appeared to almost reach the speed of the maximum measured flow velocities. Two cases with the highest velocities shows the greatest discrepancy between the flow speeds and the debris velocities. Additionally, debris velocity appeared to decrease with addition of nonstructural mass.

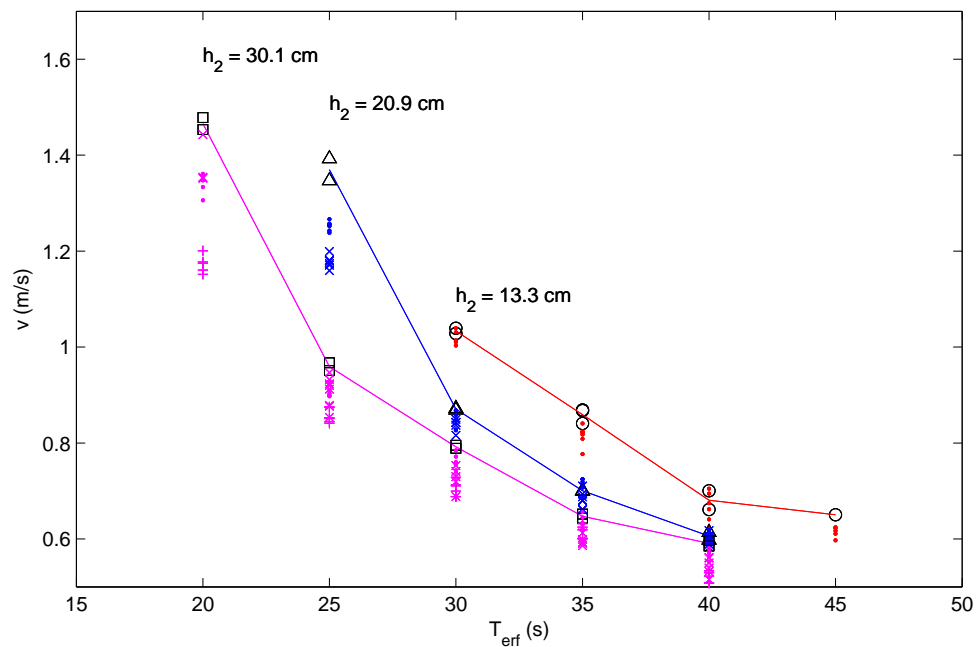


Figure 4.11: Maximum flow speeds compared with debris impact velocities for In-Water longitudinal aluminum tests. For flow speeds, $h_2 = 13.3$ cm (\circ), $h_2 = 20.9$ cm (\triangle), $h_2 = 30.1$ cm (\square). For debris impact velocities, $M_{NS} = 0$ kg (\cdot), $M_{NS} = 50.2$ kg (\times), $M_{NS} = 99.4$ kg ($+$). Red represents $h_2 = 13.3$ cm, blue represents $h_2 = 20.9$ cm, and magenta represents $h_2 = 30.1$ cm.

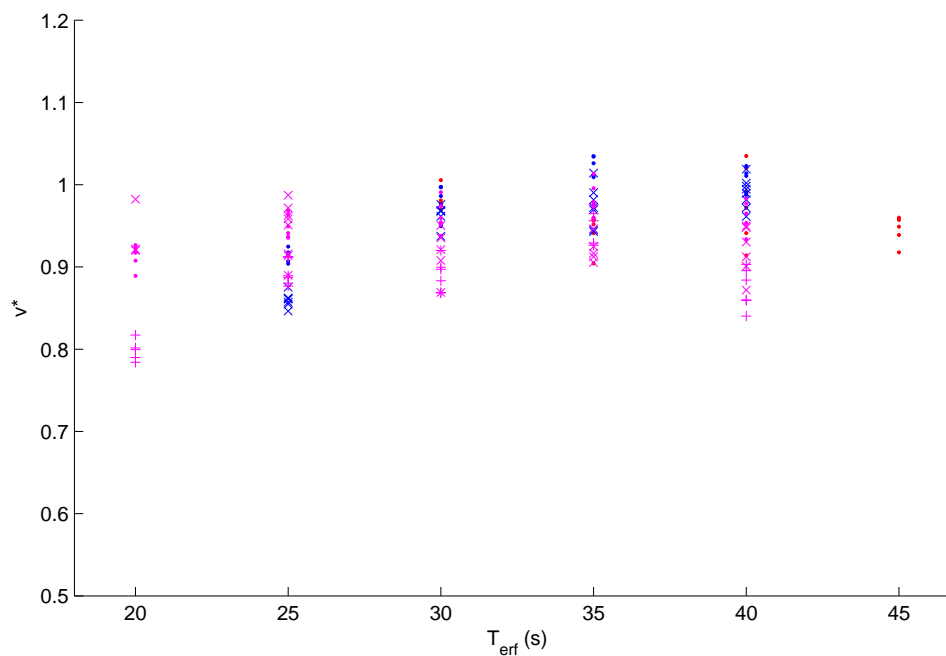


Figure 4.12: Normalized aluminum debris impact velocities, v^* with respect to the average measured surface flow speeds from PIV. The impact velocities from Fig. 4.11 were divided by the flow velocity lines shown. $M_{NS} = 0$ kg (\cdot), $M_{NS} = 50.2$ kg (x), $M_{NS} = 99.4$ kg (+). Red represents $h_2 = 13.3$ cm, blue represents $h_2 = 20.9$ cm, and magenta represents $h_2 = 30.1$ cm.

Fig. 4.12 shows the normalized debris impact velocities, v^* with respect to the average measured surface flow speeds from PIV. These values ranged from 0.78 to 1.04. These normalized values suggested that the debris was moving in the range of 80% to 100% of the water velocity. The slowest debris impact velocities were the cases with the highest M_{NS} .

4.3.1.2 Impact Force Time History comparison

4.3.1.2.1 Comparison to In-Air Impact Force

Fig. 4.13 shows the average impact force time history from 5 trials of In-Water longitudinal aluminum test with $v_I = 0.66$ m/s. The 90% confidence interval for the peak force was calculated by using the student's t-distribution with a sample size of 5.

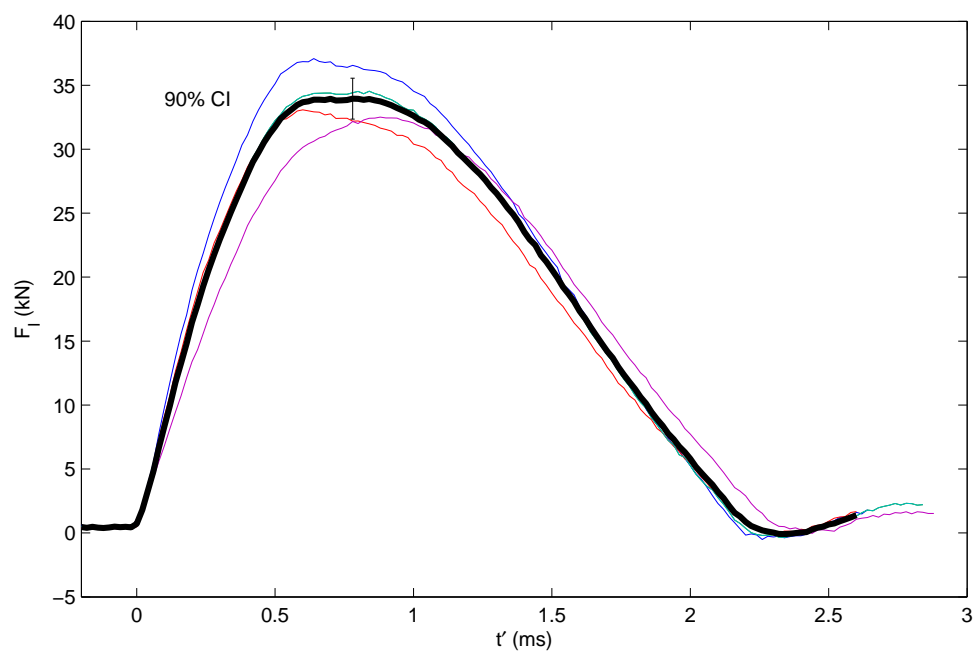


Figure 4.13: Average impact force time history for In-Water longitudinal aluminum test with $v_I = 0.66$ m/s. Determined from 5 time histories, 90% confidence interval for peak force shown. Thick black line represents averaged impact force time history.

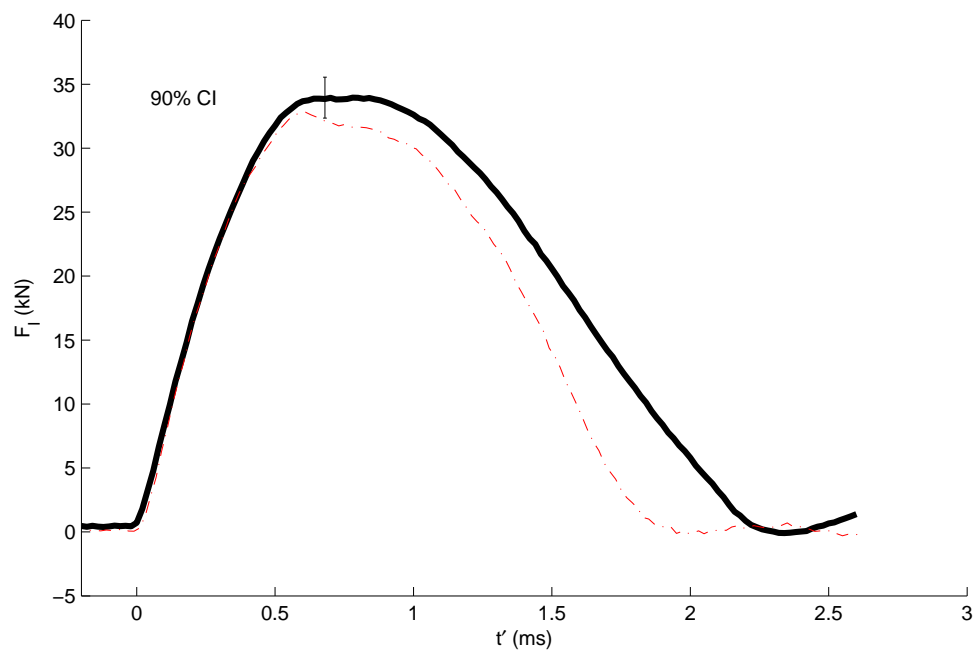


Figure 4.14: Average impact force time history for In-Water longitudinal aluminum test with $v_I = 0.66$ m/s compared with In-Air longitudinal aluminum test at approximately the same impact velocity. 90% confidence interval for peak force for In-Water test shown. Dashed line represents In-Air impact force time history.

Fig. 4.14 shows that the In-Water and In-Air impact force time histories had similar shapes at $v_I = 0.66$ m/s. Additionally, the magnitude of the peak impact force of In-Air test fell within the 90% confidence interval of the In-Water test. There was also an observed increase in impact duration in the In-Water test.

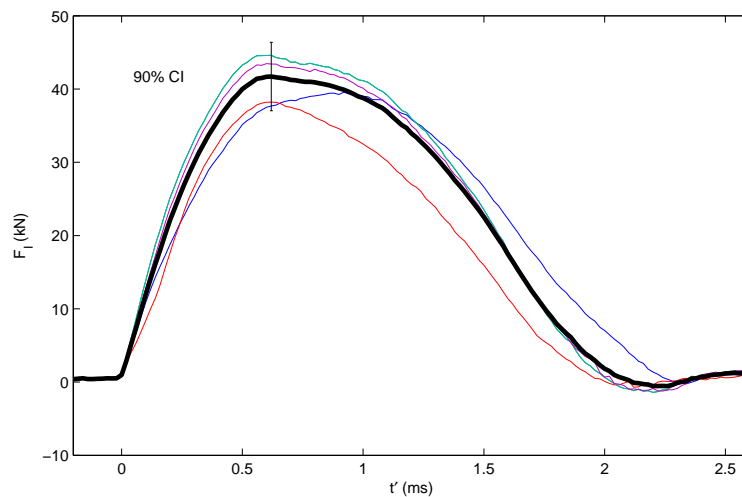


Figure 4.15: Average impact force time history for In-Water longitudinal aluminum test with $v_I = 0.85$ m/s. Determined from 5 time histories, 90% confidence interval for peak force shown. Thick black line represents averaged impact force time history.

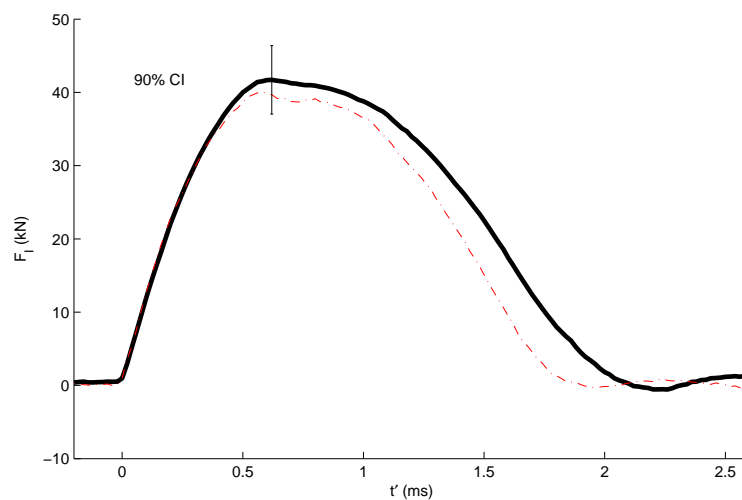


Figure 4.16: Average impact force time history for In-Water longitudinal aluminum test with $v_I = 0.85$ m/s compared with In-Air longitudinal aluminum test at approximately the same impact velocity. In-Air impact force impact history (- - -).

Fig.4.16 shows the comparison between the average impact force time history for In-Water longitudinal aluminum test with $v_I = 0.85$ m/s and In-Air longitudinal aluminum test trial at approximately the same impact velocity. The comparison was very similar to that shown in Fig. 4.14. The magnitude of the peak impact force of In-Air test fell within the 90% confidence interval of the In-Water test. There was also an observed increase in impact duration in the In-Water test.

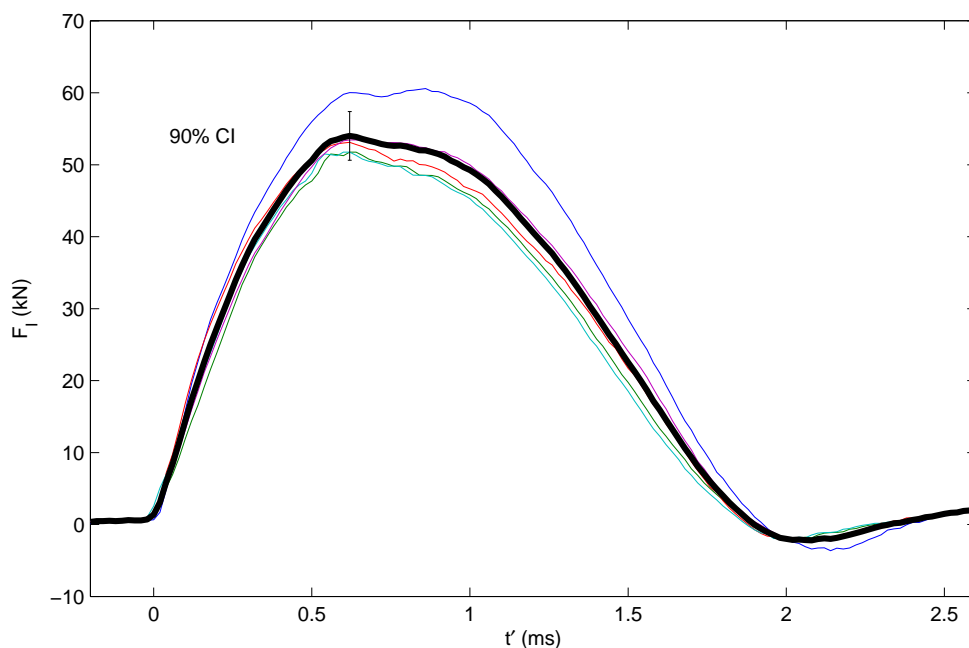


Figure 4.17: Average impact force time history for In-Water longitudinal aluminum test with $v_I = 1.2$ m/s. Determined from 5 time histories, 90% confidence interval for peak force shown. Thick black line represents averaged impact force time history.

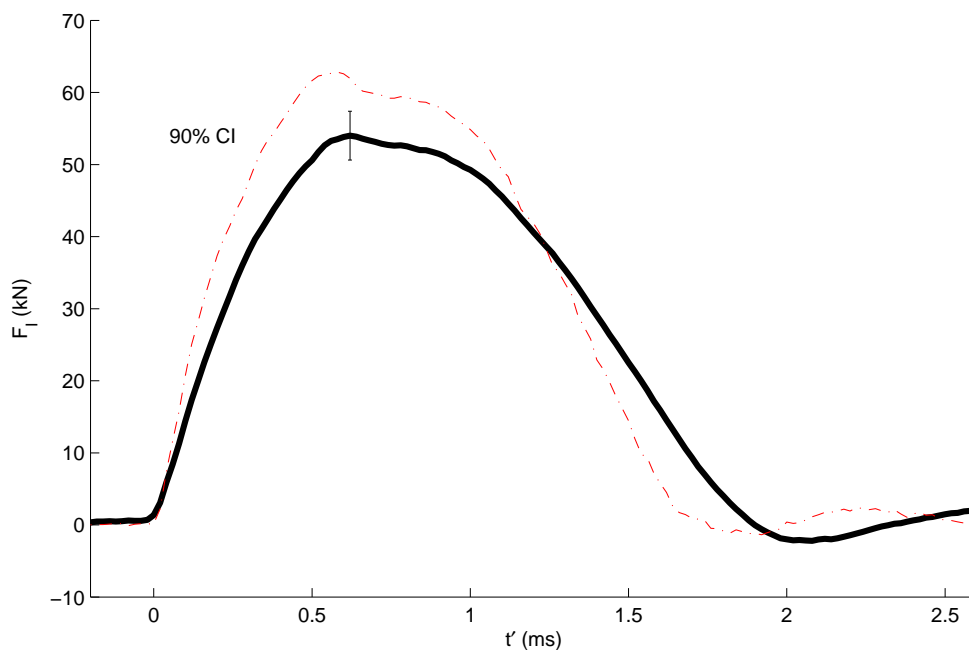


Figure 4.18: Average impact force time history for In-Water longitudinal aluminum test with $v_I = 1.2$ m/s compared with In-Air longitudinal aluminum test at approximately the same impact velocity. In-Air impact force impact history (- - -).

Fig. 4.18 shows the comparison between the average impact force time history for In-Water longitudinal aluminum test with $v_I = 1.2$ m/s and In-Air longitudinal aluminum test trial at approximately the same impact velocity. This comparison had a very different result than what was shown for the other velocities. In this case, the In-Water time history was observed to have a lower peak impact force. The impact force time history for the In-Air test was above the 90% confidence interval determined from the In-Water trials. There was, however, an observed increase in impact duration in the In-Water test as observed at the other velocities.

4.3.1.2.2 Comparison of Nonstructural Masses

Fig. 4.19 - 4.21 shows the impact force time histories for different M_{NS} at $h_2 = 30.1$ cm, $T_{erf} = 30$ s. From these plots, it appeared that the effect of the nonstructural mass was

felt after the primary peak of the impact force. The additional impact forces that appeared after the initial peak were amplified as M_{NS} was increased. This effect was consistent in all cases observed.

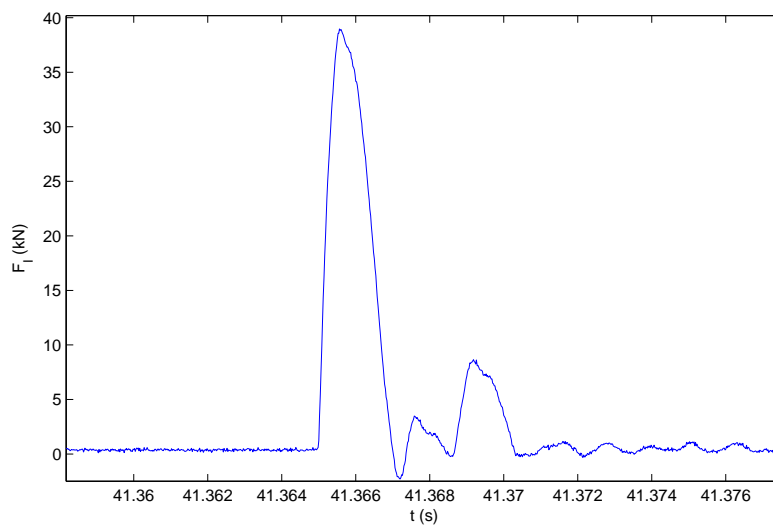


Figure 4.19: Impact force time history for In-Water longitudinal aluminum test trial 12 at $h_2 = 30.1$ cm with $M_{NS} = 0$ kg, $T_{erf} = 30$ s, $v_I = 0.75$ m/s.

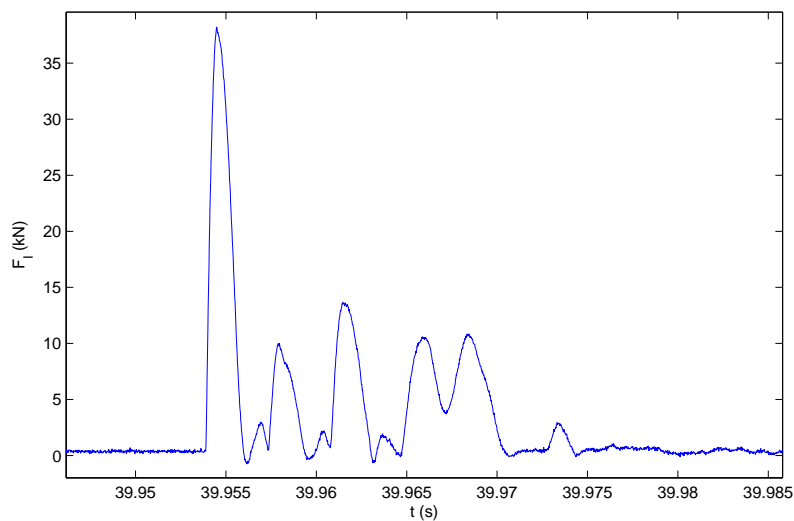


Figure 4.20: Impact force time history for In-Water longitudinal aluminum test trial 12 at $h_2 = 30.1$ cm with $M_{NS} = 50.2$ kg, $T_{erf} = 30$ s, $v_I = 0.75$ m/s.

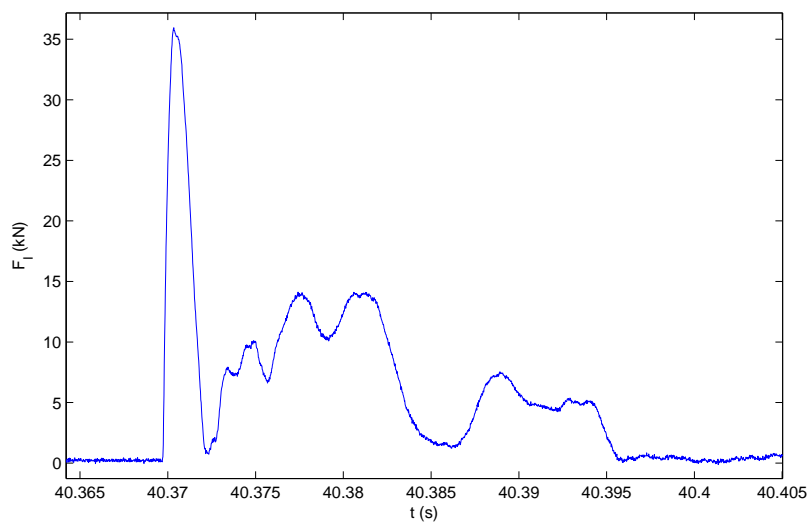


Figure 4.21: Impact force time history for In-Water longitudinal aluminum test trial 19 at $h_2 = 30.1$ cm with $M_{NS} = 99.4$ kg, $T_{erf} = 30$ s, $v_I = 0.71$ m/s

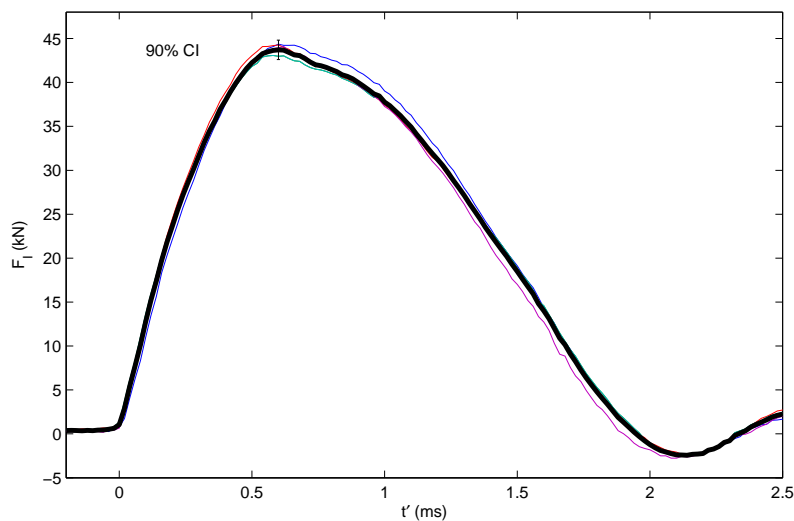


Figure 4.22: Average impact force time history for In-Water longitudinal aluminum test at $h_2 = 30.1$ cm with $v_I = 0.90$ m/s and $M_{NS} = 0$ kg. Determined from 5 time histories. Thick black line represents averaged impact force time history.

Fig. 4.22 - 4.24 shows the averaged In-Water longitudinal aluminum time histories of the primary peak of the impact force measurements for different M_{NS} at approximately the same impact velocities at $h_2 = 30.1$ cm. For $M_{NS} = 0$ kg and M_{NS} , the impact velocity for these time histories was 0.90 m/s. For M_{NS} the closest impact velocity was the 0.86 m/s case.

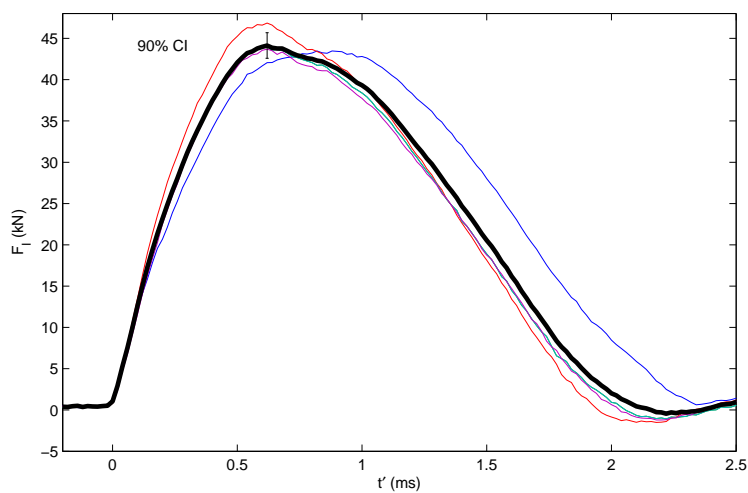


Figure 4.23: Average impact force time history for In-Water longitudinal aluminum test at $h_2 = 30.1$ cm with $v_I = 0.90$ m/s and $M_{NS} = 50.2$ kg. Determined from 5 time histories. Thick black line represents averaged impact force time history.

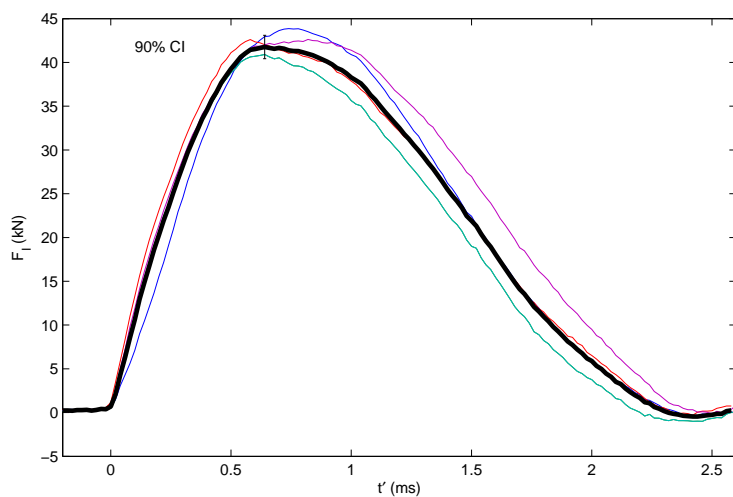


Figure 4.24: Average impact force time history for In-Water longitudinal aluminum test at $h_2 = 30.1$ cm with $v_I = 0.86$ m/s and $M_{NS} = 99.4$ kg. Determined from 5 time histories. Thick black line represents averaged impact force time history.

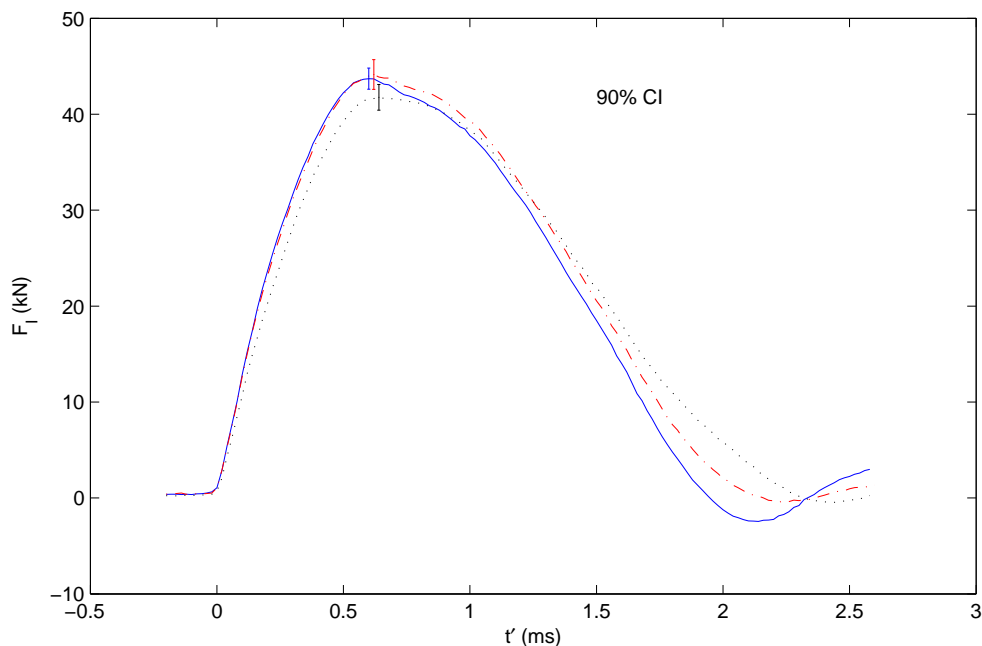


Figure 4.25: Comparison between impact force time histories of different M_{NS} for In-Water longitudinal aluminum test. $M_{NS} = 0$ kg (blue —), $M_{NS} = 50.2$ kg (red - - -), $M_{NS} = 99.4$ kg (black ···). $v_I = 0.90$ m/s for $M_{NS} = 0$ kg and $M_{NS} = 50.2$ kg. $v_I = 0.86$ m/s for $M_{NS} = 99.4$ kg.

Fig. 4.25 shows the comparison between the primary peak impact force time histories of different M_{NS} for In-Water longitudinal aluminum test. It appeared from the time history comparison that the addition of nonstructural mass had little effect on the peak impact force. The impact duration appeared to increase as nonstructural mass increased.

Fig. 4.26 shows five trials superimposed on top of one another for each different M_{NS} from In-Water longitudinal aluminum test $h_2 = 30.1$ cm with $M_{NS} = 0, 50.2,$ and 99.4 kg, $T_{erf} = 30$ s, $v_I \sim 0.9$ m/s. The plots showed that the effects in the impact force time history observed after the primary peak were consistent. Additionally, the magnitude and duration of these effects increase with increasing M_{NS} .

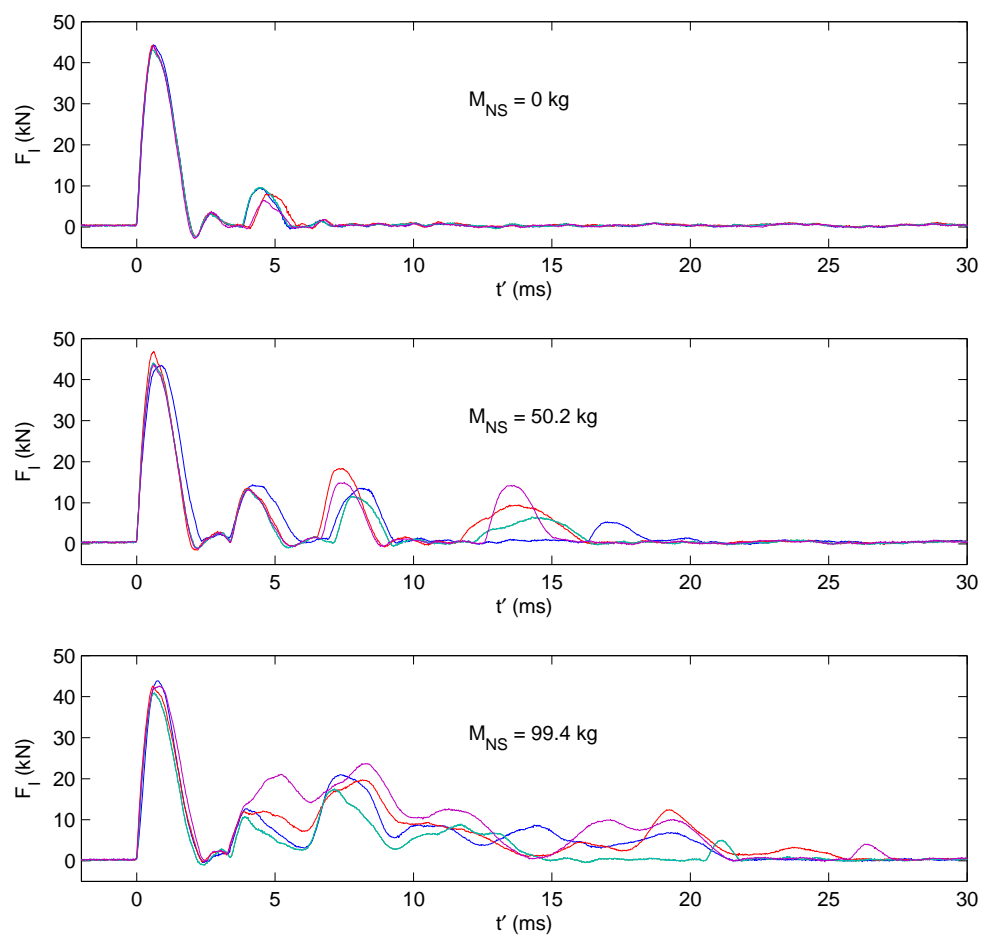


Figure 4.26: Impact force time histories for In-Water longitudinal aluminum test, five trials superimposed on one another at $h_2 = 30.1$ cm with $M_{NS} = 0, 50.2,$ and 99.4 kg, $T_{erf} = 30$ s, $v_I \sim 0.9$ m/s.

Fig. 4.27 shows the average impact force time histories for In-Water longitudinal aluminum test superimposed on one another at $h_2 = 30.1$ cm with $M_{NS} = 0, 50.2,$ and 99.4 kg, $T_{erf} = 30$ s, $v_I \sim 0.9$ m/s. Again, this plot showed that the effects of the nonstructural mass in the impact force time histories were increasing in duration and magnitude with increasing M_{NS} .

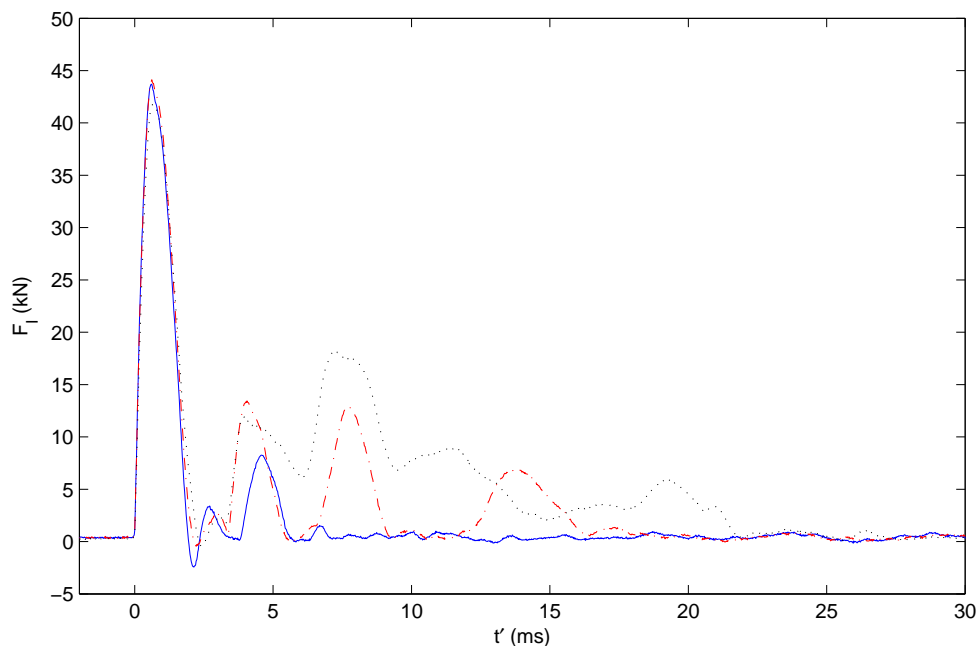


Figure 4.27: Average impact force time histories for In-Water longitudinal aluminum test superimposed on one another at $h_2 = 30.1$ cm with $M_{NS} = 0, 50.2,$ and 99.4 kg, $T_{erf} = 30$ s, $v_I \sim 0.9$ m/s. $M_{NS} = 0$ kg (blue -), $M_{NS} = 50.2$ kg (red - - -), $M_{NS} = 99.4$ kg (black ...)

4.3.1.3 Peak Force vs. Impact Velocity

4.3.1.3.1 Scatter Plot

Fig. 4.28 plotted F_p vs. v_I for all In-Water longitudinal aluminum tests, with the solid black line representing the In-Air test. Results indicated that the peak forces measured from the In-Water tests were close to that of the In-Air peak forces. The measurements from the In-Water test followed the same slope, with respect to impact velocity, as the the In-Air test. There appeared to be an offset, a slight increase in the In-Water test when compared to the In-Air test. Variability in the peak force measurements increased as the impact velocity increased above 1 m/s.

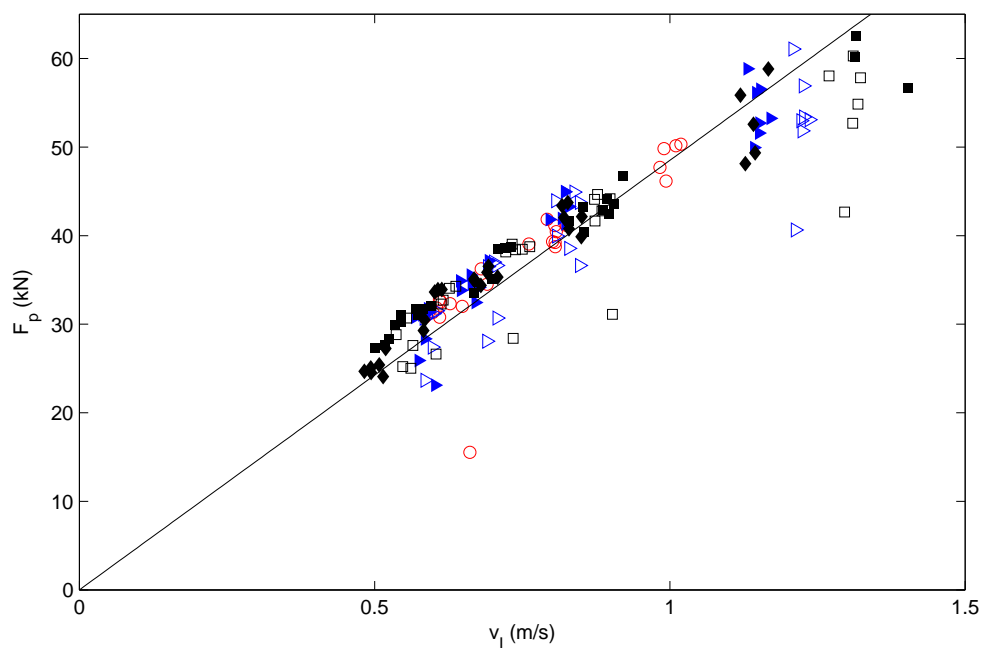


Figure 4.28: Plot of F_p vs. v_I for the In-Water longitudinal aluminum tests. $h_2 = 13.3$ cm, $M_{NS} = 0$ kg (red \circ). $h_2 = 20.9$ cm, $M_{NS} = 0$ kg (blue \triangleright). $h_2 = 20.9$ cm, $M_{NS} = 99.4$ kg (blue \square). $h_2 = 30.1$ cm, $M_{NS} = 0$ kg (black \square). $h_2 = 30.1$ cm, $M_{NS} = 50.2$ kg (black \blacksquare). $h_2 = 30.1$ cm, $M_{NS} = 99.4$ kg (black \blacklozenge). In-Air longitudinal aluminum test (—) (Fig. 4.2).

4.3.1.3.2 Averaged by Wave Condition

Fig. 4.28 plotted F_p vs. v_I for all In-Water longitudinal aluminum tests averaged by T_{erf} , with the solid black line representing the In-Air test. 90% confidence intervals for the trials averaged by the T_{erf} used were included on the plot. From $0 < v_I < 1$ m/s, the In-Air impact forces fell within the 90% confidence intervals of the In-Water impact forces. For $v_I > 1$ m/s, the averaged In-Water peak forces fell below the In-Air impact force line.

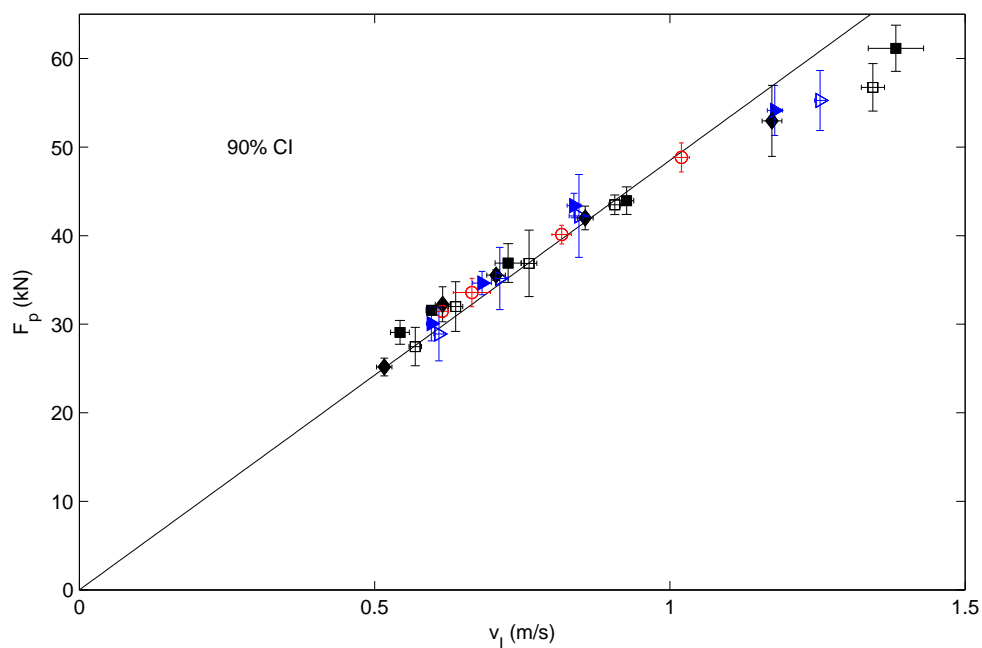


Figure 4.29: Plot of F_p vs. v_I for all In-Water longitudinal aluminum tests, averaged by T_{erf} . $h_2 = 13.3$ cm, $M_{NS} = 0$ kg (red \circ). $h_2 = 20.9$ cm, $M_{NS} = 0$ kg (blue \triangleright). $h_2 = 20.9$ cm, $M_{NS} = 99.4$ kg (blue \square). $h_2 = 30.1$ cm, $M_{NS} = 0$ kg (black \square). $h_2 = 30.1$ cm, $M_{NS} = 50.2$ kg (black \blacklozenge). $h_2 = 30.1$ cm, $M_{NS} = 99.4$ kg (black \blacklozenge). In-Air longitudinal aluminum test (—) (Fig. 4.2). 90% confidence intervals for velocity and peak force shown.

4.3.1.3.3 Normalized by Corresponding In-Air Impact Force

Fig. 4.30 plotted the In-Water peak force normalized by empirically determined In-Air impact force, F_N , vs. v_I for the In-Water longitudinal aluminum tests. This plot shows the proportional increase in force associated with the hydraulics of the In-Water test. The impact forces from the In-Water longitudinal aluminum tests appeared to be about 10% greater than the corresponding In-Air longitudinal aluminum test values for the given range of impact velocities. Additionally, the proportional increase in peak impact force appeared to decrease with increasing impact velocity.

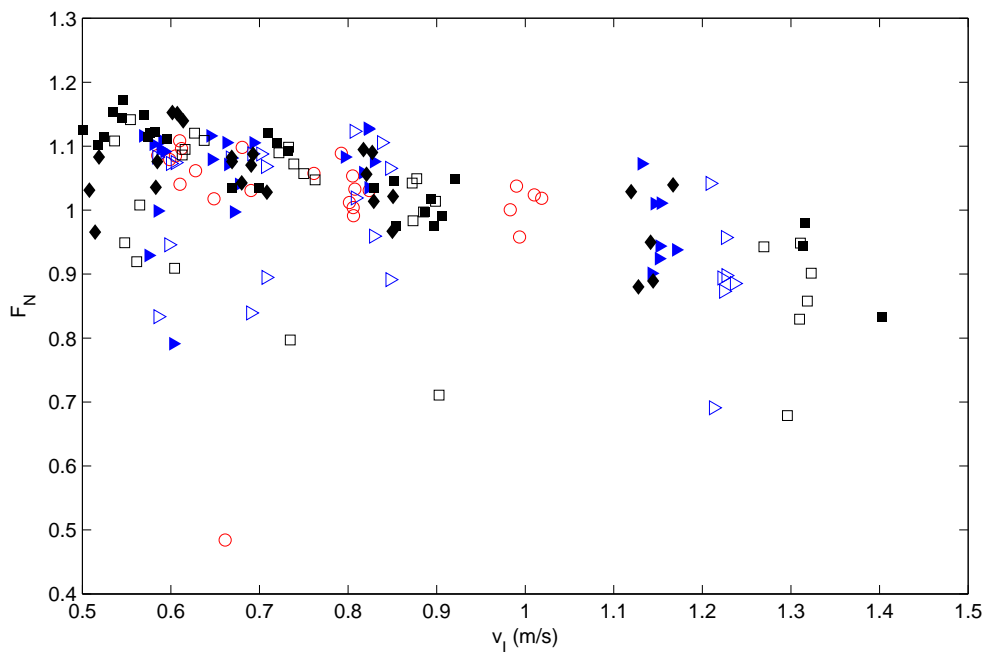


Figure 4.30: Plot of In-Water peak force normalized by empirically determined In-Air impact force, F_N , vs. v_I for the In-Water longitudinal aluminum tests. $h_2 = 13.3$ cm, $M_{NS} = 0$ kg (red \circ). $h_2 = 20.9$ cm, $M_{NS} = 0$ kg (blue \triangleright). $h_2 = 20.9$ cm, $M_{NS} = 99.4$ kg (blue \triangleleft). $h_2 = 30.1$ cm, $M_{NS} = 0$ kg (black \square). $h_2 = 30.1$ cm, $M_{NS} = 50.2$ kg (black \blacksquare). $h_2 = 30.1$ cm, $M_{NS} = 99.4$ kg (black \blacklozenge)

4.3.1.3.4 Incremental Difference

Fig. 4.31 shows the numerical incremental difference between In-Water peak force and the empirically determined In-Air impact force, F_d , vs. v_I for the In-Water longitudinal aluminum tests. A maximum increase of 5 kN from the In-Air impact force to the corresponding In-Water impact force was observed. This value was fairly consistent across the velocity range tested.

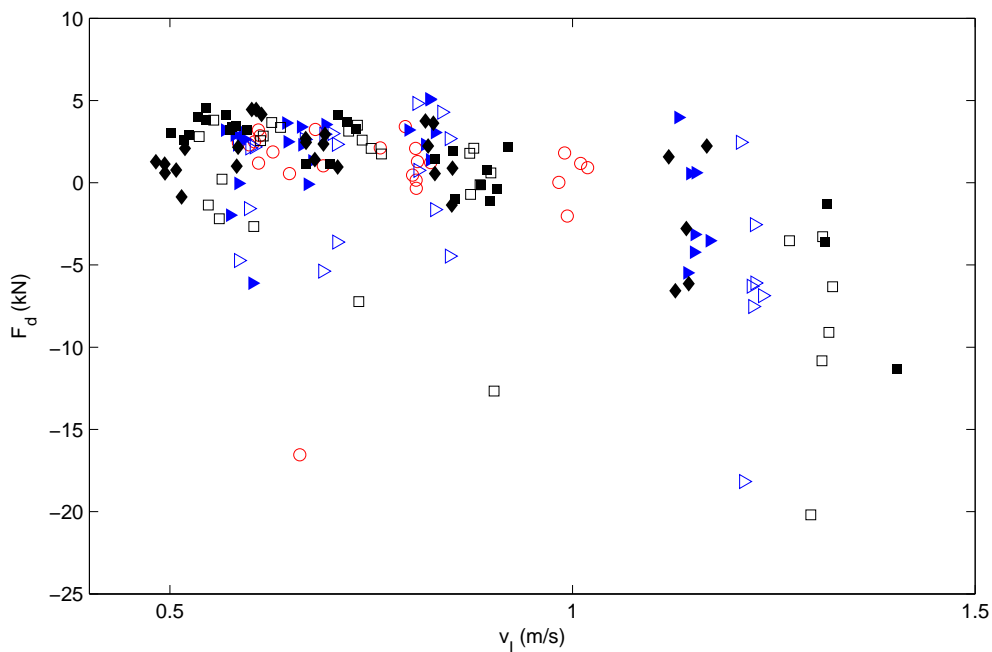


Figure 4.31: Plot of the numerical difference between In-Water peak force and the empirically determined In-Air impact force, F_d , vs. v_I for the In-Water longitudinal aluminum tests. $h_2 = 13.3$ cm, $M_{NS} = 0$ kg (red \circ). $h_2 = 20.9$ cm, $M_{NS} = 0$ kg (blue \triangleright). $h_2 = 20.9$ cm, $M_{NS} = 99.4$ kg (blue \square). $h_2 = 30.1$ cm, $M_{NS} = 0$ kg (black \square). $h_2 = 30.1$ cm, $M_{NS} = 50.2$ kg (black \blacklozenge). $h_2 = 30.1$ cm, $M_{NS} = 99.4$ kg (black \blacklozenge)

4.3.1.4 Impact Duration

Fig. 4.32 shows a plot of impact duration, t_i , vs. v_I for the In-Water longitudinal aluminum tests. Impact durations were determined by setting a threshold to determine the beginning and end of the primary peak of the impact force time series. This threshold was set at 5% of the measured peak force from the trial. The results shown in Fig. 4.32 shows that the impact durations from the In-Water tests were slightly longer than the In-Air test impact durations. Most of the impact durations were around 2 ms. Some outliers went as high as 6.3 ms. Average impact duration was calculated to be 2.36 ms.

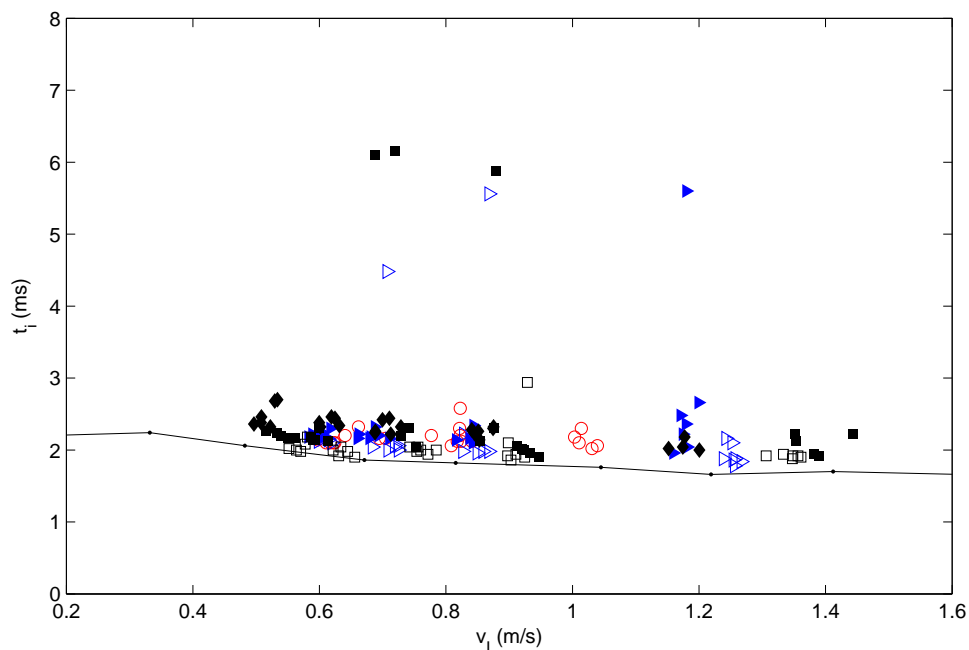


Figure 4.32: Plot of impact duration, t_i , vs. v_I for the In-Water longitudinal aluminum tests. $h_2 = 13.3$ cm, $M_{NS} = 0$ kg (red \circ). $h_2 = 20.9$ cm, $M_{NS} = 0$ kg (blue \triangleright). $h_2 = 20.9$ cm, $M_{NS} = 99.4$ kg (blue \triangleleft). $h_2 = 30.1$ cm, $M_{NS} = 0$ kg (black \square). $h_2 = 30.1$ cm, $M_{NS} = 50.2$ kg (black \blacklozenge). $h_2 = 30.1$ cm, $M_{NS} = 99.4$ kg (black \blacksquare), Measured t_i from In-Air test ($-$).

4.3.1.5 Normalized Impact Force vs. Froude Number

Froude number was calculated for each trial using Eq. 4.1.

$$Fr = \frac{v_I}{\sqrt{gH_4}} \quad (4.1)$$

Where Fr is the Froude number, g is the gravitational acceleration, and H_4 the maximum depth of inundation flow at the time of impact. The normalized force, F_N , was determined by using the same method as section 4.3.1.3.3. Fig. 4.33 plots F_N against Fr . The range of Fr observed in the In-Water longitudinal aluminum test was $0.35 < Fr < 0.85$. Overall, the behavior did not differ much from the comparison of F_N to impact velocity (Fig. 4.30).

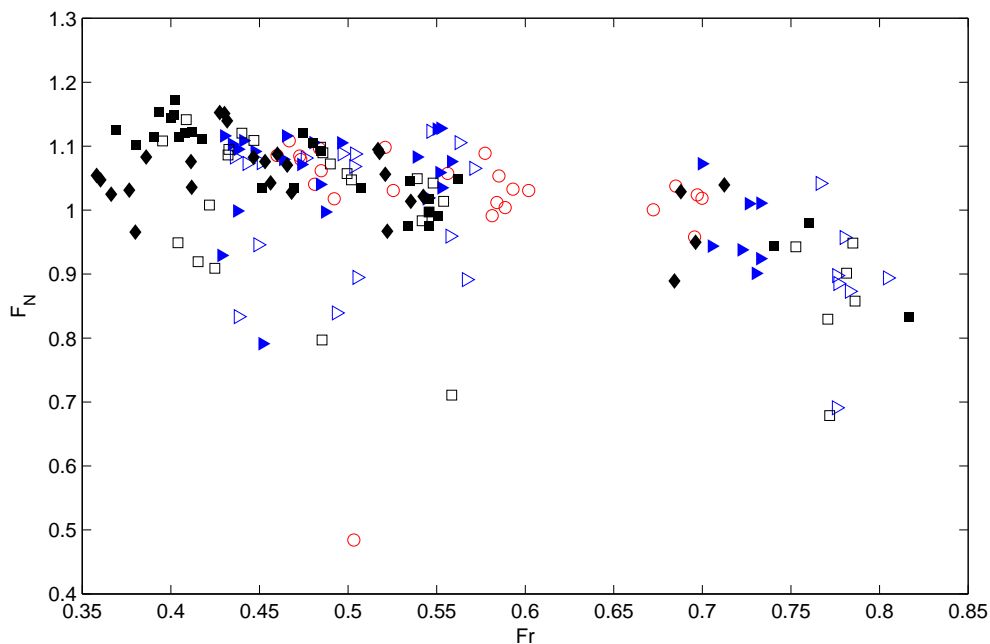


Figure 4.33: Plot of F_N vs. Fr for the In-Water longitudinal aluminum tests. $h_2 = 13.3$ cm, $M_{NS} = 0$ kg (red \circ). $h_2 = 20.9$ cm, $M_{NS} = 0$ kg (blue \triangleright). $h_2 = 20.9$ cm, $M_{NS} = 99.4$ kg (blue \triangleleft). $h_2 = 30.1$ cm, $M_{NS} = 0$ kg (black \square). $h_2 = 30.1$ cm, $M_{NS} = 50.2$ kg (black \blacksquare). $h_2 = 30.1$ cm, $M_{NS} = 99.4$ kg (black \blacklozenge).

4.3.1.6 Impulse

Impulse values J_p and J_{30} were calculated using the same methods described in section 4.2.5. Fig. 4.34 shows definitions for the integrations regions shown again using the average impact force time histories from Fig. 4.27 for clarity. Fig. 4.34 shows that J_{30} was typically capable of capturing all nonstructural mass effects.

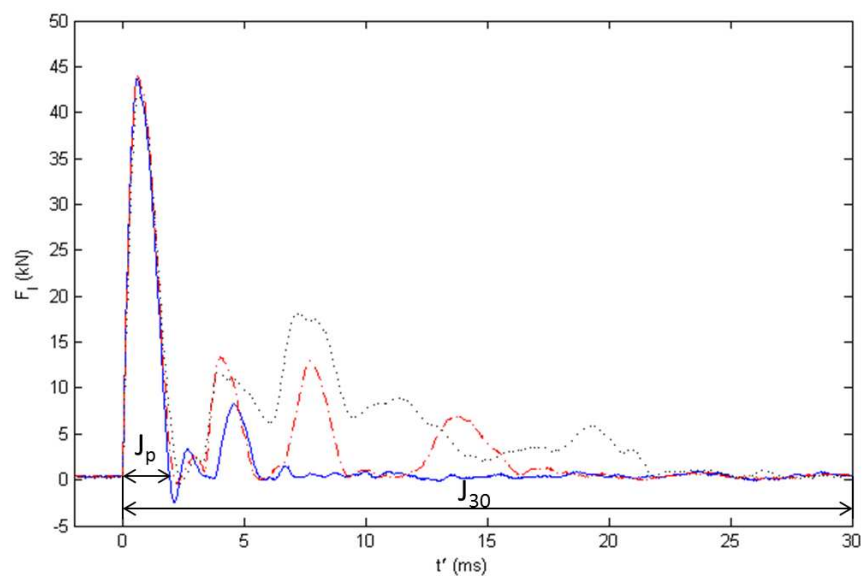


Figure 4.34: Integration regions defined for impulse values J_p and J_{30} shown on average impact force time histories for In-Water longitudinal aluminum test superimposed on one another at $h_2 = 30.1$ cm with $M_{NS} = 0, 50.2,$ and 99.4 kg, $T_{erf} = 30$ s, $v_I \sim 0.9$ m/s. $M_{NS} = 0$ kg (blue -), $M_{NS} = 50.2$ kg (red - - -), $M_{NS} = 99.4$ kg (black \cdots)

4.3.1.6.1 J_p

Fig. 4.35 shows the plot of J_p vs. v_I for In-Water longitudinal aluminum tests compared to the In-Air longitudinal aluminum test. The J_p vs. v_I relationship was observed to behave similarly to the F_p vs. v_I relationship. Overall, the In-Water J_p values appeared to be higher than their corresponding In-Air values. Additionally, no nonstructural mass effect was observed.

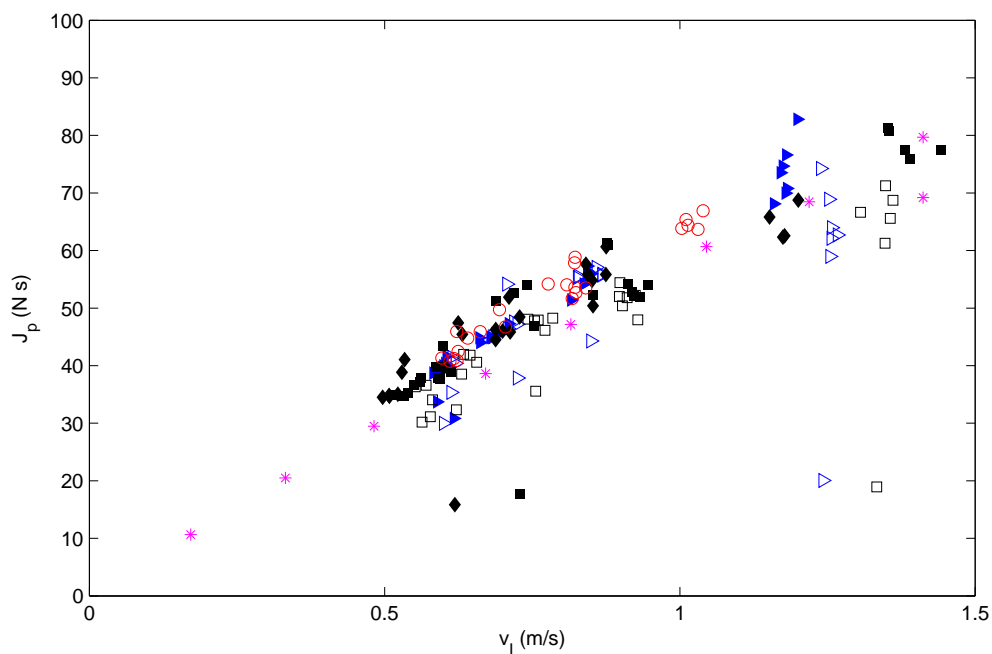


Figure 4.35: Plot of J_p vs. v_I for In-Water longitudinal aluminum tests. $h_2 = 13.3$ cm, $M_{NS} = 0$ kg (red \circ). $h_2 = 20.9$ cm, $M_{NS} = 0$ kg (blue \triangleright). $h_2 = 20.9$ cm, $M_{NS} = 99.4$ kg (blue \triangleleft). $h_2 = 30.1$ cm, $M_{NS} = 0$ kg (black \square). $h_2 = 30.1$ cm, $M_{NS} = 50.2$ kg (black \blacksquare). $h_2 = 30.1$ cm, $M_{NS} = 99.4$ kg (black \blacklozenge). In-Air longitudinal test (magenta $*$).

4.3.1.6.2 J_{30}

Fig. 4.36 shows the plot of J_{30} vs. v_I for In-Water longitudinal aluminum tests compared to the In-Air longitudinal aluminum test. The slopes for the J_{30} vs. v_I relationships for different values of M_{NS} were calculated by determining the line of best fit through the data points. The slopes for the nonstructural mass values, m_0 , m_{50} , and m_{99} were determined to be 76.5, 153, and 244 respectively. The J_{30} values from the In-Air longitudinal aluminum test, also with $M_{NS} = 0$, were shown to have a slope comparable to m_0 .

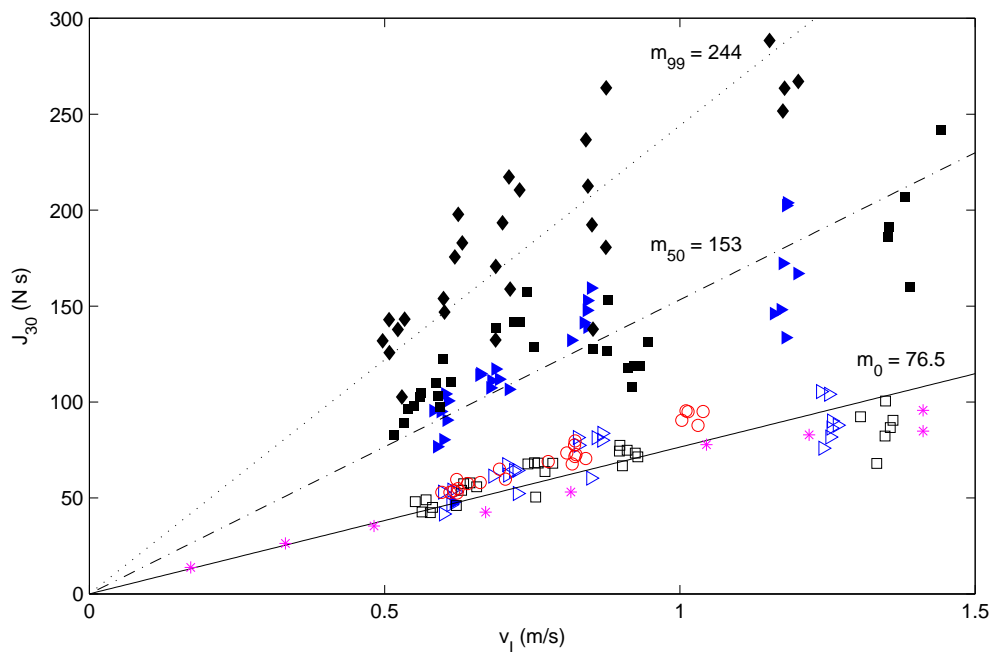


Figure 4.36: Plot of J_{30} vs. v_I for In-Water longitudinal aluminum tests. $h_2 = 13.3$ cm, $M_{NS} = 0$ kg (red \circ). $h_2 = 20.9$ cm, $M_{NS} = 0$ kg (blue \triangleright). $h_2 = 20.9$ cm, $M_{NS} = 99.4$ kg (blue \triangleleft). $h_2 = 30.1$ cm, $M_{NS} = 0$ kg (black \square). $h_2 = 30.1$ cm, $M_{NS} = 50.2$ kg (black \blacksquare). $h_2 = 30.1$ cm, $M_{NS} = 99.4$ kg (black \blacklozenge). In-Air longitudinal test (magenta $*$).

4.3.1.6.3 J_p vs. J_{30}

Fig. 4.37 shows the plot of J_p vs. J_{30} for In-Water longitudinal aluminum tests. The slopes for the J_p vs. J_{30} relationships for different values of M_{NS} were calculated by determining the line of best fit through the data points. The slopes for the nonstructural mass values, m_0 , m_{50} , and m_{99} were determined to be 1.4, 2.4, and 3.9 respectively.

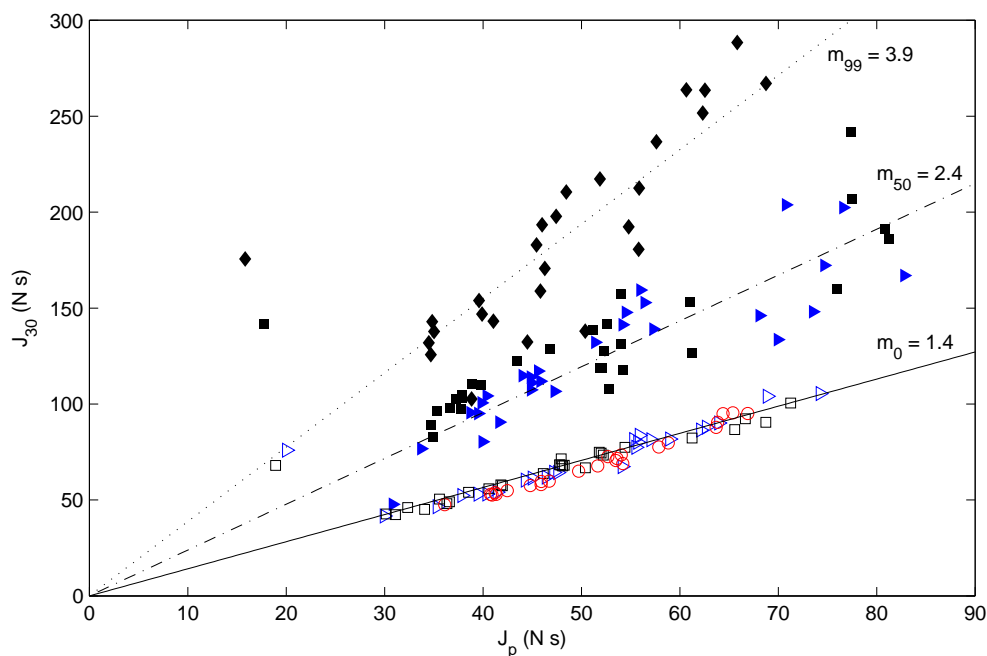


Figure 4.37: Plot of J_p vs. J_{30} for In-Water longitudinal aluminum tests. $h_2 = 13.3$ cm, $M_{NS} = 0$ kg (red \circ). $h_2 = 20.9$ cm, $M_{NS} = 0$ kg (blue \triangleright). $h_2 = 20.9$ cm, $M_{NS} = 99.4$ kg (blue \triangleleft). $h_2 = 30.1$ cm, $M_{NS} = 0$ kg (black \square). $h_2 = 30.1$ cm, $M_{NS} = 50.2$ kg (black \blacksquare). $h_2 = 30.1$ cm, $M_{NS} = 99.4$ kg (black \blacklozenge).

4.3.2 Longitudinal Acrylic

4.3.2.1 Flow Speed vs. Impact Velocity

Fig. 4.38 shows the maximum flow speeds compared with debris impact velocities for In-Water longitudinal acrylic tests. Overall, these velocities behaved similarly to the velocities observed in the longitudinal aluminum tests. The debris velocities appeared to almost reach the speed of the maximum measured flow velocities.

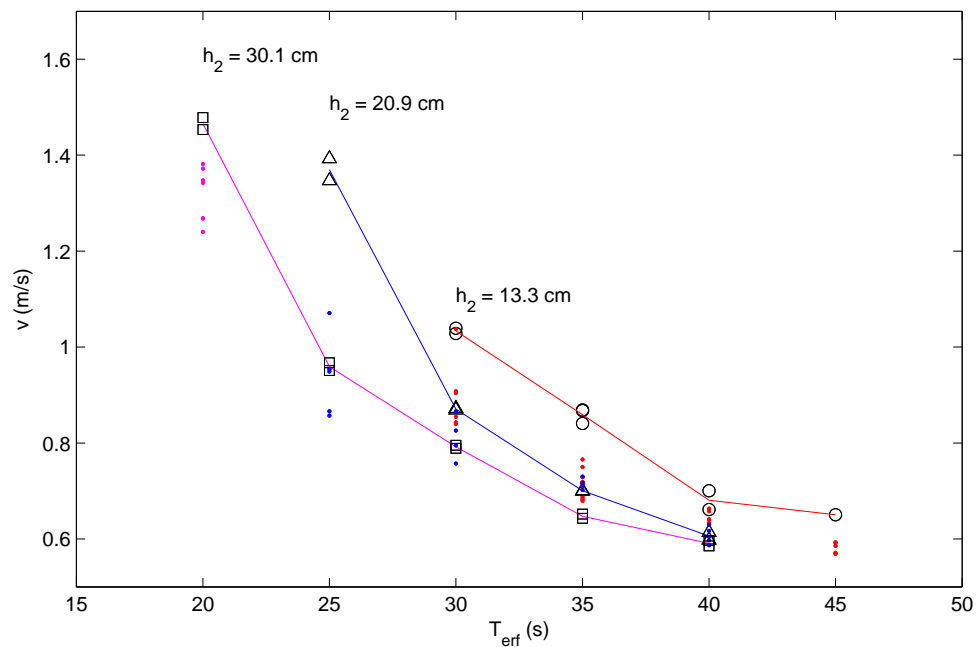


Figure 4.38: Maximum flow speeds compared with debris impact velocities for In-Water longitudinal acrylic tests. For flow speeds, $h_2 = 13.3$ cm (\circ), $h_2 = 20.9$ cm (\triangle), $h_2 = 30.1$ cm (\square). Dots represent debris impact velocities. Red represents $h_2 = 13.3$ cm, blue represents $h_2 = 20.9$ cm, and magenta represents $h_2 = 30.1$ cm.

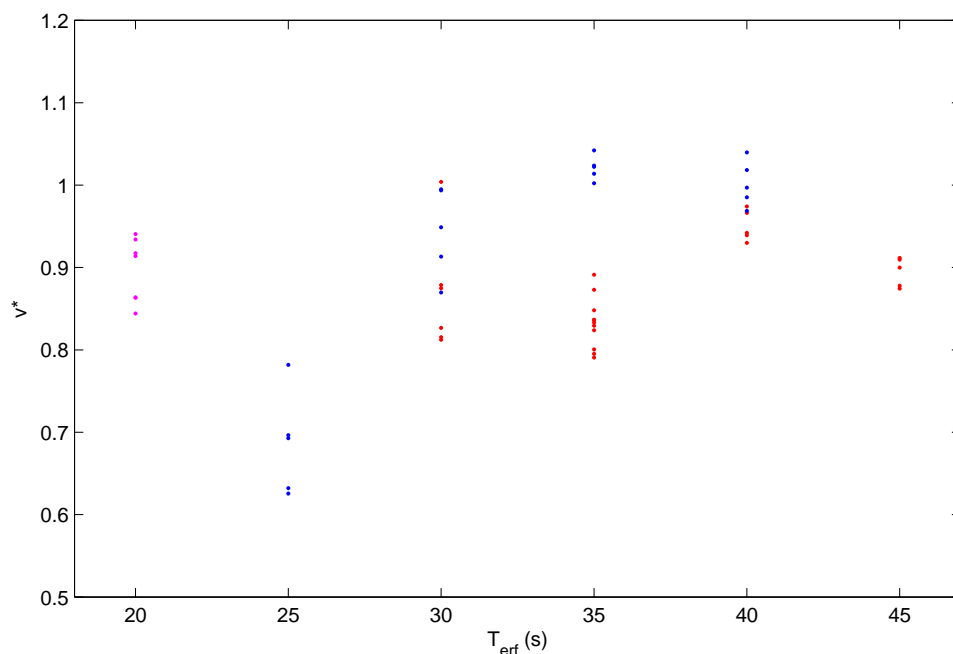


Figure 4.39: Normalized acrylic debris impact velocities, v^* with respect to the average measured surface flow speeds from PIV. The impact velocities from Fig. 4.38 were divided by the flow velocity lines shown. Red represents $h_2 = 13.3$ cm, blue represents $h_2 = 20.9$ cm, and magenta represents $h_2 = 30.1$ cm.

Fig. 4.39 shows the normalized acrylic debris impact velocities, v^* with respect to the average measured surface flow speeds from PIV. These values ranged from 0.63 to 1.04. These values suggested that the debris was moving in the range of 60% to 100% of the water velocity.

4.3.2.2 Impact Force Time History comparison

Fig. 4.40 and 4.41 shows the comparison between the average impact force time history for In-Water longitudinal acrylic test with $v_I = 0.72$ m/s and In-Air longitudinal acrylic test trial at approximately the same impact velocity. The In-Water time history was observed to have a greater peak impact force. The impact force time history for the In-Air test was below the 90% confidence interval determined from the In-Water trials. There was also

an observed increase in impact duration in the In-Water test as observed in the aluminum test.

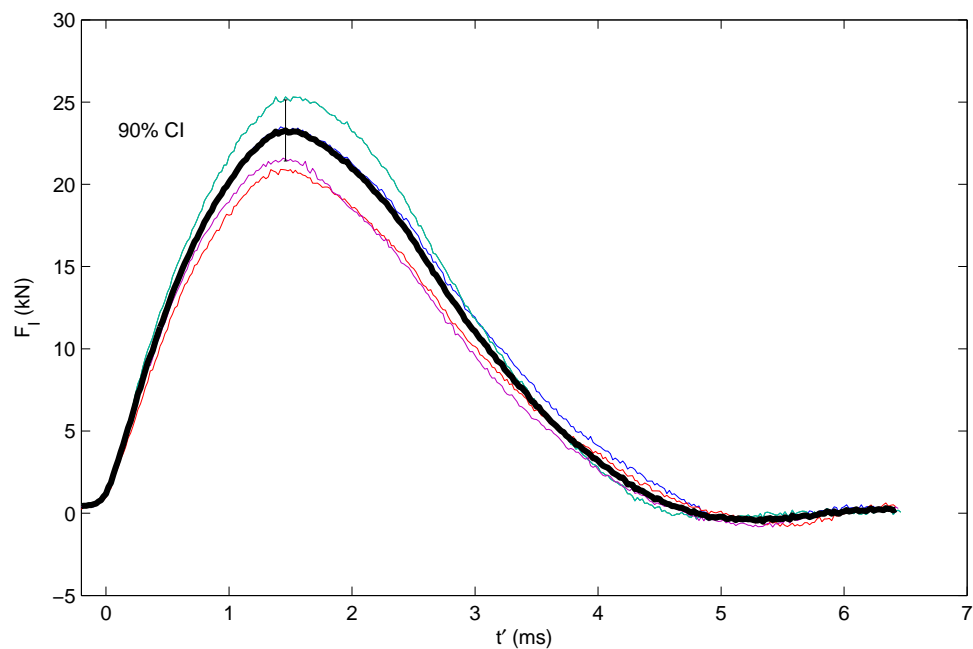


Figure 4.40: Average impact force time history for In-Water longitudinal acrylic test with $v_I = 0.72$ m/s. Determined from 5 time histories, 90% confidence interval for peak force shown. Thick black line represents averaged impact force time history.

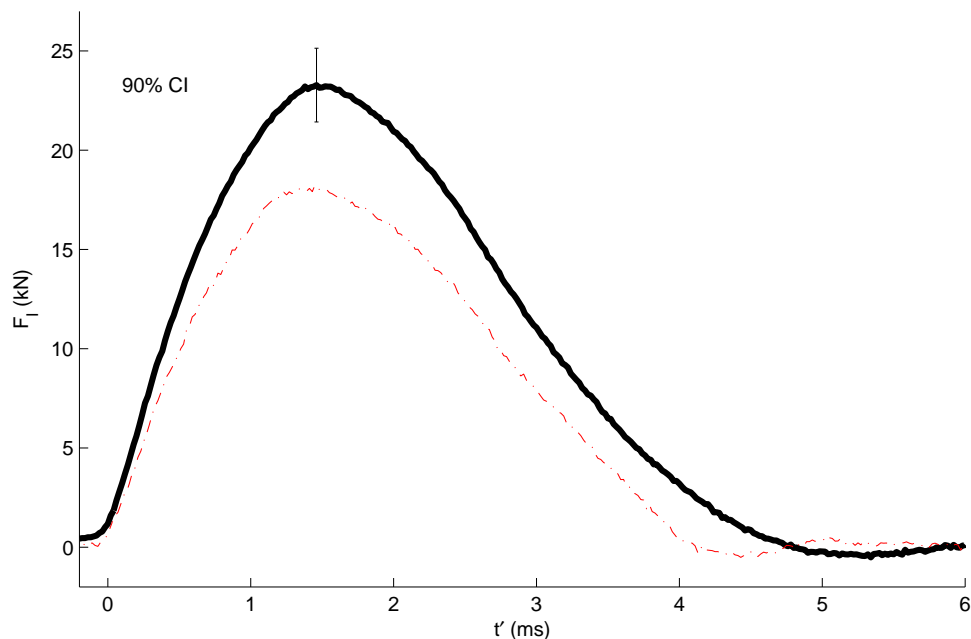


Figure 4.41: Average impact force time history for In-Water longitudinal acrylic test with $v_I = 0.72$ m/s compared with In-Air longitudinal acrylic test at approximately the same impact velocity. Dashed line represents In-Air impact force impact history. 90% confidence interval for peak In-Water force shown.

4.3.2.3 Peak Force vs. Impact Velocity

4.3.2.3.1 Scatter Plot

Fig. 4.42 plotted F_p vs. v_I for all In-Water longitudinal acrylic tests, with the solid black line representing the In-Air test. Results indicated that the peak forces measured from the In-Water tests were higher than the In-Air peak forces. The results from the In-Water test appeared to have followed the same slope, with respect to impact velocity, as the the In-Air test. There appeared to be an offset, an increase in the In-Water test when compared to the In-Air test for the range of impact velocities tested.

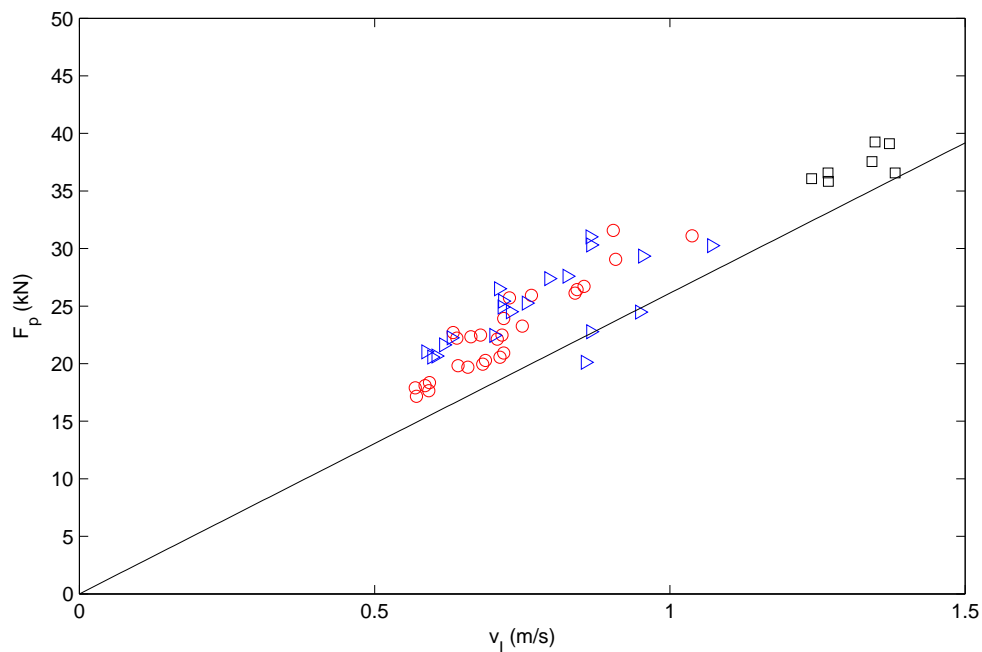


Figure 4.42: Plot of F_p vs. v_I for the In-Water longitudinal acrylic tests. $h_2 = 13.3$ cm (red \circ), $h_2 = 20.9$ cm (blue \triangleright), $h_2 = 30.1$ cm (black \square). The solid black line is taken from the In-Air longitudinal acrylic test (Fig. 4.3).

4.3.2.3.2 Averaged by Wave Condition

Fig. 4.29 plotted F_p vs. v_I for all In-Water longitudinal acrylic tests averaged by T_{erf} , with the solid black line representing the In-Air test. 90% confidence intervals for the trials averaged by the T_{erf} used were included on the plot. For every case except one, the bottom bounds of the 90% confidence interval for the In-Water impact forces were above the empirical In-Air line.

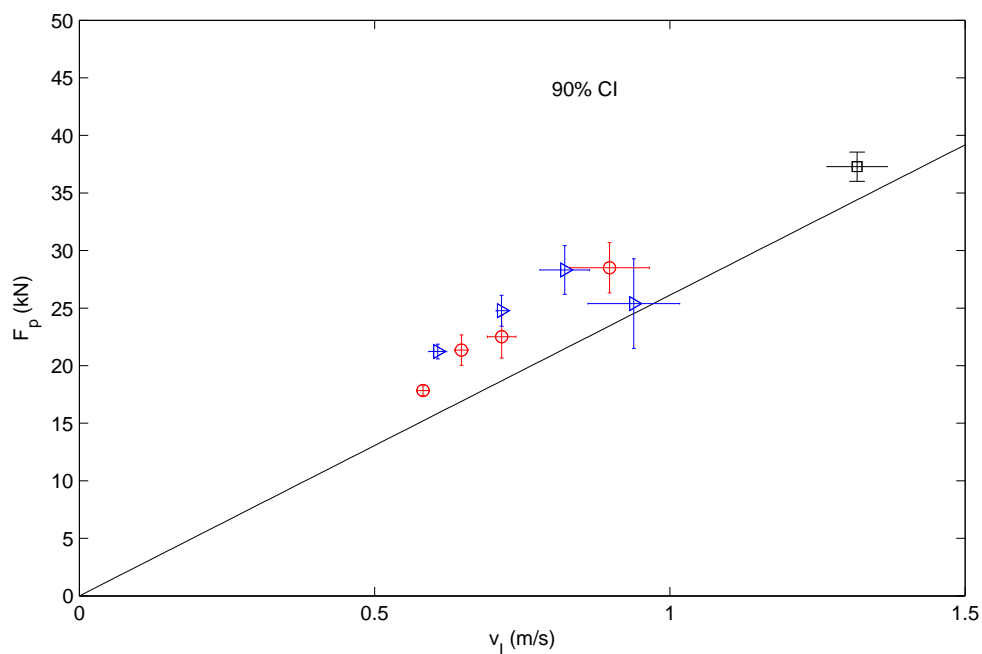


Figure 4.43: Plot of F_p vs. v_I for all In-Water longitudinal acrylic tests, averaged by T_{erf} . $h_2 = 13.3$ cm (red \circ), $h_2 = 20.9$ cm (blue \triangleright), $h_2 = 30.1$ cm (black \square). The solid black line is taken from the In-Air longitudinal acrylic test (Fig. 4.3). 90% confidence intervals for velocity and peak force shown.

4.3.2.3.3 Normalized by Corresponding In-Air Impact Force

Fig. 4.44 plotted the In-Water peak force normalized by empirically determined In-Air impact force, F_N , vs. v_I for the In-Water longitudinal acrylic tests. This plot showed that the proportional increase in force associated with the hydraulics of the In-Water acrylic test. The impact forces from the In-Water longitudinal aluminum tests appeared to be, at maximum, about 40% greater than the corresponding In-Air longitudinal acrylic test values for the given range of impact velocities. Additionally, the proportional increase in peak impact force appeared to decrease with increasing impact velocity.

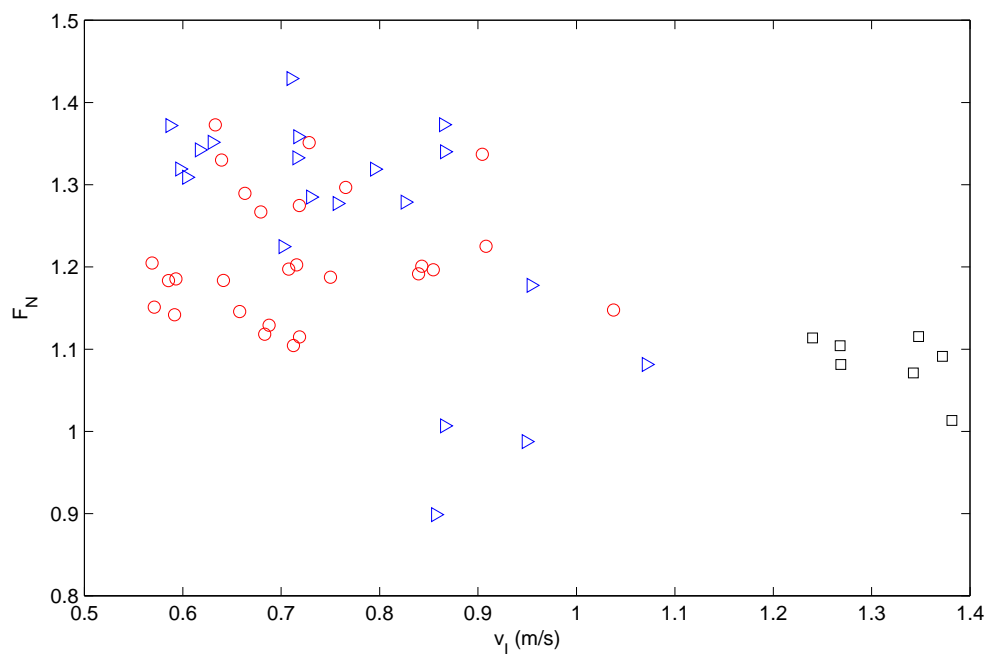


Figure 4.44: Plot of In-Water peak force normalized by empirically determined In-Air impact force, F_N , vs. v_I for the In-Water longitudinal acrylic tests. $h_2 = 13.3$ cm (red \circ), $h_2 = 20.9$ cm (blue \triangleright), $h_2 = 30.1$ cm (black \square)

4.3.2.3.4 Incremental Difference

Fig. 4.45 shows the numerical difference between In-Water peak force and the empirically determined In-Air impact force, F_d , vs. v_I for the In-Water longitudinal acrylic tests. This plot shows a maximum increase of 8 kN from the In-Air impact force to the corresponding In-Water impact force. The incremental increase mostly fell into the range of 2 - 8 kN.

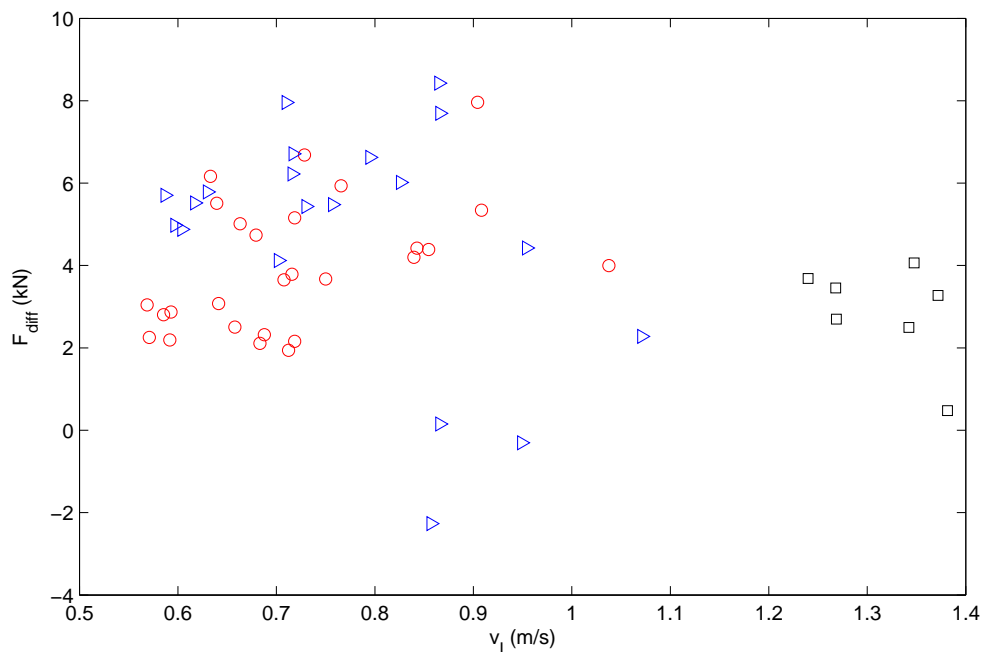


Figure 4.45: Plot of the numerical difference between In-Water peak force and the empirically determined In-Air impact force, F_d , vs. v_I for the In-Water longitudinal acrylic tests. $h_2 = 13.3$ cm (red \circ), $h_2 = 20.9$ cm (blue \triangleright), $h_2 = 30.1$ cm (black \square)

4.3.2.4 Impact Duration

Fig. 4.32 shows a plot of impact duration, t_i , vs. v_I for the In-Water longitudinal acrylic tests. Impact durations were determined using the same method as was used for the longitudinal aluminum tests. The results shown in Fig. 4.46 shows that the impact durations from the In-Water tests were slightly longer than the In-Air test impact durations by about 1 ms on average. Impact durations for the In-Air test were around 4 ms. In-Water test impact durations ranged from 4 ms to 5.5 ms. Average impact duration was calculated to be 4.87 ms.

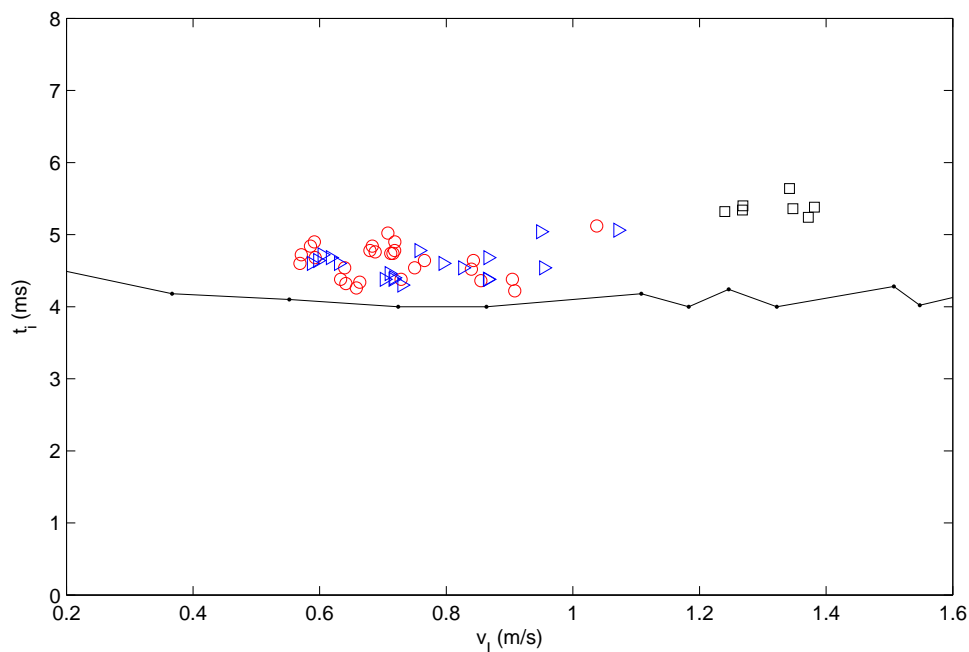


Figure 4.46: Plot t_i , vs. v_I for the In-Water longitudinal acrylic tests. $h_2 = 13.3$ cm (red \circ), $h_2 = 20.9$ cm (blue \triangleright), $h_2 = 30.1$ cm (black \square). Measured t_i from In-Air test ($-$).

4.3.2.5 Normalized Impact Force vs. Froude Number

Fr , Froude number, and F_N were determined by using the same method as section 4.3.1.5. Fig. 4.47 plots F_N against Fr . The range of Fr observed in the In-Water longitudinal acrylic test was $0.44 < Fr < 0.85$. Overall, the behavior did not differ much from the comparison of F_N to impact velocity (Fig. 4.44).

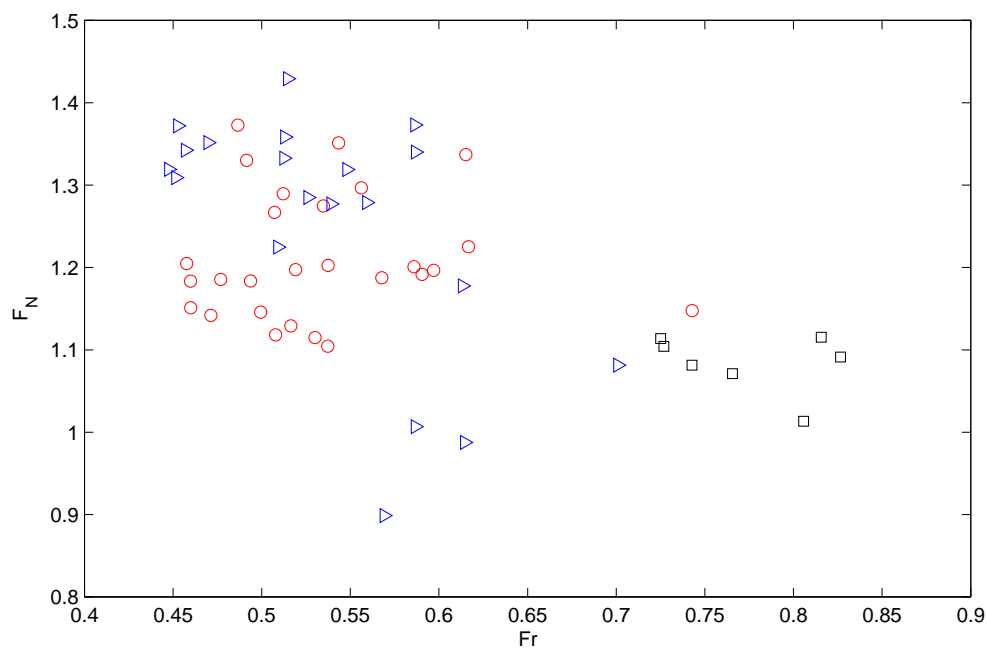


Figure 4.47: Plot of F_N vs. Fr for the In-Water longitudinal acrylic tests. $h_2 = 13.3$ cm (red \circ), $h_2 = 20.9$ cm (blue \triangleright), $h_2 = 30.1$ cm (black \square).

4.3.2.6 Impulse

Impulse values J_p and J_{30} were calculated using the same methods described in section 4.2.5 and section 4.3.1.6.

4.3.2.6.1 J_p

Fig. 4.48 shows the plot of J_p vs. v_I for the In-Water longitudinal acrylic tests compared with the In-Air longitudinal acrylic test. The J_p values relate to the v_I in a similar manner as the F_p values for the longitudinal acrylic test. The In-Water J_p were higher than their corresponding In-Air J_p .

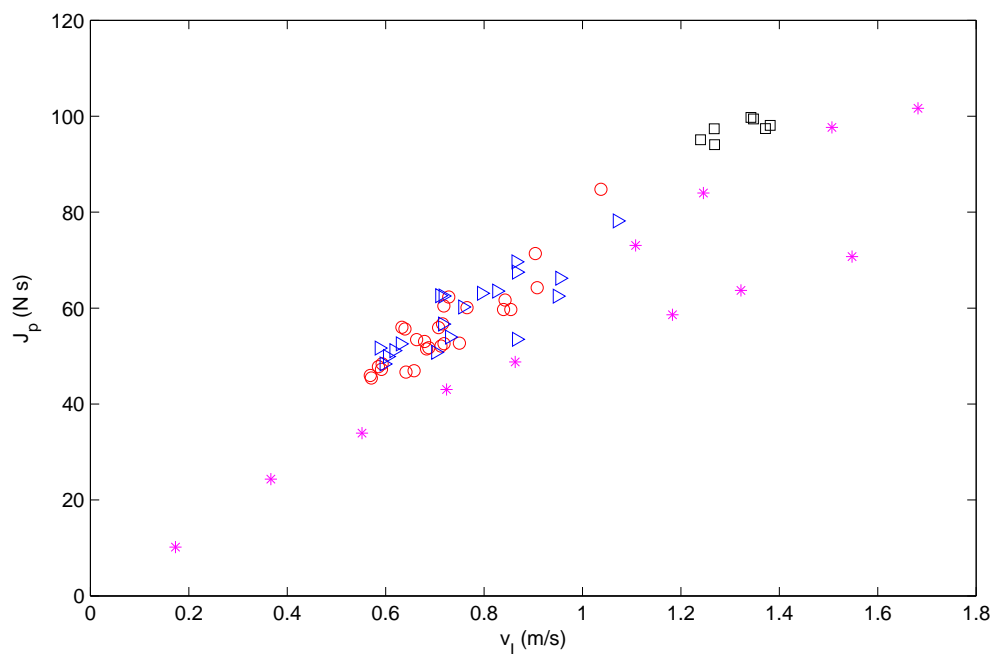


Figure 4.48: Plot of J_p vs. v_I for the In-Water longitudinal acrylic tests. $h_2 = 13.3$ cm (red \circ), $h_2 = 20.9$ cm (blue \triangleright), $h_2 = 30.1$ cm (black \square). In-Air longitudinal acrylic test (magenta $*$).

4.3.2.6.2 J_{30}

Fig. 4.49 shows the plot of J_{30} vs. v_I for the In-Water longitudinal acrylic tests compared with the In-Air longitudinal acrylic test. Since there was no nonstructural mass added for the acrylic tests, the J_{30} values relate to the v_I in a similar manner as the J_p and F_p values. The In-Water J_p were higher than their corresponding In-Air J_p .

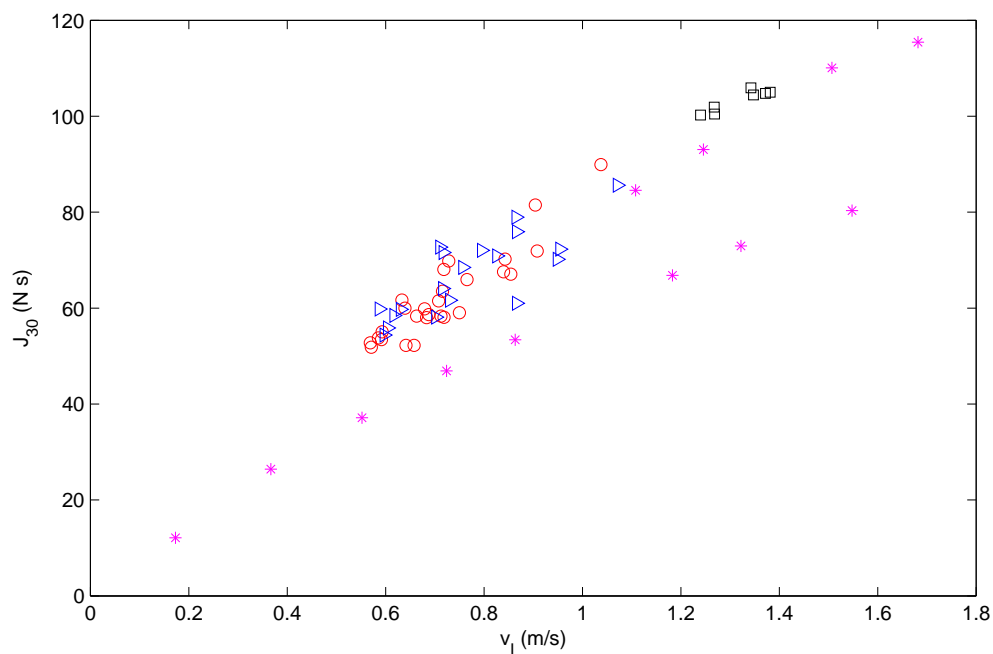


Figure 4.49: Plot of J_{30} vs. v_I for the In-Water longitudinal acrylic tests. $h_2 = 13.3$ cm (red \circ), $h_2 = 20.9$ cm (blue \triangleright), $h_2 = 30.1$ cm (black \square). In-Air longitudinal acrylic test (magenta $*$).

4.3.2.6.3 J_p vs. J_{30}

Fig. 4.50 shows the plot of J_{30} vs. J_p for the In-Water longitudinal acrylic tests. The slope of the data points, m_0 , was determined by fitting a line through the data points. m_0 was determined to be 1.12 for the longitudinal acrylic test. This value was lower than the 1.4 m_0 value determined for the In-Water longitudinal aluminum test.

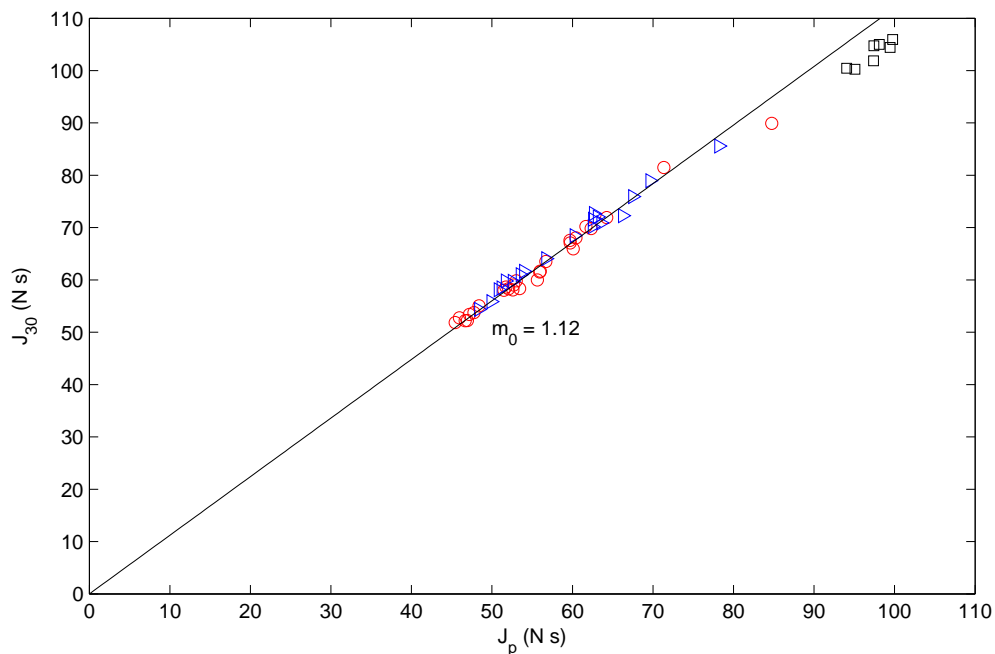


Figure 4.50: Plot of J_{30} vs. J_p for the In-Water longitudinal acrylic tests. $h_2 = 13.3$ cm (red \circ), $h_2 = 20.9$ cm (blue \triangleright), $h_2 = 30.1$ cm (black \square). Slope m_0 determined by line of best fit.

4.3.3 Transverse Aluminum

4.3.3.1 Flow Speed vs. Impact Velocity

Fig. 4.51 shows the maximum flow speeds compared with debris impact velocities for In-Water transverse aluminum tests. The debris velocities appeared to almost reach the speed of the maximum measured flow velocities.

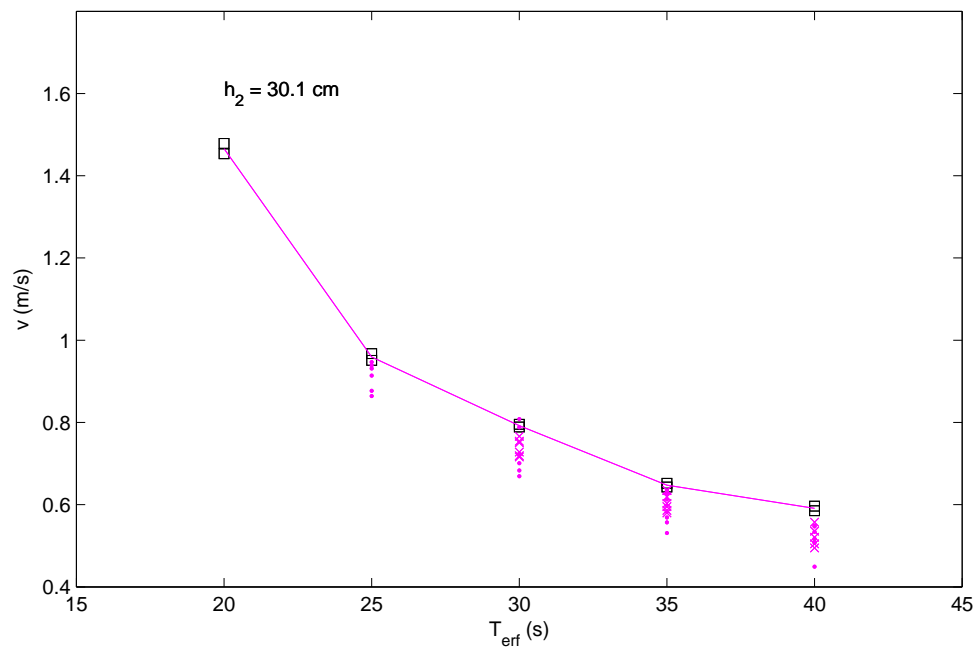


Figure 4.51: Maximum flow speeds compared with debris impact velocities for In-Water transverse aluminum tests. Flow speeds (\square). Debris impact velocities: $M_{NS} = 0$ kg (\bullet), $M_{NS} = 50.2$ kg (\times).

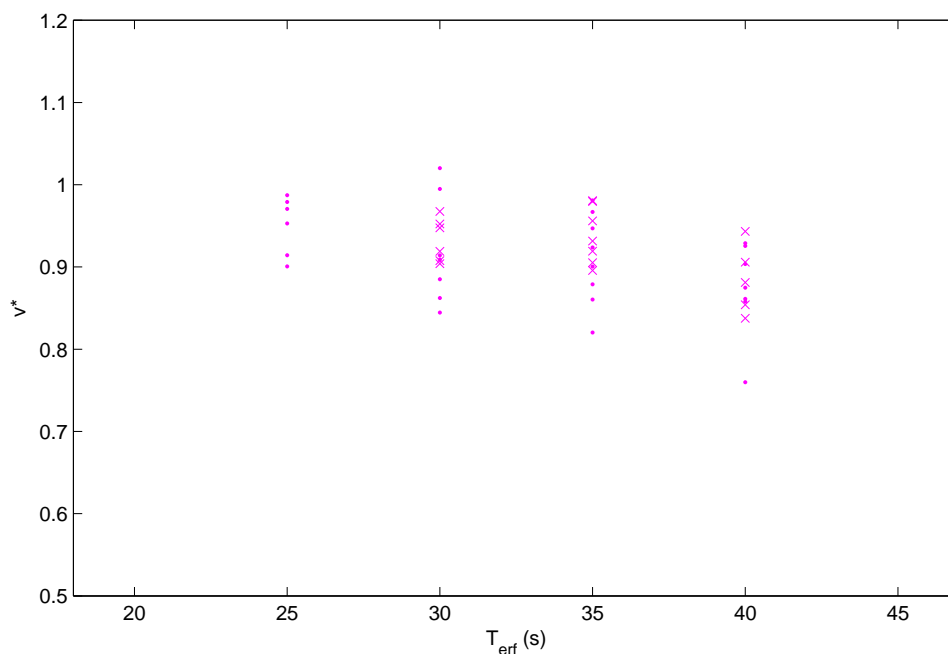


Figure 4.52: Normalized transverse aluminum debris impact velocities, v^* with respect to the average measured surface flow speeds from PIV. The impact velocities from Fig. 4.38 were divided by the flow velocity lines shown. Debris impact velocities: $M_{NS} = 0$ kg (\bullet), $M_{NS} = 50.2$ kg (\times).

Fig. 4.52 shows the normalized acrylic debris impact velocities, v^* with respect to the average measured surface flow speeds from PIV. These values ranged from 0.76 to 1.02. These results suggested that the debris was moving in the range of 70% to 100% of the water velocity.

4.3.3.2 Impact Force Time History comparison

4.3.3.2.1 Comparison to In-Air Impact Force

Fig. 4.53 shows the average impact force time history for In-Water transverse aluminum test with $v_I = 0.59$ m/s, determined from 5 time histories. This plot highlights the variability witnessed in the In-Water transverse aluminum tests. In many cases, the impact duration

was highly variable; suggesting different types of impacts were made.

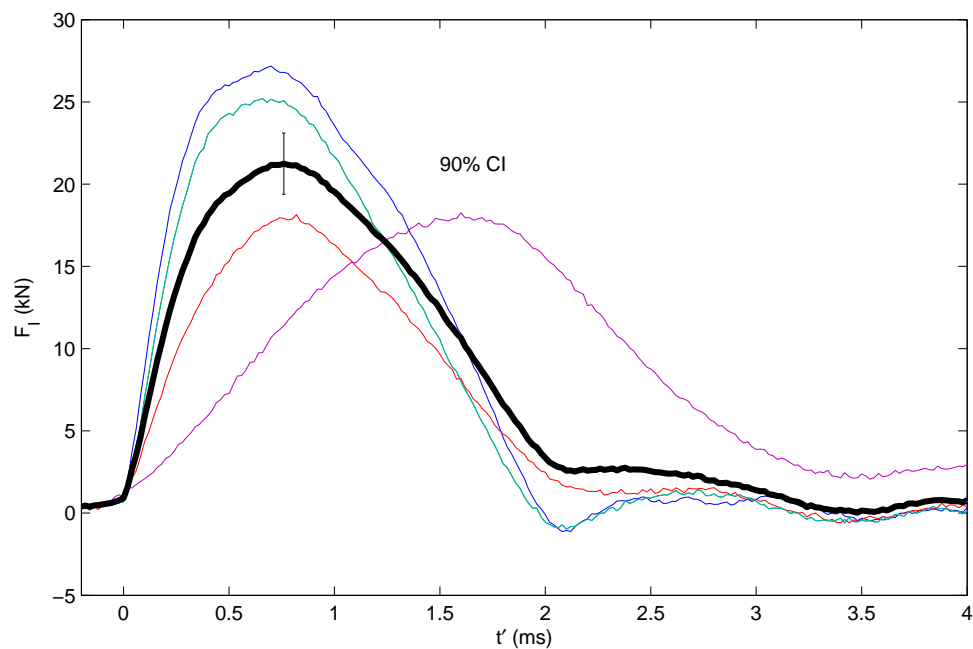


Figure 4.53: Average impact force time history for In-Water transverse aluminum test with $v_I = 0.59$ m/s. Determined from 5 time histories, 90% confidence interval for peak force shown. Thick black line represents averaged impact force time history.

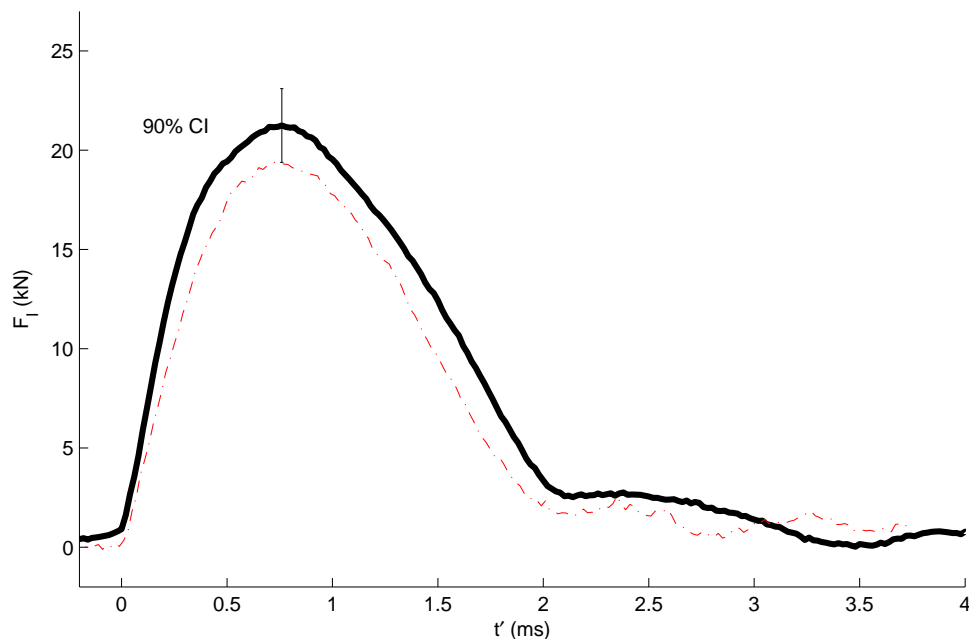


Figure 4.54: Average impact force time history for In-Water transverse aluminum test with $v_I = 0.59$ m/s compared with In-Air transverse aluminum test at approximately the same impact velocity. Dashed line represents In-Air impact force impact history. 90% confidence interval for peak In-Water force shown.

Fig. 4.54 shows the average impact force time history for In-Water transverse aluminum test with $v_I = 0.59$ m/s compared with In-Air transverse aluminum test at approximately the same impact velocity. The average force time history for the In-Water test followed a similar shape as the observed time history from the In-Air test. The peak force of the In-Water test appeared to be greater, however the In-Air test fell within the bottom bound of the 90% confidence interval of the In-Water peak force.

4.3.3.2.2 Comparison of Nonstructural Masses

Fig. 4.55 and Fig. 4.56 shows the difference between impact force time histories for different M_{NS} observed in the In-Water transverse aluminum test. Additional impact force is observed after the initial peak with the addition of nonstructural mass. This observation

was consistent with observations made in the In-Water longitudinal aluminum test.

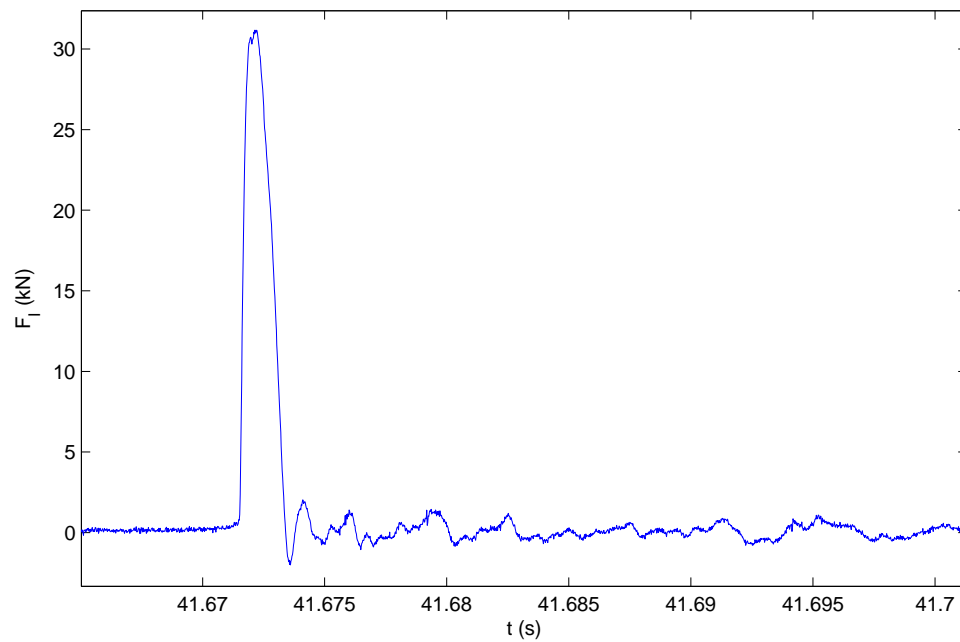


Figure 4.55: Impact force time history for In-Water transverse aluminum test trial 16 at $h_2 = 30.1$ cm with $M_{NS} = 0$ kg, $T_{erf} = 30$ s, $v_I = 0.79$ m/s.

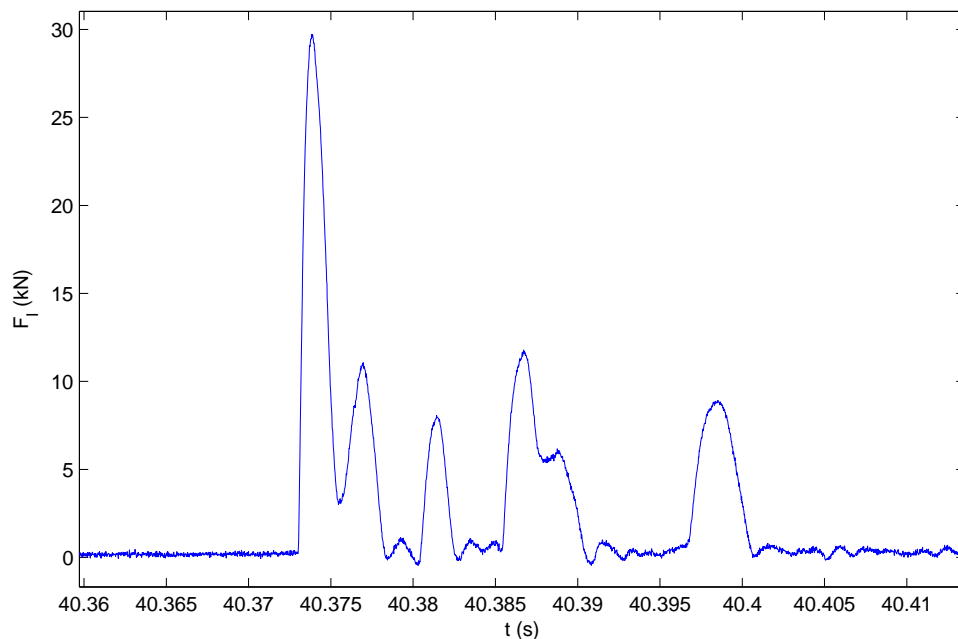


Figure 4.56: Impact force time history for In-Water transverse aluminum test trial 18 at $h_2 = 30.1$ cm with $M_{NS} = 50.2$ kg, $T_{erf} = 30$ s, $v_I = 0.75$ m/s.

4.3.3.3 Peak Force vs. Impact Velocity

4.3.3.3.1 Scatter Plot

Fig. 4.57 plotted F_p vs. v_I for the In-Water transverse tests. A large amount of scatter in the measured peak forces was observed in the transverse aluminum test. The upper envelope of these trials appeared to follow a trend similar to that observed in the longitudinal tests. The upper enveloped of measured In-Water forces appeared to have the same slope as the In-Air line, but with an offset showing increase in impact force.

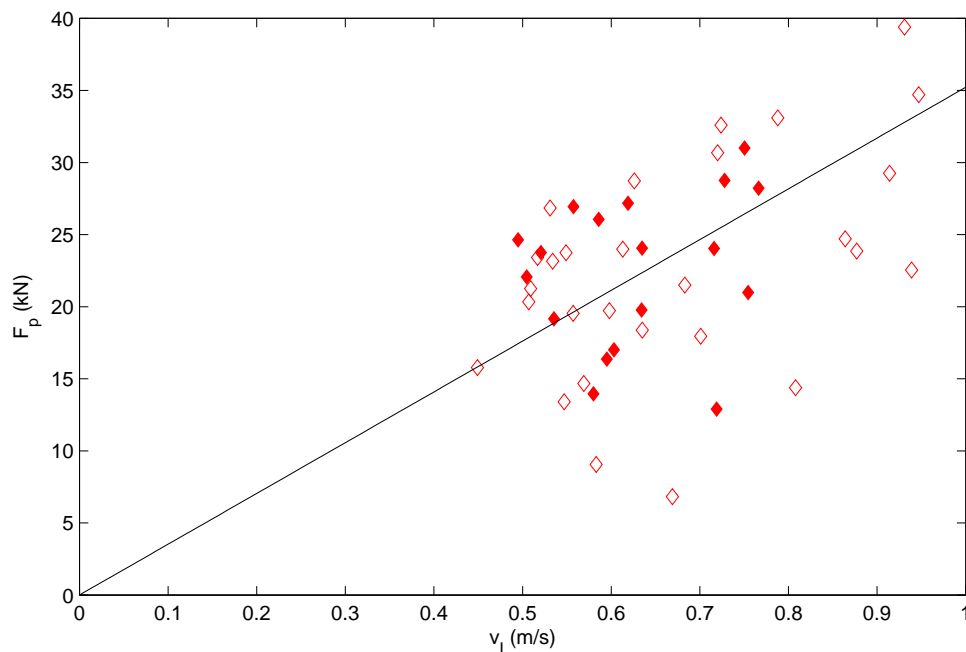


Figure 4.57: Plot of F_p vs. v_I for the In-Water transverse tests. $h_2 = 30.1$ cm, $M_{NS} = 0$ kg (\diamond), $h_2 = 30.1$ cm, $M_{NS} = 50.2$ kg (\blacklozenge). The solid black line is taken from the In-Air transverse aluminum test (Fig. 4.4).

4.3.3.3.2 Normalized by Corresponding In-Air Impact Force

Fig. 4.58 plotted the In-Water peak force normalized by empirically determined In-Air impact force, F_N , vs. v_I for the In-Water transverse aluminum tests. This plot shows the proportional increase in force associated with the hydraulics of the In-Water acrylic test. The impact forces from the In-Water longitudinal aluminum tests appeared to be, at maximum, about 35-40% greater than the corresponding In-Air transverse aluminum test values for the given range of impact velocities.

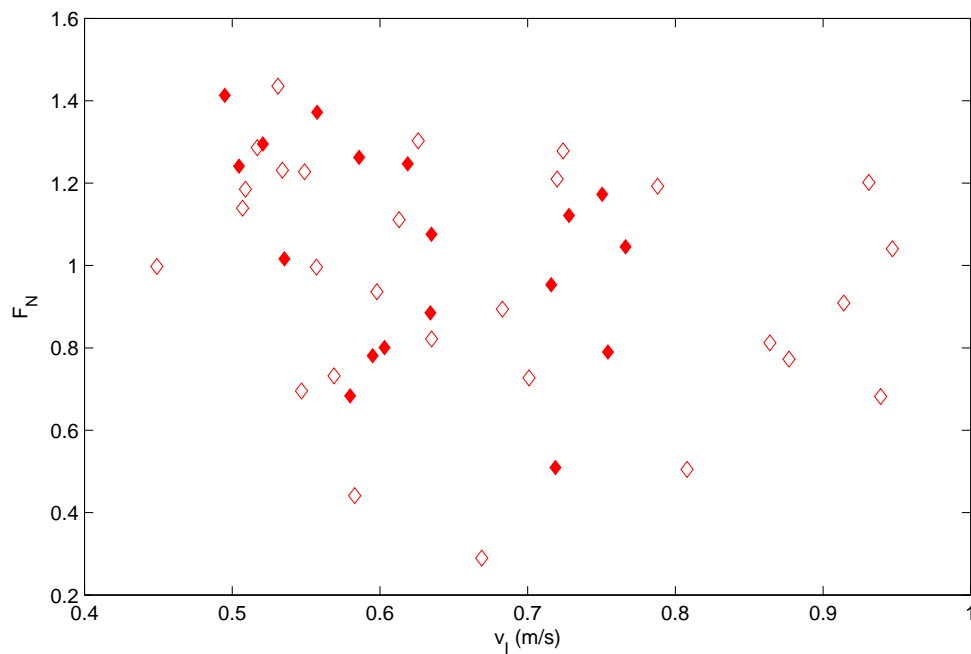


Figure 4.58: Plot of In-Water peak force normalized by empirically determined In-Air impact force, F_N , vs. v_I for the In-Water transverse aluminum tests. $h_2 = 30.1$ cm, $M_{NS} = 0$ kg (\diamond), $h_2 = 30.1$ cm, $M_{NS} = 50.2$ kg (\blacklozenge).

4.3.3.3 Incremental Difference

Fig. 4.59 shows the numerical difference between In-Water peak force and the empirically determined In-Air impact force, F_d , vs. v_I for the In-Water transverse aluminum tests. This plot shows a maximum increase of 8 kN from the In-Air impact force to the corresponding In-Water impact force.

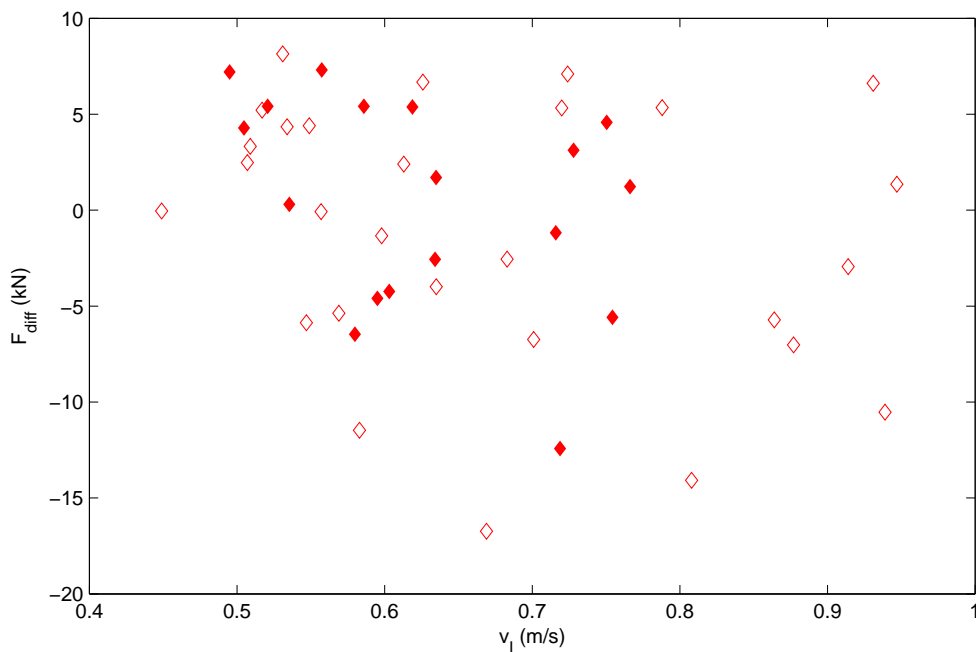


Figure 4.59: Plot of the numerical difference between In-Water peak force and the empirically determined In-Air impact force, F_d , vs. v_I for the In-Water transverse aluminum tests. $h_2 = 30.1$ cm, $M_{NS} = 0$ kg (\diamond), $h_2 = 30.1$ cm, $M_{NS} = 50.2$ kg (\blacklozenge).

4.3.3.4 Impact Duration

Fig. 4.60 plotted impact duration, t_i , vs. v_I for the In-Water transverse tests. Impact durations were determined using the same method as was used for the longitudinal aluminum and acrylic tests. These results showed a lot more variability than was witnessed in the longitudinal tests. Impact durations measured from the In-Water transverse aluminum test were observed to be higher and lower than the In-Air durations. t_i was shown to change with v_I for the In-Air tests. Average impact duration calculated to be 6.10 ms.

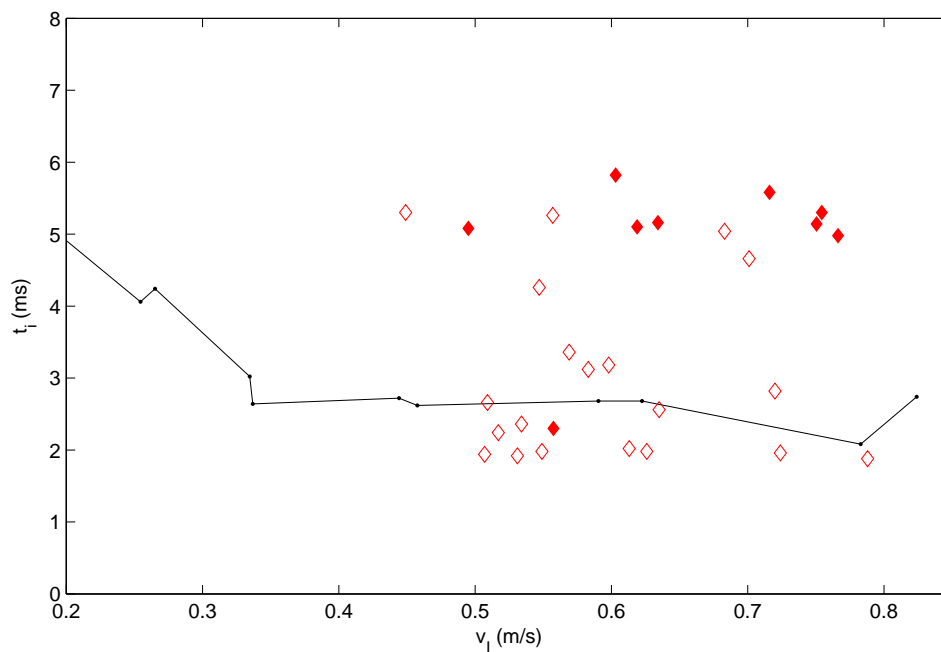


Figure 4.60: Plot t_i , vs. v_I for the In-Water transverse aluminum tests. $h_2 = 30.1$ cm, $M_{NS} = 0$ kg (\diamond). $h_2 = 30.1$ cm, $M_{NS} = 50.2$ kg (\blacklozenge). Measured t_i from In-Air test ($-$).

4.3.3.5 Normalized Impact Force vs. Froude Number

Fr , Froude number, and F_N were determined by using the same method as section 4.3.1.5. Fig. 4.61 plots F_N against Fr . The range of Fr observed in the In-Water transverse test was $0.35 < Fr < 0.60$. Overall, the behavior did not differ much from the comparison of F_N to impact velocity (Fig. 4.59).

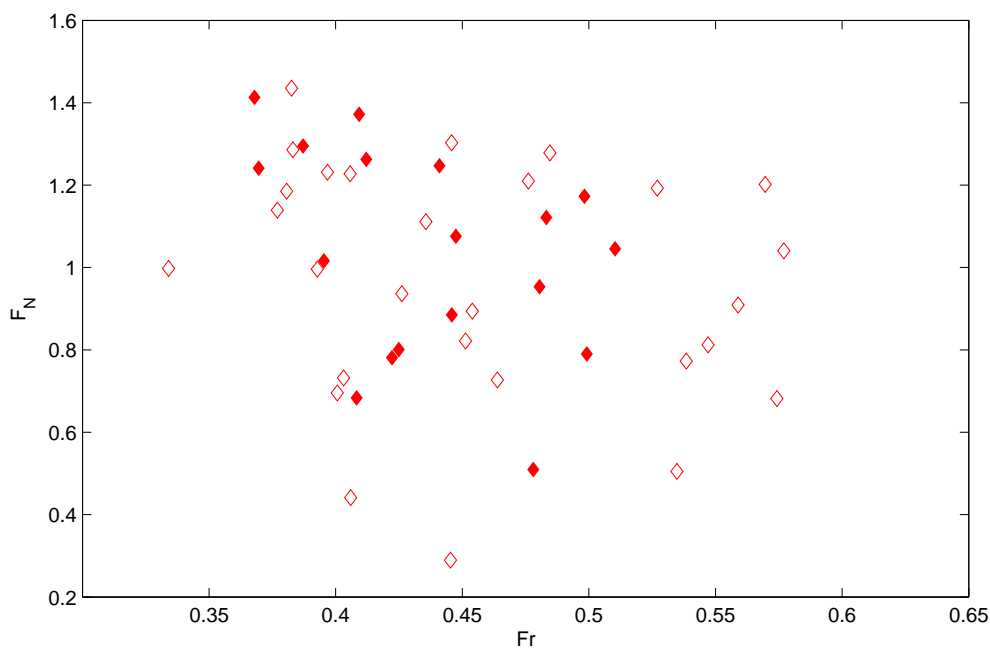


Figure 4.61: Plot of F_N vs. Fr for the In-Water transverse aluminum tests. $h_2 = 30.1$ cm, $M_{NS} = 0$ kg (\diamond). $h_2 = 30.1$ cm, $M_{NS} = 50.2$ kg (\blacklozenge).

4.3.3.6 Impulse

Impulse values J_p and J_{30} were calculated using the same methods described in section 4.2.5, section 4.3.1.6, and section 4.3.2.6.

4.3.3.6.1 J_p

Fig. 4.62 shows the plot of J_p vs. v_I for the In-Water transverse aluminum tests compared with the In-Air transverse aluminum test. The J_p values were observed to have a large amount of scatter similar to what was observed for the F_p vs. v_I relationship. In Fig. 4.62 the In-Water J_p values were observed to be consistently higher than the In-Air J_p values. Additionally, no effect of nonstructural mass was observed.

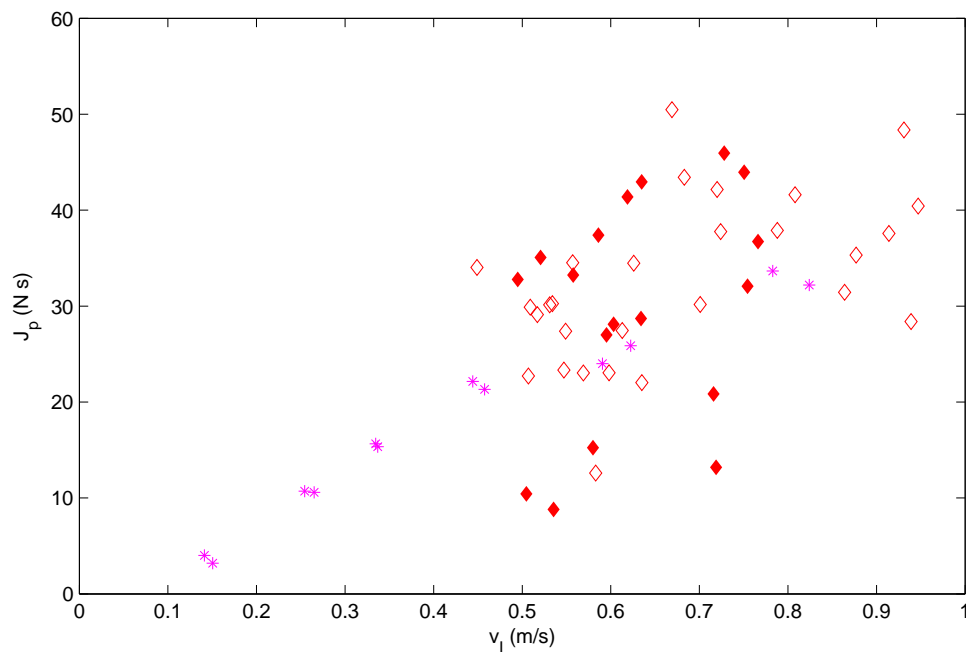


Figure 4.62: Plot of J_p vs. v_I for the In-Water transverse aluminum tests. $h_2 = 30.1$ cm, $M_{NS} = 0$ kg (\diamond). $h_2 = 30.1$ cm, $M_{NS} = 50.2$ kg (\blacklozenge). In-Air transverse aluminum test (magenta *).

4.3.3.6.2 J_{30}

Fig. 4.63 shows the plot of J_{30} vs. v_I for the In-Water transverse aluminum tests compared with the In-Air transverse aluminum test. The J_{30} values were observed to have a large amount of scatter similar to what was observed for the J_p vs. v_I relationship. In Fig. 4.63 the In-Water J_{30} values were observed to be consistently higher than the In-Air J_{30} values. J_{30} values were higher for the $M_{NS} = 50.2$ kg than for the $M_{NS} = 0$ case consistently.

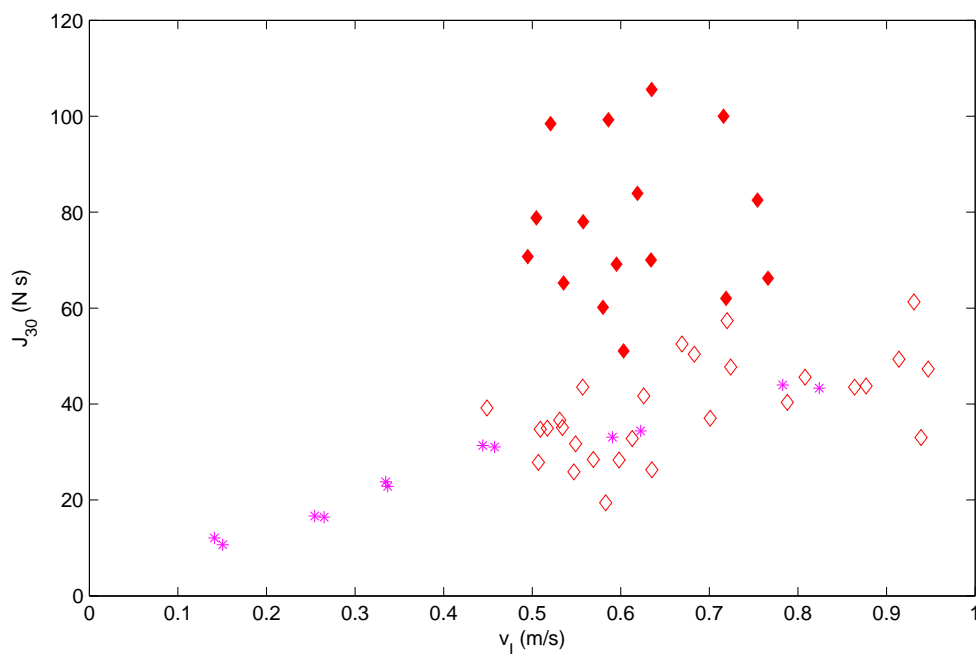


Figure 4.63: Plot of J_{30} vs. v_I for the In-Water transverse aluminum tests. $h_2 = 30.1$ cm, $M_{NS} = 0$ kg (\diamond). $h_2 = 30.1$ cm, $M_{NS} = 50.2$ kg (\blacklozenge). In-Air transverse aluminum test (magenta *).

4.3.3.6.3 J_p vs. J_{30}

Fig. 4.64 shows the plot of J_{30} vs. J_p for the In-Water transverse aluminum tests. The slope of the $M_{NS} = 0$ data points, m_0 , was determined by fitting a line through the data points. m_0 was determined to be 1.2 for the transverse aluminum test. This value was lower than the 1.4 m_0 value determined for the In-Water longitudinal aluminum test but higher than the 1.12 m_0 value determined for the In-Water longitudinal acrylic test. Line fitting was not performed for the $M_{NS} = 50.2$ kg data points due to the scatter observed.

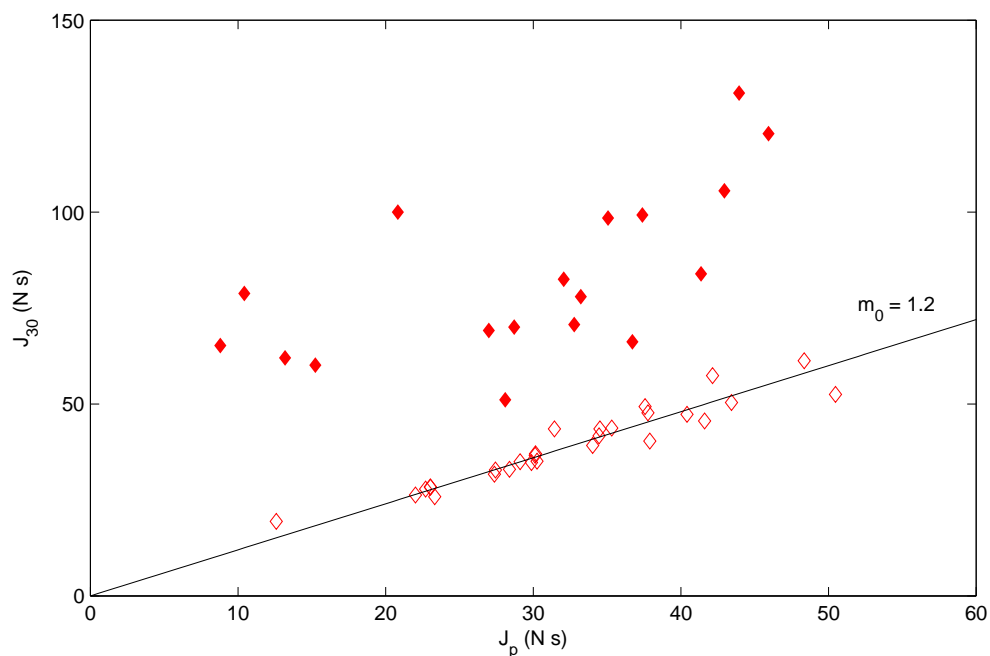


Figure 4.64: Plot of J_{30} vs. J_p for the In-Water transverse aluminum tests. $h_2 = 30.1$ cm, $M_{NS} = 0$ kg (\diamond). $h_2 = 30.1$ cm, $M_{NS} = 50.2$ kg (\blacklozenge).

4.3.4 Unconstrained Aluminum

4.3.4.1 Impact Angle Histogram

Fig. 4.65 shows the PDF histogram for change in debris orientation, θ_d , for all 31 Unconstrained aluminum trials. The majority of the trials exhibited little to no change in orientation. The vast majority of the trials fell in the $\theta_d < 5^\circ$ range. This suggested that rotation was not a concern for the debris specimen under the flow conditions simulated in the LWF.

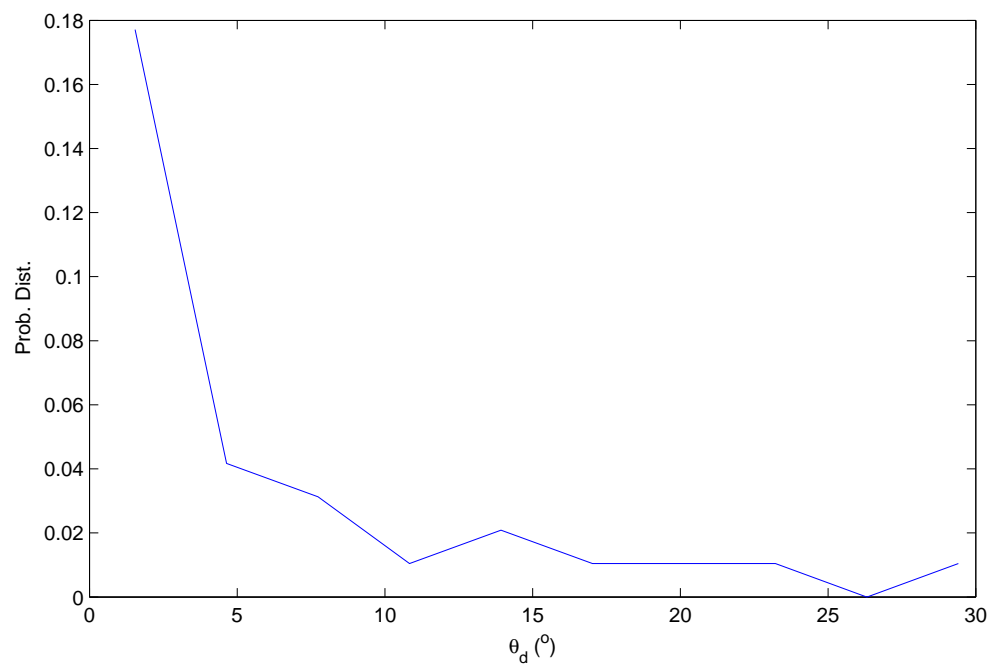


Figure 4.65: PDF histogram for change in debris orientation, θ_d , for all 31 Unconstrained aluminum trials.

4.3.4.2 Impact Angle Histogram Separated by Initial Orientation

Fig. 4.66 suggested that the results shown in Fig. 4.65 were largely dominated by the measurements obtained with $\theta_i = 0^\circ$. The other initial orientations appear to lack the sufficient number of measurements to generate useful histogram PDFs.

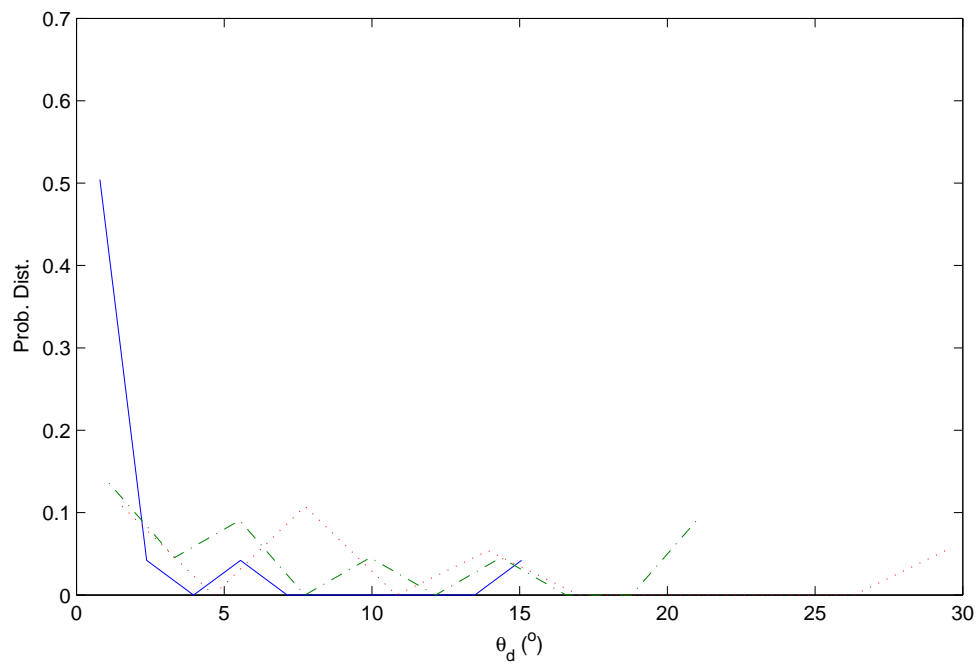


Figure 4.66: PDF histogram for change in debris orientation, θ_d , separated by initial orientation, θ_i . $\theta_i = 0^\circ$ (blue —), $\theta_i = 90^\circ$ (green - - -), $45^\circ \leq \theta_i \leq 71^\circ$ (red \cdots).

Chapter 5: Discussion

5.1 Hydrodynamics Test

5.1.1 Idealized Inundation Flow

One of the limiting factors for this study was the need to produce idealized inundation flow. This was flow defined as a strong current and not a turbulent bore. The method we used to obtain these conditions was the aforementioned error function wave paddle displacements. These error functions used the full 4 meter stroke of the wave paddle to maximize the duration of inundation. As shown in Fig. 3.36, at short T_{erf} , the free surface profile shows a steep peak. The peak shown represented an unbroken wave propagating through the test section. At lower T_{erf} , the wave broke before it reached the debris specimen with the end result being an unrealistic representation of idealized inundation flow. Due to these limitations, the impact velocity range for the debris specimen was 0.6 - 1.4 m/s. Froude number similarity resulted in this corresponding to a full scale velocity of 1.3 - 3.1 m/s (3 - 7 mph).

PIV analysis from video footage taken of the 2004 Indian Ocean Tsunami in Banda Aceh, Indonesia suggested that maximum flow speeds of floating debris were 5 m/s (Prasetya et al., 2008). This was consistent with the calculation of maximum flow rates made by Matsutomi et al. (2006) of 5.2 m/s. This suggested that our velocity range was lower than the maximum tsunami inundation flow velocity referenced in literature.

There a number of possible solutions to obtain higher flow velocities that could be implemented in future studies. The problem was generating fast enough flows that still satisfied idealized inundation criteria. Thus we needed long waves that were capable of generating strong currents without becoming too steep. For future studies, it could be pertinent to investigate whether the bathymetry setup could aid in producing more desirable flow rates. Additionally, other methods of generating inundation flow, aside from the error function wave paddle displacement, could also be investigated for their capability to produce ideal flow conditions.

5.1.2 Surface PIV

This study utilized a PIV method to track surface flow velocities. Particle image velocimetry is a common flow visualization technique that involves tracking seeded particles illuminated in the fluid. Typically PIV involves illuminated seeded particles in a dark environment using a strobe or laser. The PIV utilized in this study was capable of operating in less controlled environments. PIV operates on sequences of particle images. To utilize PIV analysis one simply requires a method to produce particle images.

The technique used to produce particle images in this study utilized the same concept as the color based object tracking. By using brightness thresholds and proper seeding materials, video frames could easily be converted to black and white images. These images serve the same function as particle images essentially as white particles moving over a black background. Using these simple video editing techniques, PIV analysis can be used in a wider range of situations.

Overall, the PIV technique used in this study proved to be effective and versatile and should be considered for future studies.

5.2 In-Air Test

5.2.1 Peak Impact Force vs. Impact Velocity

For the longitudinal aluminum, longitudinal acrylic, and transverse aluminum cases, the peak impact forces increased linearly with increasing impact velocity. This was consistent with the full scale in-air experiments conducted by Piran Aghl et al. (2013). Additionally, the longitudinal aluminum impact forces were greater than that of the transverse aluminum tests. This is consistent with observations made by Haehnel and Daly (2004) in that the maximum force was experienced when the contact was along the debris specimen's major axis.

5.2.2 Load Cells

Load cells were an integral aspect to the success of the project. Impact force data were sampled at 50 kHz. As shown throughout this study, the 50 kHz sampling was capable of attaining high resolution plots of the impact force time histories. This was important

due to the short impact durations observed. The issue with sampling at 50 kHz was that large data files were created for each trial. Considering the volume of tests conducted, an extremely large amount of hard drive space was required to store the data. Additionally, processing the data consumed a fair amount of time. Based on the high resolution of the impact force time histories, it is likely that the sampling rate could be reduced for future studies without losing any pertinent information.

5.2.3 Contact Area Considerations

One of the main sources of variability in impact force measurements was the contact area between the debris specimen and the load cell. The sensitivity to contact area was highlighted by Eq. 2.7 and Eq. 2.8. The extended bottom plate proved to be an excellent modification to control the contact area. The effect of the extended bottom plate was observable by the difference in variability between the In-Water longitudinal and transverse tests. For future studies, the usage of the extended bottom plate should be considered.

As shown in Eq. 2.7 and Eq. 2.8, the contact area was a key variable in the equations used to estimate the maximum impact force. We were unable to measure the contact area throughout this study. The contact could only be estimated empirically from the measured data. Having the capability to measure contact area would have been very useful in determining which impact forces could be appropriately compared. Devising a method to measure contact area would be very beneficial for future studies.

5.2.4 Slope Comparison

Results for the In-Air tests were shown in section 4.2. The slope for the F_p vs. v_I relationship for the In-Air longitudinal aluminum test based on the fitted black line, m_{long} , was 48.50 kN s/m. The slope for the F_p vs. v_I relationship for the In-Air longitudinal transverse test based on the fitted black line, m_{trans} , was 35.22 kN s/m. If we define κ_{air} as:

$$\kappa_{air} = \frac{m_{trans}}{m_{long}} \quad (5.1)$$

then $\kappa_{air} = 0.73$. In section 5.3.4 it will be compared to the ratio for the In-Water slopes, κ_w .

5.2.5 Impulse vs. Impact Velocity

In contrast to the peak impact force vs. impact velocity for the In-Air tests, the impulse vs. impact velocity relationship was very similar for each test. Since the masses of the debris specimen were roughly the same for each of the tests, it made sense that the measured impulses for very close to one another.

5.2.6 Impact Duration

The equation for impulse duration, t_i , is given by ASCE 7 as (ASCE, 2010):

$$t_i = \frac{2m_d u_{max}}{F_i} \quad (5.2)$$

where u_{max} is the maximum flow velocity at the site and at depths sufficient to float the debris, m_d is the mass of the debris object, and F_i is the impact force occurring over time duration t_i .

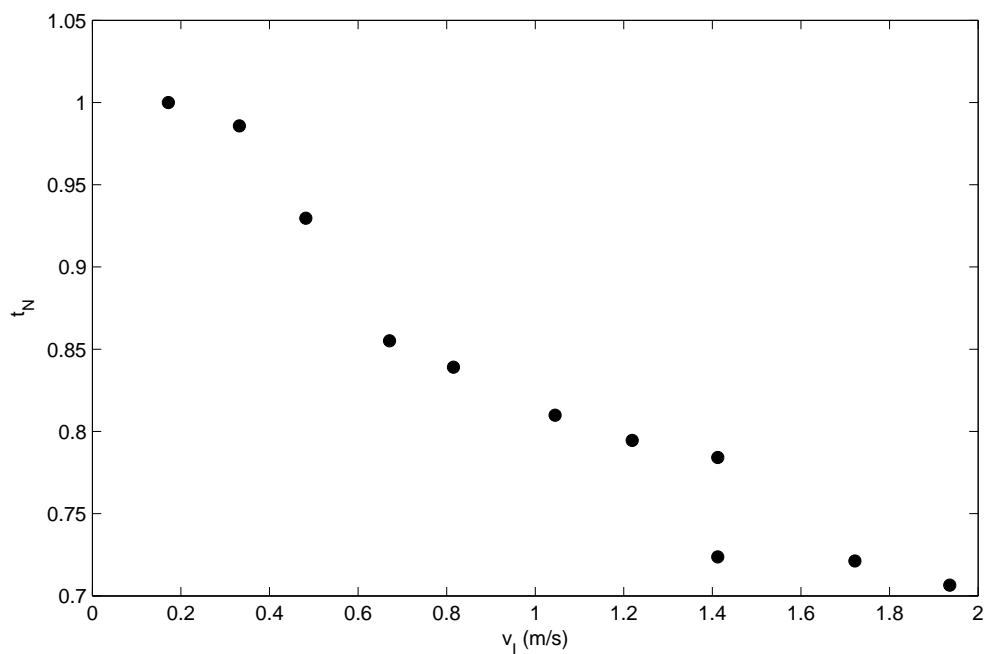


Figure 5.1: Plot of the measured impact duration normalized by the predicted value estimated by Eq. 5.2, t_N , for In-Air longitudinal aluminum test.

Fig. 5.1 shows a plot of the measured impact duration normalized by the predicted value estimated by Eq. 5.2, t_N , for In-Air longitudinal aluminum test. Measured impact durations were within 30% of the predicted value. As the impact velocity increased, the measured impact durations decreased and were lower than the predicted values.

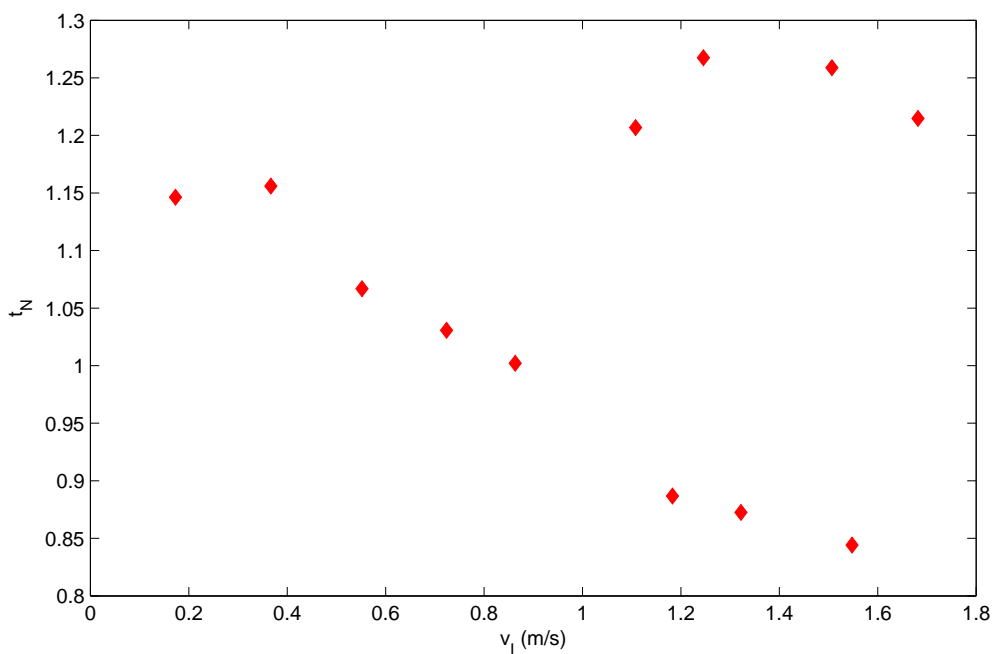


Figure 5.2: Plot of the measured impact duration normalized by the predicted value estimated by Eq. 5.2, t_N , for In-Air longitudinal acrylic test.

Fig. 5.2 shows a plot of the measured impact duration normalized by the predicted value estimated by Eq. 5.2, t_N , for In-Air longitudinal acrylic test. Measured impact durations were within 30% of the predicted value. At the higher measured impact velocities, the t_N split into high and low values. This was possibly due to some strange contacts that were occurring during the In-Air acrylic tests. The “two-banded” behavior is consistent with what was observed in the F_I vs. v_I results (see Fig. 4.3).

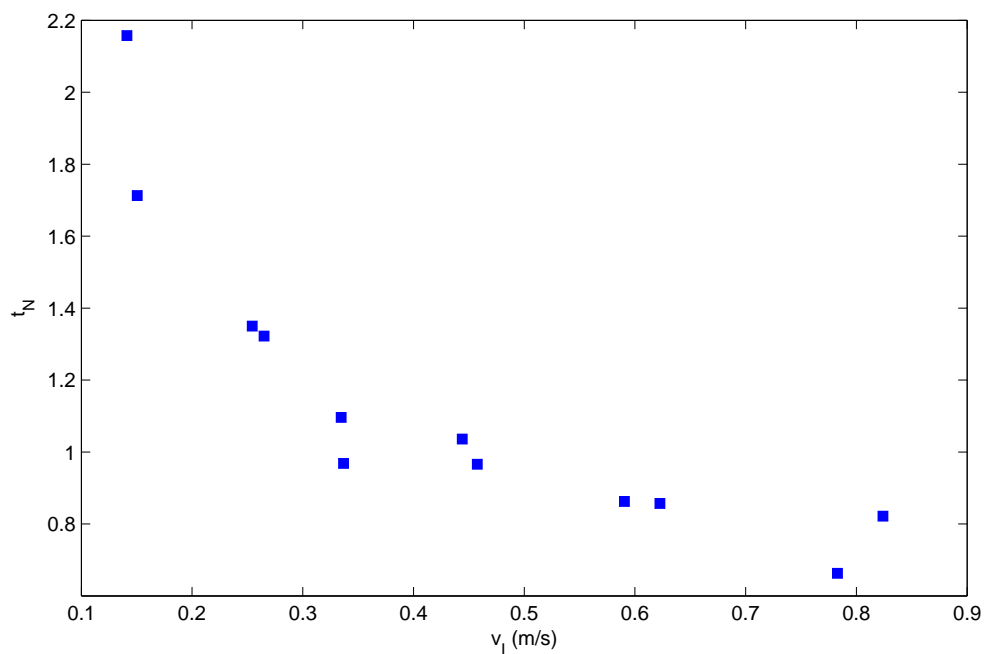


Figure 5.3: Plot of the measured impact duration normalized by the predicted value estimated by Eq. 5.2, t_N , for In-Air transverse aluminum test.

Fig. 5.3 shows a plot of the measured impact duration normalized by the predicted value estimated by Eq. 5.2, t_N , for In-Air transverse aluminum test. For velocities greater than 0.2 m/s measured impact durations were within 30% of the predicted value. As the impact velocity increased, the measured impact durations decreased and were lower than the predicted values.

Overall, it appeared that measured impact durations were within about 30% of those predicted by Eq.5.2. For each of the In-Air tests, it appeared that the relative impact duration decreased as impact velocity increased. The exceptions to this were the 4 highest data points for the In-Air acrylic test shown in Fig. 5.2. The trend of decreasing t_N to increasing velocity suggested that a different equation may have predicted the impact duration more effectively.

5.3 In-Water Test

5.3.1 Peak Impact Force vs. Impact Velocity

Overall, the results from the In-Water tests indicated that the peak contact forces increase almost linearly with increasing debris specimen velocity. The linear relationship between impact force and debris velocity agreed with results obtained through finite element analysis by Madurapperuma and Wijeyewickrema (2012). Peak impact forces from the In-Water tests appeared to be greater overall than their In-Air counterparts.

For the longitudinal aluminum case, the lower bounds of the 90% confidence interval did not exceed the peak impact forces from the In-Air tests. The upper envelope of the normalized peak impact force plot suggested a maximum 10% increase in the impact force. This corresponded to about 5 kN of additional force from the fluid.

For the longitudinal acrylic case, the In-Water peak forces were higher than their In-Air counterparts. The upper envelope of the normalized peak impact force plot suggested a maximum 35-40% increase in the impact force. This was noticeably higher than what was observed for the longitudinal aluminum tests. The 35-40% increase in impact force corresponded to an 8 kN increase in impact force.

For the transverse aluminum case, there was a large amount of scatter. The upper envelope of the peak forces followed a similar trend to what was observed in the longitudinal aluminum and longitudinal acrylic cases. The upper envelope of the normalized peak impact force plot suggested a maximum 40% increase in the impact force similar to that of the longitudinal acrylic test. This also corresponded to an increase of 8 kN in peak impact force.

While the different types of In-Water tests appeared to yield different proportional increases in peak impact force, the measured increase in force, relative to the in-air tests, in all cases was around the same range.

5.3.2 Load Cell Viability

One of the uncertainties going into this experiment was the viability of the load cell. This experiment required a load cell capable of handling dynamic impacts and handling high impact loads in addition to a high frequency response. On top of that, the load had to be waterproof. The CLC-300K load cell with applied waterproofing proved to be capable of

handling all of our needs. The load cell setup used in this experiment should be considered for future in-water impact experiments.

5.3.3 Impact Force Variability

Throughout this study, variability in the impact force measurements has been a recurring theme. Various tests conducted using the In-Air test setup identified several sources of variability associated with the nature of impact between the debris specimen and the load cell. Typically, variability arose from “poor” contacts that could be either due to contact position on the load cell or pitch angle. Every poor contact situation resulted in a lower measured impact force. Thus, it might be reasonable to consider that the highest impact force measurements represent the true impact forces for the In-Water tests.

5.3.4 Nonstructural Mass Effect

Three different amounts of nonstructural mass were used during these experiments. These values aimed to double and triple the mass of the debris specimen. In each case, the addition of nonstructural mass did not appear to alter the measurement of the peak impact force. The addition of nonstructural mass was observed to slightly increase the impact duration of the primary peak of force time history. Additional impacts were observed after the initial peak impact, but the magnitudes of the additional impacts were lower than the initial.

The additional impacts that occurred after the primary peak were taken into account with the impulse measurements. As shown by the J_{30} measurements from the In-Water longitudinal aluminum test, the addition of nonstructural mass significantly increased the impulse of the collision. Fig. ?? showed that increasing nonstructural mass increased the measured impulse in a 1:1 ratio relative to the structural mass of the debris specimen. This best described the effect of nonstructural mass on the collision.

Nonstructural mass was intended to represent cargo on a standard shipping container. Based on the experiments conducted in this study, we recommend that the nonstructural mass does not have to be taken into account when designing for peak forces. Nonstructural mass, however, could be accounted for if using other design criteria.

5.3.5 Slope Comparison

In this section we compared the slope ratio from the In-Air tests, κ_{air} , to the slope ratio from the In-Water tests, κ_w . The idea was that fluid effects would be amplified on the greater surface area exposed to the moving fluid associated with the transverse orientation. Thus, we expected $\kappa_w > \kappa_{air}$. Based on the impact force measurement variability discussed in section 5.3.2, we assumed that the only true impact forces are the highest measured cases. Thus, we based the best fit lines on the upper envelopes of the scatter plots.

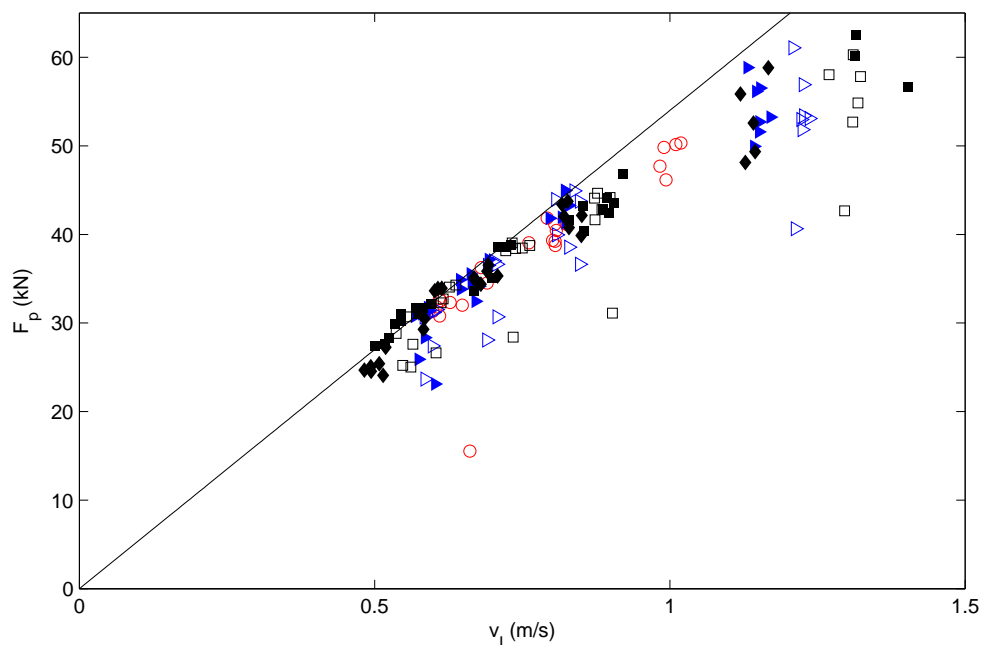


Figure 5.4: Scatter Plot of F_p vs. v_I for the In-Water longitudinal aluminum tests with line fitted to upper envelope of impact force measurements. Line fitting performed by eye, slope of the line is 54 kN s/m. $h_2 = 13.3$ cm, $M_{NS} = 0$ kg (red \circ). $h_2 = 20.9$ cm, $M_{NS} = 0$ kg (blue \triangleright). $h_2 = 20.9$ cm, $M_{NS} = 99.4$ kg (blue \triangleleft). $h_2 = 30.1$ cm, $M_{NS} = 0$ kg (black \square). $h_2 = 30.1$ cm, $M_{NS} = 50.2$ kg (black \blacksquare). $h_2 = 30.1$ cm, $M_{NS} = 99.4$ kg (black \blacklozenge).

Fig. 5.4 shows a line fitting on the upper envelope of the scatter plot of F_p vs. v_I for the In-Water longitudinal aluminum tests. The line fitting was performed by eye and has a slope of 54 kN s/m.

Fig. 5.5 shows a line fitting on the upper envelope of the scatter plot of F_p vs. v_I for the In-Water transverse aluminum tests. The line fitting was performed by eye and has a slope of 45 kN s/m.

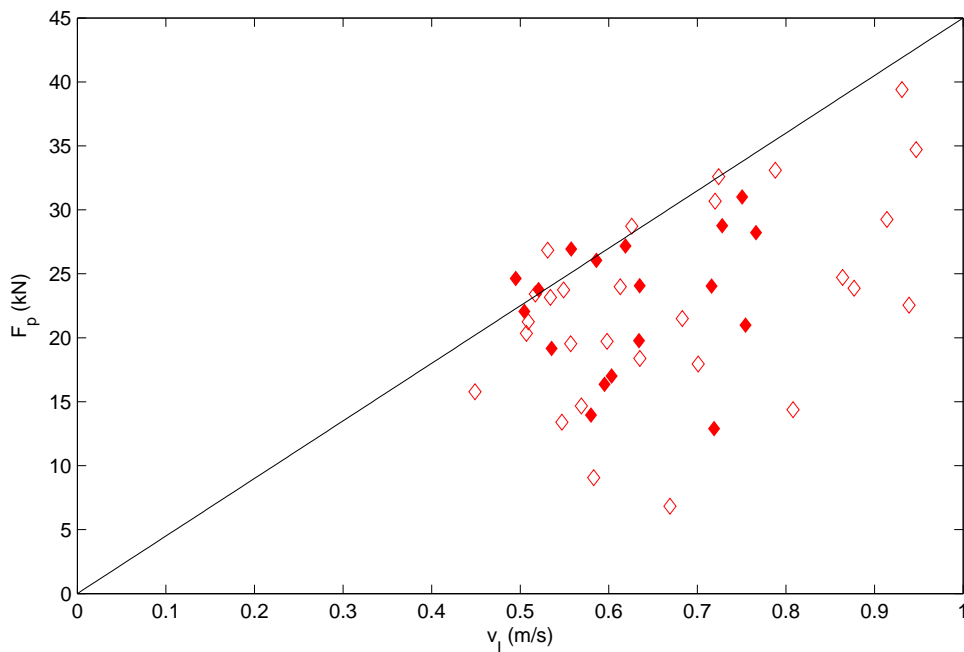


Figure 5.5: Scatter Plot of F_p vs. v_I for the In-Water transverse aluminum tests with line fitted to upper envelope of impact force measurements. Line fitting performed by eye, slope of the line is 45 kN s/m. $h_2 = 30.1$ cm, $M_{NS} = 0$ kg (\diamond), $h_2 = 30.1$ cm, $M_{NS} = 50.2$ kg (\blacklozenge).

Recall that $\kappa_{air} = 0.73$ (see section 5.2.3). κ_w can be calculated using the slopes determined from the fitted lines in Fig. 5.4 and Fig. 5.5. In this case, $\kappa_w = \frac{45 \text{ kNs/m}}{54 \text{ kNs/m}} = 0.83$. This comparison showed that, for our experimental data set, $\kappa_w > \kappa_{air}$. This suggested that there is some fluid effect that would appear to be increasing the impact force.

Fig. 5.6 shows the combined F_p vs. v_I scatter plot for the In-Water and In-Air transverse and longitudinal aluminum tests. This plot emphasized the difference observed between the In-Air and In-Water tests. As discussed in this section, the comparison between the slopes for the transverse and longitudinal tests suggested that the water had some effect

on the measured impact forces.

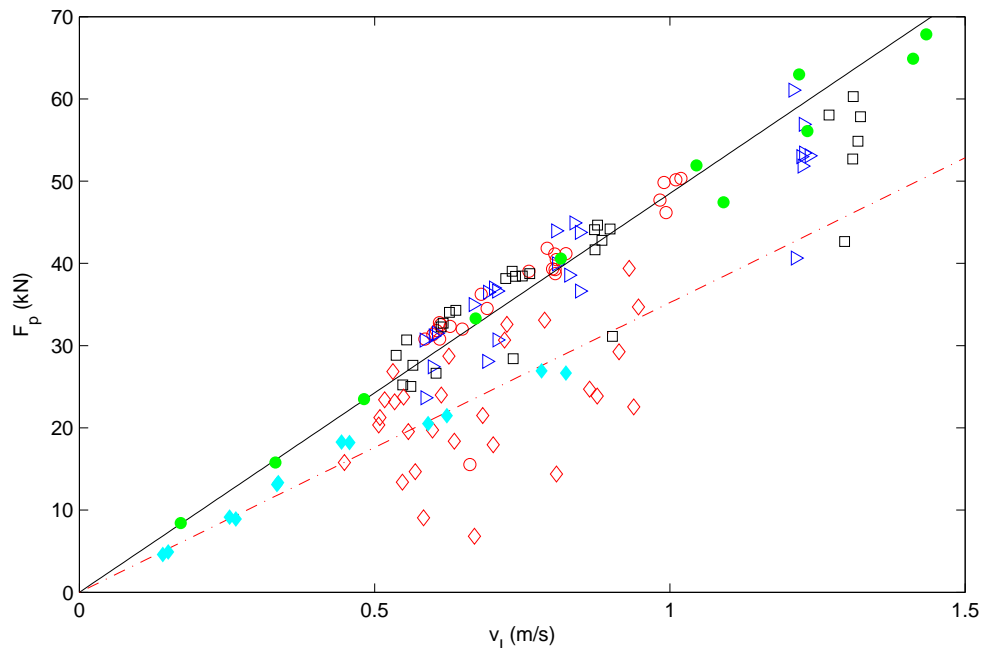


Figure 5.6: Combined scatter plot of F_p vs. v_I for the In-Water and In-Air aluminum tests without nonstructural mass. In-Water longitudinal: $h_2 = 13.3$ cm (red \circ), $h_2 = 20.9$ cm (blue \triangleright), $h_2 = 30.1$ cm (black \square). In-Water Transverse: $h_2 = 30.1$ cm (\diamond). In-Air longitudinal (green \bullet black $-$), In-Air transverse (cyan \blacklozenge and red $- -$).

5.3.6 Impact Duration

The average impact durations for the different In-Water tests were measured to be 2.36 ms, 4.87 ms, and 6.10 ms for the longitudinal aluminum, longitudinal acrylic, and transverse aluminum tests respectively. The values observed in these sets of tests were much lower than the ASCE 7 (ASCE, 2006) recommended impact duration value of 30 ms. Impact durations observed in this study were more consistent with the 7.5 ms and 1.4 ms observed by Nouri et al. (2010) and Madurapperuma and Wijeyewickrema (2012) respectively.

Following the same method as section 5.2.5, the measured impact durations from the In-Water tests were normalized by their associated estimated impact durations calculated

by Eq. 5.2.

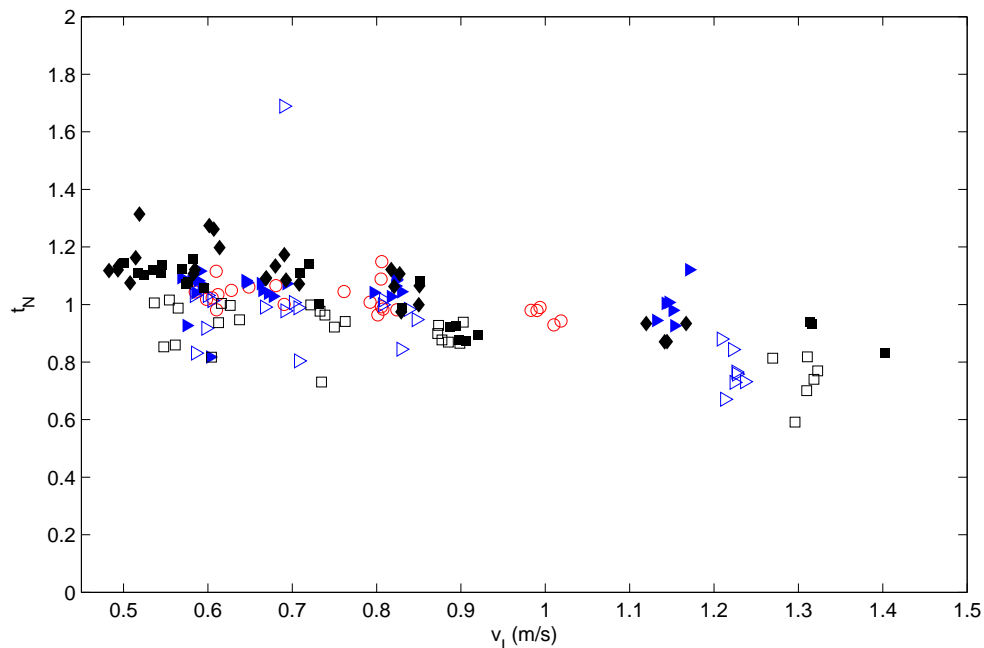


Figure 5.7: Plot of the measured impact duration normalized by the predicted value estimated by Eq. 5.2, t_N , for In-Water longitudinal aluminum test. $h_2 = 13.3$ cm, $M_{NS} = 0$ kg (red \circ). $h_2 = 20.9$ cm, $M_{NS} = 0$ kg (blue \triangleright). $h_2 = 20.9$ cm, $M_{NS} = 99.4$ kg (blue \triangleleft). $h_2 = 30.1$ cm, $M_{NS} = 0$ kg (black \square). $h_2 = 30.1$ cm, $M_{NS} = 50.2$ kg (black \blacksquare). $h_2 = 30.1$ cm, $M_{NS} = 99.4$ kg (black \blacklozenge).

Fig. 5.7 shows the plot of the measured impact duration normalized by the predicted value estimated by Eq. 5.2, t_N , for In-Water longitudinal aluminum test. According to the results Eq. 5.2 was able to reasonably predict the impact durations for the In-Water longitudinal aluminum test. Excluding the outliers, measured impact durations were within 30% of the predicted value.

Fig. 5.8 shows the plot of the measured impact duration normalized by the predicted value estimated by Eq. 5.2, t_N , for In-Water longitudinal acrylic test. In this case, Eq. 5.2 underestimated the impact durations for the In-Water longitudinal acrylic test. Overall, the measured impact durations were 40 - 60% greater than the estimated.

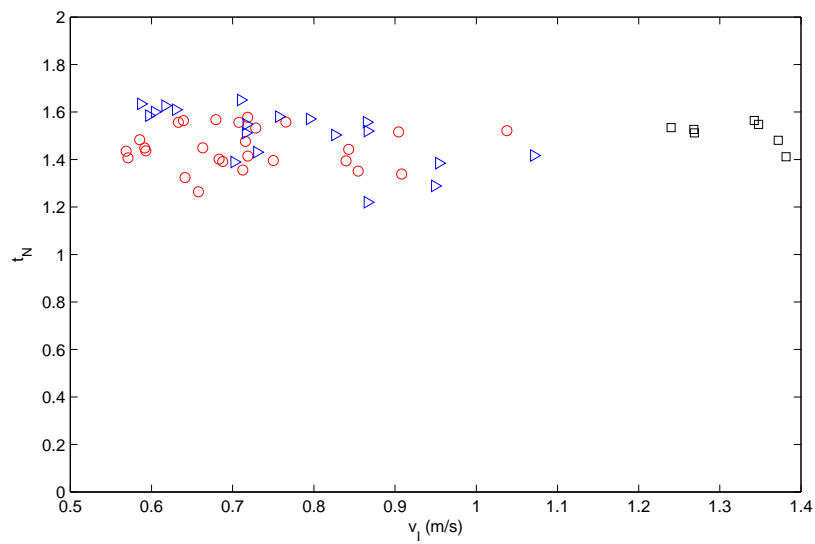


Figure 5.8: Plot of the measured impact duration normalized by the predicted value estimated by Eq. 5.2, t_N , for In-Water longitudinal acrylic test. $h_2 = 13.3$ cm (red \circ), $h_2 = 20.9$ cm (blue \triangleright), $h_2 = 30.1$ cm (black \square).

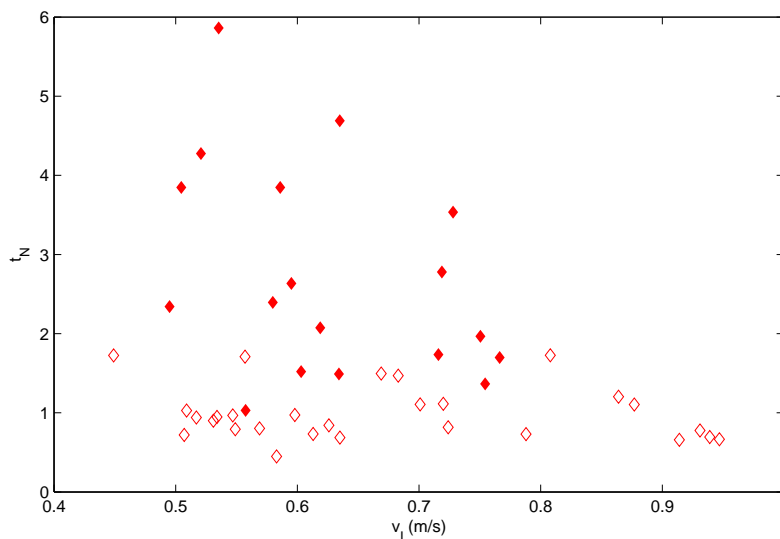


Figure 5.9: Plot of the measured impact duration normalized by the predicted value estimated by Eq. 5.2, t_N , for In-Water transverse aluminum test. $M_{NS} = 0$ kg (\diamond) $M_{NS} = 50.2$ kg (\blacklozenge).

Fig. 5.9 shows the plot of the measured impact duration normalized by the predicted value estimated by Eq. 5.2, t_N , for In-Water transverse aluminum. These results had a lot more variability. Overall, it appeared that Eq. 5.2 was able to reasonably predict the lower envelope of the impact force measurements. Most of the lower impact durations were measured for the

Overall, Eq. 5.2 was only able to reasonably predict the impact duration for the In-Water longitudinal aluminum test. In the other cases, the impact duration was underestimated. It is likely from the trends and variability witnessed, that impact duration cannot solely be predicted on the variables used in Eq. 5.2.

5.3.7 The “Added Mass” Effect

The term “added mass” has been used to reference the fluid effect on the impact force from flow-driven debris (FEMA, 2006, FEMA, 2008, Haehnel and Daly, 2004, Sarpkaya and Isaacson, 1981). This effect was introduced into design standards by using a coefficient in predictive equations (see Eq. 2.2 and Eq. 2.4). While evidence from these tests conducted

in this study suggest that it may be prudent to introduce a coefficient, it would be incorrect to refer to it as an added mass coefficient.

The added mass effect is defined as the inertia added to a system because an accelerating or decelerating body must move (or deflect) some volume of surrounding fluid as it moves through it. This effect is typically observed in vibrational motions (Faltinsen, 2005). Considering that the debris impact is a transient process occurring over an extremely short period of time, it would be inappropriate to describe the fluid effect as added mass.

Instead, we propose that a simple hydraulic coefficient, C_H would be used in the form of:

$$F_i = C_H v \sqrt{KM} \quad (5.3)$$

where F_I is the maximum impact force, C_H is the hydraulic coefficient (1.1 – 1.4), v is the impact velocity, K is the stiffness, and M is the structural mass of the container. Eq. 5.3 accounts for the effect of the fluid without improperly describing the process.

Chapter 6: Conclusion

Main Conclusions:

- The slope comparison between the longitudinal and transverse tests seems to indicate that the fluid does have an effect on the measured peak impact forces, however this effect appears to not be large.
- For range of velocities tested, the 1:5 scale In-Water longitudinal aluminum test was observed to have a maximum increase in peak impact force of 10% relative to the empirical In-Air peak impact force.
- For range of velocities tested, the 1:5 scale In-Water longitudinal acrylic test was observed to have a maximum increase in peak impact force of 40% relative to the empirical In-Air peak impact force.
- For range of velocities tested, the 1:5 scale In-Water transverse aluminum test was observed to have a maximum increase in peak impact force of 35-40% relative to the empirical In-Air peak impact force.
- Fluid effect appeared to increase the impact duration of the debris-column collision for all cases tested.
- Fluid appeared to have a consistent increase in impact force in the 5 - 8 kN range for all cases tested.
- Non-structural mass appeared to have no significant effect on measured peak impact force for the In-Air and In-Water cases.
- Increase of non-structural mass appeared to increase the measured impulse at a 1:1 ratio relative to the structural mass of the debris specimen.

Other Observations:

- Non-structural mass appeared slightly increase the impact duration of the primary peak and resulted in additional impact force occurring after the initial peak impact relative to the amount of nonstructural mass.

- Measured impulses appeared to be independent of collision stiffness and were much more dependent on the total mass of the debris specimen.
- Majority of Free Hydraulic Tests showed that debris rotated less than 5° through the wave flume test section.
- Maximum impact force was observed for impact angles at 0° .
- Debris specimen moved at 70 - 100% of the maximum inundation flow velocity.
- Contact area between the debris specimen and load cell played a significant role in measured impact force.
- Extended bottom plate on scaled model shipping containers provided a consistent contact area to provide accurate force measurements.
- Sampling rate of 50 kHz was sufficient to capture the full time history of the impact force.
- Guide wires proved capable of controlling the movement of the debris during propagation through the test section.

Recommendations:

- Consider using fluid flume that simulates river flow. Constant steady flow would likely be able to produce idealized inundation flow with higher velocities than achieved in this experiment.
- Always use underwater cameras to observe impact between debris and load cell to ensure contact is solid.
- Investigation of dispersion and rotation of debris is the vital next step to advance design standards for flow-driven debris.

Bibliography

- [1] ASCE. “Minimum design loads for buildings and other structures”. Technical Report for the American Society of Civil Engineers, Report no. ASCE/SEI 7-05, 2006.
- [2] ASCE (2010). “Minimum design loads for buildings and other structures.” ASCE/SEI 7-10, American Society of Civil Engineers, 608 pp.
- [3] Braudrick, Christian A. and Grant, Gordon E. “Why do logs move in rivers?” *Water Resources Research*, 2000; Vol. 36, No. 2, Pages 571-583.
- [4] Faltinsen, Odd M. “Hydrodynamics of High-Speed Marine Vehicles.” Cambridge, NY: Cambridge University Press, 2005.
- [5] FEMA. “Coastal Construction Manual. Technical Report for the Federal Emergency Management Agency”. Report no. FEMA P-55, 2006.
- [6] FEMA. “Guidelines for design of structures for vertical evacuation from tsunamis”. Technical Report for the Federal Emergency Management Agency. Report no. FEMA P646, Washington, DC, 2008.
- [7] FEMA (2011). “Coastal Construction Manual, Volume 2.” FEMA, 400 pp.
- [8] FEMA (2012). “Guidelines for design of structures for vertical evacuation from tsunamis, second edition.” FEMA P646, Federal Emergency Management Agency, 194 pp.
- [9] Fieguth, P. and Terzopoulos, D. “Color-based tracking of heads and other mobile objects at video frame rates”. In *IEEE Conference on Computer Vision and Pattern Recognition (CVPR) 1997*: 21-27
- [10] Goring, Derek G. and Nikora, Vladimir I. “Despiking Acoustic Doppler Velocimeter Data”. *Journal of Hydraulic Engineering*, Vol. 128, No. 1, January 1, 2002: 117 - 126.
- [11] Gupta, Karan and Anjali V. Kulkarni. “Implementation of an Automated Single Camera Object Tracking System Using Frame Differencing and Dynamic Template Matching”. *Advances in Computer and Information Sciences and Engineering*, 2008: 245-250.

- [12] Haehnel, R. B., and Daly, S. F. (2002). "Maximum impact force of woody debris on floodplain structures." ERDC/CRREL TR-02-2, US Army Corp of Engineers, Engineer Reserach and Development Center, 40 pp.
- [13] Haehnel R and Daly S. "Maximum impact force of woody debris on floodplain structures". J Hydraul Eng 2004; 2: 112–120.
- [14] Kobayashi Marcelo H, Genest R, Riggs H Ronald and Paczkowski K. (2012) "Simple hydroelastic impact models for water-borne debris". Proc IMechE Part M: J Engineering for the Maritime Environment; 226(2): pp. 170–179.
- [15] Kumagai, K., Oda, K., and Fujii, N. (2006). "Applicability of simulation model for drift behavior of containers due to tsunامي." Proc. Techno-Ocean 2006/19th JASNAOE Ocean Engineering Symposium, 6 pp.
- [16] Kriebel, David. "Impact Loads From Flood-Borne Debris". Prepared for American Society of Civil Engineers, 2000.
- [17] Madurapperuma, K. M. and Wijeyewickrema, A. C. (2010). "Nonlinear Behavior of Reinforced Concrete Columns impacted by a Tsunami Water-Borne Shipping Container." Proc. Seventh Int. Conf. Urban Earthquake Engineering (7CUEE) and Fifth Int. Conf. Earthquake Engineering (5ICEE), Tokyo, Japan, pp. 1795-1804.
- [18] Madurapperuma, K. M. and Wijeyewickrema, A. C. (2012). "Inelastic Dynamic Analysis of an RC Building Impacted by a Tsunami Water-Borne Shipping Container." Journal of Earthquake and Tsunami Vol. 6, No. 1.
- [19] Matsutomi., H., Sakakiyama, T., Nugroho, S., and Matsuyama, M. (2006). "Aspects of inundated flow due to the 2004 Indian Ocean tsunami". Coastal Engineering Journal Vol. 48(2): 167-195.
- [20] Matsutomi H. "Method for estimating collision force of driftwood accompanying tsunami inundation flow". J Disast Res 2009; 6: 435–440.
- [21] Mizutani N, Takagi Y, Shiraishi K, Miyajima S and Tomita T. "Study on wave force on a container on apron due to tsunamis and collision force of drifted container". Ann J Coast Eng 2005; 52: 741–745.

- [22] Mizutani, N., Takagi, Y., Shiraishi, K., Miyajima, S., and Tomita, T. (2006). "Forces on a container due to tsunami and collision force by drifted container." Proc. Second International Workshop on Coastal Disaster Prevention, pp. 63-71.
- [23] Nouri, Y, Nistor, I, and Palermo D. "Experimental investigation of tsunami impact on free standing structures". Coastal Engineering Journal 2010; 52: 4370.
- [24] NRC. "Preventing earthquake disasters: the grand challenge in earthquake engineering: a research agenda for the network for earthquake engineering simulation (NEES)". Technical Report for the National Research Council, Washington, DC, 2004.
- [25] Paczkowski, K., Riggs, H. R., Naito, C. J., and Lehmann, A. (2012). "A one-dimensional model for impact forces resulting from high mass, low velocity debris." Structural Engineering and Structural Mechanics, 42(6), pp. 831-847.
- [26] Piran Aghl, P., Naito, C. J., and Riggs, H. R. (2013) "Effect of additional non-structural mass on impact force and duration." In preparation.
- [27] Prasetya, G. S. , Healy, T. R. , de Lange, W. P. , and Black, K. P. (2008). "Extreme Tsunami run up and inundation flows at Banda Aceh, Indonesia: Are there any solutions to this type of coastal disaster?". Proc., Solutions to Coastal Disasters: Tsunamis 2008 Conf. , ASCE, New York, 1326.
- [28] Riggs, H.R., Cox, D.T., Naito, C. J., Kobayashi, M.H., Piran Aghl, P., Ko, H. T.-S., and Khowitar, E. (2013). "Water-Driven Debris Impact Forces on Structures: Experimental and Theoretical Program." Proceedings of the ASME 2013 32nd International Conference on Ocean, Offshore and Arctic Engineering, OMAE2013. June 9-14, 2013, Nantes, France.
- [29] Robertson, I. N., Carden, L., Riggs, H. R., Yim, S., Young, Y. L., Paczkowski, K. and Witt, D. (2010a) "Reconnaissance following the September 29, 2009 tsunami in Samoa, Research report UHM/CEE/10-01, Department of Civil and Environmental Engineering, University of Hawaii at Manoa, Honolulu, Hawaii, <http://www.cee.hawaii.edu/reports/UHM-CEE-10-01.pdf>.
- [30] Robertson, I., Chock, G. and Morla, J. (2010b). "Tsunami effects of the February 27, 2010 Chile earthquake. EERI preliminary reports, Earthquake Engineer-

ing Research Institute, Oakland, CA, <http://www.eqclearinghouse.org/20100227-chile/publishedreports>.

- [31] Rossetto T., Peiris, N., Pomonis, A, Wilkinson, S. M., Del Re, D., Koo, R., Gallocher, S. (2007). “The Indian Ocean tsunami of December 26, 2004: observations in Sri Lanka and Thailand.” *Nat Hazards* 42: 105 - 124.
- [32] Sarpkaya, T., and Isaacson, M. (1981). “Mechanics of wave forces on offshore structures”, Van NostrandRienhold, New York.
- [33] Dibble, T.L. abd Sollitt, C.K. (1989). “New Designs for Acoustic and Resistive Wave Profilers”. O.H Hinsdale Wave Research Laboratory. Oregon State University, Corvallis, Oregon, USA.
- [34] Yeom G-S, Nakamura T and Mizutani N. “Collision analysis of container drifted by runup tsunami using drift collision coupled model.” *J Disast Res* 2009; 4: 441–449.

APPENDICES

Appendix A: Notation

A.1 List of Variables

A_{struct}	Structural area the surface area of the debris specimen that makes contact with the load cell
d	Height of load cell measured from false bottom to center of load cell
E	Modulus of elasticity
F_d	Difference between measured hydraulic peak impact force and predicted in-air peak impact force
F_I	Measured instantaneous impact force
F_p	Peak force measured from debris impact
F_N	Peak force normalized by predict in-air impact force
F_r	Froude Number
H_{max1}	Offshore wave height
H_{max4}	Maximum depth of inundation flow
h_1	Water depth at the wave paddle
h_2	Water depth at the test region
J_p	Impulse calculated by integrating the impact force time series over the primary peak of impact
J_{30}	Impulse calculated by integrating the impact force time series over 30 ms after the beginning of the primary peak of impact
K	Stiffness
L	Length of debris specimen
m_0	Slope of best fit line relating impulse to impact velocity with $M_{NS} = 0$
m_{50}	Slope of best fit line relating impulse to impact velocity with $M_{NS} = 50.2$ kg
m_{99}	Slope of best fit line relating impulse to impact velocity with $M_{NS} = 99.4$ kg
M	Structural mass
M_{NS}	Non-structural mass
N	Number of trials
r	Draft of container
S	Wave paddle displacement
T_{erf}	Error function period used to generate wave condition

t	Time variable with $t = 0$ coinciding with the start of the wave paddle stroke
t'	Time variable with $t' = 0$ coinciding with the beginning of impact
t_i	Impact duration
t_N	Measured impact duration normalized by predicted value (Eq. 5.2).
u	Flow velocity in direction of onshore direction in the wave flume
u_{ADV}	Flow velocity measured using ADVs
u_{PIV}	Flow velocity measured using PIV
v	Measured instantaneous velocity
v_I	Impact velocity of debris specimen
w	Clearance (distance from false bottom to bottom of specimen at time of impact)
X	Pullback distance for In-Air tests
θ_i	Initial orientation of debris specimen
θ_f	Orientation of debris specimen at impact
θ_d	Change in orientation of debris during propagation toward impact
ϕ	Pitch angle

Appendix B: List of Experiments

B.1 NEES Notebook Naming Convention

Table B.1: List of Experiments with NEES notebook names included.

Experiment	Date(s)	Notebook Name	Type	Special Conditions	Specimen	Orientation	Nonstructural Mass	Load Cell	N
Hydrodynamics Test	7/16 – 7/20, 9/6 – 9/10	Hydrodynamics 1DHydroPlain	Hydrodynamics	no debris	none	N/A	N/A	none	60
In-Air Longitudinal Aluminum Test	7/30 – 8/13, 9/10 – 9/12	AirAlum AirAlumWP HeightLUWP AirSshapeRound AirSshapeStand InAirAlumSlow	In-Air	Repeatability, Different load cells, Contact Position, Nonstructural Mass	Aluminum	Longitudinal 0	– 99.4 kg	CLC-300K HSW-50K	72
In-Air Longitudinal Acrylic Test	8/3, 9/12 – 9/13	InAirAcrylic AirAcrylic	In-Air	Different mounting bolts for swinging	Acrylic	Longitudinal 0		CLC-300K	29
In-Air Pitch Angle Test	9/12	InAirAlumPitch	In-Air	Loosened off-shore cables to adjust pitch angle	Aluminum	Longitudinal 0		CLC-300K	10
In-Air Transverse Test	9/13	InAirBroad	In-Air	Swinging from under cart	Aluminum	Transverse 0		CLC-300K	12
In-Water Longitudinal Aluminum Test	8/15 – 9/5	1DHydroAlum	In-Water	Longitudinal Guide Wires	Aluminum	Longitudinal 0	– 99.4 kg	CLC-300K	195
In-Water Longitudinal Acrylic Test	9/14 – 9/18	1DHydroAcry	In-Water	Longitudinal Guide Wires	Acrylic	Longitudinal 0		CLC-300K	56
In-Water Transverse Aluminum Test	9/19 – 9/21	BroadHydroAlum	In-Water	Transverse Guide Wires	Aluminum	Transverse 0	– 50.2 kg	CLC-300K	46
In-Water Unconstrained Test	9/24 – 9/25	FreeHydroAlum257	In-Water	No Guide Wires	Aluminum	All	0	CLC-300K	31

